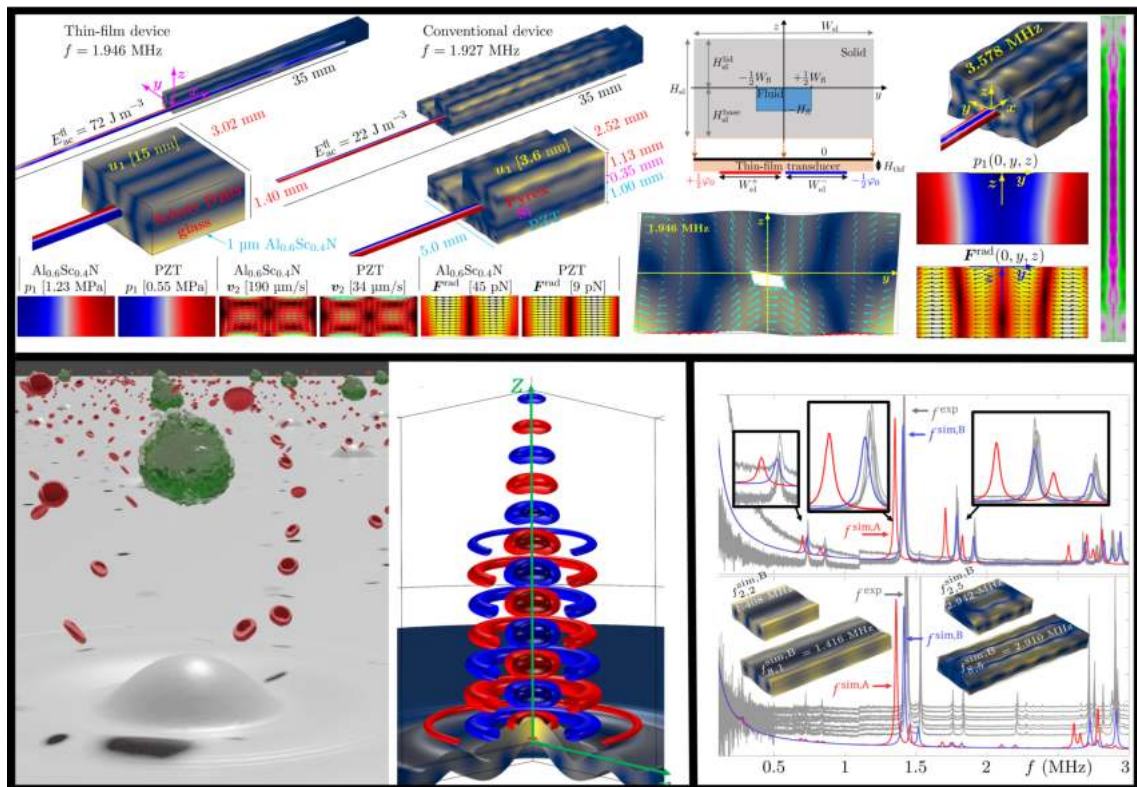


André Gugele Steckel

Theory and modeling of thin-film actuation in microscale acoustofluidics



PhD Thesis

Advised by Professor Henrik Bruus

Department of Physics
Technical University of Denmark

31 August 2021

Cover illustration: A collage of the work done in this thesis. Top pane show simulations of thin-film transducers used for acoustic particle handling, adapted from Ref. 1. Bottom right show thin-film transducers used for *in situ* determination of parameters, adapted from Ref. 2. Bottom left show an illustration of cancer cells be levitated and trapped in a fluid above a membrane, adapted from Ref. 3.

Theory and modeling of thin-film actuation in microscale acoustofluidics

Copyright © 2021 André Gugele Steckel. All Rights Reserved.
Typeset using L^AT_EX.

Department of Physics
Technical University of Denmark
DTU Physics Building 309,
DK-2800 Kongens Lyngby,
Denmark

<http://www.fysik.dtu.dk/microfluidics>

Supervisor: Professor Henrik Bruus from Technical University of Denmark.
Co-Supervisor: Professor Thomas Laurell from Lund University.

Abstract

Acoustofluidics is the field that studies sound in fluids which has been a steadily progressing research field stemming back over 200 years. From back with the study of motion of small particles driven by air currents above Chladni plates, vibrated by dragging a violin bow on the edge of metal plates. Till today with systems manufactured in microelectromechanical systems (MEMS) compatible clean rooms, where they are designing and using devices with micrometer precision in liquid filled channels the widths of a few hairs. Especially the interplay between acoustofluidics and microfluidics has as of late shown many interesting applications, utilizing in part the acoustic radiation force and the acoustic streaming to move particles submersed in fluids, in what is generally called acoustophoresis.

These acoustofluidic devices have in the literature seen uses from, but not limited to, inkjet printers to cancer cell sorting, continuous flow separation of blood cells from blood plasma, label-free trapping and sorting, microfluidic mixers, acoustic tweezers, and much more. The field is a rapidly expanding and evolving field and there are still room for innovations and improvements. In particular are there two problems that the field is facing that relates to this thesis. One of the common way to produce acoustofluidic devices to this day is to fabricate it in ways that make them difficult to reproduce results from device to device, as well as make them difficult to mass produce, by for example gluing lead zirconate titanate (PZT) piezoelectric transducers to the devices. This is done in ways that make each device different from each other, since small changes in the glue makes large difference end results. The acoustofluidic device being based on the use of PZT piezoelectric transducers also means their systems contains lead, which for example the European Union has legislated in order to out phase, as lead is an environmentally hazardous material. However lead is a difficult material avoid in piezoelectric transducers, as it works much better than most other lead free alternatives.

This thesis has investigated ways to implement thin-film piezoelectric (PZE) transducer into acoustofluidic devices. One thin-film PZE that is commonly used in clean room fabrication and which is MEMS compatible is aluminum nitride (AlN), and its newer and more exotic variant, aluminum scandium nitride (AlScN) which is a stronger PZE material, but more difficult to manufacture. How these thin-films can be used to actuate acoustofluidic devices, understanding the underlying mechanism, as well as comparing our model to experiments and using that model to make predictions on thin-film acoustofluidic devices have been the main goal of the thesis. This has been achieved in this thesis and the results have been done in two published papers and one in which is still in preparation.

In the first article an ensemble of millimeter-sized glass blocks with AlN thin-film on top

and different top electrode patterns were investigated. In the Paper I it is described how they were made, characterized, simulated, and how the Young's modulus and Poisson's ratio of the glass was fitted by minimizing the difference between measured impedance spectra and the calculated impedance spectra from the simulations. These device showed high reproducibility, that glass bulk devices can be actuated by a thin-films, and that good agreement with between simulations and measurements could be made. It was found that after having fitted Young's modulus and Poisson's ratio of the glass the relative deviation between simulated and measured resonance peaks of $(-0.5 \pm 0.1)\%$, which was a order of magnitude lower than the parameter values from the manufacturer, and therefore showed that this could be a method for *in situ* characterization of parameters. These parameter values are important, as they play a central role in the accuracy of our predictive simulations.

The second paper is about the acoustofluidic applications that lies in using PZE thin-films for driven bulk acoustofluidic devices. Building upon the confirmation of the solid mechanical part of the model in the first paper, we have simulated glass devices with microfluidic channels, of a few hundreds micrometers in width and height, actuated with thin-film transducers of the type AlN, AlScN, and PZT thin-films all showing acoustofluidic behavior. In order to compare how the acoustofluidics, such as acoustic streaming and radiation force, compares to a traditional device we simulate a conventional device driven by a bulk PZT that constitutes 57% of the total volume of the device whereas the thin-film transducer only constitutes less than 0.1% of the volume. The pressure, acoustic streaming, and acoustic radiation force fields were then compared qualitatively between the two types of devices and it was found that the devices preformed comparably, and this was seen again when comparing them in more quantitative terms, such as the average acoustical energy in the fluid, and the average time it took in each device to focus particle in the center of the channel. Different aspects of the mechanism were investigated, such as the underlying physical mechanism that governs the principle of thin-film actuation, how the mechanical quality factor and thickness of the film does not effect the system significantly. Also shown was how electrode patterning can enhance the acoustic modes and that the system also works for the standing full-wave solution in the channel, that the modes look very clean and are easy to identify, and that the system is robust to channel off-set.

The last significant result in the thesis is the use of 1- μm -thick AlScN thin-film actuator on a circular 10- μm -thick membrane of silicon. The membrane investigated then has the electrode on the thin-film patterned in order to increase the mechanical actuation of the membrane which allows for the effective actuation of higher order membrane modes. These higher order membrane modes then allows the pressure nodes to have a focus above the center of the membrane. The patterning increases the pressure hot spot for the fourth order mode many fold and the radiation force that follows, as a second order field, scales squared with this increase. The mechanism is investigated and shown that the system is a combination of standing and traveling waves, which stems from waves traveling out from the anti-nodes in the membrane. This amplification of the membrane mode from effective electrode patterns is even more pronounced when going to higher order modes, and for such a device it is shown that the acoustic hot spot above the center of the membrane gives

rise to acoustic trapping of cancer cells of the type MCF-7, when tuning the medium such that the acoustic contrast factor for the cells are negative, by adding Iodixanol which is a biologically inert fluid that is more compressible than water. It is shown that even with acoustic streaming there is a hot spot, and the that the barrier that needs to be overcome when entering the trap can be minimized by playing with parameter values of the liquid that the cells are submersed in.

The final thoughts on the thesis are given in the conclusion and outlook where the results that were shown this thesis summarized and it is discussed how they might be used in the future, as well what would be investigated had the PhD project continued.

Resumé

This is the obligatory abstract in Danish. It is equivalent to the abstract except for the language.

Akustofluidik er et forsknings felt der handler om studiet af lyd i væsker, hvilket er et forsknings område der går over 200 år tilbage. Fra studiet af små partikler der driver rundt in luft hvirvler over en Chladni plade i Ørsteds tid, som sættes i vibrationer af en violin bue trykket over kanten på af en metal plade, til den dag i dag hvor man fabrikere systemer i mikroelektromekaniske systemer (MEMS) og ren rum, hvor de designer systemer med mikrometer præcision og væske kanaler på brede og høje af nogle få menneske hår. Specielt sammenspillet mellem akustofluidik og mikrofluidic har på det seneste kastet mange interessante applikationer af sig, specielt ved hjælp af den akustiske strålings kraft og the akustiske drevet strømning som bruges til at flytte partikler i væsker, generelt kaldet akustophorese.

Disse akustofluid systemer er i litteraturen blevet brugt til alt fra inkjet printere til sortering af kræft celler, kontinuert flow separation af blod celler fra blod plasma, mærkat-fri indfangelse og sortering af celler, mikrofluid mikserer, akustisk pincetter, og meget mere. Forsknings feltet er i konstant udvidelse og udvikling, alligevel er der stadig plads til mere udvikling. I sær er der to typiske problemer i forsknings feltet som relatere til denne afhandling. En af de typiske måder at fabrikere akustofluid systemer på er ved at f.eks. at lime en blyzirkonat titanat (PZT) til systemerne, hvilket giver ikke særlig reproducerbare resultater, og gør der det svært at masse fabrikere disse system. Den måde det typisk gøres på gør hvert system unik, eftersom at små ændringer i limlaget gør store forskelle i slut resultatet. Et andet problem med det system er at det indeholder bly, som ved europæisk lovgivning er ved at blive faset ud af Europa, siden bly er et miljøfarligt materiale, og derfor skal der ledes efter alternativer.

Denne afhandling har undersøgt hvordan man kan implementere tynd-films piezoelektriske (PZE) transducer i akustofluid systemer. En traditionel PZE tynd-films transducer er aluminiumnitrid (AlN) som er MEMS og ren rums compatible, og den nye mere eksotiske variant aluminiumscandiumnitrid (AlScN) som er et stærkere PZE materiale dog med den hage at den er svære at producere. Hvordan disse tynd-film kan bruges til at aktuerer akustofluid systemer, forståelsen af den underliggende mekanisme, såvel som at sammenligne vores model med eksperimenter har været det overordet formål i denne afhandling. Det har i afhandlingen været opnået igennem to publiceret artikler og en der stadig er under udvikling.

I den første artikel bruges en ensemble af millimeter størrelse glas blokke med AlN tynd-film på toppen med forskellige topelektrode design til at undersøge deres egenskaber. I første artikel er der beskrevet hvordan de er lavet, karakteriseret, simuleret, og hvordan Youngs modulet og Poissons forholdet i glasset var fittet ved at minimere forskellen mellem impedans spektret fra målingerne og simuleringerne. Disse enheder viste at systemet er ganske reproducerbart, at glas blokke der er over 500 gange større end tynd-filmen kan aktueres af tynd-films transducere, og at der er god overensstemmelse mellem simuleringer og eksperimenter. Efter fittet af Youngs modulet og Poissons forholdet i glasset var der en relativ afvigelse mellem resonans toppene i simuleringen og eksperimenterne på $(-0.5 \pm 0.1)\%$, hvilket var en størrelses orden lavere end for de originale parameterværdier. Disse parameterværdier spiller en afgørende rolle for hvor god vores modeller passer med eksperimenter og hvor gode de er til at forudsige nye fænomener.

Den anden artikel handler om de appikationer der ligger i at bruge PZE tynd-film for at drive en tykke akustofluid systemer, hvor tykke PZT transducere sammenlignes med en tynd-films transducere der er tusind gange mindre. Der bygges videre på den gode overensstemmelse der blev fundet i glas blok systemet, hvor der nu også er en fluid kanal indbygget på et par hundred mikrometer i højde og brede. Systemet undersøges med AlN, AlScN, og PZT tynd-films transducere, og for alle tre typer ses der akustofluid aktion i fluid kanalen, i form af akustisk strømning og akustisk strålings kraft. Disse sammenlignes med en traditionel enhed der drives af en mere traditionel tyk PZT, hvor PZT transducere udgør 57% af det totale volumen i den traditionelle enhed, og kun udgør 0.1% volumen i tynd-films enheden. Det akustiske tryk, strømning og strålings kraft sammenlignes på tværs af enhederne, i en mere kvalitativ sammenligning, hvor det var set at de to typer af aktivering gav nogenlunde de samme akustiske felter. Derefter blev der lavet en mere kvantitativ sammenligning hvor den gennemsnitlige akustiske energi densitet i væsken og den gennemsnitlige tid det tog at fokusere mikropartikler in kanalens center var sammenlignet. Forskellige aspekter af den underliggende mekanisme var undersøgt, så som det grundlæggende fysiske princip bag aktiveringen og hvordan den mekaniske kvalitets faktor, eller dæmpningen i filmen, ikke spillede en rolle for systemet samt at tykkelsen af filmen heller ikke ændrede systemet synderligt. Det var også undersøgt hvordan elektrode mønstret spillede en rolle for at øge det akustiske system i det fuld stående bølge system der også blev undersøgt. Det sås at enhedens resonanser var meget symmetriske og nemme at genkende, og at systemet var robust overfor at kanalen kunne placeres en smule væk fra symmetri linjen uden at det gjorde den store forskel.

Det sidste af de betydelige resultater i denne afhandling kom ved at undersøge en 1 μm tyk AlScN tynd-films transducer på en 10 μm tyk silicium membran. Det er derefter undersøgt hvordan membranen påvirkes af at elektroderne på tynd-film transducere mønstres sådan at membranen effektivt kan aktueres på dens højere ordens mekaniske membran modes. Disse højere ordens membran modes giver en tryknode der har et maksimum der er placeret over membranen, for den fjerde ordens membran mode. Den effektive aktivering af den højere ordens membran mode giver et meget kraftigere trykfelt, når elektrode mønstret er optimeret, hvilket gør at højere ordens akustiske effekter som f.eks. den akustiske strålings kraft er endnu kraftigere, siden de skalere med første ordens felter i anden potens. Denne forøgelse er endnu kraftigere for højere orden membran modes og

for sådan et system var det fundet at trykfeltet fra en højere ordens membran mode kunne lave et kraft felt der kunne fange og fastholde kræft celler af typen MCF-7, hvis vel og mærke væsken ændres sådan at cellerne havde negativt akustisk kontrast faktor. Dette var gjort ved at bruge Iodixanol, som er en væske der ikke reagere med de biologisk celler, men som er mere komprimerbar væske end vand. Det var vist at selv med den akustiske strømning så var der et minimum hvor celler kunne fanges over membranen. Det var også vist at ved at ændre parameterverdierne i væsken så kunne den kraft barrier som cellerne skal overkomme for at komme ind i fælden minsket så meget at den næsen var væk.

De sidste tanker for afhandlingen samles op i en konklusion og udsyn, hvor resultaterne sammenfattes og det diskuteres hvordan de potentielt kunne bruges i fremtiden. Der gives også et kortoverblik på hvad der gerne ville have været undersøgt hvis der havde været mere tid i projektet.

Preface

This thesis is submitted as partial fulfillment for candidacy of a degree of *Doctor of Philosophy* (PhD) from Technical University of Denmark (DTU). The work presented in this thesis was carried out from 1 September 2018 to 31 August 2021, in the Department of Physics, Section of Biophysics and Fluids, in the Theoretical Microfluidic Group, with Professor Henrik Bruus, from DTU, as main supervisor and Professor Thomas Laurell, from Lund university, as co-supervisor. This PhD project was funded by the *BioWings* project which in turn was funded by the European Union's Horizon 2020 *Future and emerging technologies* (FET open) program with grant number 801267. The project included a 3-month external research stay at École polytechnique fédérale de Lausanne (EPFL), from 20 October 2019 to 20 December 2019, which was supported by the funds Otto Mønstedts, Reinholdt W. Jorck and Wife, and Augustinus. Of the 36 months of PhD study, 6 of those were spend taking obligatory courses, and 18 of what was left has been under the COVID-19 pandemic, with large portions under strict lock down.



André Gugele Steckel
Department of Physics
Technical University of Denmark
31 August 2021

Acknowledgments

This PhD thesis is the result 3 years of work, and without the many people surrounding me this thesis would not have been the same. A special thanks goes out to my supervisor Prof. Henrik Bruus, whose dedication to, and understanding of, the field of acoustofluidics has been an invaluable support. A thanks goes out to the Theoretical Micro Fluidics (TMF) group alumni who helped define the field, and upon which shoulders I stood so I could do the research that I did, and in particular Dr. Nils R. Skov, Dr. Jacob S. Bach, and Wei Qiu, whom I had the pleasure of working with. A thanks goes to the current members of TMF Assoc. Prof. Massimiliano Rossi, PhD stud. Jonas H. Jørgensen, William N. Bodé, Fabian Lickert, and Bjørn G. Winckelmann, for making a enjoyable work environment. I would like to thank the BioWings team for a nice collaboration and the EPFL team where I did my external research stay. Lastly, but not least, I would also like to thank my family and friends for their support and understanding when my attention was focused on my studies.

Contents

Abstract	iii
Resumé	vii
Preface	xi
Acknowledgments	xiii
List of publications	xvii
List of figures	xix
List of tables	xxi
List of symbols	xxiii
List of symbols	xxiii
1 Introduction to acoustofluidics	1
1.1 Acoustofluidics - top down approach of Sound	2
1.2 Microfluidic real world applications for acoustofluidics	3
1.3 Acoustofluidics in this thesis	4
1.4 Thesis structure	5
2 Theory	7
2.1 Fundamental equations and definitions	8
2.1.1 Solidmechanical equations and Voigt notation	9
2.2 Perturbation expansion in fluid	12
2.2.1 1st order fields	13
2.2.2 2nd order field	14
2.2.3 Effective boundary conditions and acoustic streaming	14
2.2.4 Radiation force	17
2.2.5 Particle velocity	18
2.2.6 Acoustical energy density	19
2.3 Axisymmetric models	20

3	Numerical modeling and validation of FEM in COMSOL	23
3.1	Finite element method	23
3.1.1	Weak form formulation	24
3.1.2	Boundary conditions	24
3.2	COMSOL implementation	25
3.2.1	Material parameters	26
3.2.2	Adaptive frequency stepping	29
3.3	Numerical validation	30
3.3.1	Axisymmetric compared to full 3D	30
3.3.2	Mesh convergence analysis	33
3.3.3	Comparison with experiments	34
3.3.4	Mesh of thin-films and electrodes	34
4	Summery of Results	37
4.1	Paper I	37
4.2	Paper II	42
4.3	Paper III	49
4.4	Conference Paper I	50
4.5	Minor results I - Optimization of device width	53
4.6	Minor results II - GHz acoustofluidic dampening	54
5	Publications	57
5.1	Paper I: Phys. Rev. Appl. 16 , (2021)	58
5.2	Paper II: J. Acoust. Soc. Amer. 150 , 634-645 (2021)	70
5.3	Paper III: Manuscript in preparation	88
5.4	Conference Paper I: Acoustofluidics 2020	104
6	Conclusion and outlook	107
6.1	Conclusion	107
6.2	Outlook	108
	Bibliography	112

List of publications

Peer-reviewed journal papers

- I André G. Steckel, Henrik Bruus, Paul Muralt, and Ramin Matloub, *Fabrication, Characterization, and Simulation of Glass Devices with AlN Thin-Film Transducers for Excitation of Ultrasound Resonances*, Phys. Rev. Appl. **16**, (2021). [2]
- II A. G. Steckel and H. Bruus, *Numerical study of bulk acoustofluidic devices driven by thin-film transducers and whole-system resonance modes*, J. Acoust. Soc. Amer. **150**, 634-645 (2021). [1]

Papers pending review

- III André G. Steckel and Henrik Bruus, *Numerical study of acoustic cell trapping above circular elastic membranes driven by thin-film transducers with patterned electrodes*, Manuscript in preparation (*NOT peer-reviewed yet*) [3]

Patent

- I André G. Steckel, Henrik Bruus, and Thomas Laurell, [*Title under Non-disclosure agreement until August 2022*], Patent application 21154133.9, submitted 28 January 2021.

Peer-reviewed conference contributions

- I André G. Steckel and Henrik Bruus, *Numerical studies of acoustic actuation in glass capillaries by thin-film piezoelectric transducers*, The Swedish Center for Acoustofluidics and Cell Separation (SWECACS), 17 December 2018, **Oral presentation**.
- II André G. Steckel and Henrik Bruus, *Mode anti-crossing in thin-film-membrane-driven acoustofluidics*, Complex Motion in Fluids 18-24 August 2019, **Poster presentation**.

-
- III André G. Steckel and Henrik Bruus, *Simulation of $\text{Al}_{0.6}\text{Sc}_{0.4}\text{N}$ thin-film-membrane-driven acoustophoresis*, Acoustofluidics conference, 26-28 August 2019, **Poster presentation**.
- IV André G. Steckel and Henrik Bruus, *Numerical simulation of acoustic streaming generated by GHz AlN-thin-film transducers on AlN-SiO₂-Bragg-reflector substrates*, Acoustofluidics conference, 26-27 August 2020, **Oral presentation**. Remark: Contributed talk at virtual conference
- V André G. Steckel and Henrik Bruus, *Numerical investigation of thin-film transducers for exciting whole-system resonances in bulk acoustofluidics devices*, Acoustofluidics conference, 26-27 August 2021, **Oral presentation**. Remark: Contributed talk at virtual conference

List of Figures

1.1	Introduction figure showing an artistic illustration of a acoustofluidics application example from this thesis.	1
2.1	Polystyrene particles being focused in acoustofluidic microchannel.	19
3.1	Sketch of adaptive frequency stepping method.	29
3.2	Shows the the fields in both full 3D and 2D axisymmetric simulations for a 1- μ m-thick Pyrex membrane.	31
4.1	Paper I - Shows the design of glass devices and electrode patterns	38
4.2	Paper I - Impedance measurements on the devices A8-G8 and C2-G2	40
4.3	Paper I - Simulations of glass devices and comparison of calculated impedance spectra to measured	41
4.4	Paper II - Sketch of thin-film actuated acoustofluidic bulk device.	43
4.5	Paper II - Cross section of an simulation of a device showing the core concept of the thin-film actuated bulk devices.	43
4.6	Paper II - Compares thin-film actuated device with bulk actuated device in terms of first and second order fields	44
4.7	Paper II - Shows device dependence on thin-film Q-factor and thickness	46
4.8	Paper II - Simulations of full-wave standing pressure mode in channel and the effect of electrode patterning	47
4.9	Simulations and optimization of the width of the device in Paper II	52
4.10	Simulations of GHz acoustics pressure, displacement, steaming and dampening.	54
4.11	Simulation of GHz acoustics pressure and displacement in axisymmetric system.	55

List of Tables

3.1	Parameter values of water	26
3.2	Parameter values of Iodixanol	26
3.3	Parameter values of piezoelectric materials AlN, AlScN, and PZT	27
3.4	Parameters values of solids, Schott D263, Pyrex, and Silicon.	28
3.5	Parameters for 5- μm -diameter polystyrene particles	28

List of symbols

Symbol	Description	Unit
c	Speed of sound	m s^{-1}
c_{fl}	Speed of sound in fluid	m s^{-1}
c_{lo}	Longitudinal speed of sound	m s^{-1}
c_{tr}	Transverse speed of sound in fluid	m s^{-1}
f	Frequency	Hz
λ	Wavelength	m
\mathbf{r}	Spacial coordinate	m
t	Time	m s^{-1}
ρ	Density	kg m^{-3}
ρ_{sl}	Density in the solid	kg m^{-3}
ρ_0	Zero order density in fluid	kg m^{-3}
ρ_1	First order density in fluid	kg m^{-3}
ρ_2	Second order density in fluid	kg m^{-3}
ρ_{pa}	Second order density in fluid	kg m^{-3}
\mathbf{v}	Velocity	m s^{-1}
$\boldsymbol{\sigma}$	Stress tensor	N m^{-2}
p	Pressure	Pa
p_0	Zero order pressure in fluid	Pa
p_1	First order pressure in fluid	Pa
p_2	Second order pressure in fluid	Pa
η_0	Dynamic viscosity	mPa s
η_0^{b}	Bulk viscosity	mPa s
\mathbf{u}_1	Displacement	m
\mathbf{S}	Strain tensor	1
\mathbf{C}	Coupling tensor	Pa
\mathbf{E}	Electric field	V m^{-1}
φ	Electric potential	V
\mathbf{e}	Piezoelectric coupling tensor	C m^{-2}
\mathbf{D}	Dielectric field	C m^2
$\boldsymbol{\varepsilon}$	Permittivity matrix	F m^{-1}
ω	Angular frequency	rad s^{-1}
i	Imaginary number	1

Symbol	Description	Unit
κ_0	Compressibility in the fluid	TPa ⁻¹
κ_{pa}	Compressibility in particle	TPa ⁻¹
\mathbf{v}_1	First order velocity field in the fluid	m s ⁻¹
\mathbf{v}_2	Second order velocity field in the fluid	m s ⁻¹
\mathbf{v}_1^δ	Divergence free velocity field	m s ⁻¹
\mathbf{v}_1^d	Rotation free velocity field	m s ⁻¹
k_s	Boundary layer dampening length scale	m ⁻¹
δ	Viscous boundary layer length scale	m
ζ	Transverse coordinate	m
ϵ	Small factor	1
d	Compressional length scale	m
V	Velocity in the solid	m
η	Parallel coordinate	m
ξ	Parallel coordinate	m
k_c	Compressional wave number	m
Γ_{fl}	Damping coefficient in fluid	1
T_0	Time of a full period	s ⁻¹
ν_0	Kinematic viscosity	m ² s ⁻¹
\mathcal{L}_{ac}^d	acoustic Lagrangian density	J m ⁻³
\mathcal{S}_{ac}^d	acoustic energy flux density	J m ⁻² s ⁻¹
\mathbf{F}_{rad}	Acoustic radiation force	N
\mathbf{F}_{drag}	Drag force	N
\mathbf{F}_{garv}	Buoyancy corrected gravitational force	N
\mathbf{F}_{rad}	Radiation force	N
a	Particle radius	m
f_0	Monopole scattering coefficient	1
f_1	Dipole scattering coefficient	1
U^{rad}	Gorkov potential	J
E_{ac}^{fl}	Average acoustic energy density	J m ⁻³
V_{fl}	Fluid volume	m ³
x	Cartesian coordinate	m
y	Cartesian coordinate	m
z	Cartesian coordinate	m
r	radial coordinate	m
ϕ	Angular coordinate	1

Symbol	Description	Unit
$\hat{\mathbf{I}}$	Unit tensor	
∂_t	partial time derivative	
$\nabla \cdot$	Divergence operator	
∇	Gradient operator	
$\tilde{\cdot}$	Full time dependence	
$\langle \cdot \rangle$	Time average	
$\nabla_{\parallel} \cdot$	parallel divergence operator	
\mathbf{J}	Generalized flux tensor	
\mathbf{F}	Generalized force vector field	
h	FEM solution function	
Θ_n	FEM test function	
\mathbf{N}	Flux condition on the boundary	
\mathbf{n}	Normal vector	
C	Convergence parameter	
g_n	n 'th solution to field g	
g_{ref}	Reference solution to field g	
Ω	Computational domain	
$\partial\Omega$	Domain boundary	

Chapter 1

Introduction to acoustofluidics

This section is the introduction chapter to the PhD thesis and will contain a short introduction to the field of acoustofluidics, by taking a top-down approach starting from a more broad reaching and general description of sound and music to how this is connected to acoustofluidics in microfluidic channels the width of a few human hairs. Then a more technical description of the acoustofluidic field and references to state-of-the art literature in this rapid expanding field. The acoustofluidics that relates more specific to this thesis is then explained in more depth. Lastly the thesis structure is explained.

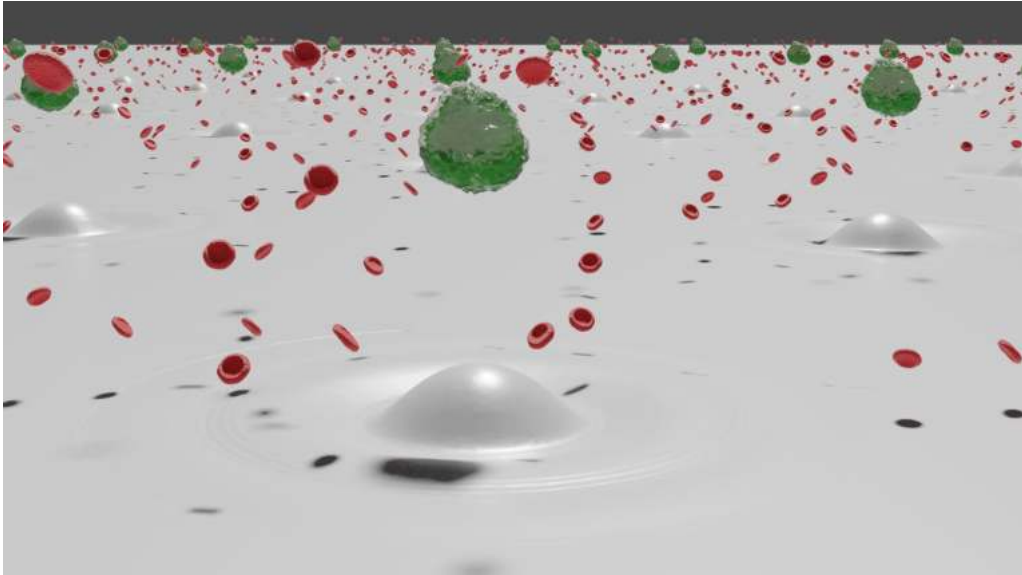


Figure 1.1: Artistic illustration of a acoustofluidic application discussed in this thesis. In the illustration cancer cells (green) are levitated and trapped above an array of membranes (grey surface), in a fluid with red blood cells (red) which are not trapped. The cancer cells can then be studied with them sedimenting. Further discussed in Paper III, Section 5.3. Adapted from Ref. 3

1.1 Acoustofluidics - top down approach of Sound

Acoustics is the study of sound and therefore acoustofluidics is the study of sound in fluids, and it is this research field that this thesis will be revolving around. Most people are familiar with sound, as they grow up with the ability to hearing their surroundings, before they can walk or talk. As one of the senses that just seems to be there as we develop, most people take it for granted and often just accept it without explanation. Sound is in its fundamental nature simply mechanical vibrations that we see in solids, like a wineglass struck with a spoon, or fluids, such as the air around the wineglass which allows the sound to travel from the wineglass to our ears. In this context a solid is something than can uphold tangential forces, where as fluids can not, and the term fluids cover both liquids and gasses. Sound needs a medium to travel trough because it is needs the traveling compression and decompression in the mechanical stresses of the material to propagate. Like when springs are compressed and released they will spring back, do does the materials that can transmit sound. These material could be considered as a series of minute springs, where when sound travels through it would be like a chain reaction of small springs pulling and pushing on each other in turn. One such phenomenon could be a sharp push on air, for example from a loud speaker, then the air right next to it will also experience the push, and the effect would travel outward though the medium at the speed of sound, because of this traveling mechanical stress.

The vibrational stresses that can be exerted in a bulk fluid are compressional in nature, which is fluctuations in the pressure of the fluid, which gives rise to longitudinal waves. On the other hand solids can maintain not only longitudinal, or compressional, stresses but also transverse, or shear, stresses, and therefore both longitudinal and transverse waves exist in solids. Waves will travel though mediums at the mediums speed of sound, c , and therefore if the waves are actuated at specific frequency, f , then the wavelength is $\lambda = \frac{c}{f}$. The human hearing is typically capable of discerning frequencies in the range from 20 hertz (Hz) and up to 20 kilohertz (kHz), and with a speed of sound in dry air at 20 °C is around 343 meters per second[4] the wavelength of the audible range is around 17 m to 1.7 cm. Music instruments that rely on the acoustocal resonances typically follow a similar scheme where larger instruments produce deeper notes, lower frequency and larger wavelengths, and smaller version of the same instrument produce higher notes, higher frequencies and smaller wavelengths. A typical example would be the violin family with the large contrabass producing deep notes and the smaller violin producing higher notes.

Sound waves come in both traveling and standing waves. Standing waves can be produced by interference of traveling waves, and one typical example is waves interfering with its reflections in an acoustical cavity, such as guitar. The waves in an acoustical cavity match the round trip of the waves in the system, such that when they are reflected on the surfaces, they interfere constructively with them self, and therefore over many oscillation sound is amplified. This is used many in different types of instruments, such as violins or guitars, to selectively amplify some frequencies and not others by designing the shape and the cavity of the instrument.

Sound waves at interfaces between different mediums experience reflections and re-

fractions, and one of the applications of this that most people are familiar with are the ultrasound scanning, used to noninvasively scan internal organs or fetuses. This is based on producing ultrasound, that is to say sound at the frequency above the limits of the human hearing, and to picking up the reflected and scattered waves to reproduce a image of the scanned medium.

All these properties explained in this short general section has been to introduce acoustofluidics in terms that are familiar to a general audience. Many of the same ideas and concepts are still valid when going to a regime unfamiliar to many, acoustofluidics in microfluidics, and therefore the general introduction can hopefully help the novice in such fields to visualize and understand it better.

1.2 Microfluidic real world applications for acoustofluidics

Microfluidics is the regime of fluidics where the critical length scale is in the micrometer range, from 1 μm to 1000 μm , where a micrometer is a thousand of a millimeter. In this regime fluids such as water behave very differently from what we are used to in our everyday life, and yet such fluids exist in every person, in that their blood vessels which can be less than 10 micrometers in diameter in the capillaries[5]. Working with microfluidics opens up for handling of small amounts of fluids at the time, and has spawned a field of research called lab-on-a-chip technology which, as the name suggest simulate the operations that a lab might do in some specific diagnosis, identification, or classification, but which can be handled on a chip[6–9]. Among the many lab-on-a-chip applications to choose from, one could highlight the use of many arrays on a chip for genome sequencing, by for example Nanopore DNA detection, that over the last decades have brought whole genome DNA sequencing down by orders of magnitude in cost, to a point where it is possible to do on a diagnosis basis [10, 11].

In microfluidics the momentum in the fluid usually plays a much smaller role compared to the viscosity[12]. This makes it so that laminar flows are typical and turbulent flows are not[13]. This comes with its own advantages and disadvantages, one being that fluid flows in a channel will in general not mix such that fluid inserted from the right in the channel will stay on the right, while the fluid moves trough the channel. This opens up possibilities such as for example placing cells in the right side of a channel they will usually stay in the right side, which can be used as a feature in the design. It can also be a problem as many lab operations require that some fluids be mixed for various reasons, and something that in larger fluid channels are a given, for example that diffusion there will be some mixing, is no longer the case without specifically designed mixers.

Blood is not only a good example of microfluidic flows in the body, but in general also a very interesting fluid to work with because it can be used to diagnose a lot of different conditions, such as sepsis[14, 15], early detection and diagnosis of circulating tumor cells[16–18], and many other applications, and therefore the handling, sorting, up concentrating, and manipulation of cells in microfluidics are important. There are many techniques out there for this purpose, however a promising candidate for doing this is acoustofluidics, as it is a label free[19] and gentle method for archiving this, and partly

therefore it has risen to prominence in recent years.

Acoustofluidics is one of the tools that have applications in microfluidics, that range from up concentrating cells in small volume or droplets[20–24], cleaning cells by moving them one fluid to and other[25, 26], to separate cells based on size label free[19, 27] or acoustical impedance[26], to trapping cells for changing the suspension fluid[28, 29], to selective sorting of individual cells[30], to mixing of fluids[31–34], and manipulation in many forms like acoustic tweezers[35–38], and acoustic levitation[39–50].

Acoustofluidics in microfluidics is a field that spans many orders of magnitude in frequency, from kHz regime[51, 52] which uses sharp edge structures to generate streaming to the GHz[53–55] where they use also use it to generate streaming but also other types of particle manipulation and trapping by actuating close to the bulk acoustic resonance of the thin-films.

The list of applications are long, but in general fall into categories of bulk acoustic wave (BAW) devices[56–60], surface acoustic wave (SAW) devices[61], and membrane devices[60, 62, 63]. Some use acoustic radiation force[64–72], which works by the mechanism that acoustic waves that scatters off cells or particles changes the momentum of the outgoing wave, which then will effect the cells or particles with a force. Some use the acoustic streaming[73–76], which is the time averaged effect of the nonlinear term in Navier–Stokes to generate flowrolls, either by bulk attenuation[77] or by boundary driven streaming[78]. These are used for acoustophoresis, meaning motion by sound, and it has been utilized in the manipulation and trapping of cells and particles in fluids by ultrasound[79–83], particle separation in flow[81, 84, 85], and many of the previously named applications also rely on these phenomenon.

The field of acoustofluidics is driven by a creative community, which shows a lot of different applications and the methods for archiving these. The field is still flourishing and developing rapidly with avenues for further exploration. In Section 1.3 will be discussed some of the thing that this thesis has been worked on specifically.

1.3 Acoustofluidics in this thesis

While acoustofluidics is a well developed and mature field, there are still challenges, some which will be investigate in this thesis. Each sub-field within acoutofluidic has their own advantages, disadvantages, possibilities, and limitations. This thesis has primarily looked at bulk acoustic wave (BAW) systems and investigated how thin-film technology could find applications in such systems. BAW systems can sometimes be tricky, and getting reproducible results from two devices, designed to be numerically equal can sometimes be difficult, as small details can have large effects in a high quality-factor (Q-factor) system. Some of the ways devices are produced today have many elements that critical for the performances of the devices, such as the glueing of piezoelectric actuators to the devices by hand, where changes in the glue layer thickness and uniformity of only a few tens of micrometers off can have large impacts on the device[86]. Sometimes even production tolerances from device to device can be large enough such that the acoustic resonances are not predictable enough for mass fabrication. This is a problem from an industrial point

of view. Not all acoustofluidic devices systems have these problems, and a great example of how reliable the systems can be is the droplet dispensers in ink-jet printer which shows that microscale acoustofluidics do work in an industrial environment.

An other problem is that many devices use lead zirconate titanate (PZT) as the actuator, since PZT has such large piezoelectric coupling coefficients compared to most other piezoelectric materials, and therefore it is one of the most common piezoelectric material[87]. However since lead is a heavy metal and an environmental hazardous material it is being phased out in the European union (EU)[88], and therefore it is not a very enticing material to use in a mass production setting. Especially in devices intended for the bio medical industry, since most of the time they are intended as single use devices because biological cross contamination is unacceptable. Therefore a change of material away from lead is almost a requirement for mass production devices that require permanently glueing of a piezo unto the device. The search for new piezoelectric materials to replace PZT is ongoing[89–91], and in particular the development within very strong electrostrictive gadolinium-doped ceria show great promise[92].

In this thesis we have looked to thin-films for solving specifically these two problems, reproducibility and lead-free actuators. Using an aluminum nitride (AlN) thin-film on top of glass block devices showed that the devices are indeed reproducible, and that the simulations give good agreement with the experiments. The AlN film is of course lead free, and therefore a good alternative to PZT. The second paper showed by simulation of acoustofluidic devices with AlN and AlScN thin films can perform on par with conventional devices, when taking into account their acoustofluidic action on fluids. The thin-film driven devices are almost a drop-in displacement for PZT actuators in devices designed for the bulk PZT transducers. The disadvantages of the thin-film devices are that they are more technical demanding to manufacture, compared to a PZT transducer which can be bought and glued onto the device, the films need to be deposited in a clean-room which is not a trivial matter. The last results in the thesis showed how thin-films, with optimized electrodes patterns on a membrane, can be used for trapping of cells above the membranes. These are some of the subjects that will be discussed in this thesis, and the structure of the thesis is explained in Section 1.4.

1.4 Thesis structure

The thesis is structured into chapters, each covering a part of the thesis, and then with articles at the end that are self-contained.

Chapter 1 Introduction — Is an introduction to a general understanding of acoustics and then into acoustofluidics as well as a short introduction to advantages and problems that this thesis has tried to solve.

Chapter 2 Theory — Presents the general introduction to the theory that is used in this thesis. It contains the solid mechanical equations, acoustofluidic equation that is derived by going into perturbation theory to first and second order, a short description of

boundary conditions, radiation force and particle velocity, and axisymmetric equations.

Chapter 3 Numerical modeling in COMSOL — Is dedicated to the numerics done in this thesis. It starts with a description of the finite element method, with weak form formulation, and the boundary conditions in such a method. The COMSOL implementation is described, as well as the material parameters used in the thesis, with a discussion of them, and the adaptive frequency stepping method. A section is dedicated to numerical validation.

Chapter 4 Summary of results — Has a summary of some of the results that was produced during this thesis. It includes the papers I-III, as well as a conference contribution to Acoustofluidics 2020, and minor results that have not been published.

Chapter 5 Papers — Includes the papers, (I) *Fabrication, Characterization, and Simulation of Glass Devices with AlN Thin-Film Transducers for Excitation of Ultrasound Resonances*, (II) *Numerical study of bulk acoustofluidic devices driven by thin-film transducers and whole-system resonance modes*, (III) *Numerical study of acoustic cell trapping above circular elastic membranes driven by thin-film transducers with patterned electrodes*, and peer-reviewed conference contribution (IV) *Numerical simulation of acoustic streaming generated by GHz AlN-thin-film transducers on AlN-SiO₂-Bragg-reflector substrates*.

Chapter 6 Conclusion and outlook — Ends the thesis with the overall conclusion of this thesis where the results are discussed in a collective conclusion and how results might be used in the future as well as what would have been interesting to further explore is written in an outlook.

Chapter 2

Theory

Acoustofluidics has a rich history stretching back over 200 years[80] with important developments along the way by historically important figures. Much of the fundamental theory is well established in the literature[93, 94] and a special mention to the tutorial series [95–114], wherein most all of the necessary background in acoustofluidics one would need is mentioned. The specific model worked with in this thesis has seen experimental validation[2, 93], whereas much of the theory used here can be dated back decades, recent development has enabled effective numerical simulations in 3 dimensions (3D) leading to the investigations of devices as well as a precision that were not possible before. In particular the recent development of Bach and Bruus Ref. 78 with their effective boundary layer theory of pressure acoustics, has allowed larger models, especially 3D. Combining this with the development of including solids[115] and then piezoelectric (PZE) materials[93] in the simulations, has allowed to simulate devices that are closer to real experiments. This change from predefined displacements[66, 116–119] and going closer to how the actual devices work has enabled the investigation of devices that were not possible before[1, 93].

The theory presented in this section should be seen as a short summary of the theory that is necessary for reproducing the numerical simulations in this thesis. The presentation of the theory follow very much the standard formulation of the theory available in for example Ref. 93 and Ref. 78, and is almost the same model as in those references, albeit with a sometimes slightly different implementation, and sometimes a slightly different interpretation. The structure of this chapter is: Section 2.1 is a short introduction to the fundamental equations in acoustofluidics and some definitions used throughout the thesis. In Section 2.2.1 is a short introduction to the first order perturbation theory and in Section 2.2.2 to second order steady state streaming. The radiation force is described in Section 2.2.4 and the effective boundary conditions (BC) on the acoustic streaming in Section 2.2.3. With these the particle motion can be explained in Section 2.2.5. Lastly in Section 2.3 the axisymmetric equations are touched upon for simulation where this was used.

2.1 Fundamental equations and definitions

In order to describe the acoustofluidic systems we assume that the physics we are working with can be described by continuous fields. Fundamentally the systems consist of atoms, which in nature are discrete, however at large enough scales the individual atoms behave as continuous fields in space and time that we describe as $\tilde{F}(\mathbf{r}, t)$ for scalar fields and $\tilde{\mathbf{F}}(\mathbf{r}, t)$ for vector fields, where \mathbf{r} is the special coordinate, t is the time, and the tilde over the fields indicate dependence on both space and time. The convention of notation in this thesis is that vector and tensor fields are written in boldface, whereas scalar fields are not. Each field is a local average over a small, but still of finite, volume and a discussion on the lower limit of validity of the continuous field approximation can be found in Ref. 94, and for all simulations we assume we are far above this lower limit.

The fundamental physics we want to describe adheres to the principles of conservation of mass and momentum and from these relations, in a continuous medium, the following can be written,

$$\partial_t \tilde{\rho} = \nabla \cdot (-\tilde{\rho} \tilde{\mathbf{v}}), \quad (2.1a)$$

$$\partial_t (\tilde{\rho} \tilde{\mathbf{v}}) = \nabla \cdot [\tilde{\boldsymbol{\sigma}} - (\tilde{\rho} \tilde{\mathbf{v}}) \tilde{\mathbf{v}}], \quad (2.1b)$$

where $\tilde{\rho}$ is the mass density, $\tilde{\mathbf{v}}$ is the velocity, ∂_t is the partial time derivative, $\nabla \cdot$ is the divergence operator, and $\tilde{\boldsymbol{\sigma}}$ is the stress tensor. Eq. (2.1a) is the continuity equation which states that the changes in mass in a small volume will require a net flow of mass through the surface on that volume and Eq. (2.1b) is the conservation of momentum, stating that changes in the collective momentum of a small volume must require either a force acting on the volume or a net inflow of momentum.

The physics of the system be made more concrete by requiring limitations on the definition of the stress tensor. For Newtonian fluids we have that [120],

$$\tilde{\boldsymbol{\sigma}} = -\tilde{p} \hat{\mathbf{I}} + \eta_0 \left[\nabla \tilde{\mathbf{v}} + (\nabla \tilde{\mathbf{v}})^T - 2/3 (\nabla \cdot \tilde{\mathbf{v}}) \hat{\mathbf{I}} \right] + \eta_0^b (\nabla \cdot \tilde{\mathbf{v}}) \hat{\mathbf{I}}, \quad (2.2)$$

where $\hat{\mathbf{I}}$ is the unit tensor, \tilde{p} is the pressure, η_0 is the dynamic viscosity, η_0^b is the bulk viscosity, and ∇ is the gradient operator. Inserting Eq. (2.2) into Eq. (2.1b) gives the Navier–Stokes equation,

$$\partial_t (\tilde{\rho} \tilde{\mathbf{v}}) = -\nabla \tilde{p} + \eta_0 \nabla^2 \tilde{\mathbf{v}} + \left(\eta_0/3 + \eta_0^b \right) \nabla (\nabla \cdot \tilde{\mathbf{v}}) - \nabla \cdot [(\tilde{\rho} \tilde{\mathbf{v}}) \tilde{\mathbf{v}}], \quad (2.3)$$

where it was assumed that η_0 and η_0^b do not vary in space for the systems investigated in this thesis. The Navier–Stokes equation will prove useful later for the explanation of pressure acoustics in Section 2.2. The momentum conservation also applies to solids so Eq. (2.1b) must also define the movement of solids, where instead of a velocity, we are working with the displacement vector, $\tilde{\mathbf{u}}_1$, such that $\partial_t \tilde{\mathbf{u}}_1 = \tilde{\mathbf{v}}_1$. We assume that momentum does not flow in solids and that the strain, $\tilde{\mathbf{S}} = \frac{1}{2} (\nabla \tilde{\mathbf{u}}_1 + (\nabla \tilde{\mathbf{u}}_1)^T)$, is very small and therefore the nonlinear term in Eq. (2.1b) is not present in the solids we are calculating, which then gives,

$$\rho_{\text{sl}} \partial_t^2 \tilde{\mathbf{u}}_1 = \nabla \cdot \tilde{\boldsymbol{\sigma}}, \quad (2.4)$$

which is also called Cauchy's momentum equation[121], where we assumed that the mass density in the solid, ρ_{sl} , is time independent. If we assume we are working within the linear regime of the solid, then there is a relation between the stress and the strain such that,

$$\tilde{\boldsymbol{\sigma}} = \mathbf{C} : \tilde{\mathbf{S}}, \quad (2.5)$$

where \mathbf{C} is the coupling four tensor with parameters that depend on the material. If we are working with piezoelectric materials then the stress tensor does not only depend on the strain matrix but also the electric field, $\tilde{\mathbf{E}}$, defined from the electric potential, $\tilde{\varphi}$, as $\tilde{\mathbf{E}} = -\nabla \tilde{\varphi}$, so that for piezoelectric materials,

$$\tilde{\boldsymbol{\sigma}} = \mathbf{C} : \tilde{\mathbf{S}} - \mathbf{e}^T \cdot \tilde{\mathbf{E}}, \quad (2.6)$$

where \mathbf{e} is the piezoelectric coupling three tensor. We can supplement the system with the quasi electrostatic Maxwell equation for the dielectric field,

$$\nabla \cdot \tilde{\mathbf{D}} = 0, \quad (2.7)$$

where for piezoelectric materials,

$$\tilde{\mathbf{D}} = \mathbf{e} : \tilde{\mathbf{S}} + \boldsymbol{\varepsilon} \cdot \tilde{\mathbf{E}}. \quad (2.8)$$

Notice that so far we have not used Voigt notation, but from Section 2.1.1 and forward we will.

2.1.1 Solidmechanical equations and Voigt notation

The equations can be cumbersome because of many high rank tensors, however because of the symmetry requirements on the stress and strain tensors, the equations can be more conveniently expressed in Voigt notation. This reduces the 3×3 stress and strain tensors into 1×6 vectors, where only the 6 unique components are kept. The mechanical \mathbf{C} tensor is then reduced from $3 \times 3 \times 3 \times 3 \times 3$ into a 6×6 , thereby keeping the elements down without loss of generality. Because of symmetries that exist in some materials, such as in crystals or isotropic materials such as glass, the system will be invariant under some types of rotations, and exactly which operations depend on the specific symmetry of the material. Which rotations the system is invariant under puts limitations on the amount of possible coupling coefficients in \mathbf{C} . In practice this means that many of the maximal possible free coefficients in \mathbf{C} are often zero or the same, for example for isotropic glass there are only two free variables out of the nine nonzero elements, which relate to transverse and longitudinal waves in glass. For isotropic materials, such as glass, and for cubic symmetric crystals, such as silicon, the \mathbf{C} matrix in Voigt notation is[93]

$$\mathbf{C} = \left(\begin{array}{ccc|ccc} C_{11} & C_{12} & C_{12} & 0 & 0 & 0 \\ C_{12} & C_{11} & C_{12} & 0 & 0 & 0 \\ C_{12} & C_{12} & C_{11} & 0 & 0 & 0 \\ \hline 0 & 0 & 0 & C_{44} & 0 & 0 \\ 0 & 0 & 0 & 0 & C_{44} & 0 \\ 0 & 0 & 0 & 0 & 0 & C_{44} \end{array} \right), \quad \text{for cubic symmetry,} \quad (2.9)$$

where for isotropic materials there is the additional constraint that $C_{12} = C_{11} - 2C_{44}$, and all the parameter values used in this thesis for a specific materials can be found in Table 3.4. The two only free coefficients in isotropic materials are often given in other forms, such as with either Young's modulus, E , and Poisson's ratio, s , or with the longitudinal and transverse speeds of sound, with symbols c_{lo} and c_{tr} respectively. The translations among the different notations are unambiguous, and can be calculated as,[122]

$$C_{11} = \rho c_{lo}^2 = \frac{1-s}{(1-2s)(1+s)} E, \quad (2.10a)$$

$$C_{44} = \rho c_{tr}^2 = \frac{1}{2(1+s)} E. \quad (2.10b)$$

For hexagonal crystal structures, such as lead zirconate titanate (PZT) and aluminium nitride (AlN), the mechanical couplings matrix in Voigt notation is[93],

$$\mathbf{C} = \left(\begin{array}{ccc|ccc} C_{11} & C_{12} & C_{13} & 0 & 0 & 0 \\ C_{12} & C_{11} & C_{13} & 0 & 0 & 0 \\ C_{13} & C_{13} & C_{33} & 0 & 0 & 0 \\ \hline 0 & 0 & 0 & C_{44} & 0 & 0 \\ 0 & 0 & 0 & 0 & C_{44} & 0 \\ 0 & 0 & 0 & 0 & 0 & C_{66} \end{array} \right), \quad \text{for hexagonal symmetry,} \quad (2.11)$$

and the additional restriction that $C_{66} = \frac{1}{2}(C_{11} - C_{12})$, again with the material parameters in Table 3.3. The piezoelectric coupling matrix e also is simplified from a tensor of rank three, $3 \times 3 \times 3$ to a tensor of rank two, 3×6 , in Voigt notation, such that for a hexagonal piezoelectric materials, such as PZT and AlN, in Voigt notation is[93],

$$\mathbf{e} = \begin{pmatrix} 0 & 0 & 0 & 0 & e_{15} & 0 \\ 0 & 0 & 0 & e_{15} & 0 & 0 \\ e_{31} & e_{31} & e_{33} & 0 & 0 & 0 \end{pmatrix}, \quad (2.12)$$

with parameter values in Table 3.3. For thin-films where the film is free to expand in the direction perpendicular to the surface there is a correction to the piezoelectric coefficient e_{31} , such that, [60, 123–125]

$$e_{31,f} = e_{31} - \frac{C_{13}}{C_{33}} e_{33}. \quad (2.13)$$

The permittivity matrix, $\boldsymbol{\varepsilon}$, is not changed because of the Voigt notation and for hexagonal materials is defined as,

$$\boldsymbol{\varepsilon} = \begin{pmatrix} \varepsilon_{11} & 0 & 0 \\ 0 & \varepsilon_{11} & 0 \\ 0 & 0 & \varepsilon_{33} \end{pmatrix}. \quad (2.14)$$

The coefficients for the coupling tensors \mathbf{C} , \mathbf{e} , and $\boldsymbol{\varepsilon}$ are complex valued where the imaginary parts are responsible for losses and the attenuation of the waves. The imaginary part is difficult to measure, and as we do not know them we assume that the system can be described by an overall dampening factor for each material given in Table 3.3 and Table 3.4.

These equations together with the appropriate boundary conditions are enough to simulate the solid mechanical part of the simulations. The boundary conditions for the solids mechanical part is a continuity of stress and velocity, and zero free changes on the surface for the electric part. Furthermore the electric field is driven by the the electric potential which is defined at some surfaces by electrodes attached to the piezoelectric materials. The potential oscillates with a specific frequency which drives the acoustics in the system. The boundary conditions can therefore be written as,

$$\tilde{\boldsymbol{\sigma}} \cdot \mathbf{n} = \mathbf{0} \quad \text{and} \quad \tilde{\mathbf{D}} \cdot \mathbf{n} = 0, \quad \text{at solid and PZE air interface,} \quad (2.15a)$$

$$\tilde{\varphi} = 0, \quad \text{at ground electrode,} \quad (2.15b)$$

$$\tilde{\varphi} = \frac{1}{2}\varphi_0 e^{-i\omega t}, \quad \text{at positive electrode,} \quad (2.15c)$$

$$\tilde{\varphi} = -\frac{1}{2}\varphi_0 e^{-i\omega t}, \quad \text{at negative electrode,} \quad (2.15d)$$

where φ_0 is half the potential amplitude, f is the frequency, ω is the angular frequency, and $i = \sqrt{-1}$ is the imaginary number corresponding to the square root of negative one. When the solid and PZE is in contact with a fluid, then the boundary condition is also continuous stress and velocity, however since we use the effective boundary conditions described later, there are slight changes to these and therefore they will be defined there. The boundary condition Eq. (2.15a) means that we are neglecting the effect air has on the system. As anyone who has taped a wine glass at a party to get attention knows, the mechanical oscillations in the glass generates pressure waves which we hear as sound, and hence the boundary condition can not be completely true, as there must be losses into the air. However for the systems we simulate the displacement is very small and it has been experimentally observed by Reichert *et al.* Ref. [60], in a membrane system where the displacements comparatively larger, compared to a bulk system, and therefore more sensitive to air. They showed that running the system in air vs. vacuum did not change the resonance frequency but did change the Q factor of the system by 60%. Since we do not fully know the dampening in the system, and since we are working with much smaller displacements in our bulk systems, we elect to neglect the effects of the air.

Since we in Eq. (2.15c) actuate with a time harmonic electric potential, the displacement fields are also time harmonic in nature, because of the linearity of the equations.

However because of the non-linearity of the Navier–Stokes equation there is a possibility of these time harmonic motions, to result in time steady behavior, which will be discussed in the Section 2.2 about perturbation expansion in fluids.

2.2 Perturbation expansion in fluid

In the acoustofluidic systems we want to describe in this thesis, the fields are time harmonic with a fundamental frequency defined by the applied electric potential boundary condition. Explicit reference to time dependent fields are denoted with a tilde. Fields that are purely time harmonic have had their time dependence split off from their spacial dependence, and are denoted without a tilde. This means that for scalar fields and vector fields,

$$\tilde{F}(\mathbf{r}, t) = F(\mathbf{r})e^{-i\omega t}, \quad \omega = 2\pi f, \quad (2.16a)$$

$$\tilde{\mathbf{F}}(\mathbf{r}, t) = \mathbf{F}(\mathbf{r})e^{-i\omega t}, \quad \text{with } i = \sqrt{-1}. \quad (2.16b)$$

To proceed further with the governing fluid equations, we will need to introduce perturbation theory of the pressure, p , the mass density of the fluid, ρ , and the velocity, v , such that

$$\tilde{p} = p_0 + p_1e^{-i\omega t} + \tilde{p}_2, \quad (2.17a)$$

$$\tilde{\rho} = \rho_0 + \rho_1e^{-i\omega t} + \tilde{\rho}_2, \quad (2.17b)$$

$$\tilde{\mathbf{v}} = \mathbf{0} + \mathbf{v}_1e^{-i\omega t} + \tilde{\mathbf{v}}_2, \quad (2.17c)$$

where each term in the series is smaller than the previous one, such that $\mathbf{v}_1/c_{\text{fl}} \ll 1$, where c_{fl} is the speed of sound in the fluid, $\rho_1/\rho_0 \ll 1$ and $p_1/p_0 \ll 1$, and likewise for the second order compared to the first order. We split up the time dependence such that the zero order fields are time independent, the first order fields are time harmonic, to match the time harmonic boundary conditions from the displacement field that actuate the fluid. In Section 2.2.2 it is shown that the second order fields have a time steady and double harmonic component, however for now the second order fields simply have some general time and space dependence. We are working with a quiescent fluid, hence the zero order velocity is zero.

Lastly, with the systems as we treat in this thesis, it is also required that the adiabatic assumption is valid, such that the isentropic compressibility, κ_0 can be calculated as,

$$\kappa_0 = \frac{1}{\rho_0} \left(\frac{\partial \rho}{\partial p} \right)_S = \frac{1}{\rho_0 c_{\text{fl}}^2}, \quad (2.18)$$

where it follow from Eq. (2.18) that $\frac{1}{\rho_0} \left(\frac{\partial \rho}{\partial p} \right) = \frac{1}{\rho_0 c_{\text{fl}}^2} \Rightarrow \rho_1 = \frac{1}{c_{\text{fl}}^2} p_1$. Using this in combination with the Navier–Stokes equation, Eq. (2.3), makes it possible to explain the pressure acoustics, and subsequently, the effective boundary conditions developed by Bach and Bruus[78] that have been used in this thesis.

2.2.1 1st order fields

The perturbation fields Eq. (2.17a), Eq. (2.17b), and Eq. (2.17c), can be inserted into Navier–Stokes equation, Eq. (2.3), and continuity equation, Eq. (2.1a), and collecting the terms to first order gives,

$$-i\omega\rho_1 = -\rho_0\nabla\cdot\mathbf{v}_1, \quad (2.19a)$$

$$-i\omega(\rho_0\mathbf{v}_1) = -\nabla p_1 + \eta_0\nabla^2\mathbf{v}_1 + \left(\eta_0/3 + \eta_0^b\right) [\nabla(\nabla\cdot\mathbf{v}_1)], \quad (2.19b)$$

where the explicit time dependence on the first order fields have been used and subsequently divided out. Taking the divergence of Eq. (2.19b), and inserting Eq. (2.19a), together with the relation from Eq. (2.18), $\rho_1 = \frac{1}{c_0^2}p_1$, gives the equation for pressure acoustics,

$$\frac{i\omega}{\rho_0 c_{\text{fl}}^2} p_1 = \nabla\cdot\mathbf{v}_1, \quad (2.20a)$$

$$\frac{\omega^2}{c_{\text{fl}}^2} p_1 = -\nabla^2 p_1 - \frac{-i\omega(4\eta_0/3 + \eta_0^b)}{\rho_0 c_{\text{fl}}^2} (\nabla^2 p_1). \quad (2.20b)$$

Here we see that the equation has solutions of a damped wave equation in the pressure field, and by introducing some constants we see that we get the Helmholtz equation,

$$k_c^2 p_1 + \nabla^2 p_1 = 0, \quad k_c^2 = k_0^2 \frac{1}{1 - i\Gamma_{\text{fl}}}, \quad k_0 = \frac{\omega}{c_{\text{fl}}}, \quad \Gamma_{\text{fl}} = \frac{\omega(4\eta_0/3 + \eta_0^b)}{\rho_0 c_{\text{fl}}^2}. \quad (2.21)$$

However going a back to the divergence of continuity equation it is apparent that this would lead to Helmholtz decomposition, of a divergence free velocity field, \mathbf{v}_1^δ , and a rotation free velocity field, \mathbf{v}_1^d , which has been done before by Ref. 78, 126, 127 and others,

$$\mathbf{v}_1 = \mathbf{v}_1^\delta + \mathbf{v}_1^d, \quad \nabla \times \mathbf{v}_1^d = \mathbf{0}, \quad \nabla \cdot \mathbf{v}_1^\delta = 0. \quad (2.22)$$

This also makes sense since transverse waves cannot propagate in liquids, but can in the solids that surround the fluid, therefore there must be a transition phase at the boundary, where such waves are damped to comply with the no-slip boundary condition in liquids. Inserting Eq. (2.22) into Eq. (2.19a) and Eq. (2.19b) gives,

$$\partial_t \rho_1 = -\rho_0 \nabla \cdot \mathbf{v}_1^d, \quad (2.23a)$$

$$\rho_0 \partial_t (\mathbf{v}_1^\delta + \mathbf{v}_1^d) = -\nabla p_1 - \eta_0 \nabla \times (\nabla \times \mathbf{v}_1^\delta) + \left(4\eta_0/3 + \eta_0^b\right) [\nabla(\nabla\cdot\mathbf{v}_1^d)]. \quad (2.23b)$$

where we have used the vector identity $\nabla^2 \mathbf{B} = \nabla(\nabla\cdot\mathbf{B}) - \nabla \times \nabla \times \mathbf{B}$ [128]. We can solve for the individual fields, \mathbf{v}_1^δ and \mathbf{v}_1^d , separately, since they work on different length

scales. Another way to see that they must separate is to realize that since one velocity represents transverse waves and the other represents longitudinal waves, we can take either the rotation or divergence of Eq. (2.23b) respectively, and seeing that after doing so each operation only leaves one of the fields. By separating the solutions and combining Eq. (2.23a) and Eq. (2.23b) as well as the relation from Eq. (2.18), $\rho_1 = \frac{1}{c_0^2} p_1$ we are left with the following equations for the short and long range first order velocities,

$$\nabla^2 \mathbf{v}_1^\delta + k_s^2 \mathbf{v}_1^\delta = \mathbf{0}, \quad k_s = \frac{1+i}{\delta}, \quad (2.24a)$$

$$\nabla^2 \mathbf{v}_1^d + k_c^2 \mathbf{v}_1^d = \mathbf{0}, \quad \delta = \sqrt{\frac{2\nu_0}{\omega}}, \quad (2.24b)$$

as was found in Ref. [78], where we see that \mathbf{v}_1^δ is damped within the boundary layer dampening length scale, k_s , where δ is the length scale of the viscous boundary layer.

By this separation into bulk and boundary layer fields Bach and Bruus Ref. [78] developed the effective boundary conditions on a curved elastic cavities, see Section 2.2.3.

2.2.2 2nd order field

With the equations for the first order fluid fields, one can then expand Navier–Stokes and the continuity equation to second order and take the time average. Because the second order fields are driven by products of first order fields we expect the second order fields to have either a steady state or a double harmonic solution. By taking the time average, the double harmonic solutions give zero contribution to the equation, and only the time steady second order contributions are left. The time average of a second order field is here defined as $\mathbf{F}_2 = \langle \tilde{\mathbf{F}}_2 \rangle = \frac{1}{T_0} \int_0^{T_0} \tilde{\mathbf{F}}_2(\mathbf{r}, t) dt$, where T_0 is the time of a full period, and the definition here is that any second order field that is without tilde, $\tilde{\cdot}$, and brackets, $\langle \cdot \rangle$, is time averaged. For a product of two first order fields it is defined as $\langle \text{Re} [\tilde{\mathbf{A}}_1(\mathbf{r}, t)] \text{Re} [\tilde{\mathbf{B}}_1(\mathbf{r}, t)] \rangle = \frac{1}{T_0} \int_0^{T_0} \frac{1}{2} (\mathbf{A}_1 e^{-i\omega t} + \mathbf{A}_1^* e^{i\omega t}) \frac{1}{2} (\mathbf{B}_1 e^{-i\omega t} + \mathbf{B}_1^* e^{i\omega t}) dt = \frac{1}{2} \text{Re} [\mathbf{A}_1(\mathbf{r}) \mathbf{B}_1^*(\mathbf{r})]$, where \mathbf{B}_1^* is the complex conjugate of \mathbf{B}_1 . The second order time averaged equations of the continuity equation and Navier–Stokes are therefore,

$$0 = -\nabla \cdot \left(\frac{1}{2} \text{Re} [\rho_1 \mathbf{v}_1^*] + \rho_0 \mathbf{v}_2 \right), \quad (2.25a)$$

$$\mathbf{0} = -\nabla p_2 + \eta_0 \nabla^2 \mathbf{v}_2 + \left(\eta_0/3 + \eta_0^b \right) \nabla (\nabla \cdot \mathbf{v}_2) - \rho_0 \nabla \cdot \left(\frac{1}{2} \text{Re} [\mathbf{v}_1 \mathbf{v}_1^*] \right). \quad (2.25b)$$

These equations can then be used to calculate the acoustic streaming, however the boundary conditions are still missing, and they will be discussed in Section 2.2.3.

2.2.3 Effective boundary conditions and acoustic streaming

The effective boundary layer theory used in this thesis is the one developed by Bach and Bruus in Ref. 78, where it analytically accounts for the boundary layer in curved elastic

cavities. Since the boundary layer no longer needs to be resolved to the same degree, it enables the effective simulation of large systems such as the many wavelength systems in 2D, or in particular in 3D, where without this effective theory it would not have been possible to simulate these systems. Because of the importance in for the simulations in this thesis, the effective boundary conditions derived by Bach and Bruus Ref. 78 should be mentioned and its validity for the systems simulated in this thesis should be discussed. However since the boundary conditions are not trivial to explain, it can be confusing to the reader to simply state the boundary conditions, without at least tell how Bach and Bruus Ref. 78 derived it, and what assumptions were made. Therefore a short summary of the two boundary conditions used in this thesis will be given in this section, however all credit goes to the authors for the results, and for a full and very thorough explanation see the article by Bach and Bruus Ref. 78, and for a slight different take on it see the PhD thesis by Bach 129.

Effective boundary theory first order

The effective boundary conditions were developed for a generalized coordinate system, where ζ is the transverse coordinate at any point on the surface. This allows them to do some general approximations on how the fields look close to the surface. These approximations require that $\epsilon = \frac{\delta}{d} \ll 1$, where $\delta = \sqrt{\frac{2\nu_0}{\omega}}$ is the boundary layer length scale, and that $d = \min\{k_0^{-1}, R\}$ which is the lower bound on the wavelength or surface variations. This allows them to throw away terms on the order of $\mathcal{O}(\epsilon)$, as they are supposed to be small, and the theory is only expected to be correct to the order of ϵ . On the boundary, $\zeta \lesssim \delta \ll d$, they do separation of variables of the fields by denoting them with a superscript of zero $\mathbf{A}(\xi, \eta, \zeta) = \mathbf{A}^0(\xi, \eta, 0)a(\zeta)$. Therefore surface fields $\mathbf{A}^0(\xi, \eta, 0)$ have vector component orthogonal to the surface, but not derivatives in that direction. The first order boundary condition on the surface is the no slip velocity on the surface, which for the short and long range fields are defined as,

$$\mathbf{V}_1^0 = \mathbf{v}_1^0 = \mathbf{v}_1^{d0} + \mathbf{v}_1^{\delta 0}. \quad (2.26)$$

Now the idea is to implement the boundary condition without explicit reference to the velocity. This can be done by looking at the orthogonal component of Eq. (2.26),

$$v_{1\zeta}^{d0} = V_{1\zeta}^0 - v_{1\zeta}^{\delta 0}. \quad (2.27)$$

The last term can be replaced by using that the transverse waves are incompressible, $\nabla \cdot \mathbf{v}_1^{\delta 0} = 0$, and that on the surface the field is $\mathbf{v}_1^{\delta 0}(\xi, \eta, \zeta) = \mathbf{v}_1^{\delta 0}(\xi, \eta, 0)e^{ik_s\zeta} + \mathcal{O}(\epsilon)$, then,

$$v_{1\zeta}^{\delta 0} = \frac{i}{k_s} \nabla_{\parallel} \cdot \mathbf{v}_{1\parallel}^{\delta 0} = \frac{i}{k_s} \nabla_{\parallel} \cdot (\mathbf{V}_{1\parallel}^0 + \mathbf{v}_{1\parallel}^{d0}), \quad (2.28)$$

where $\nabla_{\parallel} \cdot$ is the parallel divergence operator. Inserting this into Eq. (2.27) gives,

$$v_{1\zeta}^{d0} = V_{1\zeta}^0 - \frac{i}{k_s} \nabla_{\parallel} \cdot (\mathbf{V}_{1\parallel}^0 + \mathbf{v}_{1\parallel}^{d0}). \quad (2.29)$$

Using that at the surface $\nabla_{\parallel} \cdot \mathbf{v}_{1\parallel}^{d0} = \nabla_{\parallel} \cdot \mathbf{v}_{1\parallel}^d = \nabla \cdot \mathbf{v}_1^d - \partial_{\zeta} \mathbf{v}_{1\zeta}^d$, and $\mathbf{v}_1^d = \frac{1 - i\Gamma_{\text{fl}}}{i\omega\rho_0} \nabla p_1$ we get,

$$\partial_{\zeta} p_1 = \frac{i\omega\rho_0}{1 - i\Gamma_{\text{fl}}} \left(V_{1\zeta}^0 - \frac{i}{k_s} \nabla_{\parallel} \cdot \mathbf{V}_{1\parallel}^0 \right) - \frac{i}{k_s} (k_c^2 p_1 + \partial_{\zeta}^2 p_1), \quad \text{at } \zeta = 0. \quad (2.30)$$

The final expression seen in Bach and Bruus, Ref. 78 Eq. 25, can be achieved by using the approximation given in that article, $(i/k_s)\nabla \cdot (\mathbf{v}_1^{d0} - \mathbf{V}_1^0) = (i/k_s)\nabla_{\parallel} \cdot (\mathbf{v}_{1\parallel}^{d0} - \mathbf{V}_{1\parallel}^0) + \mathcal{O}(\epsilon)$, which is correct to the order of ϵ , on Eq. (2.29). The boundary condition implemented in the models in this thesis are the one stated in Eq. (2.30), because it is easy to implement in COMSOL, and does not need the last approximation.

The equation for the effective boundary condition from the fluid onto the solid is also described in Bach and Bruus Ref. 78, and can be calculated by assuming continuous stress across the boundary. More specifically it means that the stress in the solid, Eq. (2.5), should be equal to the stress in the fluid, Eq. (2.2), at the boundary. For the stress in the fluid, Eq. (2.2), the divergence terms are an order of Γ_{fl} smaller than the other terms, therefore the remaining terms are dominated by the perpendicular derivative of the stress such that $\boldsymbol{\sigma}_{\text{sl}} \cdot \mathbf{e}_{\zeta} = -p_1 \mathbf{e}_{\zeta} + \eta_0 \partial_{\zeta} \mathbf{v}_1^{\delta}$. Using Eq. (2.26), the fact that the $\partial_{\zeta} \mathbf{v}_1^{\delta} = ik_s \mathbf{v}_1^{\delta}$ at the boundary, and the definition of the bulk velocity, $\mathbf{v}_1^d = \frac{1 - i\Gamma_{\text{fl}}}{i\omega\rho_0} \nabla p_1$, the final solid boundary condition in contact with the fluid is,

$$\boldsymbol{\sigma}_{\text{sl}} \cdot \mathbf{e}_{\zeta} = -p_1 \mathbf{e}_{\zeta} + \eta_0 ik_s \left(\mathbf{V}_1^0 - \frac{1 - i\Gamma_{\text{fl}}}{i\omega\rho_0} \nabla p_1 \right). \quad (2.31)$$

Effective boundary theory second order

Bach and Bruus Ref. 78 derived effective boundary conditions for the second order time average streaming $\langle \mathbf{v}_2 \rangle$ that analytically integrates the contributions of the boundary layer, to decrease the necessary numerical resolution and therefore make computation many times faster. The derivation is done in detail by their article, as well as the numerical validations of their results. For the purpose of enabling a discussion of the of the assumptions made and the expected accuracy, necessary for justifying its use in this thesis, and especially in Section 5.4, a short summery is given here. The effective boundary conditions are derived in Bach and Bruus by splitting the fields, p_2 and \mathbf{v}_2 into short- and long-range fields. The divergence of the long-range second order velocity are approximated to zero, from the second order continuity equation, $\nabla \cdot \mathbf{v}_2^d = \Gamma_{\text{fl}} k_0 |\mathbf{v}_1^d|^2 / (2c_{\text{fl}}) \approx 0$, which gives the governing equation for the second order long-range streaming given in Ref. 78 Eq. 52b,

$$\mathbf{0} = -\nabla \left(p_2^d - \langle \mathcal{L}_{\text{ac}}^d \rangle \right) + \eta_0 \nabla^2 \mathbf{v}_2^d + \frac{\Gamma\omega}{c_{\text{fl}}^2} \langle \mathcal{S}_{\text{ac}}^d \rangle, \quad (2.32)$$

where $\langle \mathcal{L}_{\text{ac}}^d \rangle = \frac{1}{4} \kappa_0 |p_1|^2 - \frac{1}{4} \rho_0 |\mathbf{v}_1^d|^2$ is the time averaged acoustic Lagrangian density and $\langle \mathcal{S}_{\text{ac}}^d \rangle = c_0^2 \langle \rho_1 \mathbf{v}_1^d \rangle$ is the time averaged acoustic energy flux density. The boundary

condition of the short range velocity fields were found by Bach and Bruus by first analyzing individual term and keeping those to lowest order in ϵ . Secondly Taylor expanding the first order bulk velocity field $\mathbf{v}_1^d(\xi, \eta, \zeta) = \mathbf{v}_1^{d0}(\xi, \eta) + (\partial_\zeta \mathbf{v}_1^d(\xi, \eta, \zeta))|_{\zeta=0}\zeta$, which is only applicable for $\zeta \ll d$. And thirdly integrating up the boundary contribution on the perpendicular direction from the surface up to infinity. This boundary condition of the short-range fields can then be inserted into the equations of the boundary condition of the long-range fields, \mathbf{v}_2^d . By recommendation from the lead author of Bach and Bruus [78], the final boundary conditions for the long-range bulk fields are their Eq. 55 but where some of the perpendicular components from their Eq. 54c have been kept instead of assumed to be small, which should increase the accuracy in some cases, so that the boundary condition is,

$$\begin{aligned} \mathbf{v}_2^{d0} = & -\frac{1}{2\omega} \text{Re} \left\{ \mathbf{v}_1^{\delta 0*} \cdot \nabla \left(\frac{1}{2} \mathbf{v}_1^{\delta 0} - i \mathbf{V}_1^0 \right) - i \mathbf{V}_1^{0*} \cdot \nabla \mathbf{v}_1^d \right. \\ & + \left. \left[\frac{2-i}{2} \nabla \cdot \mathbf{v}_1^{\delta 0*} + i \left(\nabla \cdot \mathbf{V}_1^{0*} - \partial_\zeta v_{1\zeta}^{d*} \right) \right] \mathbf{v}_1^{\delta 0} \right\} \cdot (\mathbf{e}_\xi \mathbf{e}_\xi + \mathbf{e}_\eta \mathbf{e}_\eta) \\ & + \frac{1}{2\omega} \text{Re} \left\{ \nabla_{\parallel} \cdot \left(i \mathbf{v}_{1\parallel}^{\delta 0} V_{1\zeta}^{0*} \right) - \frac{1+i}{\delta} V_{1\zeta}^{0*} v_{1\zeta}^{\delta 0} \right. \\ & \left. + \left[i V_1^{0*} \cdot \nabla \left(\mathbf{v}_1^d + \mathbf{v}_1^{\delta 0} \right) \right] \cdot \mathbf{e}_\zeta \right\} \mathbf{e}_\zeta. \end{aligned} \quad (2.33a)$$

Under the assumption that the system is on resonance in the liquid with a high Q-factor of the standing wave such that $\mathbf{V}_1^0 \ll \mathbf{v}_1^d$, then from Eq. (2.33a) the expression can be approximated, as was shown in Bach and Bruus[78] in their equation Eq. 61, to be

$$\begin{aligned} \mathbf{v}_2^{d0} = & -\frac{1}{2\omega} \text{Re} \left\{ \mathbf{v}_1^{\delta 0*} \cdot \nabla \left(\frac{1}{2} \mathbf{v}_1^{\delta 0} \right) \right. \\ & + \left. \left[\frac{2-i}{2} \nabla \cdot \mathbf{v}_1^{\delta 0*} - i \left(\partial_\zeta v_{1\zeta}^{d*} \right) \right] \mathbf{v}_1^{\delta 0} \right\} \cdot (\mathbf{e}_\xi \mathbf{e}_\xi + \mathbf{e}_\eta \mathbf{e}_\eta) \\ & + 0 \mathbf{e}_\zeta \mathbf{e}_\zeta. \end{aligned} \quad (2.34a)$$

This is a good assumption in paper II, as the Q-factor is high in the fluid, as the standing waves build up in the acoustical cavity, as but it is not a good assumption in paper III.

2.2.4 Radiation force

The radiation force in acoustofluidics, is the force that a particle experience, when it is hit with a incoming pressure wave and scatters it. This scattered wave interacts with the incoming pressure wave, and though nonlinear terms in the Navier–Stokes equation, ends up exerting a force on the particles. In Settnes and Bruus, Ref. 130, they calculated this force on a spherical and compressible particle suspended in a viscous fluid, where they expanded the scattering field to the mono- and dipole terms, and derived the force[130],

$$\mathbf{F}_{\text{rad}} = -\pi a^3 \left[\frac{2\kappa_0}{3} \text{Re}(f_0^* p_1^* \nabla p_1) - \rho_0 \text{Re}(f_1^* \mathbf{v}_1^* \cdot \nabla \mathbf{v}_1) \right], \quad (2.35)$$

where a is the particle radius, and f_0 and f_1 are the mono- and dipole scattering coefficients defined as [93, 130],

$$f_0 = 1 - \frac{\kappa_p}{\kappa_0}, \quad f_1 = \frac{2[1 - \gamma(\delta/a)](\rho_p - \rho_0)}{2\rho_p + \rho_0[1 - 3\gamma(\delta/a)]}, \quad (2.36)$$

where κ_p and κ_0 is the compressibility of the particle and fluid respectively, while ρ_p and ρ_0 are the density of the particle and fluid respectively, and where $\gamma(\delta/a)$ is $\gamma(\delta/a) = -\frac{3}{2}[1 + i(1 + \delta/a)]\delta/a$, where as a reminder δ is the viscous boundary layer.

In the case of a small particle, ($a \ll \lambda$), in the inviscid case, $\delta = 0$, it can be approximated by minus the gradient of the Gorkov potential [131][93]

$$U^{\text{rad}} = -\pi a^3 \left[\frac{\kappa_0}{3} \text{Re}(f_0) |p_1|^2 - \frac{1}{2} \rho_0 \text{Re}(f_1) |\mathbf{v}_1|^2 \right], \quad (2.37a)$$

$$\mathbf{F}_{\text{rad}} = -\nabla U^{\text{rad}}, \quad (2.37b)$$

but in general the equation that has been used in this thesis is Eq. (2.35). One of the parameters that can quickly convey the direction a particle will move in a traditional 1D standing wave, based on the scattering coefficients, is the acoustic contrast factor[66],

$$\Phi = \frac{1}{3} f_0 + \frac{1}{2} \text{Re}(f_1), \quad (2.38)$$

2.2.5 Particle velocity

The particles time averaged velocity in a fluid can be calculated by Newtons momentum equation on all the forces that effect the particle. In this thesis we will limit us self to the acoustic radiation force, the drag force, \mathbf{F}_{drag} , and the buoyancy corrected gravitation force, \mathbf{F}_{grav} , such that the total force on the particle is,

$$\mathbf{F}_{\text{tot}} = \mathbf{F}_{\text{rad}} + \mathbf{F}_{\text{drag}} + \mathbf{F}_{\text{grav}}, \quad (2.39)$$

where[93],

$$\mathbf{F}_{\text{drag}} = 6\pi\eta_{\text{fl}}a(\mathbf{v}_2 - \mathbf{v}_p) \quad \mathbf{F}_{\text{grav}} = \mathbf{g}(\rho_p - \rho_0), \quad (2.40)$$

where $\mathbf{g} = -9.82 \text{ N/kg } \mathbf{e}_z$, \mathbf{v}_p is the particle velocity. By inserting this into Newtons momentum equation and numerically integrating up the time it is possible to calculate the time-dependent position of all the particles in the system. While it is completely feasible to do, especially for few particles over a small time scale, when calculating for many particles this quickly becomes tedious as a fine time resolution is necessary because of the large forces in Eq. (2.39) almost cancel out as soon as the particle has reached terminal velocity. Since we are usually working with low Reynolds numbers, the particle

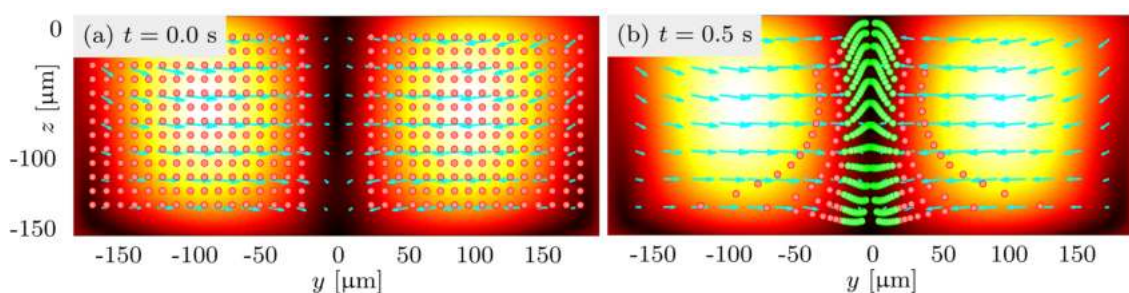


Figure 2.1: Example of particle focusing by the acoustic radiation force. Shows a simulation of how 5- μm -diameter polystyrene particles are being focused in the center of a microfluidic channel filled with water and actuated at 1.946 MHz, by a thin-film transducer shown in Fig. 4.6(a), with simulations explained further in Section 4.2 and paper Section 5.2. (a) show the original particle position and (b) show the particles after 0.5 s. The color plot shows the effective particle velocity magnitude, $|\mathbf{v}_p|$, from 0 $\mu\text{m}/\text{s}$ in black and 394 $\mu\text{m}/\text{s}$ in white, with the direction indicated by the cyan arrows. The particle trajectories are calculated by numerically integrating up \mathbf{v}_p from Eq. (2.41). The color of the particles were for illustration purposes changed from red to green when they were within four particle diameters from the center line, $y = 0$, of the channel. Adapted from supplementary material in Ref. 1.

momentum plays a small role on the overall motion of the particle, and the particle motion quickly reaches a velocity such that there is force balance on the particle, $\mathbf{F}_{\text{tot}} = 0$. This means that the force field can be translated to a effective particle velocity field,

$$\mathbf{v}_p = \mathbf{v}_2 + (\mathbf{F}_{\text{rad}} + \mathbf{F}_{\text{grav}}) / (6\pi\eta_{\text{fl}}a), \quad (2.41)$$

which is much easier to numerically integrate, and therefore when calculating for many particles this is much more effective. This has been done several times in the literature, for example in Ref. 93 or 66, and was also used in paper II, in Section 5.2, for calculating the average focus times of 3,536 particles in each device for several devices.

2.2.6 Acoustical energy density

The average acoustic energy density is one of those parameters that is usually mentioned in a standing wave system because it is easy to reference and conveys a lot of information about the system. It also adheres to scaling laws that make it easy to predict how the system will change the average average acoustic energy. The average acoustic energy density is[80],

$$E_{\text{ac}}^{\text{fl}} = \frac{1}{V_{\text{fl}}} \int_{V_{\text{fl}}} \left(\frac{1}{4} \kappa_0 |p_1|^2 + \frac{1}{4} \rho_0 |\mathbf{v}_1^{\text{fl}}|^2 \right) dV, \quad (2.42)$$

where V_{fl} is the fluid volume that is integrated over to make the average. It can be seen as the volume average of the time averaged potential and kinetic energy in the system.

Because of the linearity of the first order equations, for any particular frequency, the displacements scale proportional with the applied electric potential, the first order pressure and velocity field therefore scale proportional with displacement. Therefore the average acoustic energy density scales proportional with the square of the applied electric potential. Since the acoustic radiation force and acoustic streaming are second order effects they to scale proportional with the electric potential squared, and therefore proportional with the average acoustic energy density. This has also been observed experimentally in Ref. 132.

2.3 Axisymmetric models

When a model is axisymmetric, then the 3D numerics can be reduced to 2D because there is no angular dependence in the model, and by appropriate choice of coordinate system it is easy to exploit this. Axisymmetric models were used in paper III, Section 5.3, and as a early result in the GHz acoustofluidics section.

The theory in the previous sections has been formulated without reference to any specific coordinate system, with the exception is the solid mechanical equations in Voigt notation, in Section 2.1.1, which was formulated in Cartesian. In order to translate between them the definitions we define $[x, y, z] = [r \cos(\phi), r \sin(\phi), z]$, where if we assume that the first order scalar fields have no ϕ dependence,

$$p_1(x, y, z) = p_1(r, z), \quad \varphi(x, y, z) = \varphi(r, z), \quad (2.43)$$

as well as that the first order vector fields \mathbf{u}_1 and \mathbf{v}_1 have no ϕ dependence and no ϕ component then,

$$\mathbf{u}_1(x, y, z) = u_{1,r}(r, z) \mathbf{e}_r + u_{1,z}(r, z) \mathbf{e}_z, \quad \mathbf{v}_1(x, y, z) = v_{1,r}(r, z) \mathbf{e}_r + v_{1,z}(r, z) \mathbf{e}_z. \quad (2.44)$$

We can look at the derivatives, where it is defined as $\nabla = \left(\mathbf{e}_r \partial_r + \mathbf{e}_\phi \frac{1}{r} \partial_\phi + \mathbf{e}_z \partial_z \right)$, and since the unit vector of r and ϕ depend on the position, their partial derivative are $\partial_\phi \mathbf{e}_r = \mathbf{e}_\phi$ and $\partial_r \mathbf{e}_\phi = -\mathbf{e}_r$, and therefore we need to be careful when taking the derivatives.

Applying coordinate transformations to the equations Eq. (2.6) and Eq. (2.8), as well as assume that the fields \mathbf{u}_1 and φ are axisymmetric, makes it possible to calculate the strain and electric field system in cylindrical coordinates where it here is given in Voigt notation,

$$\begin{pmatrix} \sigma_{rr} \\ \sigma_{\phi\phi} \\ \sigma_{zz} \\ \sigma_{\phi z} \\ \sigma_{rz} \\ \sigma_{r\phi} \\ D_r \\ D_\phi \\ D_z \end{pmatrix} = \begin{pmatrix} C_{11} & C_{12} & C_{13} & 0 & 0 & 0 & 0 & 0 & -e_{31} \\ C_{12} & C_{11} & C_{13} & 0 & 0 & 0 & 0 & 0 & -e_{31} \\ C_{13} & C_{13} & C_{33} & 0 & 0 & 0 & 0 & 0 & -e_{33} \\ \hline 0 & 0 & 0 & C_{44} & 0 & 0 & 0 & -e_{15} & 0 \\ 0 & 0 & 0 & 0 & C_{44} & 0 & -e_{15} & 0 & 0 \\ 0 & 0 & 0 & 0 & 0 & C_{66} & 0 & 0 & 0 \\ \hline 0 & 0 & 0 & 0 & e_{15} & 0 & \varepsilon_{11} & 0 & 0 \\ 0 & 0 & 0 & e_{15} & 0 & 0 & 0 & \varepsilon_{11} & 0 \\ e_{31} & e_{31} & e_{33} & 0 & 0 & 0 & 0 & 0 & \varepsilon_{33} \end{pmatrix} \begin{pmatrix} \partial_r u_r \\ u_r/r \\ \partial_z u_z \\ \hline 0 \\ \partial_r u_z + \partial_z u_r \\ \hline 0 \\ -\partial_r \varphi \\ 0 \\ -\partial_z \varphi \end{pmatrix}, \quad (2.45)$$

for a hexagonal piezoelectric material. Non piezoelectric materials can be calculated the same way however where the piezoelectric couplings coefficients simply are zero. For isotropic material there are the further requirements that $C_{13} = C_{12}$, $C_{33} = C_{11}$ and $C_{66} = C_{44}$. Notice that the Voigt coupling matrix is not changed under the transformation, and that is because the hexagonal piezoelectric material coefficients are defined exactly such that they are invariant under rotation in the plane. This is also why anisotropic materials such as silicon (100), where the parameters depend on the orientation in the plane[133], cannot properly be simulated in axisymmetric simulations. As silicon is such a stable in microelectromechanical systems (MEMS), if one needs to design a system that involves silicon then one can instead use silicon (111) as plates of that behaves as an isotropic material [134].

The fluid mechanical equations in this chapter have been stated without reference to any specific coordinate system, and as long as they are applied with the appropriate derivative, can be calculated in such a system. By being careful when taking the derivative, since the derivative of the basis functions need to be accounted for, one can find the appropriate derivative in cylinder coordinates, and for convenience the gradient of a scalar and divergence of a vector is[128],

$$\nabla A = e_r \partial_r A + e_\phi \frac{1}{r} \partial_\phi A + e_z \partial_z A, \quad (2.46)$$

$$\nabla \cdot \mathbf{B} = \frac{1}{r} [\partial_r (r B_r) + \partial_\phi B_\phi + r \partial_z B_z]. \quad (2.47)$$

Chapter 3

Numerical modeling and validation of FEM in COMSOL

This chapter will briefly describe the numerical modeling in general terms that was used in this thesis. COMSOL[135] was used as a finite element method (FEM) solver to simulate the acoustofluidic and acoustomechanical systems that were investigated in the papers and later sections. MATLAB[136] was sometimes used as a more flexible way of controlling COMSOL through the LiveLink package and sometimes to post-process the results. None of the extra COMSOL packages were used, instead the weak form solver was used that is built in to the fundamental COMSOL Multiphysics program. The description of the numerical FEM solver will be kept basic in Section 3.1 with weak form formulation in Section 3.1.1 and boundary conditions in Section 3.1.2. The concrete COMSOL implementation will be described in Section 3.2, with the use of the adaptive frequency stepping method in Section 3.2.2, and some short discussion in of the numerical validation, convergence analysis, comparison with experiments, and axisymmetric comparison to the full 3D, and rounded off by a discussion of thin-films and electrodes in Section 3.3 to Section 3.3.4.

3.1 Finite element method

The theory chapter, Chapter 2, presented the partial differential equations (PDE) that we would like solve in various types of system in order to understand or predict the behavior in specific acoustofluidic phenomenon. While it is possible to solve these equations analytically in some limited, simplified, or very specific systems[77, 137] it is in general not possible, or at least very difficult and time consuming, to find the analytical solutions to the coupled PDE's in the theory chapter, and instead a numerical solution to the equation can be sought. One such numerical method is the finite element method (FEM) which can be used for solving partial differential equations (PDE) on a grid of points, referred to as a mesh in the thesis. The method works by solving for a large but finite number of elements of test functions which can be used to approximate any continuous function.

3.1.1 Weak form formulation

Let us first assume that the PDE's can be written in terms of a generalized flux tensor field, \mathbf{J} , a generalized force vector field, \mathbf{F} , and a solution, $\mathbf{h}(\mathbf{r}, t)$, such that,

$$\nabla \cdot \mathbf{J} [\mathbf{h}(\mathbf{r}, t)] - \mathbf{F} [\mathbf{h}(\mathbf{r}, t)] = 0, \quad (3.1)$$

then the task becomes to find the solution, $\mathbf{h}(\mathbf{r}, t)$. In order to make a computer able to guess $\mathbf{h}(\mathbf{r}, t)$ in an automated way, we expand it into a weighted sum over a complete set of polynomial functions. Each is defined piecewise on each element, called a test function, $\Theta_n(\mathbf{r}, t)$, and the task is now to find the weighing, C_n , of each element on each function. $\mathbf{h}(\mathbf{r}, t) = \sum_n C_n \Theta_n(\mathbf{r}, t)$. However it is still a problem finding the weighing in an efficient manner, and the problem of showing that solution is indeed a solution. The problem can be turned into showing that the projection unto an arbitrary function is zero. This can be done by projecting the equation Eq. (3.1) onto every test function and integrating over the volume, we can require each integral over each test function to be zero, as the left hand of Eq. (3.1) should be equal to the right hand if we indeed have the correct solution. Therefore,

$$\sum_n \left\{ \int_{\Omega} \Theta_m(\mathbf{r}, t) \cdot \nabla \cdot \mathbf{J} [C_n \Theta_n(\mathbf{r}, t)] - \Theta_m(\mathbf{r}, t) \cdot \mathbf{F} [C_n \Theta_n(\mathbf{r}, t)] \right\} dV = 0, \quad (3.2)$$

where the sum has been taken out of the integral. By assuming that \mathbf{J} is linear and by using Gauss theorem,

$$\sum_n \left\{ \oint_{\partial\Omega} \Theta_m \cdot \mathbf{J}(\Theta_n) \cdot \mathbf{n} dA + \int_{\Omega} -\nabla \Theta_m : \mathbf{J}(\Theta_n) - \Theta_m \cdot \mathbf{F}(\Theta_n) dV \right\} C_n = 0, \quad (3.3)$$

where moving the derivative over to the test function is easier for the solver as the derivative on the test functions can be done analytically, and we have dropped the special and temporal dependence of the test functions for clarity. Now by only expanding to a finite order of test functions, since higher order polynomials will have diminishing effect on expansion if the elements that each test function spans are small enough, we get a finite number of integrals, such that the problem of finding the coefficients becomes a inverse matrix problem $\sum_n K_{nm} C_n = 0$, where K_{nm} is the integral over the n and m test functions which can be calculated, and therefore through matrix operations the C_n coefficients can be found.

3.1.2 Boundary conditions

The boundary integral in Eq. (3.3) gives the possibility to implement boundary conditions on the problem. The two types of boundary conditions that are used in the thesis is the Neumann boundary condition, which in COMSOL is called the weak contribution, and the Dirichlet boundary condition. The Neumann boundary condition is setting the

flux at the boundary to a specific value, and therefore it means setting the generalized flux, $\mathbf{J}[\Theta_n] \cdot \mathbf{n} = \mathbf{N}(\Theta_n)$, to the desired flux boundary condition, where $\mathbf{N}(\Theta_n)$ is the flux condition on the boundary. The Dirichlet boundary condition sets the value of the function at that boundary to a specific value. Examples on how they are used in this thesis is written in the COMSOL implementation Section 3.2.

3.2 COMSOL implementation

COMSOL is the software that is used to solve PDE's given in the theory chapter Chapter 2, that is, Cauchy equation Eq. (2.4), Maxwell's first equation, Eq. (2.7), and pressure acoustic equation, Eq. (2.24b), and it uses its own built in FEM solver based on the method described in Section 3.1. In order to solve the physics for these specific systems we use the weak form formulation, defined in COMSOL multiphysics base program, under the name "Weak form PDE", and find the generalized flux, \mathbf{J} , and the generalized force, \mathbf{F} , for each of the fields, as well as defining the boundary conditions on each domain. For the Cauchy equation, Eq. (2.4), the generalized flux and force is, where we have assumed time harmonic first order fields,

$$\nabla \cdot \boldsymbol{\sigma}_{\text{sl}} + \rho \omega^2 \mathbf{u}_1 = 0, \quad \mathbf{J} = \boldsymbol{\sigma}_{\text{sl}}, \quad \mathbf{F} = -\rho_{\text{sl}} \omega^2 \mathbf{u}_1, \quad (3.4)$$

with the definition of the stress in solids in Eq. (2.6) and for piezoelectric materials in Eq. (2.6). For Maxwell's first equation, Eq. (2.7), the generalized flux and force is,

$$\nabla \cdot \mathbf{D} = 0, \quad \mathbf{J} = \mathbf{D}, \quad F = 0, \quad (3.5)$$

where \mathbf{D} for a piezoelectric material is defined in equation Eq. (2.8). For the pressure acoustic equation, Eq. (2.24b), the generalized flux and force is,

$$\nabla \cdot \nabla p_1 + k_c^2 p_1 = 0, \quad \mathbf{J} = \nabla p_1, \quad F = -k_c^2 p_1. \quad (3.6)$$

The boundary condition from the solid unto the pressure is a weak contribution, or Neumann boundary condition, such that

$$N(p_1, \mathbf{V}_1) = \partial_\zeta p_1 = \frac{i\omega\rho_0}{1 - i\Gamma_{\text{fl}}} \left(V_{1\zeta}^0 - \frac{i}{k_s} \nabla_{\parallel} \cdot \mathbf{V}_{1\parallel}^0 \right) - \frac{i}{k_s} (k_c^2 p_1 + \partial_\zeta^2 p_1), \quad (3.7)$$

and the boundary condition on the solid from the fluid is also a Neumann boundary condition, such that

$$\mathbf{N}(p_1, \mathbf{V}_1) = \boldsymbol{\sigma}_{\text{sl}} \cdot \mathbf{e}_\zeta = -p_1 \mathbf{e}_\zeta + \eta_0 i k_s \left(\mathbf{V}_1^0 - \frac{1 - i\Gamma_{\text{fl}}}{i\omega\rho_0} \nabla p_1 \right). \quad (3.8)$$

The boundary condition from the electric potential defined in equation, Eq. (2.15b), Eq. (2.15c), Eq. (2.15d), are defined as Dirichlet boundary conditions on the surface of the piezoelectric material in question, which simply is defining the desired values at the surface in COMSOL. The remaining boundary condition are simply zero flux, which are the standard boundary condition that is defined in COMSOL if nothing else defined, which translates to $\mathbf{N}(\Theta_n) = 0$.

3.2.1 Material parameters

In order to modeling specific systems, in order to be more concrete instead of only investigating in more general descriptions of *fluids* and *solids*, require the parameter values for each material that is needed in order to simulate the systems. In this thesis there are used many different materials, and the parameter values have come from many different sources. Although more materials have been used during the PhD project than is presented in this thesis, the material parameters needed to reproduce the simulation in presented in this thesis, are summarized in the tables, Table 3.1 for water, Table 3.2 for Iodixanol concentrations, Table 3.3 for piezoelectric materials, and Table 3.4 for the solids, with the references to the sources for all the parameters in the tables.

Table 3.1: Parameter values for water as used in this thesis. The values are calculated based on polynomials that are fitted in temperature and are here presented at 25 C° and are from Ref. 117

Parameter	symbol	value	unit
Density	ρ_0	997	kg m ⁻³
Speed of sound	c_{fl}	1497	m s ⁻¹
Compresibility	κ_0	448	TPa ⁻¹
Bulk viscosity	η_{fl}^b	2.485	mPa s
Dynamic viscosity	η_{fl}	0.890	mPa s
Dampening	Γ_{fl}	10.3	THz ⁻¹ f

Table 3.2: Parameter of Iodixanol of varying concentrations. The polynomial fit is done in Ref. 28, and restated here for convenience, as these parameters plays a role in Paper III, Section 5.3.

Parameter	symbol	value	unit
Density	ρ_0^{Iod}	$1005 + 5.245x$	kg m ⁻³
Speed of sound	c_{fl}^{Iod}	$1507 - 0.7308x + 8.053 \cdot 10^{-3}x^2 + 2.557 \cdot 10^{-5}x^3$	m s ⁻¹
Compresibility	κ_{fl}^0	$438.4 - 1.853x + 3.116 \cdot 10^{-3}x^2$	TPa ⁻¹
Dynamic viscosity	η_{fl}^{Iod}	$0.954 + 1.952 \cdot 10^{-2}x + 2.419 \cdot 10^{-4}x^2 + 2.173 \cdot 10^{-5}x^3$	mPa s
Iodixanol concen.	x	from $x = 0$ to $x = 60$	%

Table 3.3: Parameter values for all the of piezoelectric materials used in this thesis, where the relation $C_{66} = \frac{1}{2}(C_{11} - C_{12})$ applies since the materials are hexagonal in structure, or at least to fair approximation in average, with films being textured with grain boundaries randomly oriented in the film and bulk PZT being a ceramic typically with randomly oriented grain structures that have a polarization along the z axis.

Parameter	symbol	value	unit	Parameter	symbol	value	unit
<i>Thin-film aluminum nitride, AlN [138–140]</i>							
Density	ρ_{sl}	3300	kg m^{-3}	Mech. dampening	Γ_{sl}	0.0005	
Elastic modulus	C_{11}	410.2	GPa	Elastic modulus	C_{33}	385.0	GPa
Elastic modulus	C_{12}	142.4	GPa	Elastic modulus	C_{44}	122.9	GPa
Elastic modulus	C_{13}	110.1	GPa	Elastic modulus	C_{66}	133.9	GPa
PZE coefficient	$e_{31,f}$	-1.05	C m^{-2}	PZE coefficient	e_{15}	-0.39	C m^{-2}
PZE coefficient	e_{33}	1.46	C m^{-2}	El. dampening	Γ_{ε}	0.0005	
Permittivity	ε_{11}	9	ε_0	Permittivity	ε_{33}	11	ε_0
<i>Thin-film aluminum scandium nitride, Al_{0.6}Sc_{0.4}N [138, 140]</i>							
Density	ρ_{sl}	3300	kg m^{-3}	Mech. dampening	Γ_{sl}	0.0005	
Elastic modulus	C_{11}	313.8	GPa	Elastic modulus	C_{33}	197.1	GPa
Elastic modulus	C_{12}	150.0	GPa	Elastic modulus	C_{44}	108.6	GPa
Elastic modulus	C_{13}	139.2	GPa	Elastic modulus	C_{66}	81.9	GPa
PZE coefficient	$e_{31,f}$	-2.65	C m^{-2}	PZE coefficient	e_{15}	-0.32	C m^{-2}
PZE coefficient	e_{33}	2.73	C m^{-2}	El. dampening	Γ_{ε}	0.0005	
Permittivity	ε_{11}	22	ε_0	Permittivity	ε_{33}	22	ε_0
<i>Bulk and thin-film lead zirconium titanate, PZT [141]</i>							
Density	ρ_{sl}	7700	kg m^{-3}	Mech. dampening	Γ_{sl}	0.005	
Elastic modulus	C_{11}	168	GPa	Elastic modulus	C_{33}	123	GPa
Elastic modulus	C_{12}	110	GPa	Elastic modulus	C_{44}	30.1	GPa
Elastic modulus	C_{13}	99.9	GPa	Elastic modulus	C_{66}	29.0	GPa
PZE coefficient	$e_{31,f}$	-14.7	C m^{-2}	PZE coefficient	e_{31}	-2.8	C m^{-2}
PZE coefficient	e_{33}	14.7	C m^{-2}	PZE coefficient	e_{15}	9.86	C m^{-2}
Permittivity	ε_{11}	828	ε_0	Permittivity	ε_{33}	700	ε_0
				El. dampening	Γ_{ε}	0.005	

Table 3.4: Parameter values of the most used solids used in this thesis. Reference values for the different materials are in the table. Some of the parameter values for Schott D263 and Pyrex are calculated by using Eq. (2.10a) and Eq. (2.10b), and using the relation, for isotropic materials $C_{12} = C_{11} - 2C_{44}$.

Parameter	symbol	value	unit	Parameter	symbol	value	unit
<i>Glass, Schott D263</i> [142, 143]							
Density	ρ_{sl}	2510	kg m ⁻³				
Young's modulus	E	72.9	GPa	Poisson's ratio	s	0.208	
Elastic modulus	C_{11}	81.8	GPa	Elastic modulus	C_{44}	30.2	GPa
Elastic modulus	C_{12}	21.5	GPa	Mech. dampening	Γ_{sl}	0.0004	
Long. speed of sound	c_{lo}	5710	m s ⁻¹	Tran. speed of sound	c_{tr}	3467	m s ⁻¹
<i>Glass, Pyrex</i> [143, 144]							
Density	ρ_{sl}	2230	kg m ⁻³				
Young's modulus	E	62.8	GPa	Poisson's ratio	s	0.20	
Elastic modulus	C_{11}	69.8	GPa	Elastic modulus	C_{44}	26.2	GPa
Elastic modulus	C_{12}	17.4	GPa	Mech. dampening	Γ_{sl}	0.0004	
Long. speed of sound	c_{lo}	5594	m s ⁻¹	Tran. speed of sound	c_{tr}	3425	m s ⁻¹
<i>Silicon</i> (100) [133, 143]							
Density	ρ_{sl}	2329	kg m ⁻³	Mech. dampening	Γ_{sl}	0.0001	
Elastic modulus	C_{11}	165.7	GPa	Elastic modulus	C_{44}	79.6	GPa
Elastic modulus	C_{12}	63.9	GPa				

Table 3.5: Parameter values for 5- μ m-diameter polystyrene particles in water, with all parameters at 25 °C except for the speed of sound in polystyrene which was measured at 20 °C. The parameter values are from Ref. 145, except that the scattering coefficients f_0 and f_1 are calculated from Eq. (2.36) using the particle radius $a = 2.5 \mu\text{m}$.

Parameter	symbol	Value	Unit
Density	ρ_{ps}	1050	kg m ⁻³
Compressibility	κ_{ps}	249	TPa ⁻¹
Poisson's ratio	ν_{ps}	0.35	
Speed of sound at 20 °C	c_{ps}	2350	ms ⁻¹
Monopole coefficient, Eq. (2.36)	f_0^{ps}	0.44	
Dipole coefficient, Eq. (2.36)	f_1^{ps}	0.034 + 0.0002 i	

3.2.2 Adaptive frequency stepping

One of the methods used during the project is the adaptive frequency stepping procedure, as a method for controlling COMSOL through Matlab and the LiveLink module, which was mentioned in Paper I, but not explained in depth. When doing frequency sweeps in systems of high Q-factor systems, the peaks are very narrow and often spaced far apart in the frequency domain. This means that if the same resolution that is necessary to properly resolve the peaks is used everywhere, the time spent to make long sweeps in frequency would increase dramatically. As an example with the adaptive stepping method used in paper I, a typical frequency sweep over the range 0.1-3 MHz was done with 450-500 points, where the lowest frequency step necessary to resolve the peaks was 15 Hz, and at large flat sections the frequency stepping increased to 16000 Hz. This simulation on a workstation with a 3.7-GHz Intel Core i9 7960X processor took roughly 40 min with adaptive frequency stepping, and should the entire simulation have been run at the minimum required resolution at 15 Hz the frequency sweep would have taken roughly 4 days, without the higher resolution solutions being different enough to notice with the naked eye.

While the method dramatically sped up the computation speed of long frequency sweeps, the procedure is not very complicated and is a standard tool in numerical computations. The implementation in this case is to use COMSOL to do the simulation of a

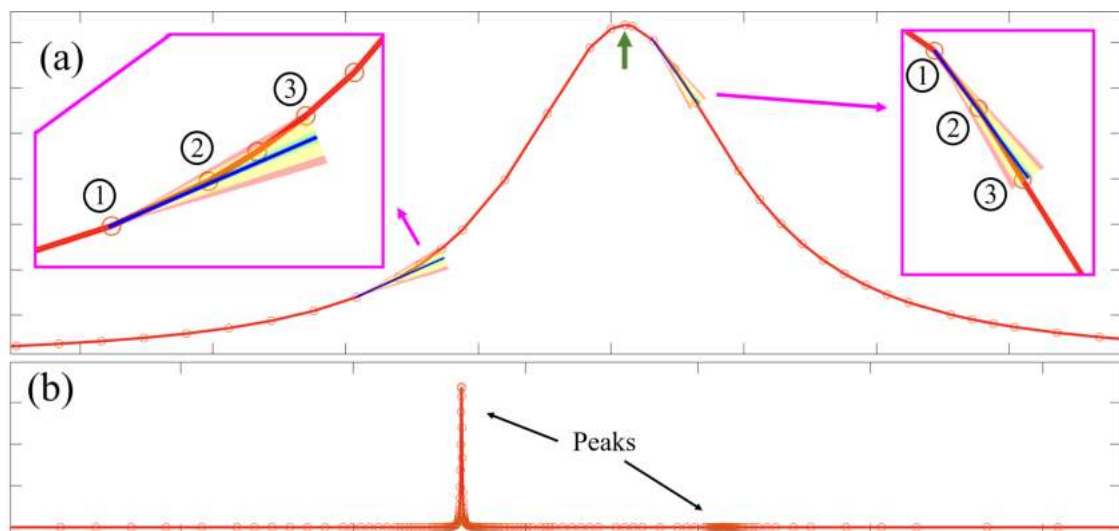


Figure 3.1: Sketch of adaptive frequency stepping method. (a) Sweep of a peak using stepping method. Insert on the left is a zoom in of a the down stepping, since the linear interpolation from 1 and 2 was to far from 3, shown in red bars that is outside tolerance, and insert on the right shows a up stepping since the interpolation within tolerance, shown as 3 being close enough to the interpolation. Green arrow on the center peak show the point that was simulated at the frequency estimated by fitting the points around the peak. (b) Show a zoom out of the sweep where it is seen that the peaks, a large one on the left and a small one on the right, are resolved much higher than the area in between peaks.

single frequency at a time controlled through Matlab by using COMSOL-Matlab livelink module. This allows for more control in a coding friendly environment. At each frequency a value is taken which is what is desired parameter to be resolved, this is done through a COMSOL probe. The next frequency to be simulated is chosen by taking a step size and adding it to the last frequency. The probe value from the simulation at this new frequency is compared to a predicted probe value by using a linear interpretation from the last two frequencies. If the actual probe value at this frequency differs from the predicted probe value by a predefined maximum tolerance, then the frequency step was too large, and step size is decreased and the last step is repeated. An example of this is seen on Fig. 3.1(a) on the insert to the left. If the difference between the predicted and simulated probe value is sufficiently smaller than some other predefined minimum tolerance then the step size is increased for the next step, see insert on right of Fig. 3.1(a). By choosing the minimum and maximum tolerances for when to change the step size up or down one can design the smoothness of the returned probe values compared to the time the sweep will take to complete. One could use a higher order interpolation in the prediction, however while this would increase the predictability, one would need to compensate by decreasing the tolerances correspondingly, and the end result would not change.

One additional process was used in this method for increasing the precision of the peak value. After a frequency sweep had passed a peak by some number of points, say n , the peak was fitted to a Lorentzian distribution by taking the point from $-n$ to n from the peak value, and from that fit the peak frequency was calculated and then simulated and added to the frequency sweep in order to have a more precise peak value, seen on Fig. 3.1(a) as the point the green arrow is pointing at.

On Fig. 3.1(b) is seen on a larger scale how the resolution on the sweep changes dramatically from resolving the peaks to resolving the large flat area in between. It also finds small peaks as seen in the large difference between the peak on the left and the one on the right.

3.3 Numerical validation

The numerics were validated in different ways throughout the thesis. The axisymmetric simulations are compared with full 3D simulations, mesh convergence analysis was carried out and is shown here on 2D axisymmetric simulations, where it is possible to increase the mesh drastically, the model of glass blocks AlN film is compared to measured frequency sweeps in paper I where 173 peaks spread over 35 devices presented in paper I, Section 5.1, and lastly the convergence of thin-film piezoelectric film and the effect of thin electrodes on them.

3.3.1 Axisymmetric compared to full 3D

Models where the system is axisymmetric can be simulated by changing coordinate system from cartesian to cylindrical, where if it is completely axisymmetric it is easy to convert into 2D simulations which are equal to simulations done in full 3D in Cartesian coordinates. This allows us to simulate systems that would otherwise not have been possible, either

because the system would have been too large to simulate in terms of random access memory (RAM) or in terms of the time necessary for one simulation that needs to be repeated many times, like frequency sweeps or even parameter fitting on large frequency spectrum. A system which is perfectly axisymmetric should have a solution calculated in full 3D be equal to axisymmetric simulations in 2D, and that is what is tested on Fig. 3.2 by using a toy model for our investigations. We simulate a 1- μm -thick circular membrane of Pyrex

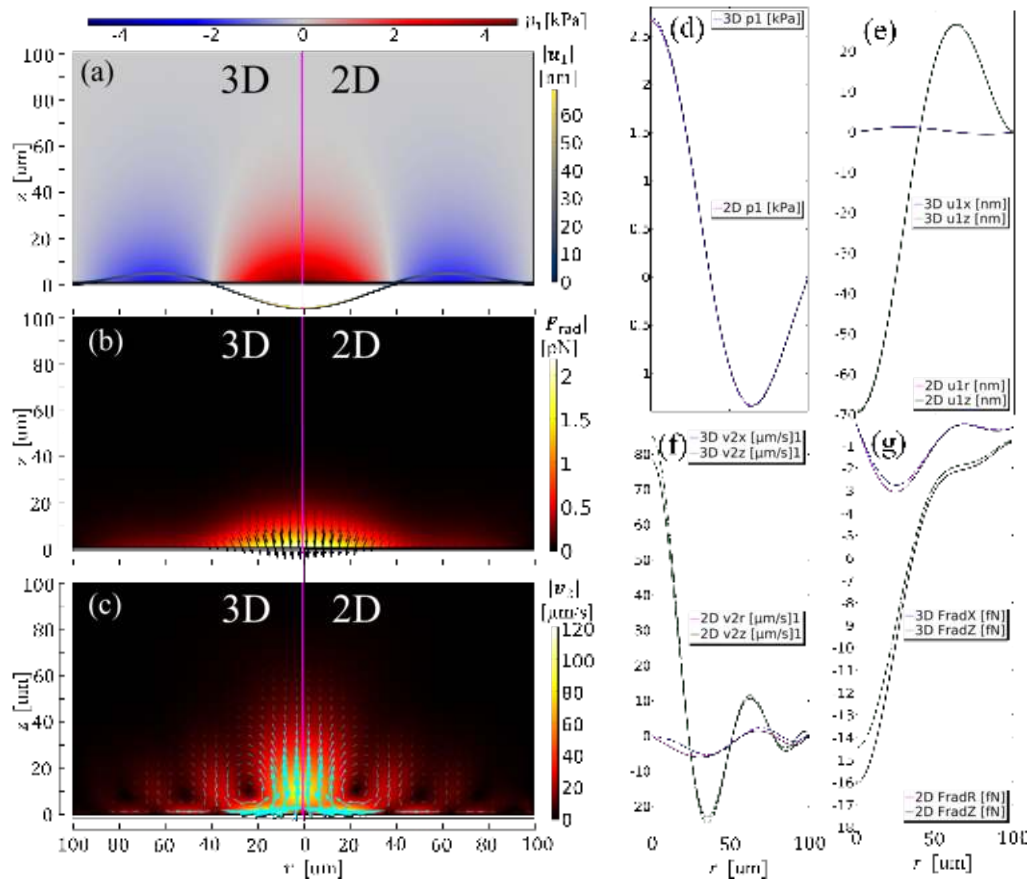


Figure 3.2: Shows the the fields in both full 3D and 2D axisymmetric simulations for a the second order resonance mode of a 1- μm -thick Pyrex membrane. (a)-(c) simulation cross section of a full 3D model on the left and a 2D axisymmetric on the right, with color bars to the right. (a) Pressure field, p_1 , and displacement field, \mathbf{u}_1 . (b) Radiation force, F_{rad} . (c) Acoustic streaming, \mathbf{v}_2 . (d)-(e) shows line plots of the different fields, where (d), (f), and (g) are taken at the horizontal line $z = 10 \mu\text{m}$ and (e) is taken at the horizontal line $z = 0 \mu\text{m}$. The line plots that correspond to 3D are dashed blue and green lines, and for 2D they are solid lines of the color magenta and black. (d) show the line plot of the pressure field, p_1 , (e) shows a line plot of the displacement components, $u_{1,r}$ and $u_{1,z}$, (f) shows the streaming components, $v_{2,r}$ and $v_{2,z}$, (g) shows the radiation force components, $F_{\text{rad},r}$ and $F_{\text{rad},z}$. As is seen the first order fields fit better than the second order fields.

with water above it. The membrane is actuated with a displacement of ± 1 nm at the edge of the membrane and the fluid above is contained with soft wall boundary conditions¹ on the edges at the top and sides. The simulations were done at the resonance of the second harmonic of membrane, which for the 3D model was 0.326 MHz and for the 2D system it was at 0.325 MHz. With 3D models on the left and 2D models on the right of Fig. 3.2 (a)-(c), the pressure, p_1 , and displacement field, \mathbf{u}_1 , are shown and compared on Fig. 3.2(a) qualitatively and through line plots in (d) and (e), as well as the radiation force, \mathbf{F}_{rad} , in (b) with line plots of the components in (g), and the second order acoustic streaming, \mathbf{v}_2 , in (c) and line plots components in (f). The line plots are taken at the line $z = 10$ μm , in the radial direction in 2D and in the x direction in 3D for all fields, except the displacement field which is taken likewise but at $z = 0$ μm , which corresponds to the top of the Pyrex membrane. As is seen in the simulated fields of the full 3D and axisymmetric 2D are very much alike, as one would expect them to be. There is no scaling for getting them to fit, they are simulated as presented, where the differences are discussed further down.

The main difference between the two is the use of RAM and computation time it takes to simulate the systems. The first order fields in 3D took 20 GB of RAM, 1.2 million degrees of freedom (DOF) and 8 minutes and 42 seconds to compute, where the 2D system took 3.0 GB of RAM, 159 thousand DOF, and 10 seconds to compute, and the mesh resolution, that is mesh elements per wavelength, was much higher 2D case compare to the the 3D case. The real advantage came with the second order fields, where the effective boundary theory was used for both 3D and 2D models. To compute the 3D system it took 371 GB of RAM, 3.3 million DOF and 1 hour and 20 minutes to compute on a high performance computer cluster (HPC) available at DTU, where as the 2D simulations took 2.2 GB of RAM, 105 thousand DOF, and 5 seconds to compute. The second order 3D fields sat the resolution limit on the system to be calculated as it was not possible to go much higher in requested RAM amount on the available HPC cluster. The simulation time, usage of RAM and DOF are rough guidelines as exactly how COMSOL does not seem to make a lot of sense, and results are only reproducible within $\pm 20\%$.

On Fig. 3.2 it is seen that the first order fields fit fairly well, and as one might expect, the difference between 3D and 2D becomes more pronounced in the second order fields, as difference from the first order fields will be squared, by the nature of the first and second order fields. While the over all structure is the same in 3D and 2D, the most pronounced difference lies in the differences in $v_{2,r}$, and the exact reason for this, whether it lies in the model implementation or mesh resolution, is not yet known, but if not in the model then it could lie in one of the follow. There could be many explanations for the difference seen, and the most obvious is the mesh resolution where the 3D model could not be converged to the same degree as the 2D model, and with the resolution that was possible in 3D it would not have been expected that the results would be accurate within more than a percent, so that is one possibility of the error. An other possibility is the artificial actuation in the model, which was implemented as a harmonic displacement with 1 μm in amplitude

¹Soft wall boundary conditions in this case means that the pressure is set to zero at the edges, by the Dirichlet boundary condition. This is equivalent to have a perfectly soft wall, hence the name, where the wall would move if any pressure is put on it, and therefore the pressure is zero to accommodate this change.

at the edge of the Pyrex membrane, which borders right up the the fluid domain. At this boundary we should not expect the effective boundary condition to hold, as it is beyond the range of validity as stated in Bach and Bruus Ref. 78. The overall experience with the effective boundary conditions have been that even though sharp corners could be a problem for them, it is in general very robust to such, but in this fairly extreme case it could maybe introduce some error that might explain the differences. Lastly the 3D model and the 2D model in the simulations presented in Fig. 3.2 are two different iteration of the same model with the difference that in the 3D model it simulates the velocity field in the solid and calculates the displacement field in the solid, whereas the 2D model simulates the displacement field in the solid and calculates the velocity fields in the solid. Whereas it might introduce some differences, in general it seems to give good agreement between the two models on Fig. 3.2.

This, in general, good agreement in Fig. 3.2 gives us confidence to use this model to simulate systems that require either higher resolution than is possible in full 3D. One such system is the membrane modes in Paper III, Section 5.3, where at the frequencies in question and the large water volume, it would not have been possible to simulate in full 3D even by going to the HPC cluster.

3.3.2 Mesh convergence analysis

The numerical simulations should be independent of the specific mesh for there to be any hope of the simulations being a correct simulation of a real world physical device. In order to check that we do mesh convergence analysis of our numerics to see if there is any mesh dependence. Here we will show an example of mesh convergence analysis by investigating the 2D toy model that was also used in Section 3.3.1 to compare axisymmetric simulations to full 3D simulations, and thereby the toy model serves two purposes. We say that the model has reached mesh convergence if the solved fields do not deviate from higher mesh resolutions by some fraction. If we do not have an analytical solution to compare to, which we often do not, then we must see how the convergence trend goes by comparing to the highest mesh possible, with the system we have access to. In order to quantify the difference between two solutions we calculate the L2-norm difference divided L2-dorm of the highest resolution, calculated as[122],

$$C(g_n) = \sqrt{\frac{\int_{\Omega} |g_n - g_{\text{ref}}|^2 dV}{\int_{\Omega} |g_{\text{ref}}|^2 dV}}, \quad (3.9)$$

where g_n is the n 'th solution of g , where g is a stand in to one of the fields in the solution, in the convergence analysis and g_{ref} is the reference value of that field, often best guess of the solution, which often translates to highest resolution that was possible.

Sometimes convergence analysis and comparison to analytical models are not enough, in particular if the model is wrong to being with. In such cases comparing to experiments in the only solution, which will be discussed in Section 3.3.3.

3.3.3 Comparison with experiments

Some comparison with experiments were done, in particular in Paper I, Section 5.1, where we used the model to fit to 173 peaks spread over 35 devices of 9 different types. Both the amount of peaks spread across the different devices and geometries, as well as the overall fit gives us confidence that the solid mechanical modeling does indeed fit the real devices. This is important in particular as it shows that the modeling of the film seems to be consistent over a host of nominally equivalent devices as well as across some different device geometries. One of the critique points that still could be made is that we only look at the impedance spectra, and fitted peaks to peaks, and do not know if the modes look the same in the real devices and they do in the simulations. However when one takes a look at the resulting modeling, seen as animation in the supplemental material of Paper I, Ref. 2, it is difficult to see how the modes could look much different that they do. With that and the fact that we are not fitting to few peaks individually but to the entire spectra and are seeing all the experimental peaks in the simulation as well suggests that the modes are the same.

This agreement with simulation and experiments in the solid mechanical part in Paper I when actuated by a piezoelectric thin-film is good news for the results of the Paper II, Section 5.2. In some sense the system is essentially a mechanical bulk resonator, where the fluid constitutes only roughly 1.2% of the total volume, and the film is less than 0.1% of the total volume. Therefore having a good understanding of the thin-film and mechanical system that governs the roughly 99% of the device is a good place to start. The solid mechanical part of the model in Paper I and Paper II is the same. The fluid mechanical simulations in Paper II were compared to a device that was studied in the literature, where they had a bulk PZT transducer attached to their device. By using the same model for the thin-film driven device as was used to compare the bulk PZT devices to the literature, we hope that this would be an indirect way of testing the thin-film device. The only thing remaining is to compare to a real thin-film driven acoustofluidic bulk device, which we very much look forward to.

As a side note, simulations were compared to several different results published in peer-reviewed journals, other than the one mentioned in the previous paragraph. This was in order to validate the model, both in terms of simulations and experiments, from other groups, in order to see if our model replicated what what was already published. This has however not been included in this thesis.

3.3.4 Mesh of thin-films and electrodes

A general rule of thumb the mesh should contain atleast 6 nodes per wavelength[93], however as the wavelength is large because of the high speed of sound in for example AlN or AlScN, and because the film is so thin, this would mean that not very many mesh elements ever are necessary. Because of the small thickness of the film often the electric field is very large, and although it is usually linear when actuating it far away from the bulk resonance of the thin-film, it can have large gradients at the boundary of the electrodes. The largest problems with the mesh in the film is that if one is not careful

there can come elements with very large aspect ratios, which can happen when COMSOL tries to match the film-mesh with other parts of the system. One way that seemed to work fairly consistently was to generate a mesh on the film surface, roughly four times as large as the desired mesh in the solid that the film is deposited on, then sweep the mesh through the film volume and refine it twice. This gives a mesh that at the surface interface between the film and the substrate is roughly the same size and four mesh elements in thickness direction, which is more than the 6 nodal elements that because of the element order always being at least quadratic. In most simulations however there where usually no effect seen on the simulation by changing from having one mesh element in the thickness to four or even more, however since the film is such a small part of the system it usually does not impact the simulation time much to have a higher resolution in the film, and therefore most of the time four elements were chosen.

An other part of the thin-films that seemingly would impact on the system is the electrodes on the thin-film. While the electrodes play a great role in the practice since the electrodes help define the polarization of the crystal structure, in the simulations the electrodes usually plays a smaller role. The electrodes of the film is on the order of roughly 100 nm, which with typical thin-film thickness of 1 μm means that they are fairly large compared to the thin-film. In the simulations we assume that they do not do not change the electric field as they represent equipotential surfaces for the electric potential. They do contribute to the solid mechanical resonance frequency, but for the large bulk systems presented in Paper I and II, they contribute so little to the changes in frequency that it is usually not observable on the system whether they are included or not. This is because the frequency changes would vanish within other uncertainties in the system, either measurement uncertainties in paper I, or fabrication or parameter uncertainties. Therefore it is often not practical to include them. In both Paper I and Paper II they were originally included, however after having investigating the minute effect they had on the system they were omitted again. The role that the electrodes have in practice for the growth of the film, the actuation of the film, or the attachment to the substrate has not been explored in this thesis.

Chapter 4

Summery of Results

The purpose of this section is to give an overview of some of the results that has been produced in this thesis. The summery of results include the three papers, a conference contribution, and two minor results that have not been published. The intention with this summery of results is have something in-between the short abstract that are in the papers and reading the whole article, as well as having a chapter to give information that for one reason or other did not make it into the papers. It is also a way to convey information which might be of interest to some reader, which did not fit into a traditional article format, such as motivation and underlying idea before going into a project, and in general give a slightly different perspective. If the reader is so inclined they are welcome to skip this section and go to the paper which are each self contained.

4.1 Paper I

Paper I refers to the paper titled: *Fabrication, Characterization, and Simulation of Glass Devices with AlN Thin-Film Transducers for Excitation of Ultrasound Resonances*, with the authors *André G. Steckel, Henrik Bruus, Paul Muralt, and Ramin Matloub*. For a very quick summery see the abstract of paper I in Section 5.1, and here will be a slightly longer summery with a few extra details that were omitted because the format of traditional scientific papers.

Original idea: The paper springs from the idea of whether it would be possible to characterize the material parameters of a substrate by depositing a thin-film piezoelectric film on top of it and characterize its impedance spectra. It was assumed that in order to validate the results there would need to be an ensemble of different shapes and a host of nominally equivalent devices.

Motivation: There were several points that were interesting to investigate by this research, that is other than to test the main hypothesis of whether the core concept of the original idea was possible at all. Firstly it was to test that the solid mechanical part of the modeling was correct. Without having had access to acoustofluidic devices

that showed a high degree of reproducibility, as they always have either had large tolerances because of either the manufacturing process or unreproducible human handling, the device simulation-experiment correspondence have at best been phenomenological equivalent, without exact one-to-one correspondence in the entire frequency domain. Also there was the question of whether the model correctly simulated thin-film devices. Of course the first step in that process was to show that the nominally equivalent devices indeed gave reproducible results, which they did. Lastly it was to see if it was possible to improve the accuracy of the material parameters on a glass type that might be used for acoustofluidic devices later in the project. No matter how good the model is, if the material parameter values are not correct the final modeling will not be very accurate.

Design: The design of the devices were to be compatible with the photolithography method in terms of smallest sizes. The devices also to be designed such that they could

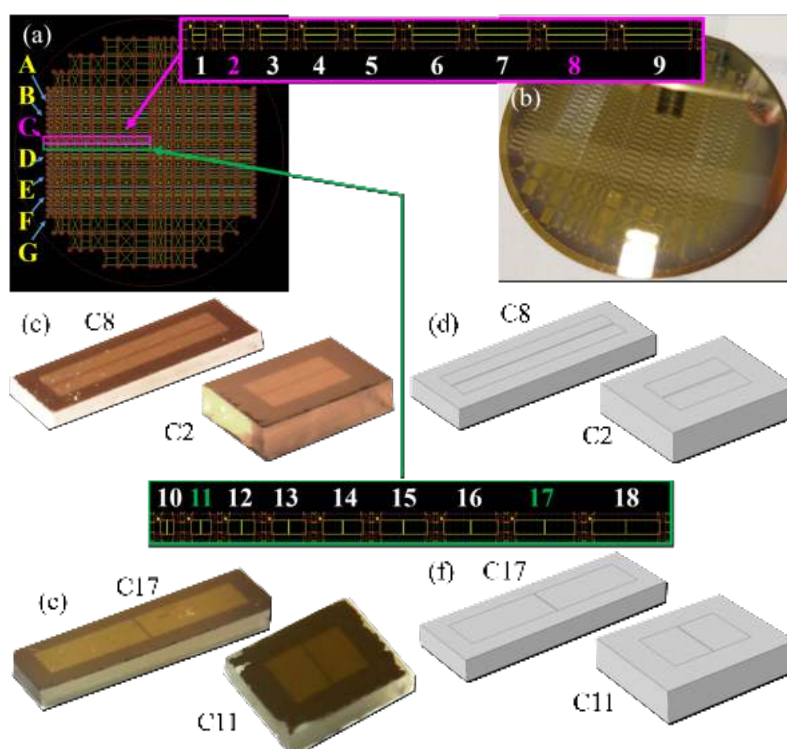


Figure 4.1: Shows the design of glass devices and electrode patterns. (a) is the mask of the top electrode on the 4-inch wafer. Purple and green boxes show zoom in on devices that are designed with a split along the device (purple) and with the split across the device (green). (b) show the wafer before it was diced with the top electrodes patterning in gold. (c) shows images of the devices C8 and C2 after they were diced, with the modeling counter part on (d). (e) shows images the devices C17 and C11 after they were diced, again with their model counterpart on the right in (f). Adapted from [2]

be diced with long straight cuts. Lastly the closest distance the electrodes could be to the edges of the devices, without risking short-circuits, between the top electrodes and the bottom electrodes, when dicing the devices, was chosen to be 500 μm in order to be on the safe side. Three main types of electrode designs were made, across nine different device lengths, with 14 repetitions of the set was chosen. The electrodes were split along the length of the device, split along the width of the device, and unbroken top electrode, all of them with a fully covering bottom electrode. The fully covering top electrode should have had part of the top electrode and film removed later in the fabrication, but the step was skipped in the fabrication process and therefore these devices were never tested, as it was not possible to access the bottom electrode for impedance measurements. At the edges of the wafer the remaining space was used for devices of different dimensions and electrode shapes than the standard devices, with the idea that these devices would then be used as a validation of the parameters that were fitted to the other devices.

Fabrication: The fabrication of the devices was carried out at clean-room facility Ecole Polytechnique Fédérale de Lausanne (EPFL) by Ramin Matloub, co-author of the paper. The devices were fabricated on 4-inch wafers of soda-lime-silicate float-glass whereupon 10 nm of titanium were sputtered, as an adhesion layer, after which 100 nm of platinum was sputtered, which is necessary for defining the crystal growth orientation of the 1- μm -thick aluminum nitride (AlN) film. The platinum film also acts as a bottom electrode for the film. The AlN film is grown in the Wurtzite crystal structure in the (0001) orientation with randomly orientated grains in the plane, which does not matter as the hexagonal structure is isotropic in the plane. On top of that was 10 nm of chrome, as an adhesion layer, and then 100 nm of gold sputtered on top of AlN film, followed by a photoresist film which was used to etch the inverse of the top electrode design of the gold and chrome such that the gold patterns left become the top electrodes. The devices were then diced out from the wafer by a 120 μm wide diamond circular saw. For the details on the fabrication see Paper II.

Characterization: The characterization of the dimensions of the devices were done with a electronic micrometer and their electrical impedances were measured by a Agilent 4294A Precision Impedance Analyzer (Agilent Technologies AG, Basel, Switzerland), with details on the instruments and measured dimensions in Paper I. For the impedance spectra it was important that the connector leads were as short as possible since even small parasitic inductances made large changes to the impedance spectra. It was also important that the connections did not effect the system, and therefore spring loaded needle electrodes were chosen, as they would have smallest impact while still staying connected. The reflections from the surface that the device was placed on were eliminated by placing the device on a piece of folded tissue paper. For the measurements a box was built that plugged into the impedance analyzer that allowed for the smallest electrical leads, which had grounded coaxial electrode in a four point measurement setup. The box allowed for quick and easy change of devices, and for consistent measurements. Measurements were done from 0.1 to 10 MHz in steps of 500 Hz, which required a LabVIEW program to control and collect the data, and each measurement took roughly 20 minutes. Of the devices

that were available 144 devices were tested, where some devices were discarded if they had a short circuit between the top and the bottom electrode on both top electrodes. That is to say if only one of the top electrode was shorted, the measurements were still taken, and is included in the 144 measurements, which gave different electrode impedance spectra that the ones that were not shorted. Of the 144 measurements, 35 measurements made it into Paper I, where they were analyzed further. The paper was only focused on devices with top electrodes split along the length of the device, not those split across, and only the measurements that did not have obvious faults, like a device that had one of the top electrodes shorted, or if the connection was momentarily lost because someone walked by. One thing that is apparent when seeing the curves on Fig. 4.2 is that the spectra shown on (c) look to have similar peaks and the overall structures seem to be the same but they

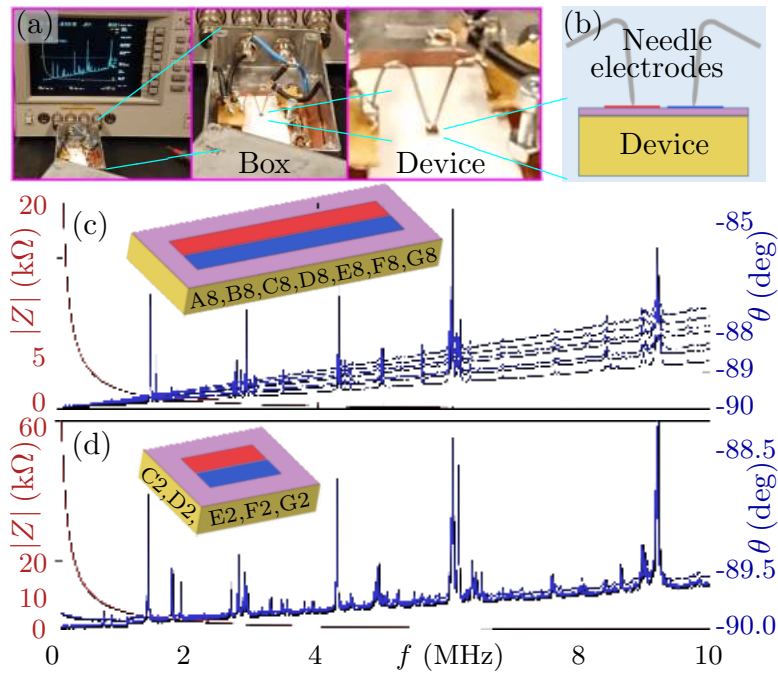


Figure 4.2: Impedance measurements on the devices A8-G8 and C2-G2. (a) shows from the left the impedance measurement device, Agilent 4294A Precision Impedance Analyzer, the box made to do the measurements in a consistent and reproducible way, and a zoom in on the device. (b) a sketch of the device showing the needle electrodes that were spring loaded by torsioning a spring further up in the system. (c) shows the impedance measurements of the devices A8-G8, with the absolute value of the impedance spectra in orange and the phase in blue. Notice that the phase plots does not lie on top of each other as there is a slope that is different for each device, which is a result of not having the discharge the electrodes. (d) Measurements of the impedance spectra of devices C2-G2. Notice that here the electrodes were short circuited in order to discharge the film before each spectra, such that the spectra now lies on top of each other. Adapted from [2]

all have different slopes. This was solved on Fig. 4.2 (d) by discharge the devices by before each spectra short circuit the top electrodes with a conducting piece of metal. By looking on the spectra on Fig. 4.2 it is seen that the curves of many nominally identical devices lie on top of each other. This is important as reproducibility is one of the first requirement we wanted to show, and is a minimum requirement for having any chance to determine the parameters *in situ*.

Simulations: The simulations for the 9 different geometries of the devices with the split along the device were done according to the theory described in Chapter 2, but without the fluid, and the adaptive frequency stepping, as described in Section 3.2.2, was also

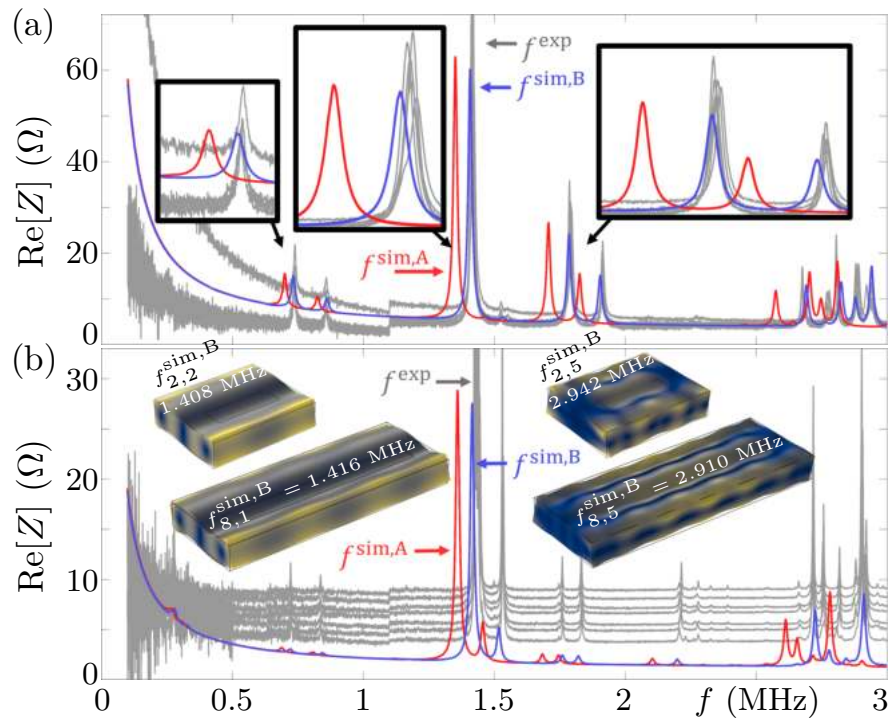


Figure 4.3: Simulations of glass devices and comparison of calculated impedance spectra to measured. (a) Measurements of the real value of the impedance spectra for devices C2-G2 in gray. Red curves show simulations with manufacturer parameter values and blue curves show the simulations with fitted parameter values, Young's modulus and Poisson's ratio, for the glass substrate. As is seen on the inserts, which are zoom-ins on the curves, the blue curve fits significantly better than the red curve. (d) The curves for measurements in gray for devices A8-G8, simulations on the original parameter values in red and the fitted parameter values in blue, with inserts showing two four modes in the simulations. The two top are from the spectra shown in (a) with the mode numbers (2,2) and (2,5) referring to the modes described in the table II in paper I. The two bottom inserts are for simulations shown in the spectra in (b). Adapted from [2]

used. With the adaptive frequency stepping method the frequency changed between 15 Hz and 16000 Hz and a typical sweep from 0.1 to 3 MHz was resolved with 450-500 points and took 40 min per device on a workstation with 128 GB of random access memory (RAM) and a Intel core i9 7960X processor at 3.7-GHz with 16 cores. Without the adaptive frequency stepping the a device at the same max resolution would take roughly 4 days to compute for one device, and for all the nice geometries it would roughly take a month of computation time, per time all the devices were simulated, which was many times as the parameter values were refined iteratively.

Comparison with experiments: The simulations gave curves that had the same overall structure as the measured impedance curves but seemed to have a trend of the resonance peaks being systematically to low, when using the manufacturers parameter values. This was quantified by comparing the 5 most prominent and identifiable resonance frequencies in the spectra of each device and comparing them to experiments. 45 simulation peaks were compared to 173 experimental peaks, and the peak values the simulations were found to be $(-4.6 \pm 0.1)\%$ of relative deviation off from the experimental resonance peaks. The spectra of the original parameter values can be seen as the red curves on Fig. 4.3 where it is seen that they are consistently lower than the grey peaks.

Parameter value correction: By changing the Young's modulus and Poission's ratio from and to respectively $70 \text{ GPa} \rightarrow (76 \pm 1) \text{ GPa}$ and $0.23 \rightarrow (0.21 \pm 0.01)$ then the relative deviation between the fitted simulation and the experiments changed to $(-0.5 \pm 0.1)\%$. This was done by hand fitting the parameter values, and this opens up for more precise and automatized methods in the full 0.1 to 10 MHz regime in the future, and thereby increasing the precision for *in situ* determination of the parameter values. Hopefully a further deep dive into the system would also give a better understanding of the dampening of the system. The spectra of the fitted parameter values can be seen on Fig. 4.3 in the blue curves.

Conclusion and outlook: In this paper we showed it possible that by actuating bulk substrate devices with thin piezoelectric film and using the impedance spectra of these resonances in the bulk glass, we can through simulations find *in situ* parameters for the bulk substrate, by matching the peaks.

4.2 Paper II

Paper II refers to the paper titled: *Numerical study of bulk acoustofluidic devices driven by thin-film transducers and whole-system resonance modes*, with the authors *André G. Steckel and Henrik Bruus*. The abstract of paper II in Section 5.2, will give a good and quick overview of the article and this section is a slightly longer summery with a slightly different take than presented in the article.

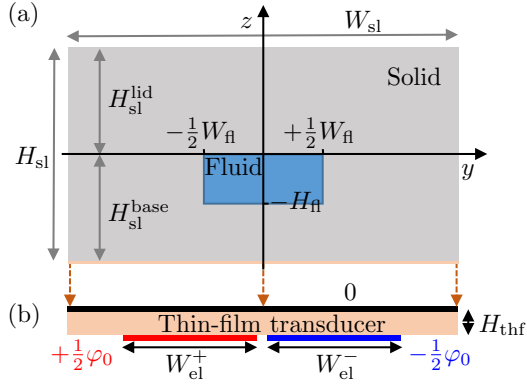


Figure 4.4: Sketch of thin-film actuated acoustofluidic bulk device. (a) Sketch of the cross section yz -plane of a acoustofluidic device with purely elastic solid in gray, fluid channel in blue, and a piezoelectric thin-film transducer in tan, which has been artificiality enhanced to make it visible in (b). The thin-film transducer is much smaller than the device and typically less than 0.1% the device height. (b) is a zoom in on the thin-film transducer and from the top is the ground electrode in black, thin-film transducer in tan, and electrodes in red and blue, which are actuated with $\frac{1}{2}\varphi$ and π out of phase with respect to each other. Adapted from [1]

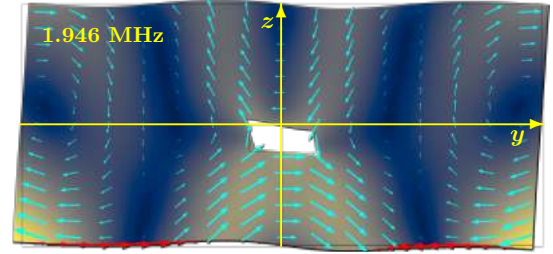


Figure 4.5: Cross section of a simulation of the device, shown in Fig. 4.6, of the yz -plane at $x = 0$ showing the underlying mechanism in how the thin-film transducer devices work. The cyan arrows are displacement vectors, the color plot is the amplitude of the displacement field, u_1 , going from 0 in dark blue to 15 nm in yellow, and the system displacement has been artificially scaled by 7000 to make it visible on the figure. The red arrows show the in-plane strain multiplied with the y -basis vector, $\partial_y u_{1,y} e_y$, in order to make the scalar visible. As seen on the direction and spacing of the arrows the film is expanding on the left and contracting on the right. Adapted from [1]

Motivation: The idea with the paper is to show that it is possible to use 1- μm thick piezoelectric thin-films to actuate acoustofluidic devices that is much larger than the thin-film, where the system is driven at the whole system resonance of the bulk part of the device. A sketch of such a device is shown on Fig. 4.4. This would solve problems with reproducibility, as the thin-film devices in Paper I showed that electromechanically these devices were indeed reproducible. It would also open up for large scale manufacturing of acoustofluidic devices, using roll-to-roll manufacturing, and all in all do so in a lead free way. Mainly the technique would also open up for a different manufacturing technique when designing new acoustofluidic device, where this technique has its advantages and disadvantages. Some of the advantages were just mentioned and probably the most prominent disadvantages is the technological barrier of entry there is the depositing piezoelectric thin-films.

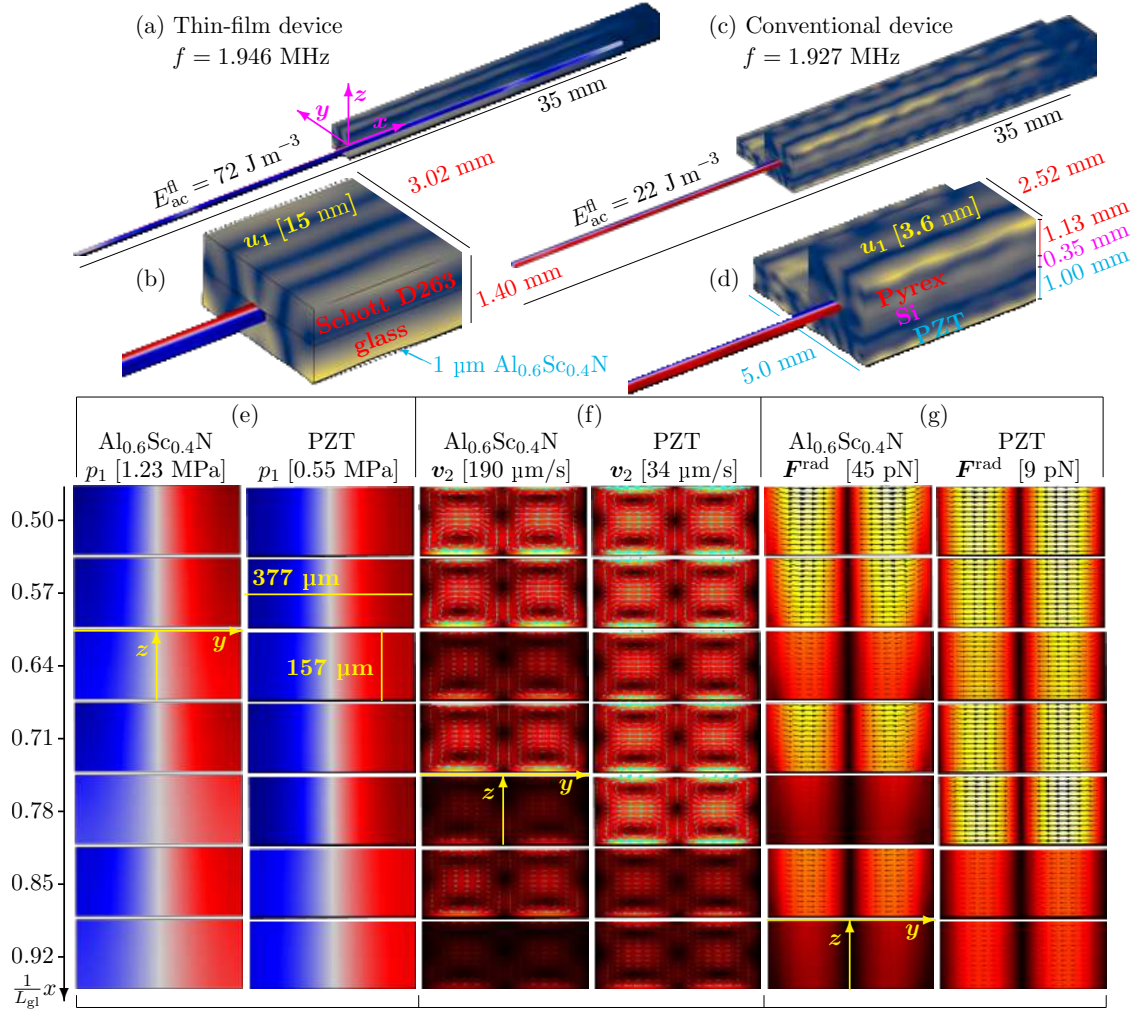


Figure 4.6: Compares thin-film actuated device with bulk actuated device in terms of first and second order fields. (a,b) Acoustofluidic device driven by a 1- μm -thick $\text{Al}_{0.6}\text{Sc}_{0.4}\text{N}$ thin-film, with displacement amplitude, $|u_1|$, shown in the color plot from 0 nm in dark blue to 15 nm in yellow, and pressure field defined in (e). (c,d) Conventional device actuated by a 1-mm-thick PZT transducer, with displacement field as in (a,b) but going from 0 nm to 3.6 nm. (e)-(g) Fields are displayed for thin-film device on the left and the bulk PZT device on the right, with cross section plots from the mid point to $0.92\frac{x}{L_{gl}}$, in seven equally spaced steps. (e) Pressure field from minimum, in blue, to maximum, in red, with symmetrized color scales and max amplitude in square brackets. (f) Acoustic streaming amplitude, $|v_2|$, from of 0 $\mu\text{m/s}$ in black to max amplitude in squared brackets, in white, with intermediate colors of red and yellow. (f) Radiation force magnitude, $|\mathbf{F}^{\text{rad}}|$, from 0 pN, in black, to maximum in the square brackets, in white, going over red and yellow. The radiation force is for 5- μm -diameter polystyrene particles. Adapted from [1]

Core concept: That a piezoelectric thin-film could in-fact actuate such a system was narrowed down to three core concepts that make it possible: (1) The thin-film expansion perpendicular to the thin-film due to the piezoelectric component e_{33} is negligible because the film is free to expand in that direction and is far from the thickness resonance of the film. However it will contribute to the piezoelectric component e_{13} which causes a, along the surface, in-plane expansion, and contraction, which cumulatively allows for actuation of the device. An example of this is seen on Fig. 4.5 where the in-plane strain pattern is displayed as red arrows. (2) The actuation of the device is possible if the strain pattern in the mode of the device, at that frequency, matches that of the stress generated by the electrode pattern in the thin-film. Therefore if a mode in the glass does not have a strain pattern in the film that can be matched electrodes, it would not be possible to actuate that mode. As an example of such a mode one could imagine a vertical standing mode, that would not have a strain pattern in the in-plane direction of the film. A resonance only in the fluid and not the glass would not be actuated as well because of the lack of a strain pattern and acoustic resonance in the glass. A mode that has a proper strain pattern, a good resonance in the glass, and fluid channel will be referred to as whole body resonance. Comparing it to a violin, the strings, the wood, or the design of the cavity inside does not individually make a good instrument, only when all the component are working together will there be the desired effect. (3) The high mechanical Quality factor (Q-factor) at resonance that materials such as glass and silicon has, makes it so that the device acts as an acoustical whole body resonator, which builds up instead of dampening the waves. This allow for high strains and stresses in the film which intern helps build up the resonances, perpetuating the cycle. The energy is the lost on the bulk of the device, and also lost in the fluid channel, where it drives the acoustofluidic action, but because the thin-film constitutes such a small part of the device the dampening in the film almost does not matter, see later in Fig. 4.7.

Model: The theory of the model is as described in Chapter 2 excluding the axisymmetric part, as everything is done Cartesian coordinates. The device was based on, and compared to a acoustofluidic device developed and described by Augustsson *et al.* Ref. 146, which was taken as a conventional acoustofluidic device driven by a bulk PZT transducer. The thin-film driven devices is made in glass of the type Shcott D263 as it is widely available, biocompatible, and the datasheets containing Young's modulus and Poisson's ratio is on their website[142]. The device could just as well have been made out of silicon, for the the purpose of showing the concept, but it would make it difficult to observe the internal acoustics in such a real world device. Making the device of a silicon base and glass lid, makes it more difficult to optimize the modes, by changing the dimensions of the device, and the modes will not be as clean as they are for a homogeneous device, and therefore not as illustrative. What is important is that the Q-factor in the system is high, which is both the case for silicon and glass[143], since if the dampening in the solid is low, then mechanical energy the film deposit on the larger device surface will find it's way to the water channel.

Simulation: The simulations were done on a workstation with 128 GB of RAM with

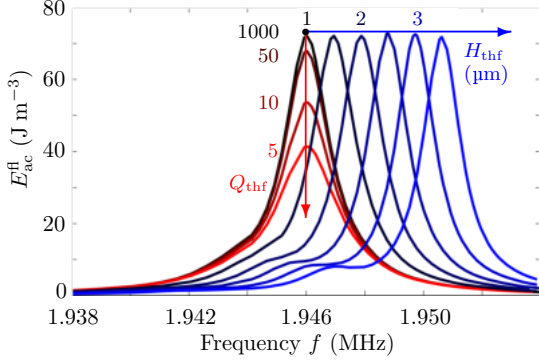


Figure 4.7: Simulations of the $\text{Al}_{0.6}\text{Sc}_{0.4}\text{N}$ thin-film driven system on Fig. 4.6, shown in the black frequency spectra. The progressively red curves show how the resonance peak changes when in the simulation the mechanical quality factor of the thin-film is changed from 1000 to 5, where the energy changes only by half for this change. The progressive blue curves show how the resonance changes when the thin-film is changed from a thickness from 1 μm to 3.5 μm , where the frequency changes from 1.938 to 1.954 MHz. Adapted from [1]

an Intel core i9 7960X processor at 3.70 GHz with 16 cores. The numerics were done in the finite element solver program COMSOL[147], and the mesh of the simulations were such that there was at least 12 nodal points per wavelength at 2 MHz with at least 18 in the fluid. Standard convergence analysis was performed and the variations in the acoustofluidic response was seen to be around 1% when comparing with the highest mesh resolution possible in our system.

Comparison with traditional device: When comparing the thin-film driven device with the conventional device, at $1\text{-}V_{\text{pp}}$ then the $\text{Al}_{0.6}\text{Sc}_{0.4}\text{N}$ thin-film device would perform on par or sometimes even better than the conventional device, as seen on Fig. 4.6. For the mode that was found in the conventional device the mode was strong all the way through the channel whereas the device with the thin-film device was strongest in the center, and the pressure field gradually decreased towards the end of the device. This is however not a general trend of these devices, but particular to these specific modes, as other modes found showed both modes that were more uniform across the lengths and modes that showed irregularity and waves in the length direction. These modes were chosen because they showed good acoustofluidic action, and that the modes were fairly uniform and robust to changes. By changing the materials of the thin-film it was shown that the AlN , $\text{Al}_{0.6}\text{Sc}_{0.4}\text{N}$, and the PZT thin-films were shown to also work for actuating the device. While the PZT gave the strongest response for $1\text{-}V_{\text{pp}}$, followed by $\text{Al}_{0.6}\text{Sc}_{0.4}\text{N}$ and then AlN , the maximal electric field that is possible before the film experiences a breakdown is a $1\text{-}\mu\text{m}$ -thick PZT film can probably not even reach $1\text{-}V_{\text{pp}}$, and $\text{Al}_{0.6}\text{Sc}_{0.4}\text{N}$ can reach higher and AlN even higher breakdown voltages that more than make up for the lower piezoelectric coefficients, since the acoustical energy scales with applied voltage squared[132]. When comparing the different devices in acoustical energy density per unit of piezoelectric factor, $e_{13,f}$, squared they were comparable, and the acoustical focusing time multiplied with the acoustical energy density was roughly the same across the devices which also is shown in that the acoustical modes in the devices also look similar.

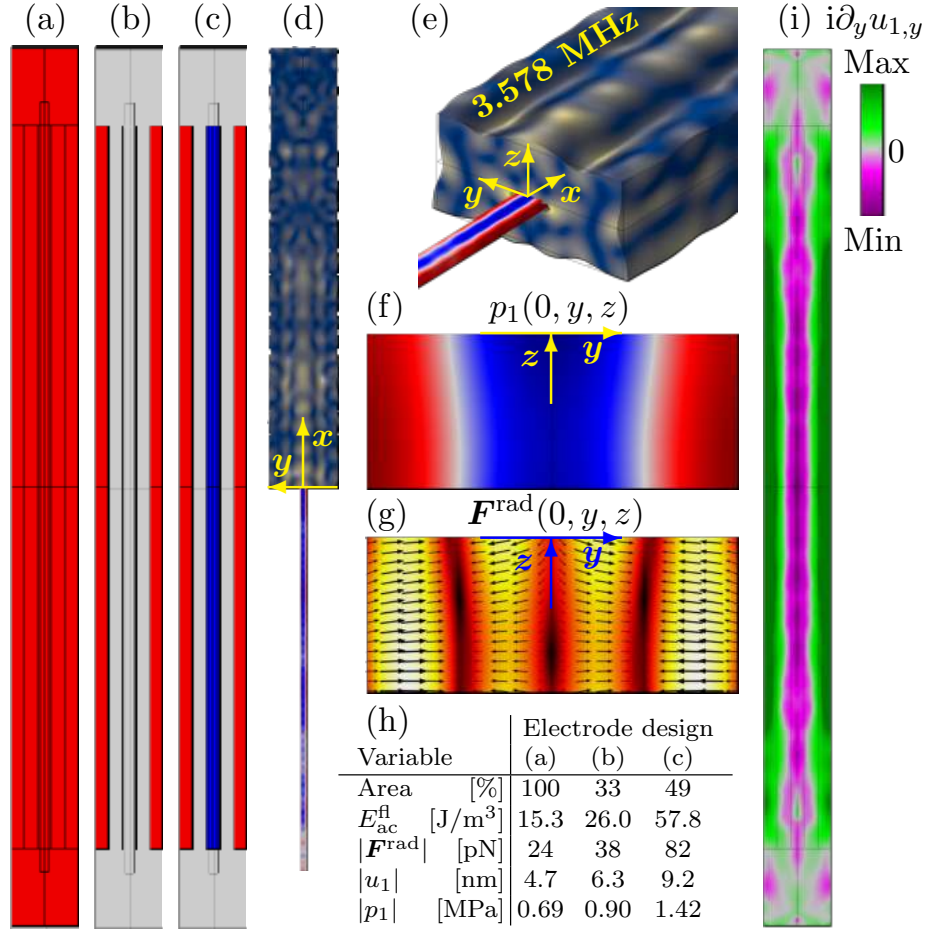


Figure 4.8: Simulations of full-wave standing pressure mode in channel and the effect of electrode patterning. (a)-(c) Electrode pattern where red and blue are π out of phase and grey is not actuated. The electrode patterns are symmetric in order to be able to actuate the symmetric mode, in the channel. (d)-(g) Simulation of the electrode pattern shown in (a) at a resonance of 3.578 MHz where the max displacement amplitude, $|u_1|$, pressure amplitude, $|p_1|$, radiation force magnitude, \mathbf{F}^{rad} , are given in (h). Furthermore the table in (h) gives percentage area covered by electrodes in (a)-(c) and also the average acoustic energy density. The differences of the modes for the different electrode patterns are not visible with the naked eye and look like the fields given (d)-(g), however the acoustofluidic action does increase for the more optimized electrode pattern in (b) and (c), which is summarized in the table in (h). In (i) is shown the out of phase in-plane strain, $i\partial_y u_{1,y}$, with symmetrical colorbar on the right, where the colors indicate where to place the positive electrode (green area), and negative electrode (purple area) for maximal efficiency. Adapted from [1]

Film Q-factor and thickness: A interesting aspect of the system is that since the PZE thin-film is such a small part of the system, the mechanical dampening of the film does almost not effect the system, as seen on Fig. 4.7. It is shown that a Q-factor of 50 in the $\text{Al}_{0.6}\text{Sc}_{0.4}\text{N}$ thin-film only slightly changes the average acoustical energy density at resonance, and that it is only halved with the low Q-factor of 5, and that is for film that typically have Q-factors above 1000[148, 149]. The thickness of the $\text{Al}_{0.6}\text{Sc}_{0.4}\text{N}$ thin-film did not seam the matter much for the specific mode, where the average acoustical energy remained high for the system when changing the film thickness from 1 μm to 3.5 μm , which changed the resonance frequency from 1.938 to 1954 MHz as seen on Fig. 4.7.

Electrode shape: By going to the standing-full-wave-horizontal mode of the device at 3.578 MHz, seen on Fig. 4.8, and changing the electrode shape so that it is symmetric and therefore enables symmetric modes in the device, we see the double nodal line mode in the horizontal direction which would focus particles in two lines. At this frequency the device has several wavelengths in the glasses width direction and therefore there might be some possibility of optimizing acoustofluidic action by changing the electrode coverage and polarization. Indeed by only actuating roughly 33% of the outer sides of the electrode the average acoustic energy density changes from 15.3 J/m^3 to 26.0 J/m^3 , and by again changing some of the middle electrode to again be actuated, but now π out of phase from the first electrode, such that the coverage is now roughly 49%, the average acoustical energy density is changed to 57.8 J/m^3 , with the other fields following suit according to the scaling laws. The short answer is that the part of the electrode was working against it self with the full electrode, in that some parts were expanding while at the same time others were contracting, and by only actuation the expanding part, the energy was increased, and by actuating the part that was contracting out of phase such that the film was also contracting, then it increased the effect even more.

Spacial modes and symmetry breaking: Another feature of these systems are the clean modes that it enables in the devices. Because there is such a high level of symmetry in the systems, and it is driven almost purely in the bulk glass resonance, then it is easy to identify each individual modes. This is explained further in the paper where the first standing half wave mode in the system was shown at 0.956 MHz, and the five subsequent modes show the progressive standing waves in the length direction. The modes however are not limited to systems that exhibit perfect symmetry, and it is also shown in the paper that even when moving the channel out from the symmetry point in the center to the side, by 50 and 100 μm in the y -direction, it is possible to still actuate the device and generate standing field in the channel.

Conclusion and outlook: The conclusion is that a 1- μm -thick piezoelectric thin-film does indeed seam able to actuate a bulk acoustofluidic device in a manner that is as good as a conventional device. There are many advantages to the PZE thin-film driven devices and by bringing this method of actuation to the acoustofluidic community's attention we hope that this will inspire our experimental colleagues to make the device and to test them in the future.

4.3 Paper III

This section is here for completion, as since the paper is still in preparation, and any details that the author of this thesis thought was missing from the article, was added to the article if time allowed. Also where the other articles were published at the time of this thesis the sections of those summaries gave the opportunity to add information, new understanding, or a different view on the subject. Paper III as presented in Section 5.3 was before any revisions from other authors, except for a few pointers, mostly on figure presentation. This section will therefore be very short, and intended as a slightly more informal discussion than what was in the article.

Original idea: The original idea for the paper originated from the desire to use optimized electrode coverage of thin-films for applications in acoustofluidics, combined with the idea that the Bessel modes from a membrane must send out waves from the anti-nodes that through interference would create a pressure hot spot at some place above the membrane center. It was thought that this hot spot might enable trapping, however it soon became apparent, because of the boundary condition on the axisymmetric axis, that the pressure would be a anti-node, and therefore particles with positive acoustic contrast factor would not be focused in the center, only particles with negative acoustic contrast factor would be focused. Therefore by changing the fluid it is possible to change the acoustic contrast factor of some cells, and what has been used in the literature for this, with a good parameter fit, is Iodixanol[28].

Model: The model used for this paper is the same as in Chapter 2, specifically the axisymmetric equations of Section 2.3, and shown with a comparison between 3D and 2D axisymmetric models in Section 3.3.1. It is explained in more details in Paper III, about the specifics of the model with mesh, simulation time, and degrees of freedom.

Simulations and discussion: The simulations in this paper has been of two different geometries. Both geometries had a 1- μm -thick $\text{Al}_{0.6}\text{Sc}_{0.4}\text{N}$ thin-film and a 10- μm -thick membrane of silicon (111) in the axisymmetric model. The first geometry had a membrane diameter of 200- μm , and the second had a membrane diameter of 1000- μm . This was done because of several things. Firstly, the fourth order membrane mode of the smaller membrane was a clearer example in describing the physical phenomenon. It showed that matching the electrode patterning with the out-of-phase in-plane strain increased the acoustofluidic action, and the in-plane strain was much clearer for the small membrane than for the even higher order mode of the larger membrane. Secondly, it is also showing the phenomenon of the hot spot in the pressure field above the membrane. It also showed how the waves in the r -direction were standing waves, and in the z -direction were traveling waves. So in most aspects it showed the fundamentals of how the system worked in both the small and the larger membrane, but it was in general clearer for the small membrane. Thirdly, the dimension of this small membrane matched nicely with a recent result published in Ref. 150, where they had a roughly 200- μm in diameter and 10- μm -thick membrane of silicon, with AlN thin-film on top. The top electrodes however

were not made to efficiently actuate the membrane, and in fact the way they actuated the membrane was with a SAW actuator where the device was placed on top of the SAW device. It however showed that it is possible to fabricate such devices, and that such devices are interesting for the acoustofluidic community. However our device at these dimensions, and at the forth order membrane mode, had an actuation frequency of 52 MHz, and at this frequency the wavelength in water was roughly the same length as the diameter of the MCF-7 cells that were to be investigated. This was not possible with the model for the radiation force that we were using, and therefore a larger membrane was used for the radiation force calculations as this lowered the frequency to 18.5 MHz.

The simulations of the larger membrane then showed that the radiation force would have anti-focus in the middle of the membrane for water and the cancer cells in question, MCF-7. However when changing the suspension medium with different concentrations of Iodixanol it was possible to turn the device into a trap. There was still a barrier, that the cells had to overcome in order to enter the trap, and the trapping in the z -direction was not as good as in the radial direction. The barrier was shown to diminish when the density of the fluid was changed, and was significantly lower when the cells were neutrally buoyant, and even had a hole in it when the density was lowered even further and the streaming drag force was taking into account. The fluid with the modified density was purely theoretical, as no known fluid has such parameters, but it showed that there are further room for optimization. As a side note, while it was not shown in the paper, placing the thin-film at the bottom of the membrane, instead of the top of the membrane, show just as good acoustofluidic action, and the differences in the resulting fields were almost not possible to see with the naked eye. Whether it is possible to fabricate a device, with the film at the bottom, is a different story, but at least the system seem to be robust to such changes. An other element that was not mentioned in the paper was that by using a AlN thin-film instead of a $\text{Al}_{0.6}\text{Sc}_{0.4}\text{N}$ thin-film it was also possible to actuate the system, but one had to account for the lower piezoelectric coefficient by having a higher actuation voltage to get the same results.

Conclusion and outlook: We showed that the higher order membrane modes could be enhanced, by choosing a top electrode pattern that matched the out of phase strain pattern in the film. Also shown was that such a system could be turned into a trap for cancer cells, if the suspension medium was changed. There were some discussion of the how the trapping could be improved, by changing the density of the medium, and also a discussion of what could have be studied in the future. In particular it would be interesting to have a look at the devices that have axial mode number different form one in the membrane, as it might allow for there to be a pressure node in the central axis of the simulation, and therefore focusing of cells without a change of suspension medium.

4.4 Conference Paper I

Original idea: We wanted to investigate GHz acoustofluidics as that is a field with interesting and emerging research within the field. Simulations of GHz acoustofluidics can

be difficult because of the large frequencies makes the wavelengths in the system very small. As an example at 1.5 GHz the wavelength in water is roughly 1 μm and the viscous boundary layer is 14 nm. This makes it difficult to simulate the system of any larger volume, and especially without the effective boundary conditions developed by Bach and Bruus 78. However with these tools we did some simulations to try and understand the system.

Model: The model was based on the same model as presented in Chapter 2, and the geometry was designed to match what has been published in the literature. Because of the small wavelengths, it was only possible to do 3D simulations of the actuator alone whereas the simulations with fluids were done in 2D. A remark on the validity of the model is that the effective boundary conditions require that $\epsilon = \frac{\delta}{d} \ll 1$, and for the simulations at 1.5 GHz, $\epsilon \approx 0.087$. As the effective boundary layer theory throws away terms in the order of ϵ , we should not expect the model of the system to be correct to at least an upper bound of ϵ .

Simulations: The simulations show that the system has a quite complicated structure, because of the many wavelengths in the system. The solid mechanical resonator shows that if the clamping on the system happens to close to the actuation then thin-film bulk resonances become very simple, and this was done in order to replicate what was done in the literature, and at least some freedom is needed in order to there to be a reasonable resonance. If however there were no PML layer, then the mode was very complicated. In the 2D simulations of a cross section of the device with a fairly small water channel of only 40 μm high, the waves were almost damped in the system, which will be investigated in Section 4.6. It was seen that it generated fairly high streaming of 3.5 mm s^{-1} , at a resonance of 1.545 GHz.

Conclusion and outlook: The results are early and rough but they give a glimpse into how complicated the systems can look because of it being a many wavelength system. The field has much to offer in terms of further investigations in the future.

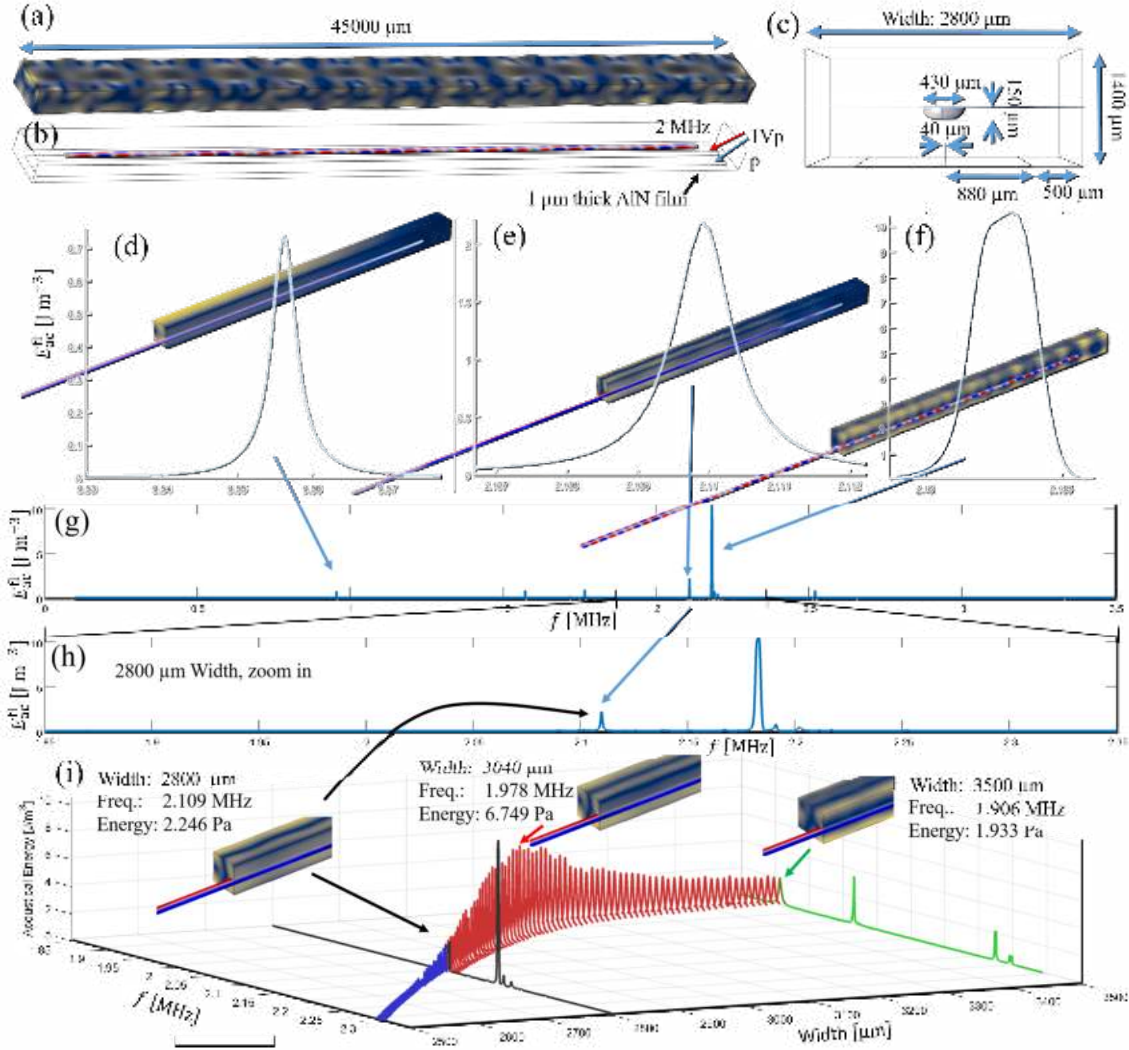


Figure 4.9: Simulations and optimization of the width of the device in Fig. 6 of Paper II. (a) the displacement field, and (b) the pressure field not at resonance but simply at 2 MHz, with a 1- μm -thick AlN thin-film device actuated with 1 V_{pp} , with dimensions in the sketch of (c). (d) - (f) show zoom-in on three peaks in the spectra that is seen in (g), with acoustic energy density, E_{ac}^{fl} , plotted against frequency, f . (h) shows a zoom in on the spectra from 1.85 MHz to 2.35 MHz, and which is also shown as the in black spectra in (i). In (i) the peak in (e) was followed when changing width of the device from 2500 μm to 3500 μm where a peak for that mode was found at a width of 3040 μm .

4.5 Minor results I - Optimization of device width

This section presents some minor results that came before Paper II, and was the reason for why the width of the device in Paper II ended being, 3020 μm for the $\text{Al}_{0.6}\text{Sc}_{0.4}\text{N}$ device in Paper II. The fitting of the width shows the strength of controlling COMSOL through Matlab by using the LiveLink, as well as using the frequency stepping method, since simulations such as these otherwise would have taken to long without it.

Original idea: The idea was to take the device of Paper II, and do a long frequency sweep with the antisymmetric actuation, see if there was a strong and robust mode, and then change the width while following the mode in frequency to see if there was a maximum acoustical energy for that mode.

Simulations: On Fig. 4.9(a)-(b) is seen as a typical off-resonance behavior, taken at 2 MHz. At the off resonance the system the modes are usually very messy and not very strong. It is only when on-resonance for a mode that corresponds well with the electrode pattern, that there is any significant acoustic response. These strong modes are typically more clean looking, but there are examples where this is not true, see the later discussion of (f). Because of the high Q-factor of the glass, which constitutes the bulk of the device, the width of the peaks are very narrow. A traditional frequency sweep, with constant step size, would have taken months to simulate. This is because of the frequency resolution needed to resolve the fine peaks over so long a frequency span, where each step takes a couple of minutes. With the frequency stepping method it still took a few days, and the long sweep seen on Fig. 4.9(g), for the dimensions in (c), which is the same system as in Paper II, Section 5.2, Fig. 6. Select peaks are shown in Fig. 4.9(d)-(f), which are zoom ins on the long sweep, and where the peak in (d) is mode zero in Fig. 6 of Paper II, and mode (e) is the mode that eventually ends up as the primary mode in the system. Mode Fig. 4.9(f) is an example of a mode that is not very clean looking. When looking at it in detail the mode pattern at the electrode interface is good and homogeneous, but internally the mode has a lot of going on in the length direction. The resonance peak in the frequency spectra in (f) also looks lopsided, and it is believed that the this is the result of two modes being close to each other. The mode seams to split up into two modes very easily when changing the dimension, and in general was much more sensitive to small variation than the other modes. Therefore, although the the mode has a high acoustic energy, it was has not been chosen as a candidate for optimizing the width. The peak chosen for optimization was Fig. 4.9(e), and the zoom in on the spectra in (g) can be seen on (h). The resonance spectra in (h) is seen on (i) as the black lined frequency sweep. The width of the device was then changed slightly, a frequency sweep around the peak center of the previous width was performed, and the cycle repeated, such that the peak was followed and recorded. First the sweep was done from a width of 2800 μm to 2500 μm , seen on (i) as the blue curves, and it was observed that the average acoustical energy density in the channel fell. Then it was increased from 2800 μm to 3500 μm , and a maximum was found at a width of 3040 μm . When changing into $\text{Al}_{0.6}\text{Sc}_{0.4}\text{N}$ it was observed that the best width was 3020 μm , which became the width that was used in the Paper II, as the main example. Notice however that it is a fairly wide maximum, and therefore hopefully also robust to manufacturing tolerances.

4.6 Minor results II - GHz acoustofluidic dampening

When investigating the GHz acoustofluidics, shown in conference paper I, Section 5.4, it was investigated slightly further than what was described in the paper. Two small results are here included to just show examples of it. The mechanism behind the dampening was looked into, shown on Fig. 4.10, and a system in the GHz simulated with the axisymmetric model is shown in Fig. 4.11. The systems pressure, p_1 and displacement, \mathbf{u}_1 is shown on Fig. 4.10(a) and the resulting streaming is seen on Fig. 4.10(b). At GHz frequency the system behaves differently, as the dampening in the system, $\Gamma_{\text{fl}} \propto \omega$, is proportional to frequency, and therefore the the term in the streaming that is responsible for the Eckart streaming, $\frac{\Gamma_{\text{fl}} \omega}{c_0^2} \langle \mathbf{S}_{\text{ac}}^d \rangle$ is proportional to frequency squared. Therefore the streaming in these systems are very much driven by the bulk dampening in the system. This can be seen by looking on figure Fig. 4.10 (c) and (d), where minus the divergence of the time averaged acoustic energy flux density, $-\nabla \cdot \langle \mathbf{S}_{\text{ac}}^d \rangle$, is shown in the color plot, and the time averaged acoustic energy flux density, $\langle \mathbf{S}_{\text{ac}}^d \rangle$ is plotted in the red arrows, which is pro-

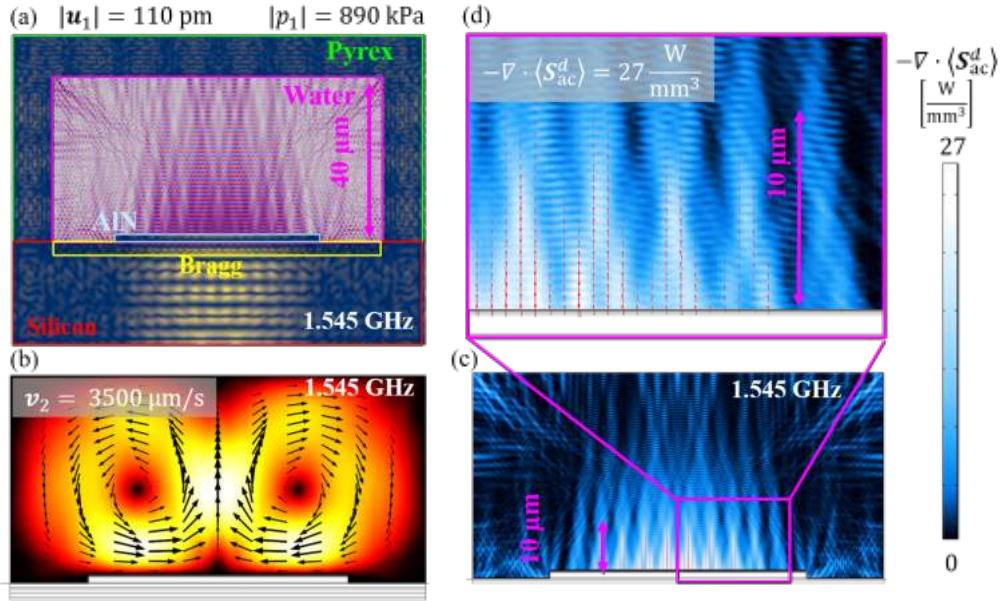


Figure 4.10: Simulations of GHz acoustics pressure, displacement, steaming and dampening. (a) displacement amplitude, $|\mathbf{u}_1|$, seen as the color plot from 0 pm in dark blue to 110 pm in yellow and the pressure, p_1 , going from -890 kPa in dark blue to $+890 \text{ kPa}$ in dark red with zero as grey. The dimensions are in Section 5.4. The streaming is seen on (b) going from $0 \mu\text{m s}^{-1}$ in black to $3500 \mu\text{m s}^{-1}$ in white, with red and yellow as intermediate colors. On (c), and the zoom in in (d), is seen minus the divergence of the time averaged acoustic energy flux density, $-\nabla \cdot \langle \mathbf{S}_{\text{ac}}^d \rangle$, as the color scale with the colorbar on the right, and the red arrows are the time averaged acoustic energy flux density, $\langle \mathbf{S}_{\text{ac}}^d \rangle$.

portional to the Eckart streaming. As is seen most of the dampening is happening in the length scale of $10\ \mu\text{m}$, and if ones compares the streaming with the Eckart streaming term it is seen that this must be the way the system would stream. Considering that there is conservation of fluid, such that the Eckart streaming is pushing the fluid up in the center and it rolls around and flows back again. It is not a purely damped traveling wave as in this system there are also reflections from the fluid channel ceiling. Therefore there are some standing wave pattern that is seen on the zoom in on Fig. 4.10(d), where the dampening also has a wave pattern.

While the system is small compared to the usual device worked with in this thesis, they are typically in the lower end of the MHz regime, whereas here we are in the GHz regime and therefore the wavelengths in fluid and the solid are much smaller. This means that the resolutions has to be high as well, as the same rule apply for mesh elements, and nodal points, per wavelength remains the same as always. This means that it is not possible to simulate the system in full 3D, with out current systems, however it is possible to simulate in axisymmetric 2D, and then interpolate into 3D, and a early example of this is seen on Fig. 4.11.

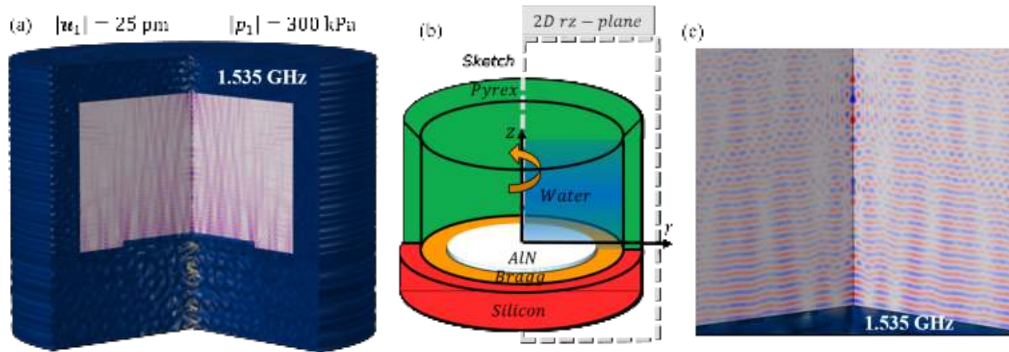


Figure 4.11: Early results of the a simulation of GHz acoustics pressure and displacement in a axisymmetric system. (a) The pressure, p_1 , going from $-300\ \text{kPa}$ in dark blue to $+300\ \text{kPa}$ in dark red and the displacement amplitude, $|\mathbf{u}_1|$, seen as the color plot from $0\ \mu\text{m}$ in dark blue to $25\ \mu\text{m}$ in yellow. (b) Sketch of the system, adapted from Ref. [3]. (c) Zoom in on the fluid shown in (a)

Chapter 5

Publications

During the PhD project 2 peer-reviewed journal papers were published and one was in preparation to be submitted to a journal and awaits being peer-reviewed. They represent a large portion of the work done in the PhD and are attached in this chapter.

Of the several conference papers written during this PhD, one in particular was not connected to a paper, and has been added to this chapter. It was presented orally to the Acoustofluidics conference 2020, and appears in the conference book.

Patent application André G. Steckel, Henrik Bruus, and Thomas Laurell, [*Title under Non-disclosure agreement until August 2022*], Patent application 21154133.9, submitted 28 January 2021.

5.1 Paper I: Phys. Rev. Appl. 16, (2021)

Fabrication, Characterization, and Simulation of Glass Devices with AlN Thin-Film Transducers for Excitation of Ultrasound Resonances. [2]

DOI: [10.1103/PhysRevApplied.16.014014](https://doi.org/10.1103/PhysRevApplied.16.014014)

Authors: [André G. Steckel](#), Henrik Bruus, Paul Muralt, and Ramin Matloub.

Journal: Physical Review Applied **16**, (2021)

Fabrication, Characterization, and Simulation of Glass Devices with AlN Thin-Film Transducers for Excitation of Ultrasound Resonances

André G. Steckel,^{1,*} Henrik Bruus^{1,†} Paul Muralt,^{2,3,‡} and Ramin Matloub^{3,§}

¹*Department of Physics, Technical University of Denmark, DTU Physics Building 309, Kongens Lyngby DK-2800, Denmark*

²*Materials Science, EPFL, Station 12, Lausanne 1015, Switzerland*

³*PIEMACS Sàrl, EPFL Innovation Parc, Bâtiment C, Lausanne 1015, Switzerland*

 (Received 16 November 2020; revised 2 April 2021; accepted 27 May 2021; published 7 July 2021)

We present the fabrication of 570- μm -thick millimeter-sized soda-lime-silicate float-glass blocks with a 1- μm -thick AlN thin-film piezoelectric transducer sandwiched between thin metallic electrodes and deposited on the top surface. The electromechanical properties are characterized by electrical-impedance measurements in the frequency range from 0.1 to 10 MHz with a peak-to-peak voltage of 0.5 V applied to the electrodes. We measure the electrical-impedance spectra of 35 devices, all of width 2 mm, but with nine different lengths ranging from 2 to 6 mm and with two to seven copies of each individual geometry. Each impedance spectrum exhibits many resonance peaks, and we carefully measure the five most prominent ones in each spectrum. We compare the resulting 173 experimental resonance frequencies with simulation results from a finite-element-method model that we develop. When we use the material parameters from the manufacturer, we obtain an average relative deviation of the 173 simulated resonance frequencies from the experimental values of $(-4.6 \pm 0.1)\%$. When we optimize the values of the Young's modulus and Poisson's ratio of the float glass in the simulation, this relative deviation decreases to $(-0.5 \pm 0.1)\%$. Our results suggest a method for an accurate *in situ* determination of the acoustic parameters at ultrasound frequencies of any elastic solid onto which a thin-film transducer can be attached.

DOI: [10.1103/PhysRevApplied.16.014014](https://doi.org/10.1103/PhysRevApplied.16.014014)

I. INTRODUCTION

Aluminum nitride (AlN) is one of the most commonly used materials in integrated thin-film piezoelectric transducers for actuating microelectromechanical systems (MEMS). Because of their low dielectric and mechanical loss tangents, their structural and chemical stability, and their compatibility with standard silicon-based CMOS microfabrication techniques, AlN sputtered thin films are commercially used in thin-film bulk-wave acoustic-resonator filters [1]. The academic literature reports applications of AlN thin-film transducers as rf filters [2], contour-mode resonators [3], switches [4,5], suspended microchannel resonators [6], and accelerometers [7].

Detailed studies of AlN-thin-film-actuated high-tone bulk acoustic resonators with high quality factors have been performed in the 0.3–3 GHz range on 350- μm -thick substrates of sapphire, crystal quartz, fused silica, and silicon [8], and on 30- μm -thick Si membranes [9,10].

Because AlN is a nonferroelectric polar material, reorientation of the polar axis is not possible. The material growth process therefore has to provide a textured structure that includes the alignment of the polar directions [11], since otherwise the random orientations of the grains constituting the AlN thin film would result in a zero average piezoelectric effect. In the work presented here, we therefore follow the process developed in our previous work on pure [12] and Sc-doped [13,14] AlN films, and select Pt/Ti as the seed layer for the bottom electrode stack as it promotes nucleation of (002)-oriented AlN grains.

Over the past few years, piezoelectric thin films made of nonferroelectric polar materials, such as zinc oxide (ZnO) and AlN, have found a broad range of lab-on-a-chip applications such as biosensing, particle or cell concentrating, sorting, patterning, pumping, mixing, nebulization, and jetting. Integrated devices with acoustic transducers, sensors, and microfluidic channels have been fabricated by depositing such piezoelectric films onto a wide range of materials

*angust@fysik.dtu.dk

†bruus@fysik.dtu.dk

‡paul.muralt@epfl.ch

§ramin.matloub@piemacs.ch

Published by the American Physical Society under the terms of the [Creative Commons Attribution 4.0 International](https://creativecommons.org/licenses/by/4.0/) license. Further distribution of this work must maintain attribution to the author(s) and the published article's title, journal citation, and DOI.

beyond the usual silicon substrates, such as ceramics, diamond, glass, and, more recently, also polymers, metallic foils, and flexible glass, for making flexible devices. Such thin-film acoustic-wave devices have great potential for implementing integrated, disposable, or bendable lab-on-a-chip devices into various sensing and actuating applications [15]. To advance such applications, we focus in the present work on AlN thin-film transducers deposited on glass substrates and driven in the 0.1–10 MHz range.

The deposition of AlN thin films and the control of their texture are more difficult than in the case of ZnO films [16], and their integration into MEMS is not a trivial task, as they tend to have a high in-plane stress with a sharp transition around zero stress [17]. However, the thermal conductivity of AlN is more than 3 times larger than of ZnO, which enables the operation of AlN films at a higher power level, an important feature for applications in rf technology. AlN films are normally sputter deposited at moderate temperatures (typically 200–400 °C) to achieve optimal performance, although “room temperature” deposition with a local temperature near the target of around 150 °C is sometimes used [18]. Also, the deposition conditions, especially the amount of oxygen or moisture in the vacuum chamber, have significant effects on the growth and microstructure of AlN films. Growing AlN films thicker than a few micrometers is particularly challenging because of the potentially large film stress and the tendency to form microcracks.

In the present work, we use our titanium-seed-layer technique [12] to improve the fabrication of AlN thin-film transducers deposited on glass substrates for future use in biosensing and lab-on-a-chip applications. In Sec. II, we describe the design of the devices, followed in Sec. III by a presentation of the fabrication and characterization processes. In Sec. IV, we then present the characterization of the acoustic properties of the devices by measuring electrical-impedance spectra in the frequency range from 0.1 to 10 MHz. A numerical model and its finite-element-method implementation is described in Sec. V. A comparison of the simulation results with the results of the experiments presented in Sec. VI shows such good agreement that our numerical handling of the measured impedance spectra can be turned into an improved *in situ* determination of the acoustic properties of the glass substrate. Finally, concluding remarks are presented in Sec. VII.

II. DEVICE DESIGN

Figure 1 shows the design of the devices under study. This design is chosen to ease the microfabrication, the experimental characterization, and the subsequent validation of a finite-element method model of the system. All devices consist of a simple box-shaped 570- μm -thick and 2-mm-wide block of soda-lime-silicate (SLS) float glass [19] of length L diced from a wafer. L is in the range

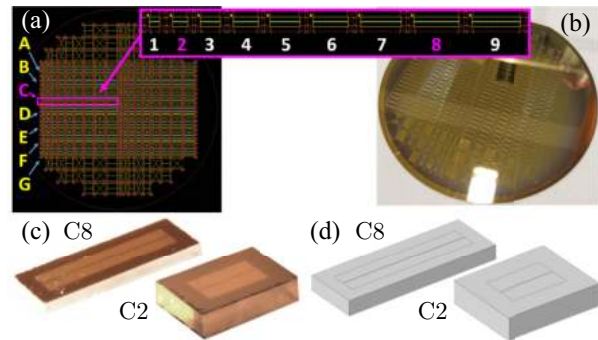


FIG. 1. (a) Design of the electrode mask for the lithography step in the fabrication process that defines the gold electrodes on the top surface of the glass wafer. The relevant devices are taken from rows A–G and columns 1–9. The inset shows row C, columns 1–9. Devices with the same column index are nominally identical. (b) Photograph of the fabricated wafer before dicing it into individual devices. (c) Microscope images of the actual devices C2 and C8. (d) Rendering of the two 2-mm-wide and 0.57-mm-high devices C2 (2.5 mm long) and C8 (5.5 mm long), showing the outline of the 1-mm-wide top electrode split into two halves by a 40- μm -wide gap.

from 2 to 6 mm in steps of 0.5 mm, thus resulting in nine groups of nominally identical devices. A 1- μm -thick AlN thin-film piezoelectric transducer, sandwiched between submicrometer-thick metal electrodes, is deposited on the top surface of the glass block. To ease the dicing process and to avoid short-circuiting between the two electrodes, the top electrode of the transducer has its width reduced to $W_{\text{TE}} = 1$ mm and its length to $L_{\text{TE}} = L - 1$ mm. Moreover, to allow antisymmetric voltage actuation, the top electrode is split in half by a 40- μm -wide gap perpendicular to the length direction. As listed in Table I, there are up to seven nominally identical copies, A, B, C, D, E, F, and G, in each group of devices.

TABLE I. A list of the 35 devices under study. The rectangular glass blocks are all 0.57 mm thick and have a nominal width $W = 2$ mm and a length L in the range from 2 to 6 mm. The deposited AlN thin-film piezoelectric transducer is 1 μm thick and is sandwiched between a 0.1- μm -thick bottom and a 0.15- μm -thick top metal electrode. The top electrode has a total width $W_{\text{TE}} = 1$ mm and length $L_{\text{TE}} = L - 1$ mm. All devices with the same column index are nominally identical.

Device column	Device row	L (mm)	L_{TE} (mm)
1	C, D, G	2.0	1.0
2	C, D, E, F, G	2.5	1.5
3	A, B, C, G	3.0	2.0
4	A, B, D	3.5	2.5
5	A, B, C	4.0	3.0
6	B, C	4.5	3.5
7	A, B, C, D, E	5.0	4.0
8	A, B, C, D, E, F, G	5.5	4.5
9	C, D, E	6.0	5.0

III. FABRICATION AND CHARACTERIZATION OF THE PIEZOELECTRIC THIN-FILM TRANSDUCER

The device fabrication is based on a 4-in. SLS float-glass wafer (Schott Suisse SA, Yverdon). This glass has a low thermal expansion, a high thermal-shock resistance, and an ability to withstand temperatures up to 490 °C for long periods, so by not raising the process temperature above 300 °C, we ensure high quality and reproducibility in our fabrication process. Following a microfabrication process similar to the one described in Ref. [12], and sketched in Fig. 2, the first step is cleaning of the glass substrate with isopropyl alcohol and acetone to remove organic contamination. Additional plasma cleaning is performed immediately before the deposition of the bottom electrode in the deposition tool. We prepare textured Ti, Pt, and AlN thin films using a dedicated cluster sputtering chamber (Pfeiffer Vacuum), and then sputter-deposit 10 nm of Ti at 300 °C to serve as an adhesion layer between the glass substrate and the Pt bottom electrode. Next, the 100-nm-thick Pt electrode is deposited with the same tool in a different chamber, also at 300 °C, without breaking the vacuum. Subsequently, 1 μm of (0001)-textured AlN is deposited using a dedicated reactive pulsed direct-current magnetron sputtering chamber at 300 °C, and on top of the AlN film 10 nm of Cr and 150 nm of Au are sputter deposited as the top electrode, with Cr being used as the adhesion layer between the AlN and Au. In the next process step, standard photolithography is exploited to transfer the intended pattern onto the top electrode, and this pattern is realized by ion-beam etching (Veeco). Finally, the wafer is diced into smaller chips ready for use, as shown in Fig. 1(c).

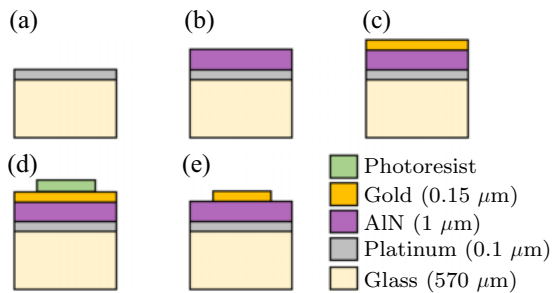


FIG. 2. Sketch of the fabrication process, where a stack consisting of a bottom electrode, an AlN thin film, and the top electrode is deposited on a glass block. (a) Deposition of a 10-nm-thick Ti adhesion layer (not shown) followed by a 100-nm-thick platinum layer. (b) Deposition of the 1-μm-thick AlN film. (c) Deposition of a 10-nm-thick Cr adhesion layer (not shown) followed by a 150-nm-thick gold layer. (d) Deposition and development of photoresist. (e) Patterning of the top electrode by ion-beam etching of the exposed gold, followed by removal of the photoresist.

After fabrication and dicing, the quality of the resulting devices is checked by visual inspection with a microscope, and their dimensions are measured using an electronic micrometer (RS Pro 705-1229, RS Components). By measuring all available devices, the average height and width are found to be $(571 \pm 1) \mu\text{m}$ and $(2031 \pm 2) \mu\text{m}$, respectively, and the average lengths of devices 1–9 are determined to be (2011 ± 1) , (2512 ± 1) , (3013 ± 1) , (3514 ± 1) , (4016 ± 1) , (4500 ± 1) , (5016 ± 1) , (5509 ± 1) , and $(6018 \pm 1) \mu\text{m}$, respectively. The uncertainties represent one standard deviation of several repeated measurements, and the relative uncertainty ranges from 0.2% for the height down to below 0.1% for the longest length.

IV. MEASURED ELECTRICAL IMPEDANCE

The electrical impedance of the 35 devices listed in Table I is measured as a function of frequency from 0.1 to 3 MHz in steps of 500 Hz using an Agilent 4294A Precision Impedance Analyzer (Agilent Technologies AG, Basel, Switzerland) with a 0.5-V_{pp} ac voltage applied in

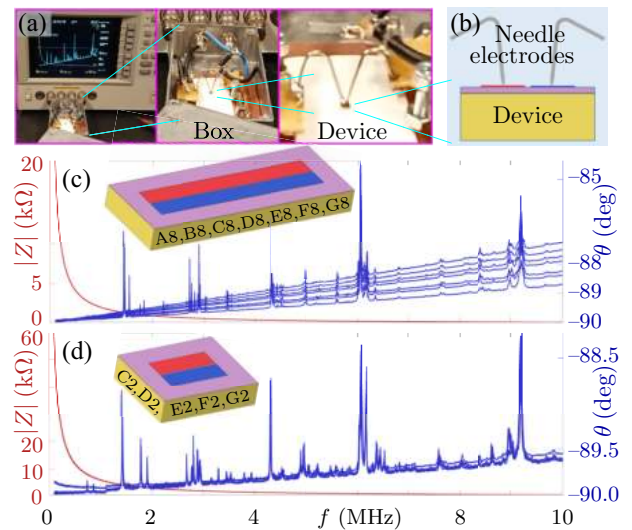


FIG. 3. (a) Three photographs of the spectrum analyzer and the attached metal box that provides electrical shielding of the device, but here with its lid removed to reveal the device mounted inside. An enlargement of the interior of the metal box shows the coaxial connectors and the wires leading to the device. A further enlargement shows the spring-loaded electrodes attached to the device. (b) End-view sketch of the spring-loaded electrodes attached to the device, consisting of a glass block (beige) and an AlN thin-film transducer (purple) with a split top electrode (red and blue). (c) Impedance spectra, showing the magnitude $|Z(f)|$ (red curves) and the phase $\theta(f)$ (blue curves) for the seven nominally identical devices A8, B8, C8, D8, E8, F8, and G8 shown in the inset. The phase curves differ, as the devices are not discharged initially. (d) As part (c) but for the five nominally identical devices C2, D2, E2, F2, and G2. Here, the phase curves are nearly identical, as the devices are discharged initially.

antiphase between the two halves of the split top electrode. The bottom electrode is left floating.

To reduce the electrical noise, each device under study is placed in a grounded metal box, from where it is connected with short coaxial cables to the impedance analyzer by pressing spring-loaded needle electrodes onto each half of the split top electrode; see Figs. 3(a) and 3(b). The setup is also designed to minimize undesired parasitic components: the parasitic inductance in the system is reduced to somewhere around $L_{\text{ext}} = (28 \pm 15)$ nH, the parasitic resistance is roughly $R_{\text{ext}} = (5 \pm 3)$ Ω , and the parasitic capacitance is negligible compared with the intrinsic capacitance C_{dev} of the device formed by the electrodes separated by the thin AlN film, ranging from 18 pF for the smallest device to 86 pF for the largest. This design ensures that the resonance frequency $f_{\text{ext}} = (1/2\pi)(L_{\text{ext}}C_{\text{dev}})^{-1/2}$ involving the external inductance is pushed up in value, such that $100 \text{ MHz} \lesssim f_{\text{ext}} \lesssim 220 \text{ MHz}$, much larger than 10 MHz, and therefore does not interfere with the intrinsic resonances of the device under study. Finally, the device under

study is placed on a folded soft piece of tissue paper to acoustically isolate it from the environment.

Examples of the 35 recorded impedance spectra $Z(f) = |Z|e^{i\theta}$ are shown in Figs. 3(c) and 3(d), where we plot the magnitude $|Z(f)|$ and the phase $\theta(f)$. We first note that the intrinsic resonances of the devices are most clearly visible in the phase plots $\theta(f)$. Because of the parasitic impedances of the system, the base level of $\theta(f)$ shows a linear increase from the -90° of an ideal capacitor in the dc limit to a value between -89.7° and -87.8° at 10 MHz. The device resonances appear as sharp peaks in the phase curve, with a width of around 0.01 times the resonance frequency itself and with an amplitude ranging from 0.1° to 3.5° . This technique is a variant of standard resonant ultrasound spectroscopy (RUS) [20–22]. However, in contrast to conventional RUS, the ultrasound transducers in our case are an integrated but tiny part of the structures to be characterized.

Next, we note that the positions and amplitudes of the resonance peaks are nearly identical for samples with

TABLE II. For each of the nine device geometries, labeled by the column index $k = 1-9$ in Table I, five resonance peaks (k, n) of increasing frequency with $n = 1-5$ are selected from the impedance spectrum for comparing the simulations with the measurements. Peaks (4, 1) and (4, 2), marked with asterisks, are not measured on device B in column $n = 4$. The experimental value $f_{k,n}^{\text{exp}}$ is the average resonance frequency of peak n over all devices (row indices A–G in Table I) with column index k . The simulation result $f_{k,n}^{\text{sim,A}}$ is the corresponding resonance frequency obtained from the numerical modeling described in Sec. V using the parameter values given in the literature. The simulation result $f_{k,n}^{\text{sim,B}}$ is obtained by using the optimized values listed in Table IV of the Young's modulus and Poisson's ratio for the glass block. Finally, for $X = \text{A or B}$, $\Delta_{k,n}^X = (f_{k,n}^{\text{sim,X}} - f_{k,n}^{\text{exp}})/f_{k,n}^{\text{exp}}$ is the relative deviation of the simulation result from the experimental value for resonance peak n and device geometry k .

Peak k, n	$f_{k,n}^{\text{exp}}$ (MHz)	$f_{k,n}^{\text{sim,A}}$ (MHz)	$f_{k,n}^{\text{sim,B}}$ (MHz)	$\Delta_{k,n}^{\text{A}}$ (%)	$\Delta_{k,n}^{\text{B}}$ (%)	Peak k, n	$f_{k,n}^{\text{exp}}$ (MHz)	$f_{k,n}^{\text{sim,A}}$ (MHz)	$f_{k,n}^{\text{sim,B}}$ (MHz)	$\Delta_{k,n}^{\text{A}}$ (%)	$\Delta_{k,n}^{\text{B}}$ (%)
1, 1	0.943	0.886	0.927	-6.0	-1.6	5, 4	2.712	2.607	2.722	-3.9	0.4
1, 2	1.424	1.355	1.411	-4.9	-0.9	5, 5	2.901	2.774	2.903	-4.4	0.1
1, 3	2.065	1.954	2.045	-4.1	-1.0	6, 1	1.425	1.353	1.410	-5.0	-1.1
1, 4	2.717	2.613	2.722	-5.4	0.2	6, 2	1.537	1.465	1.531	-4.7	-0.4
1, 5	2.896	2.764	2.894	-4.5	-0.1	6, 3	1.606	1.531	1.595	-4.7	-0.7
2, 1	0.737	0.699	0.732	-5.2	-0.7	6, 4	2.741	2.634	2.742	-3.9	0.0
2, 2	1.418	1.351	1.408	-4.7	-0.7	6, 5	2.910	2.784	2.913	-4.3	0.1
2, 3	1.791	1.707	1.786	-4.7	-0.3	7, 1	0.321	0.314	0.322	-2.3	0.3
2, 4	1.915	1.826	1.904	-4.6	-0.5	7, 2	1.440	1.366	1.421	-5.2	-1.3
2, 5	2.942	2.811	2.942	-4.5	-0.0	7, 3	1.561	1.480	1.542	-5.2	-1.2
3, 1	0.612	0.580	0.607	-5.2	-0.8	7, 4	2.733	2.626	2.735	-3.9	0.1
3, 2	1.403	1.336	1.395	-4.8	-0.5	7, 5	2.905	2.777	2.905	-4.4	0.0
3, 3	1.489	1.420	1.480	-4.6	-0.6	8, 1	1.438	1.361	1.416	-5.4	-1.6
3, 4	1.752	1.668	1.741	-4.8	-0.6	8, 2	1.533	1.456	1.518	-5.0	-1.0
3, 5	2.735	2.632	2.739	-3.7	0.2	8, 3	1.834	1.746	1.821	-4.8	-0.7
4, 1*	0.522	0.494	0.519	-5.4	-0.7	8, 4	2.718	2.613	2.726	-3.9	0.3
4, 2*	0.544	0.525	0.547	-3.4	0.7	8, 5	2.903	2.782	2.910	-4.2	0.2
4, 3	1.431	1.360	1.416	-5.0	-1.0	9, 1	1.429	1.358	1.415	-4.9	-1.0
4, 4	1.667	1.587	1.656	-4.8	-0.6	9, 2	1.511	1.436	1.498	-4.9	-0.9
4, 5	2.725	2.621	2.729	-3.8	0.2	9, 3	1.765	1.679	1.751	-4.9	-0.8
5, 1	1.429	1.358	1.415	-4.9	-1.0	9, 4	2.089	1.993	2.082	-4.6	-0.3
5, 2	1.609	1.533	1.599	-4.8	-0.6	9, 5	2.744	2.638	2.748	-3.8	0.1
5, 3	2.104	1.998	2.088	-5.0	-0.7						

nominally identical geometry from different parts of the wafer [see Fig. 1(a)], for the approximately 30 peaks that can be easily identified in the range from 0.1 to 10 MHz. About 40% of the devices selected from columns 1–9 and rows A–G have a short circuit between one or both of the top electrodes and the bottom electrode, so they are discarded from the study. This is the reason that all seven fabricated devices are listed for only column 8 in Table I. We find that the slope of the base level of the phase spectra $\theta(f)$ can vary even for nominally identical devices, as seen in Fig. 3(d). It turns out that this variance is due to spurious charging effects, perhaps due to the floating electrode. This effect can be avoided by briefly short-circuiting the electrodes with a piece of metallic wire, and thus discharging the system. After discharging, the phase spectra become nearly identical for all devices with the same geometry; see Fig. 3(e). When these precautions are taken, the impedance spectra exhibit a large degree of repeatability and reproducibility.

For each of the nine different device geometries among our 35 selected devices, labeled by the column index $k = 1$ –9 in Table I, we measure the resonance frequencies of the five most prominent isolated nonoverlapping resonance peaks, labeled by $n = 1$ –5, in the impedance-phase spectra $\theta(f)$. This results in $5 \times 35 - 2 = 173$ resonance frequencies (for device 4B, we did not measure all five peaks, but only the three highest). In Table II, we list the experimentally determined values of the resonance frequencies, but to avoid showing all 173 of them, we show only the average resonance frequency $f_{k,n}^{\text{exp}}$ of peak n over all devices (row indices A–G in Table I) with column index k , which results in $9 \times 5 = 45$ entries.

TABLE III. Material parameters at 25 °C for the AlN thin-film transducer and the SLS float-glass substrate. The frequency-dependent damping coefficients $\Gamma_{\text{sl}}(f)$ and $\Gamma_{\varepsilon}(f)$ in the solid and dielectric domain are obtained by fitting to the measured width of the resonance peaks and to the background level, respectively, for devices C2–G2. The longitudinal and transverse sound speed are called c_{lo} and c_{tr} , respectively. Since we have a thin film, we use $e_{31,f} = e_{31} - (C_{13}/C_{33})e_{33}$ instead of e_{31} [24]. ϵ_0 is the vacuum permittivity. The tiny metal electrodes are not simulated in this study.

Parameter	Value	Parameter	Value
<i>Thin-film aluminum nitride, AlN</i> [15,25]			
ρ	3300 kg m ⁻³	Γ_{sl}	0.0005
C_{11}	410.2 GPa	C_{33}	385.0 GPa
C_{12}	142.4 GPa	C_{44}	122.9 GPa
C_{13}	110.1 GPa	C_{66}	133.9 GPa
$e_{31,f}$	-1.05 C m ⁻²	e_{15}	-0.39 C m ⁻²
e_{33}	1.46 C m ⁻²	$\Gamma_{\varepsilon}(f)$	-[(1.43 MHz + 0.98f)/1 GHz]
ϵ_{11}	9.2 ϵ_0	ϵ_{33}	10.1 ϵ_0
<i>SLS float-glass substrate</i> [19]			
ρ	(2522 ± 15) kg m ⁻³	(Measured at EPFL)	
E	(70 ± 2) GPa	s	0.23 ± 0.01
C_{11}	81.1 GPa	C_{44}	28.4 GPa
$c_{\text{lo}} = \sqrt{C_{11}/\rho}$	5672 m s ⁻¹	C_{12}	24.2 GPa
$c_{\text{tr}} = \sqrt{C_{44}/\rho}$	3359 m s ⁻¹	$\Gamma_{\text{sl}}(f)$	f^{-1} 0.018 MHz

V. MODELING AND NUMERICAL SIMULATION

We want to compare the experimental results for the impedance spectra and resonance frequencies with a numerical simulation. We therefore use the three-dimensional model for acoustofluidic systems recently developed by Skov *et al.* [23]. This model couples the mechanical displacement field \mathbf{u} and the electric potential φ in a system driven by a time-harmonic electric potential $\tilde{\varphi} = \varphi_0 e^{-i\omega t}$, with angular frequency $\omega = 2\pi f$ and frequency f , applied to the interfaces between the metal electrodes and the piezoelectric AlN thin-film transducer. This time-harmonic boundary condition excites time-harmonic fields: the electric potential $\tilde{\varphi}(\mathbf{r}, t)$ in the AlN thin-film transducer and the displacement $\tilde{\mathbf{u}}(\mathbf{r}, t)$ in all solids of the system, where

$$\tilde{\varphi}(\mathbf{r}, t) = \varphi(\mathbf{r})e^{-i\omega t}, \quad \tilde{\mathbf{u}}(\mathbf{r}, t) = \mathbf{u}(\mathbf{r})e^{-i\omega t}. \quad (1)$$

Fields with a tilde are time-harmonic, whereas those without a tilde are complex-valued amplitudes.

The motion of an elastic solid with a given density ρ (in the model this is the glass, the metal electrodes, or the AlN thin-film transducer) is described by the displacement field \mathbf{u} , whereas the electrodynamics is described by the electric displacement field \mathbf{D} . The governing equations for \mathbf{u} and \mathbf{D} are Cauchy's elastodynamic equation and Maxwell's quasi-electrostatic equation, $\nabla \cdot \mathbf{D} = 0$:

$$-\rho\omega^2(1 + i\Gamma_{\text{sl}})\mathbf{u} = \nabla \cdot \boldsymbol{\sigma}, \quad \nabla \cdot [-(1 + i\Gamma_{\varepsilon})\boldsymbol{\varepsilon} \cdot \nabla\varphi] = 0. \quad (2)$$

Here, $\Gamma_{sl}, \Gamma_\varepsilon \ll 1$ are weak damping coefficients, $\boldsymbol{\varepsilon}$ is the dielectric tensor, and $\boldsymbol{\sigma}$ is the stress tensor, which is coupled to \mathbf{u} through a stress-strain relation depending on the material-dependent elastic moduli C_{ik} .

For the isotropic glass and metal electrodes, the electric field is unimportant, whereas the relation between the stress tensor σ_{ik} and the strain components $\frac{1}{2}(\partial_i u_k + \partial_k u_i)$ is given in the compact Voigt representation as

$$\begin{pmatrix} \sigma_{xx} \\ \sigma_{yy} \\ \sigma_{zz} \\ \sigma_{yz} \\ \sigma_{xz} \\ \sigma_{xy} \end{pmatrix} = \begin{pmatrix} C_{11} & C_{12} & C_{12} & 0 & 0 & 0 \\ C_{12} & C_{11} & C_{12} & 0 & 0 & 0 \\ C_{12} & C_{12} & C_{11} & 0 & 0 & 0 \\ 0 & 0 & 0 & C_{44} & 0 & 0 \\ 0 & 0 & 0 & 0 & C_{44} & 0 \\ 0 & 0 & 0 & 0 & 0 & C_{44} \end{pmatrix} \begin{pmatrix} \partial_x u_x \\ \partial_y u_y \\ \partial_z u_z \\ \partial_y u_z + \partial_z u_y \\ \partial_x u_z + \partial_z u_x \\ \partial_x u_y + \partial_y u_x \end{pmatrix}. \quad (3)$$

Here, C_{ik} are the elastic moduli, which are listed for SLS float glass in Table III, and $C_{12} = C_{11} - 2C_{44}$.

In the piezoelectric AlN film, the stress tensor $\boldsymbol{\sigma}$ and the electric displacement field \mathbf{D} are given by the strain tensor $\frac{1}{2}[\nabla \mathbf{u} + (\nabla \mathbf{u})^T]$, the electrical field $-\nabla \varphi$, the electromechanical coupling coefficients e_{ik} , the elastic moduli C_{ik} , and the electric permittivities ε_{ik} as

$$\begin{pmatrix} \sigma_{xx} \\ \sigma_{yy} \\ \sigma_{zz} \\ \sigma_{yz} \\ \sigma_{xz} \\ \sigma_{xy} \\ D_x \\ D_y \\ D_z \end{pmatrix} = \begin{pmatrix} C_{11} & C_{12} & C_{13} & 0 & 0 & 0 & 0 & 0 & -e_{31} \\ C_{12} & C_{11} & C_{13} & 0 & 0 & 0 & 0 & 0 & -e_{31} \\ C_{13} & C_{13} & C_{33} & 0 & 0 & 0 & 0 & 0 & -e_{33} \\ 0 & 0 & 0 & C_{44} & 0 & 0 & 0 & -e_{15} & 0 \\ 0 & 0 & 0 & 0 & C_{44} & 0 & -e_{15} & 0 & 0 \\ 0 & 0 & 0 & 0 & 0 & C_{66} & 0 & 0 & 0 \\ 0 & 0 & 0 & 0 & e_{15} & 0 & \varepsilon_{11} & 0 & 0 \\ 0 & 0 & 0 & e_{15} & 0 & 0 & 0 & \varepsilon_{11} & 0 \\ e_{31} & e_{31} & e_{33} & 0 & 0 & 0 & 0 & 0 & \varepsilon_{33} \end{pmatrix} \begin{pmatrix} \partial_x u_x \\ \partial_y u_y \\ \partial_z u_z \\ \partial_y u_z + \partial_z u_y \\ \partial_x u_z + \partial_z u_x \\ \partial_x u_y + \partial_y u_x \\ -\partial_x \varphi \\ -\partial_y \varphi \\ -\partial_z \varphi \end{pmatrix}. \quad (4)$$

Here, the symmetry of AlN leads to $C_{12} = C_{11} - 2C_{66}$.

In terms of volume (mass) ratios, the device consists of 99.8% (99.5%) glass, 0.2% (0.3%) AlN film, and 0.0% (0.2%) metal electrodes. We find that within the numerical uncertainties, the simulation results are unchanged when the metal electrodes and prestress effects in the AlN film are left out. So, to reduce the memory requirements and to speed up the computation times, we leave out the prestress and the tiny metal electrodes in our modeling. Consequently, the boundary conditions for the electric potential φ are as follows: (1) on the interface between the bottom electrode and the AlN film, the potential is grounded, $\varphi = 0$; (2) on the interface between one half of the split electrode and the AlN film, $\varphi = +\frac{1}{2}V_0$; (3) on the interface between the other half of the split electrode and the AlN film, the potential is in antiphase, $\varphi = -\frac{1}{2}V_0$; (4) on the side walls of the AlN film, with normal vector \mathbf{n} , the no-free-charge condition applies, $\mathbf{n} \cdot \nabla \varphi = 0$. For the mechanical displacement field in the solids, a nonstress condition is applied to all external surfaces, $\mathbf{n} \cdot \boldsymbol{\sigma} = \mathbf{0}$.

Once a solution for \mathbf{u} and φ is obtained, the electrical impedance Z can be computed in the model as the ratio of the total voltage drop V_0 to the integral over the electrical

current density \mathbf{J} through the surface $\partial\Omega_{1/2}$ of one of the halves of the split electrode:

$$Z = \frac{V_0}{I} = \frac{V_0}{\int_{\partial\Omega_{1/2}} \mathbf{J} \cdot \mathbf{n} da}. \quad (5)$$

As there are no free charges in the system, the only contribution to the current density \mathbf{J} is the polarization current density $\mathbf{n} \cdot \mathbf{J} = \mathbf{e}_z \cdot \mathbf{J}_{\text{pol}} = \partial_t P_z = -i\omega(D_z + \varepsilon_0 \partial_z \varphi)$. We compute D_z from Eq. (4) and obtain, as in Ref. [26],

$$Z = \frac{(i/\omega)V_0}{\int_{\partial\Omega_{1/2}} [e_{31}(\partial_x u_x + \partial_y u_y) + e_{33}\partial_z u_z + (\varepsilon_0 - \varepsilon_{33})\partial_z \varphi] da}. \quad (6)$$

We implement the model of the AlN-thin-film-actuated glass-block devices in the finite-element-method software package COMSOL Multiphysics 5.4 [27] following the procedure described in Ref. [23]. The coupled field equation [Eq. (2)] for the elastic-solid displacement \mathbf{u} and the electric potential φ is implemented together with the constitutive equations [Eqs. (3) and (4)] using the weak-form

interface ‘‘PDE Weak Form.’’ Examples of COMSOL scripts with a PDE-weak-form implementation of acoustofluidics are available in Ref. [23] and as Supplemental Material in Ref. [28].

The system geometry described in Sec. II is meshed fairly coarsely because we study the low end of the spectrum, mainly $f < 3$ MHz, where the wavelengths are larger than 1.1 mm. The mesh of the glass block is a free tetrahedral mesh with a maximum element size of 0.2 mm, whereas the AlN thin film is modeled as a swept structured mesh with three mesh layers in the thickness direction and the same element size along the surface as for the glass. We use quadratic Lagrangian test functions and the mesh convergence test described in Ref. [29] to verify that the numerical resolution is satisfactory.

We use an adaptive-step-size algorithm to compute the impedance spectra. Close to a resonance peak, the step size goes down to 15 Hz, but far from resonance peaks, it increases to 1600 Hz. The resonance frequency is determined as the position of the maximum of a Lorentzian fit containing the 11 closest points. A typical short 0.1–3-MHz spectrum contains 450–500 points, whereas a long 0.1–10-MHz spectrum contains 2500–2800 points. A short and a long spectrum take around 0 h 40 min and 2 h 50 min, respectively, to compute on our HP-G4 workstation with a 3.7-GHz Intel Core i9 7960X-2.8 16-core processor and a memory of 128 GB RAM.

The spatial form of the acoustic mode corresponding to a given simulated resonance peak is revealed by plotting the displacement field $|\mathbf{u}|$. In the Supplemental Material [30], movies of each of the 45 resonance peaks (k, n) listed in Table II are presented.

VI. COMPARING SIMULATION WITH EXPERIMENTAL RESULTS

We use the numerical model of Sec. V to simulate electrical-impedance spectra $Z^{\text{sim}}(f)$ through Eq. (6). In the following, we compare these simulation results with the experimental spectra $Z^{\text{exp}}(f)$ described in Sec. IV.

Two examples of such a comparison in the frequency range from 0.1 to 3 MHz are seen in Figs. 4(a) and 4(b) for device geometries 2 and 8, respectively, where we plot the resistive part $\text{Re}[Z]$ of the electrical impedance as an alternative way to reveal the resonance peaks, instead of using the phase spectra $\theta(f)$ as in Figs. 3(c) and 3(d). The single red curve in each plot shows the simulation results obtained with the parameter values listed in Table III, whereas the family of gray curves shows the experimental results for all available devices with the relevant geometry. It is seen that the experimental impedance spectra are reproduced fairly well by the simulation regarding the positions of the resonance peaks and their relative heights. We note that, similarly to Fig. 3, the off-resonance levels of the experimental curves (gray) for the real part $\text{Re}[Z]$

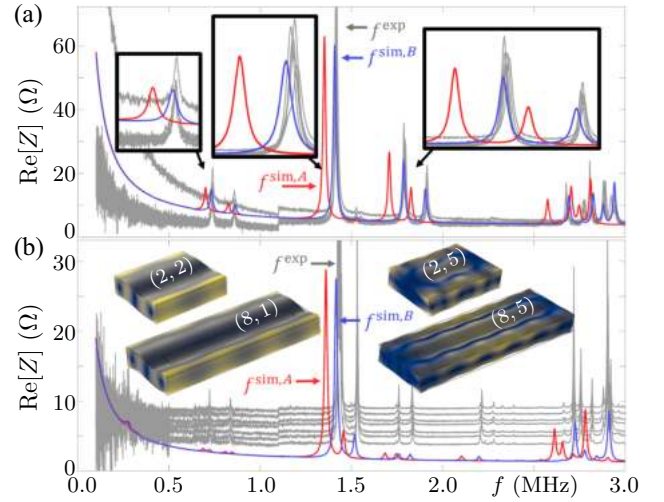


FIG. 4. (a) Resistive real part $\text{Re}[Z]$ of the impedance as a function of frequency f measured for the five devices C2–G2 of Fig. 3(d) (gray curves, f^{exp}), and simulated numerically using the parameter values from the literature listed in Table III (red curve, $f^{\text{sim,A}}$) and using the fitted parameter values listed in Table IV (blue curve, $f^{\text{sim,B}}$). (b) Similar plot of $\text{Re}[Z]$ versus f , but for the seven devices A8–G8 of Fig. 3(c). The insets are color plots of the displacement field $|\mathbf{u}|$ for four selected resonance peaks (k, n) from 0 (blue) to maximum (yellow). Movies of the modes of all the simulated resonance peaks in Table II are given in the Supplemental Material [30].

coincide for the devices C2–G2 in Fig. 4(a), which are discharged, while they are displaced for the devices A8–G8 in Fig. 4(b), which are not discharged. Moreover, we note that in Fig. 4(a), we fit the off-resonance level in the numerical model for Z in Eq. (6) using $\Gamma_\varepsilon(f)$ given in Table III.

The agreement between the experiments and simulations is quantified in Table II, where it is seen that for the 173 resonance peaks in our study, the relative deviation $\Delta_{k,n}^A$ of each simulated resonance frequency $f_{k,n}^{\text{sim,A}}$ deviates by only a few percent from the experimental value $f_{k,n}^{\text{exp}}$. The mean value and the standard deviation of the mean value of all relative deviations $\Delta_{k,n}^A$ are $(-4.6 \pm 0.1)\%$, which is a fairly good result. However, the simulation results show a statistically significant systematic underestimate of the resonance frequency. This is also clear from the insets in Fig. 4(a) showing enlargements of four resonance peaks: in all cases, the measured (gray) peaks for the seven nominally identical devices fall on top of each other, with variations much smaller than the peak width, whereas, in contrast, the simulated (red) peaks are shifted downward in frequency by a few peak widths.

This systematic shift of the simulated resonance peaks leads us to investigate whether a fitting of the two most significant but not so accurately determined material parameters, the Young’s modulus E and Poisson’s ratio ν of the SLS float-glass substrate, could lead to better numerical

TABLE IV. Fitted values for Young's modulus E' , Poisson's ratio s' , and the damping coefficient Γ_{sl} of SLS float glass for improving the agreement between the experiments and simulations. The values of C'_{11} , C'_{12} , C'_{44} , c'_{tr} , and c'_{lo} are functions of E' and s' [33].

Parameter	Value	Parameter	Value
E'	(76 ± 1) GPa	s'	(0.21 ± 0.01)
C'_{11}	85.5 GPa	C'_{44}	31.4 GPa
C'_{12}	22.7 GPa	$\Gamma_{sl}(f)$	f^{-1} 0.018 MHz
$c'_{lo} = \sqrt{C'_{11}/\rho}$	5824 m s ⁻¹	$c'_{tr} = \sqrt{C'_{44}/\rho}$	3529 m s ⁻¹

agreement with the experiments. Indeed, by using a simple stepping procedure, we find that such an improvement is obtained with the substitution

$$E = 70 \text{ GPa} \xrightarrow{\text{fit}} (76 \pm 1) \text{ GPa}, \quad s = 0.23 \xrightarrow{\text{fit}} 0.21 \pm 0.01. \quad (7)$$

This procedure extends the methods for obtaining the electromechanical coefficients of piezoelectric transducers [31,32] to determining the elastic coefficients of any elastic solid driven by vanishingly small thin-film transducers. The parameter values obtained for the best fitting to the experimental data are summarized in Table IV, and the resonance frequencies obtained from the simulation based on these values are denoted by $f_{k,n}^{\text{sim,B}}$.

The improved agreement between the simulations and experiments is seen qualitatively in Fig. 4, where the blue curves representing $f_{k,n}^{\text{sim,B}}$ more accurately reproduce the gray experimental impedance spectra. The improved agreement is also evident from the insets in Fig. 4(a), where the blue curve $f_{k,n}^{\text{sim,B}}$ now falls on top of the gray experimental curves to within a fraction of the peak width. Quantitatively, the improved agreement between the experiments and simulations is seen in Table II, where the relative deviation $\Delta_{k,n}^{\text{B}}$ of each simulated resonance frequency $f_{k,n}^{\text{sim,B}}$ deviates by less than one percent from the experimental value $f_{k,n}^{\text{exp}}$. The mean value and the standard deviation of the mean value of all relative deviations are $\Delta_{k,n}^{\text{B}} = (-0.5 \pm 0.1)\%$, or 9 times better than the first result, $(-4.6 \pm 0.1)\%$, obtained using the manufacturers' parameters.

The improved numerical agreement with the experiments using the fitted values of the Young's modulus and Poisson's ratio for the glass substrate suggests that our numerical-fitting simulation algorithm may be used as a starting point for developing a method for an improved *in situ* determination of acoustic parameters in the 0.1–10 MHz range, and possibly at higher frequencies. At the present stage, we do not know whether the relative deviation of roughly 5% between the literature values in Table III and the fitted values in Table IV is within the uncertainty generated by sample-to-sample variations in

the SLS float glass or whether it is a direct result of the fabrication process involving the deposition of the AlN thin-film transducers at 300 °C, which is, however, still in the specified range for stable properties of the float glass studied. The improved agreement between the simulations and experiments also suggests that using impedance measurements coupled with simulations is a promising way to investigate the resonance modes, since there is little ambiguity about which peaks are which. Also, from the measurements shown in Fig. 4, it is clear that by combining simulations with more varied device geometries it will be possible to predict particularly desired resonance frequencies with good accuracy and, consequently, to design appropriate device geometries.

VII. CONCLUSION

We present the fabrication of 570- μm -thick millimeter-sized SLS float-glass blocks with a 1- μm -thick AlN thin-film piezoelectric transducer sandwiched between thin metallic electrodes and deposited on the top surface. The electromechanical properties of the devices are characterized by electrical-impedance measurements in the frequency range from 0.1 to 10 MHz with a peak-to-peak voltage of 0.5 V applied to the electrodes.

We measure the electrical-impedance spectra for 35 different device geometries, all of width 2 mm, but with nine different lengths ranging from 2 to 6 mm and with two to seven copies of each individual geometry. Each impedance spectrum exhibits many resonance peaks, and we carefully measure the five most prominent ones in each spectrum. Comparing the resulting 173 experimental resonance frequencies with the result of a finite-element-method simulation, using material parameter values from the manufacturer, results in an average relative deviation of the 173 simulated resonance frequencies from the experimental values of $(-4.6 \pm 0.1)\%$.

We show that by using the Young's modulus and Poisson's ratio of the SLS float glass as fitting parameters in the simulation, we can reduce the relative deviation of the 173 simulated resonance frequencies from the experimental values by a factor of 9 to $(-0.5 \pm 0.1)\%$. Given a more sophisticated automated fitting procedure, ideally involving more resonance peaks and devices with different electrode configurations for better excitation of other resonance modes than those obtained with the current devices, this result suggests that our numerical fitting procedure could lead to an improved method for *in situ* determination of the acoustic parameters at ultrasound frequencies of any elastic solid to which a thin-film transducer can be attached.

ACKNOWLEDGMENTS

This work was supported by the BioWings project funded by the European Union's Horizon 2020 Future

and Emerging Technologies (FET) program, Grant No. 801267.

- [1] R. Ruby, in *2017 IEEE 30th International Conference on MicroElectro Mechanical Systems (MEMS)* (IEEE, New York, 2017), p. 308.
- [2] M. Dubois and P. Muralt, Properties of aluminum nitride thin films for piezoelectric transducers and microwave filter applications, *Appl. Phys. Lett.* **74**, 3032 (1999).
- [3] G. Piazza, P. J. Stephanou, and A. P. Pisano, Piezoelectric aluminum nitride vibrating contour-mode MEMS resonators, *J. Microelectromech. Syst.* **15**, 1406 (2006).
- [4] U. Zaghoul and G. Piazza, Highly scalable NEMS relays with stress-tuned switching voltage using piezoelectric buckling actuators, *IEEE Trans. Electron. Device* **61**, 3520 (2014).
- [5] N. Sinha, G. E. Wabiszewski, R. Mahameed, V. V. Felmetsger, S. M. Tanner, R. W. Carpick, and G. Piazza, Piezoelectric aluminum nitride nanoelectromechanical actuators, *Appl. Phys. Lett.* **95**, 053106 (2009).
- [6] A. De Pastina, D. Maillard, and L. Villanueva, Fabrication of suspended microchannel resonators with integrated piezoelectric transduction, *Microelectron. Eng.* **192**, 83 (2018).
- [7] R. H. Olsson III, K. E. Wojciechowski, M. S. Baker, M. R. Tuck, and J. G. Fleming, Post-CMOS-compatible aluminum nitride resonant MEMS accelerometers, *J. Microelectromech. Syst.* **18**, 671 (2009).
- [8] H. Zhang, W. Pang, H. Yu, and E. S. Kim, High-tone bulk acoustic resonators on sapphire, crystal quartz, fused silica, and silicon substrates, *J. Appl. Phys.* **99**, 124911 (2006).
- [9] J. Masson, G. Martin, R. Boudot, Y. Gruson, S. Ballandras, A. Artieda, P. Muralt, B. Belgacem, and L. Chomeloux, in *2007 IEEE International Frequency Control Symposium Joint with the 21st European Frequency and Time Forum* (IEEE, New York, 2007), p. 741.
- [10] T. Fujikura, O. Matsuda, D. M. Profunser, O. B. Wright, J. Masson, and S. Ballandras, Real-time imaging of acoustic waves on a bulk acoustic resonator, *Appl. Phys. Lett.* **93**, 261101 (2008).
- [11] P. Muralt, Recent progress in materials issues for piezoelectric MEMS, *J. Am. Ceram. Soc.* **91**, 1385 (2008).
- [12] K. M. Howell, W. Bashir, A. De Pastina, R. Matloub, P. Muralt, and L. G. Villanueva, Effect of AlN seed layer on crystallographic characterization of piezoelectric AlN, *J. Vac. Sci. Technol., A* **37**, 021504 (2019).
- [13] R. Matloub, A. Artieda, C. Sandu, E. Milyutin, and P. Muralt, Electromechanical properties of $\text{Al}_{0.9}\text{Sc}_{0.1}\text{N}$ thin films evaluated at 2.5 GHz film bulk acoustic resonators, *Appl. Phys. Lett.* **99**, 092903 (2011).
- [14] R. Matloub, M. Hadad, A. Mazzalai, N. Chidambaram, G. Moulard, C. S. Sandu, T. Metzger, and P. Muralt, Piezoelectric $\text{Al}_{1-x}\text{Sc}_x\text{N}$ thin films: A semiconductor compatible solution for mechanical energy harvesting and sensors, *Appl. Phys. Lett.* **102**, 152903 (2013).
- [15] Y. Q. Fu, J. K. Luo, N. T. Nguyen, A. J. Walton, A. J. Flewitt, X. T. Zu, Y. Li, G. McHale, A. Matthews, E. Iborra, H. Du, and W. I. Milne, Advances in piezoelectric thin films for acoustic biosensors, acoustofluidics and lab-on-chip applications, *Prog. Mater. Sci.* **89**, 31 (2017).
- [16] J.-B. Lee, D.-H. Cho, D.-Y. Kim, C.-K. Park, and J.-S. Park, Relationships between material properties of piezo-electric thin films and device characteristics of film bulk acoustic resonators, *Thin Solid Films* **516**, 475 (2007).
- [17] M. Dubois and P. Muralt, Stress and piezoelectric properties of aluminum nitride thin films deposited onto metal electrodes by pulsed direct current reactive sputtering, *J. Appl. Phys.* **89**, 6389 (2001).
- [18] C. K. Lee, F. Placido, S. Cochran, and K. J. Kirk, in *Proceedings, 2002 IEEE Ultrasonics Symposium, 2002, Vol. 2* (IEEE, New York, 2002), p. 1119.
- [19] Float glass substrates, [soda-lime-silicate glass: SiO_2 (70.8%), Na_2O (13.9%), CaO (8.4%), MgO (4.4%), Al_2O_3 (1.5%), K_2O (0.4%), SO_3 (0.3%), Fe_2O_3 (0.08%)], SCHOTT, SCHOTT Suisse SA, 2 Rue Galilée, Yverdon, Switzerland, https://www.epfl.ch/research/facilities/cmi/wp-content/uploads/2020/05/float_glass.pdf (accessed 16 November 2020).
- [20] A. Migliori, J. Sarrao, W. Visscher, T. Bell, M. Lei, Z. Fisk, and R. Leisure, Resonant ultrasound spectroscopic techniques for measurement of the elastic-moduli of solids, *Physica B* **183**, 1 (1993).
- [21] M. Radovic, E. Lara-Curzio, and L. Riester, Comparison of different experimental techniques for determination of elastic properties of solids, *Mater. Sci. Eng. A-Struct.* **368**, 56 (2004).
- [22] A. Cachiaras, L. Gilde, J. Swab, P. Patel, and G. Quinn, Soda-lime-silicate float glass: A property comparison, US Army Research Laboratory, ARL, Aberdeen Proving Ground, MD 21005-5069, USA (2017), <https://www.researchgate.net/publication/320871872> (accessed 16 November 2020).
- [23] N. R. Skov, J. S. Bach, B. G. Winkelmann, and H. Bruus, 3D modeling of acoustofluidics in a liquid-filled cavity including streaming, viscous boundary layers, surrounding solids, and a piezoelectric transducer, *AIMS Math.* **4**, 99 (2019).
- [24] P. Muralt, J. Conde, A. Artieda, F. Martin, and M. Cantoni, Piezoelectric materials parameters for piezoelectric thin films in GHz applications, *Int. J. Microw. Wirel. Technol.* **1**, 19 (2009).
- [25] M. A. Caro, S. Zhang, T. Riekkinen, M. Ylilampi, M. A. Moram, O. Lopez-Acevedo, J. Molarius, and T. Laurila, Piezoelectric coefficients and spontaneous polarization of ScAlN , *J. Phys.-Condens. Matter* **27**, 245901 (2015).
- [26] N. R. Skov, P. Sehgal, B. J. Kirby, and H. Bruus, Three-Dimensional Numerical Modeling of Surface-Acoustic-Wave Devices: Acoustophoresis of Micro- and Nanoparticles Including Streaming, *Phys. Rev. Appl.* **12**, 044028 (2019).
- [27] COMSOL Multiphysics 5.4 (2018), <http://www.comsol.com>.
- [28] P. B. Muller and H. Bruus, Theoretical study of time-dependent, ultrasound-induced acoustic streaming in microchannels, *Phys. Rev. E* **92**, 063018 (2015).

- [29] P. B. Muller, R. Barnkob, M. J. H. Jensen, and H. Bruus, A numerical study of microparticle acoustophoresis driven by acoustic radiation forces and streaming-induced drag forces, *Lab Chip* **12**, 4617 (2012).
- [30] See Supplemental Material at <http://link.aps.org/supplemental/10.1103/PhysRevApplied.16.014014> for movies of the time-dependent displacement field $|\mathbf{u}|$ for each of the 45 resonance peaks (k, n) listed in column $f_{k,n}^{\text{sim, B}}$ of Table II.
- [31] T. Lahmer, M. Kaltenbacher, B. Kaltenbacher, R. Lerch, and E. Leder, FEM-based determination of real and complex elastic, dielectric, and piezoelectric moduli in piezoceramic materials, *IEEE Trans. Ultrason. Ferroelectr. Freq. Control* **55**, 465 (2008).
- [32] C. Y. Kiyono, N. Perez, and E. C. N. Silva, Determination of full piezoelectric complex parameters using gradient-based optimization algorithm, *Smart Mater. Struct.* **25**, 025019 (2016).
- [33] J. T. Karlsen and H. Bruus, Forces acting on a small particle in an acoustical field in a thermoviscous fluid, *Phys. Rev. E* **92**, 043010 (2015).

5.2 Paper II: J. Acoust. Soc. Amer. 150, 634-645 (2021)

Numerical study of bulk acoustofluidic devices driven by thin-film transducers and whole-system resonance modes. [1]

As well as supplemental material:

Supplementary material: Numerical study of bulk acoustofluidic devices driven by thin-film transducers and whole-system resonance modes.

DOI: [10.1121/10.0005624](https://doi.org/10.1121/10.0005624)

Authors: [André G. Steckel](#) and Henrik Bruus.

Journal: Journal of the Acoustical Society of America, **150**, 634-645 (2021)

Numerical study of bulk acoustofluidic devices driven by thin-film transducers and whole-system resonance modes^{a)}

André G. Steckel and Henrik Bruus^{b)}

Department of Physics, Technical University of Denmark, DTU Physics Building 309, DK-2800 Kongens Lyngby, Denmark

ABSTRACT:

In bulk acoustofluidic devices, acoustic resonance modes for fluid and microparticle handling are traditionally excited by bulk piezoelectric (PZE) transducers. In this work, it is demonstrated by numerical simulations in three dimensions that integrated PZE thin-film transducers, constituting less than 0.1% of the bulk device, work equally well. The simulations are performed using a well-tested and experimentally validated numerical model. A water-filled straight channel embedded in a mm-sized bulk glass chip with a 1- μm -thick thin-film transducer made of $\text{Al}_{0.6}\text{Sc}_{0.4}\text{N}$ is presented as a proof-of-concept example. The acoustic energy, radiation force, and microparticle focusing times are computed and shown to be comparable to those of a conventional bulk silicon-glass device actuated by a bulk lead-zirconate-titanate transducer. The ability of thin-film transducers to create the desired acoustofluidic effects in bulk acoustofluidic devices relies on three physical aspects: the in-plane-expansion of the thin-film transducer under the applied orthogonal electric field, the acoustic whole-system resonance of the device, and the high Q -factor of the elastic solid, constituting the bulk part of the device. Consequently, the thin-film device is remarkably insensitive to the Q -factor and resonance properties of the thin-film transducer.

© 2021 Author(s). All article content, except where otherwise noted, is licensed under a Creative Commons Attribution (CC BY) license (<http://creativecommons.org/licenses/by/4.0/>). <https://doi.org/10.1121/10.0005624>

(Received 30 January 2021; revised 16 June 2021; accepted 24 June 2021; published online 29 July 2021)

[Editor: Kedar Chitale]

Pages: 634–645

I. INTRODUCTION

An increasing number of microscale ultrasound acoustofluidic devices are used for applications within clinical diagnostics, biology, and forensic sciences.^{1–5} Examples include but are not limited to rapid sepsis diagnostics by detection of bacteria in blood,⁶ enrichment of prostate cancer cells in blood,⁷ high-throughput cytometry and multiple-cell handling,^{8,9} cell synchronization,¹⁰ single-cell patterning and manipulation,^{11,12} and size-independent sorting of cells.¹³ Furthermore, acoustofluidics has been used for massively parallel force microscopy on biomolecules,¹⁴ acoustic tweezing,^{15–18} and noncontact microfluidic trapping and particle enrichment.¹⁹

Most applications rely on one of two basic methods for exciting the ultrasound field. One method is based on surface acoustic waves, excited by interdigitated metallic electrodes positioned on the surface of a piezoelectric (PZE) substrate. The other method relies on bulk acoustic waves excited in liquid-filled acoustic microchannels embedded in acoustically hard bulk devices by an attached bulk transducer that makes up 10%–50% volume-per-volume (v/v) of the device²⁰ or in microchannels with a thin silicon-membrane lid driven by a lead-zirconate-titanate (PZT) thin film that makes up around 15% v/v of the actuated

membrane, which is excited while leaving the bulk part of the device inert.²¹

Recently, the bulk-acoustic-wave method has been extended by the concept of whole-system ultrasound resonances (WSUR) in which the resonant acoustic modes are defined by the whole system and not just the microcavities.^{22,23} In this paper, we extend the WSUR concept by substituting the large bulk PZE transducer by a tiny PZE thin-film transducer integrated on the surface of the device and constituting less than 0.1% v/v of the resulting globally actuated device, a volume ratio 2 orders of magnitude smaller than any previous device.

Integrated thin-film PZE transducers have been used extensively for actuating electromechanical systems and are often made of aluminum nitride (AlN). Thin-film transducers made of AlN are structurally and chemically stable, have a low dielectric and mechanical loss, and are compatible with standard silicon-based complementary metal-oxide semiconductor (CMOS) microfabrication techniques. Academic applications of AlN thin-film transducers include radio-frequency (RF) filters,²⁴ suspended microchannel resonators,²⁵ contour mode resonators,²⁶ switches,^{27,28} and accelerometers.²⁹ AlN thin films have been deposited on substrates of sapphire, crystal quartz, fused silica, and silicon,³⁰ and 30- μm -thick Si membranes.^{31,32} Commercially, AlN-sputtered thin films are used in thin-film bulk-wave acoustic resonator filters.³³ However, hitherto thin-film transducers have not yet been applied in generic MHz bulk

^{a)}This paper is part of a special issue on Theory and Applications of Acoustofluidics.

^{b)}Electronic mail: bruus@fysik.dtu.dk, ORCID: 0000-0001-5827-2939.

acoustofluidic devices other than the aforementioned specialized silicon-membrane device.²¹

In this paper, based on a well-tested and experimentally validated numerical model,^{23,34,35} we demonstrate by three-dimensional (3D) numerical simulations that generic bulk glass chips with integrated PZE thin-film transducers constituting less than 0.1% v/v of the system, as sketched in Fig. 1, form devices with an acoustofluidic response on par with that obtained in a conventional silicon-glass device actuated by a bulk-PZT transducer using equivalent model assumptions. This result offers several advantages for the practical application of thin-film transducers within acoustofluidics: Thin-film devices do not depend on resonance properties of the thin-film transducer itself, they require no gluing, and can be fabricated by well-controlled reproducible microfabrication techniques subject to parallel mass-fabrication processes. We use 3D modeling to capture the axial variations observed experimentally even in straight, rectangular acoustofluidic channels.³⁶

The paper is organized as follows: In Sec. II, we briefly summarize the theory and numerical model used throughout the paper. In Sec. III, we present a proof-of-concept example showing that a thin-film acoustofluidic bulk device performs on par with a conventional bulk-transducer bulk device. In Sec. IV, we discuss the physical principle of the thin-film transduction process; robustness of the device to the material, thickness, and quality factor of the thin-film transducer; role of the shape of the thin-film-transducer electrodes, spatial regularity, and sensitivity of the device to shifts in the channel position away from exact centering in the glass chip. Finally, in Sec. V, we present our conclusions.

II. THEORY

Throughout this work, we use the theory and numerical model developed by Skov *et al.*,³⁴ including the effective

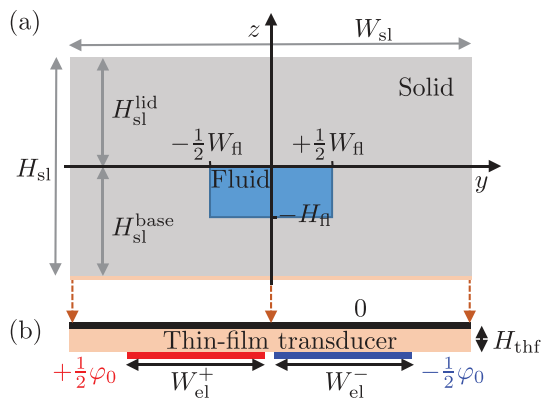


FIG. 1. (Color online) (a) A sketch of the yz -plane cross section of the long, straight thin-film driven device consisting of an elastic solid (gray) of width W_{sl} and height H_{sl} , an embedded fluid-filled microchannel (blue) of width W_{fl} and height H_{fl} , and an attached thin-film transducer (beige) of width W_{sl} and small height $H_{thf} \approx 0.001H_{sl}$. (b) A zoom-in on the thin-film transducer (beige) showing its grounded top electrode (black, of width W_{sl} and potential zero) and split-bottom electrode (red “+” and blue “-” of width W_{el}^+ and potential $\pm \frac{1}{2}\varphi_0$), made to excite the antisymmetric half-wave-like resonance mode.

boundary layer theory for the fluid domain by Bach and Bruus,³⁷ as briefly summarized in this section. This model is well-tested and experimentally validated for acoustofluidic devices,^{23,34,35} and although it was originally stated for bulk-PZT transducers, the model is trivially extended to describe other types of PZE transducers, including thin-film transducers.

A. Governing equations for the time-harmonic fields

We consider a time-harmonic electric potential $\tilde{\varphi}(\mathbf{r}, t)$, which excites the PZE transducer and induces a displacement field $\tilde{\mathbf{u}}_1(\mathbf{r}, t)$ in the solids that, in turn, leads to an acoustic pressure $\tilde{p}_1(\mathbf{r}, t)$ in the fluid channel. All of these fields $\tilde{F}(\mathbf{r}, t)$ separate into a complex-valued amplitude $F(\mathbf{r})$ and complex time-harmonic phase factor with frequency f ,

$$\tilde{F}(\mathbf{r}, t) = F(\mathbf{r}) e^{-i\omega t}, \quad \omega = 2\pi f. \quad (1)$$

The phase factor $e^{-i\omega t}$ cancels out in the following linear governing equations, leaving just the amplitude fields.

The first-order perturbation theory implies that the acoustic pressure p_1 in the fluid is governed by the Helmholtz equation with a damping coefficient Γ_{fl} ,³⁴

$$\nabla^2 p_1 = -\frac{\omega^2}{c_{fl}^2} (1 + i\Gamma_{fl}) p_1, \quad \Gamma_{fl} = \left(\frac{4}{3}\eta_{fl} + \eta_{fl}^b \right) \omega \kappa_{fl}, \quad (2)$$

where c_{fl} is the speed of sound, ρ_{fl} is the density, $\kappa_{fl} = (\rho_{fl} c_{fl}^2)^{-1}$ is the isentropic compressibility, and η_{fl} and η_{fl}^b are the dynamic and bulk viscosity of the fluid, respectively; see Table S1 in the supplementary material.³⁸ The pressure gradient governs the acoustic fluid velocity \mathbf{v}_1^{fl} ,

$$\mathbf{v}_1^{fl} = -i \frac{1 - i\Gamma_{fl}}{\omega \rho_{fl}} \nabla p_1. \quad (3)$$

For the linear PZE transducer (of either $Al_{1-x}Sc_xN$, AlN , or PZT), the electrical potential φ is governed by Gauss’s law for a linear dielectric without free charges,³⁴

$$\nabla \cdot \mathbf{D} = 0, \quad (4)$$

where \mathbf{D} is the electric displacement field, including a purely electric part $-(1 + i\Gamma_\varepsilon)\boldsymbol{\varepsilon} \cdot \nabla\varphi$, in which Γ_ε is a small damping coefficient, and $\boldsymbol{\varepsilon}$ is the dielectric tensor. The governing equation for the mechanical displacement field \mathbf{u}_1 in a linear elastic solid (including the PZE) with density ρ_{sl} is the weakly damped Cauchy equation,^{34,39}

$$-(1 + i\Gamma_{sl})\rho_{sl}\omega^2 \mathbf{u}_1 = \nabla \cdot \boldsymbol{\sigma}_{sl}, \quad (5)$$

where Γ_{sl} is a small damping coefficient. Using the Voigt notation, the linear electromechanical coupling in the PZE, which relates the stress and electric displacement to the strain and electric field, is given by

$$\begin{pmatrix} \sigma_{xx} \\ \sigma_{yy} \\ \sigma_{zz} \\ \sigma_{yz} \\ \sigma_{xz} \\ \sigma_{xy} \\ D_x \\ D_y \\ D_z \end{pmatrix} = \begin{pmatrix} C_{11} & C_{12} & C_{13} & 0 & 0 & 0 & 0 & 0 & -e_{31} \\ C_{12} & C_{11} & C_{13} & 0 & 0 & 0 & 0 & 0 & -e_{31} \\ C_{13} & C_{13} & C_{33} & 0 & 0 & 0 & 0 & 0 & -e_{33} \\ \hline 0 & 0 & 0 & C_{44} & 0 & 0 & 0 & -e_{15} & 0 \\ 0 & 0 & 0 & 0 & C_{44} & 0 & -e_{15} & 0 & 0 \\ 0 & 0 & 0 & 0 & 0 & C_{66} & 0 & 0 & 0 \\ \hline 0 & 0 & 0 & 0 & e_{15} & 0 & \varepsilon_{11} & 0 & 0 \\ 0 & 0 & 0 & e_{15} & 0 & 0 & 0 & \varepsilon_{11} & 0 \\ e_{31} & e_{31} & e_{33} & 0 & 0 & 0 & 0 & 0 & \varepsilon_{33} \end{pmatrix} \begin{pmatrix} \partial_x u_x \\ \partial_y u_y \\ \partial_z u_z \\ \partial_y u_z + \partial_z u_y \\ \partial_x u_z + \partial_z u_x \\ \partial_x u_y + \partial_y u_x \\ -\partial_x \varphi \\ -\partial_y \varphi \\ -\partial_z \varphi \end{pmatrix}. \quad (6)$$

The remaining three components of the stress tensor are given by the symmetry relation $\sigma_{ik} = \sigma_{ki}$. Similarly, the Cauchy equation (5) governs \mathbf{u}_1 in a purely elastic solid, but now the stress-strain relation (6) includes only the first six rows and first six columns as \mathbf{D} and φ do not couple to $\boldsymbol{\sigma}_{sl}$ and \mathbf{u}_1 . The parameter values are listed in Table SII of the supplementary material.³⁸

B. Governing equations for the steady time-averaged fields

The nonlinearity of the governing equations results in higher order responses to the time-harmonic actuation. Here, we are only interested in the steady time-averaged second-order response and define $F_2(\mathbf{r}) = \langle \tilde{F}_2(\mathbf{r}, t) \rangle = (\omega/2\pi) \int_0^{2\pi/\omega} \tilde{F}_2(\mathbf{r}, t) dt$. A time-average of a product of two first-order fields is also a second-order term, which is written as $\langle \text{Re}[\tilde{A}_1(t)] \text{Re}[\tilde{B}_1(t)] \rangle = \frac{1}{2} \text{Re}[A_1 B_1^*]$, where the asterisk denotes complex conjugation. The acoustic streaming \mathbf{v}_2 is such a time-averaged field. It is a steady-state, incompressible Stokes flow driven by the slip velocity stated in Sec. II C and time-averaged acoustic dissipation body force proportional to Γ_{fl} ,³⁷

$$\eta_{fl} \nabla^2 \mathbf{v}_2 = \nabla p_2 - \frac{\Gamma_{fl} \omega}{2c_{fl}^2} \text{Re}[p_1^* \mathbf{v}_1^{\text{fl}}], \quad \nabla \cdot \mathbf{v}_2 = 0. \quad (7)$$

The spatial average E_{ac}^{fl} of the time-averaged acoustic energy density in the fluid volume V_{fl} is given as the sum of the kinetic and compressional energy densities,

$$E_{ac}^{\text{fl}} = \frac{1}{V_{fl}} \int_{V_{fl}} \left[\frac{1}{4} \rho_{fl} |\mathbf{v}_1^{\text{fl}}|^2 + \frac{1}{4} \kappa_{fl} |p_1|^2 \right] dV, \quad (8)$$

where ρ_{fl} and κ_{fl} are the fluid density and compressibility, respectively.

The acoustic radiation force \mathbf{F}^{rad} acting on a single particle with radius a , density ρ_{ps} , and compressibility κ_{ps} suspended in the fluid is minus the gradient of the acoustic potential U^{rad} ,^{40,41}

$$\mathbf{F}^{\text{rad}} = -\nabla U^{\text{rad}}, \quad (9a)$$

$$U^{\text{rad}} = \pi a^3 \left(\frac{1}{3} f_0 \kappa_{fl} |p_1|^2 - \frac{1}{2} f_1 \rho_{fl} |\mathbf{v}_1^{\text{fl}}|^2 \right), \quad (9b)$$

$$f_0 = 1 - \frac{\kappa_{ps}}{\kappa_{fl}}, \quad f_1 = \frac{2(\rho_{ps} - \rho_{fl})}{2\rho_{ps} + \rho_{fl}}, \quad (9c)$$

where f_0 and f_1 are the so-called acoustic monopole and dipole scattering coefficients, respectively.

To further quantify the quality of the acoustophoretic response in the fluid volume V_{fl} of a standing half-wave-like pressure wave, which by \mathbf{F}^{rad} focuses microparticles in the vertical nodal plane $y=0$, we use the figure of merit R in V_{fl} , introduced by Moiseyenko and Bruus,²²

$$R = \frac{\int_{V_{fl}} -\text{sign}(y) F_y^{\text{rad}} dV}{\int_{V_{fl}} |F_z^{\text{rad}}| dV}. \quad (10)$$

R is large when the focusing force $-\text{sign}(y) F_y^{\text{rad}}$ with the appropriate sign is large and the magnitude $|F_z^{\text{rad}}|$ of the vertical force is small. Essentially, R expresses how many times larger the average horizontal focusing force component is compared to the vertical focusing force component.

Another quantitative measure is the time t_{foc} it takes, on average, after turning on the acoustic field to focus by acoustophoresis a dilute suspension of microparticles of radius a into the narrow region $|y| < 8a$, centered around the vertical nodal plane $y=0$ from their initial positions. We consider N particles that start from the evenly distributed positions \mathbf{r}_i , $i = 1, 2, \dots, N$, outside of the narrow region. The equation of motion for a single particle with velocity \mathbf{v}_p suspended in a fluid with a streaming velocity \mathbf{v}_2 is the force balance between the Stokes drag force and acoustic radiation force, $\mathbf{v}_p(\mathbf{r}) = \mathbf{v}_2(\mathbf{r}) + (1/6\pi\eta_{fl}a) \mathbf{F}^{\text{rad}}(\mathbf{r})$.⁴² The time, t_{fi} , when a given particle reaches the narrow region, $|y_f| = 8a$, is found by numerical integration of the trajectory as detailed in the

supplementary material.³⁸ The average focus time for the homogeneous particle distribution is, therefore, defined by

$$t_{\text{foc}} = \frac{1}{N} \sum_{i=1}^N t_{fi}. \quad (11)$$

Quantitatively, for a given actuation voltage, a good acoustophoretic resonance mode is characterized by having a large E_{ac} , large R , and small t_{foc} .

C. Boundary conditions fluids, solids, and PZE

The boundary conditions of the fields on all boundaries and interfaces of the model are specified as follows. On the surfaces facing the surrounding air, we assume zero stress on the solid and PZE as well as zero free surface charge density on the PZE. On the surfaces with electrodes, the PZE has a specified alternating current (ac)-voltage amplitude. On the internal solid-PZE and solid-fluid surfaces, the stress and displacement are continuous except for the latter in the form of the effective boundary conditions derived by Bach and Bruus.³⁷ These boundary conditions include, analytically, the shallow viscous boundary layer of thickness $\delta_{\text{fl}} = \sqrt{2\eta_{\text{fl}}/(\rho_{\text{fl}}\omega)} \approx 0.5 \mu\text{m}$, which, therefore, does not need to be resolved numerically, the complex-valued shear-wave number $k_s = (1 + i)\delta_{\text{fl}}^{-1}$ of the fluid (fl), and the velocity $\mathbf{v}_1^{\text{sl}} = -i\omega\mathbf{u}_1$ of the solid (sl),

$$\text{sl-air} : \quad \boldsymbol{\sigma}_{\text{sl}} \cdot \mathbf{n} = \mathbf{0}, \quad \mathbf{n} \text{ is the surface normal}, \quad (12a)$$

$$\text{sl-fl} : \quad \boldsymbol{\sigma}_{\text{sl}} \cdot \mathbf{n} = -p_1 \mathbf{n} + ik_s \eta_{\text{fl}} (\mathbf{v}_1^{\text{sl}} - \mathbf{v}_1^{\text{fl}}), \quad (12b)$$

$$\mathbf{v}_1 \cdot \mathbf{n} = \mathbf{v}_{\text{sl}} \cdot \mathbf{n} + \frac{i}{k_s} \nabla_{\parallel} \cdot (\mathbf{v}_{\text{sl}} - \mathbf{v}_1)_{\parallel} \quad (12c)$$

$$\text{PZE-air} : \quad \mathbf{D} \cdot \mathbf{n} = \mathbf{0}, \quad (12d)$$

$$\text{top elec.} : \quad \varphi = 0, \quad (12e)$$

$$\text{bot elec.} : \quad \varphi = \pm \frac{1}{2} \varphi_0. \quad (12f)$$

Further, at fluid–solid interfaces, the slip velocity \mathbf{v}_2^{bc} , driving the streaming, takes into account both the motion of the surrounding elastic solid and Reynolds stress induced in a viscous boundary layer in the fluid,³⁷

$$\mathbf{v}_2 = \mathbf{v}_2^{\text{bc}}, \quad \mathbf{n} \cdot \mathbf{v}_2^{\text{bc}} = 0, \quad (13a)$$

$$\begin{aligned} (\mathbf{1} - \mathbf{nn}) \cdot \mathbf{v}_2^{\text{bc}} = & -\frac{1}{8\omega} \nabla_{\parallel} |\mathbf{v}_{1\parallel}^{\text{fl}}|^2 \\ & - \text{Re} \left[\left(\frac{2-i}{4\omega} \nabla_{\parallel} \cdot \mathbf{v}_{1\parallel}^{\text{fl}*} + \frac{i}{2\omega} \partial_{\perp} v_{1\perp}^{\text{fl}*} \right) \mathbf{v}_{1\parallel}^{\text{fl}} \right], \end{aligned} \quad (13b)$$

where the subscript “ \parallel ” indicates the derivative or vector components parallel to the surface and, likewise, “ \perp ” indicates the perpendicular components. Equation (13) is the special case of the slip velocity \mathbf{v}_2^{bc} , which is only valid near the acoustic resonance, where $|\mathbf{v}_1^{\text{fl}}|$ in the bulk is much larger than $|\mathbf{v}_1^{\text{sl}}|$ of the walls at the fluid–solid interface.

Finally, we use the symmetry at the yz - and xz -planes to reduce the model to one-quarter the size in the domain $x > 0$ and $y > 0$, allowing for finer meshing and/or faster computations. We apply the symmetric boundary conditions at the yz -plane $x = 0$ and anti-symmetry at the xz -plane $y = 0$ for the first-order fields and symmetric boundary conditions at both planes for the second-order fields,

$$\text{Symmetry, } x = 0 : \quad (14a)$$

$$\partial_x \varphi = 0, \quad \partial_x p_1 = 0, \quad \partial_x p_2 = 0,$$

$$v_{1,x}^{\text{sl}} = 0, \quad \partial_x v_{1,y}^{\text{sl}} = 0, \quad \partial_x v_{1,z}^{\text{sl}} = 0, \quad (14b)$$

$$v_{2,x}^{\text{fl}} = 0, \quad \partial_x v_{2,y}^{\text{fl}} = 0, \quad \partial_x v_{2,z}^{\text{fl}} = 0, \quad (14c)$$

$$\text{Anti-symmetry, } y = 0 : \quad (14d)$$

$$\varphi = 0, \quad p_1 = 0, \quad \partial_y p_2 = 0,$$

$$v_{1,x}^{\text{sl}} = 0, \quad \partial_y v_{1,y}^{\text{sl}} = 0, \quad v_{1,z}^{\text{sl}} = 0, \quad (14e)$$

$$\partial_y v_{2,x}^{\text{fl}} = 0, \quad v_{2,y}^{\text{fl}} = 0, \quad \partial_y v_{2,z}^{\text{fl}} = 0. \quad (14f)$$

III. MAIN RESULTS COMPARING A THIN-FILM AND A BULK-TRANSDUCER DEVICE

A. The two main model devices

As a proof of concept that a tiny thin-film transducer is able to drive a bulk acoustofluidic device as well as a conventional bulk transducer, we study the two devices shown in Figs. 2(a) and 2(c), which both contain a water-filled microchannel of length $L_{\text{fl}} = 35 \text{ mm}$, width $W_{\text{fl}} = 0.377 \text{ mm}$, and height $H_{\text{fl}} = 0.157 \text{ mm}$, chosen as a typical channel size used in the literature¹ and specifically studied experimentally and theoretical in Ref. 43. We emphasize that both devices are simulated on equal footing using the same model approach with the same assumptions on damping and lack of clamping. Also, both devices are made of acoustically hard materials with high acoustic impedances relative to water, namely, 13.2 for silicon and 8.4 for glass.

The thin-film device consists of a rectangular glass block of $L_{\text{gl}} = 40 \text{ mm}$, width $W_{\text{gl}} = 3.02 \text{ mm}$, and height $H_{\text{gl}} = 1.4 \text{ mm}$. An $\text{Al}_{0.6}\text{Sc}_{0.4}\text{N}$ thin-film transducer of length $L_{\text{thf}} = L_{\text{gl}}$, width $W_{\text{thf}} = W_{\text{gl}}$, and height $H_{\text{thf}} = 1 \mu\text{m}$ is deposited on the bottom surface of the xy -plane, thus, occupying only 0.07% of the total device volume. To excite the half-wave-like pressure wave, an antisymmetric voltage actuation is effective²³ and made possible by splitting the bottom electrode in half by a 40- μm -wide gap along the x axis. The microchannel is centered along the x - and y axes, but its top aligns with the center of the glass height $\frac{1}{2}H_{\text{gl}}$ to mimic that the glass block consists of two glass slabs of equal height bonded together except that the microchannel is etched into the top surface of the bottom slab; see Fig. 1. This specific device is chosen because in a recent study, we successfully modeled and experimentally validated a similar thin-film-glass-block device without the microchannel.⁴⁴

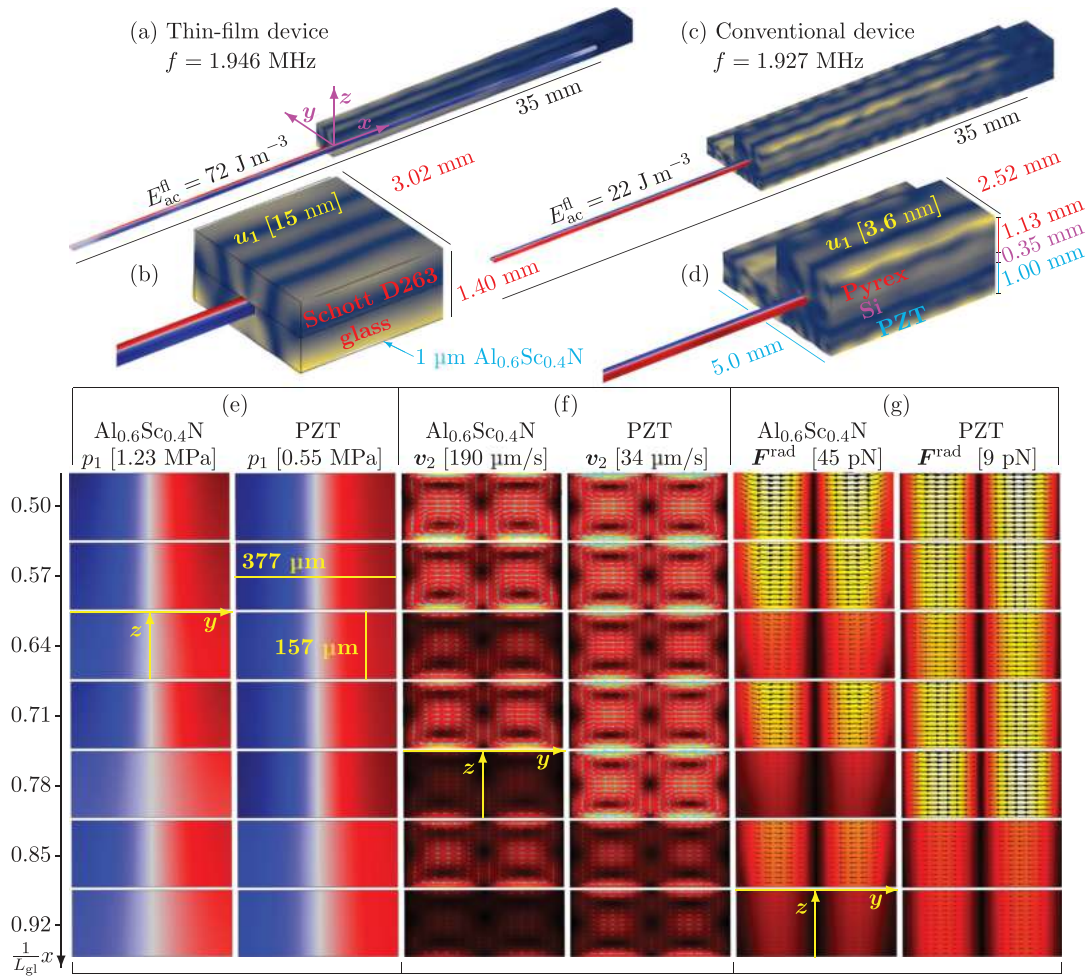


FIG. 2. (Color online) (a),(b) A bulk glass chip driven by a 1- μm -thick $\text{Al}_{0.6}\text{Sc}_{0.4}\text{N}$ thin-film transducer (not visible) actuated at resonance $f = 1.946$ MHz with $1 V_{\text{pp}}$. The 3D color plots are u_1 from 0 (blue) to 15 nm (yellow) and p_1 from -1.23 MPa (blue) to $+1.23$ MPa (red). (c),(d) A conventional Si-glass chip driven by a bulk PZT actuated at resonance $f = 1.927$ MHz with $1 V_{\text{pp}}$. The color plots are u_1 from 0 (blue) to 3.6 nm (yellow) and p_1 from -0.55 MPa (blue) to $+0.55$ MPa (red). (e) The color plots of p_1 from $-p_{\text{max}}$ (blue, value in the square bracket) to $+p_{\text{max}}$ (red) of the $\text{Al}_{0.6}\text{Sc}_{0.4}\text{N}$ -driven device on the left and PZT-driven device on the right in seven cross sections from $x/L_{\text{gl}} = 0.5$ to 0.92 in steps of 0.07 are shown. (f) The color plots as in (e) but for the streaming velocity magnitude v_2 from zero (black) to v_2^{max} (white, value in the square bracket) and with vectors showing v_2 . (g) The color and vector plot as in (f) but for the radiation force F^{rad} from zero (black) to $F_{\text{max}}^{\text{rad}}$ (white, value in the square bracket) for suspended 5- μm -diameter polystyrene particles. See the animations of the modes in the supplementary material (Ref. 38).

The bulk-transducer device has been studied extensively both experimentally and numerically in the literature.^{36,42,43} It consists of a silicon substrate of length $L_{\text{si}} = 40$ mm, width $W_{\text{si}} = 2.52$ mm, and height $H_{\text{si}} = 0.35$ mm into which the centered microchannel is etched and onto which is bonded a Pyrex glass lid of the same length and width but with the height $H_{\text{py}} = 1.13$ mm. This silicon-glass chip is placed off-center on a nominal 2-MHz PZT transducer of $L_{\text{pzt}} = 40$ mm, width $W_{\text{pzt}} = 5$ mm, and height $H_{\text{pzt}} = 1$ mm such that the rightmost side walls align. In the actual device, the transducer is glued to the chip, but here we neglect the glue layer and assume an ideal bonding instead. Note that the fraction of the total volume occupied by the bulk-PZT transducer is large, $V_{\text{pzt}}/V_{\text{tot}} = 57\%$ v/v.

Using these dimensions and the material parameters listed in Tables SI and SII of the supplementary material,³⁸ we implement these two 3D device models in the commercial finite-element software COMSOL Multiphysics 5.4,⁴⁵ closely following the implementation method described in

Ref. 34. We use tetrahedral meshes chosen to have at least 12 nodal points per wavelength at 2 MHz in all domains (18 in the fluid domain) except in the z -direction of the thin-film, where the thickness is much smaller than the wavelength. So here, a swept mesh was used to ensure at least four nodal points. Performing a standard mesh convergence analysis,³⁴ we found deviations in the acoustofluidic responses of about 1% when comparing to the highest mesh resolution possible in our setup. We observed no changes by adding additional nodal points in the thin-film thickness direction. All simulations were run on a workstation with a 16-core processor Intel i9-7960X at 3.70 GHz boost clock and 128 GB random access memory (Intel, Santa Clara, CA).

B. Mode analysis of the two devices

The first step in our analysis is to identify good acoustic resonance modes in the two devices, which we actuate in a

comparable manner with a peak-to-peak voltage of $\varphi_0 = 1$ V. In the thin-film device, the voltage amplitude of the ac-voltage on the “positive” (“negative”) half of the bottom electrode is set to $+\frac{1}{2}\varphi_0$ ($-\frac{1}{2}\varphi_0$, 180° out of phase) relative to the grounded top electrode. Similarly, the voltage amplitude on the top electrode in the bulk-PZT device is set to $+\frac{1}{2}\varphi_0$ relative to the grounded bottom electrode. The frequency of the actuation voltage is then swept from 0.1 to 3.5 MHz while monitoring the acoustic energy density E_{ac}^{fl} , Eq. (8), in the water. The frequency steps in the sweep are adaptive, ranging from $\Delta f = 16$ kHz when the local curvature in $E_{ac}^{fl}(f)$ is small (far from resonance peaks) down to $\Delta f = 0.03$ kHz when it is large (near resonance peaks).

As expected, the strongest resonance peak in E_{ac}^{fl} happens near the hard-wall standing half-wave resonance $f_0 = c_{fl}/2W_{wa} = 2$ MHz. This main resonance is located at $f_{thf} = 1.946$ MHz with a maximum energy density of $E_{ac}^{fl}(f_{thf}) = 72 \text{ J m}^{-3}$ for the thin-film device and at $f_{pzt} = 1.927$ MHz with a $E_{ac}^{fl}(f_{pzt}) = 22 \text{ J m}^{-3}$. The amplitude p_1 of the pressure and u_1 of the displacement field for these main resonance modes in the two devices are shown in Figs. 2(a)–2(d). One immediate conclusion is that the quality of the resulting resonant pressure mode in the two devices is comparable: a nearly perfect antisymmetric wave across the channel with only weak variations along the channel. The pressure amplitude of 1.23 MPa in the thin-film device is 2.2 times larger than the 0.55-MPa amplitude in the bulk-PZT device.

When inspecting the displacement field in Figs. 2(a)–2(d), it is seen that it has a more regular mode with a larger 15-nm amplitude in the thin-film device [Figs. 2(a) and 2(b)] compared to the more complex resonance mode with a smaller 3.6-nm amplitude in the larger volume of the bulk-PZT device [Figs. 2(c) and 2(d)]. Figure 2(e) shows the pressure in seven vertical channel –cross sections, equally spaced along the channel from its center to its end, showing the abovementioned weak axial variations in p_1 for both devices. Clearly on a qualitative level, the tiny 0.07% v/v thin-film transducer is seen to deliver a comparable, and perhaps even better, acoustic response in the device compared with the conventional large 57% v/v bulk-PZT transducer.

As a first rough quantitative comparison, we sample p_1 in 700 equidistant points along a straight line parallel to the x axis through the edge point $(0, \frac{1}{2}W_{fl}, -\frac{1}{2}H_{fl})$. We find the following regression lines with standard deviations: $p_1(x, \frac{1}{2}W_{fl}, -\frac{1}{2}H_{fl}) = (1.15 - 0.83\frac{2x}{L_{fl}} \pm 0.16)$ MPa for the thin-film and $(0.56 - 0.23(2x/L_{fl}) \pm 0.05)$ MPa for the bulk-PZT device. The former pressure is nearly twice as large as the latter at the center $x = 0$, namely, 1.15 versus 0.56 MPa, but they both end at the same value at the channel end $x = \frac{1}{2}L_{fl}$, namely, 0.32 versus 0.33 MPa. Clearly, the pressure is higher in the thin-film device, but the pressure variations are also three times larger, namely, 0.16 versus 0.05 MPa compared to the bulk-PZT device. In the following, for further quantitative comparison, we study the acoustic radiation force F^{rad} and related focusing time t_{foc} that it

takes to focus 5- μm -diameter particles in the vertical pressure nodal plane $y = 0$.

C. The acoustic radiation force and streaming at resonance

The acoustic modes p_1 and u_1 are the basic fields giving rise to the steady time-averaged responses used for applications in acoustofluidic devices, namely, the acoustic streaming v_2 in the fluid and the radiation force F^{rad} acting on the suspended microparticles. In Figs. 2(f) and 2(g), these responses are shown in the same seven cross sections as were used in Fig. 2(e). Being second-order responses, the amplitudes of v_2 and F^{rad} become $2.2^2 \approx 5$ larger in the thin-film than in the bulk-PZT device, where 2.2 is the aforementioned ratio in the pressure amplitudes. Similarly, the axial variations in v_2 and F^{rad} are nearly five times larger in the thin-film than they are in the bulk-PZT device.

For a more complete quantitative comparison of the acoustophoretic response, we compute the acoustic energy density E_{ac} [Eq. (8)], the figure of merit R [Eq. (10)], and the focusing time t_{foc} [Eq. (11)] for suspended 5- μm -diameter microparticles for the two main resonance modes in Fig. 2. As detailed in the supplementary material,³⁸ t_{foc} for a given mode is given by the average of the focus time of 3536 individual particle trajectories computed by numerical integration. The respective values are listed in Table I, and they support the result of the qualitative comparison of the shape of the pressure, streaming, and force fields: The time-averaged response of the $\text{Al}_{0.6}\text{Sc}_{0.4}\text{N}$ thin-film device is comparable in terms of E_{ac} , R , and t_{foc} to that of the bulk-PZT device. It supports the usual quadrupolar Rayleigh streaming pattern, and the radiation force points toward the vertical center plane along the axis, which can, thus, serve as a plane for particle focusing. Whereas R is $22.7/7.1 = 3.2$ times smaller, E_{ac}^{fl} is $72/22 = 3.3$ times larger and t_{foc} is $1.73/0.53 = 3.3$ times faster in the thin-film device compared to the bulk-PZT device. From this first example, it is, therefore, clear that the thin-film bulk device would work as an excellent acoustofluidic device and thin-film transducers can be used on generic bulk chips without fabricating the

TABLE I. The quantitative comparison of the quality of the resonance modes of three thin-film (thf) and one bulk (bulk) device: $\text{Al}_{0.6}\text{Sc}_{0.4}\text{N}$ (thf) and Pz26 (bulk) of Fig. 2, as well as AlN (thf) and Pz26 (thf) discussed in Sec. IV B. Listed are the resonance frequency f_{res} , the figure of merit, Eq. (10), the acoustic energy density E_{ac} , Eq. (8), and the focusing time t_{foc} , Eq. (11), for 5- μm -diameter microparticles. See the animations of the resonance modes in the supplementary material (Ref. 38).

Response	AlN thf	$\text{Al}_{0.6}\text{Sc}_{0.4}\text{N}$ thf	Pz26 thf	Pz26 bulk
f_{res} (MHz)	1.948	1.946	1.942	1.927
R (-)	6.7	7.1	8.5	22.7
E_{ac}^{fl} (J m^{-3})	7.3	72	2.1×10^3	22
t_{foc} (s)	5.4	0.52	0.016	1.73
$E_{ac}^{fl} t_{foc}$ (J s m^{-3})	39.4	37.4	34.2	38.1
$E_{ac}^{fl}/e_{31}^2 f$ (m F^{-1} ; Ref. 38)	7.0	10.3	9.9	—

delicate and expensive membrane devices.²¹ In the following, we investigate further the physical characteristics of the thin-film bulk device.

IV. PHYSICAL ASPECTS OF ACOUSTOFLUIDIC BULK DEVICES DRIVEN BY THIN-FILM TRANSDUCERS

In this section, we use the numerical model to study various physical aspects of acoustofluidic devices with thin-film transducers. The study includes the physical principle of the thin-film transduction process; the robustness of the device to the material, thickness, and quality factor of the thin-film transducer; the role of the thin-film-transducer electrode shape; the spatial regularity; and the sensitivity of the device to shifts in the channel position away from the exact centering in the glass chip.

A. The physics of thin-film actuation of bulk devices

The ability of the thin-film transducer to create the desired acoustophoretic microparticle focusing by radiation force or mixing by acoustic streaming in a bulk acoustofluidic device relies on three physical aspects of the system: the in-plane-expansion of the thin-film transducer under the action of the orthogonal applied electric field, the acoustic whole-system resonance of the device, and the high Q -factor of the elastic solid, constituting the bulk part of the device.

Traditional bulk PZE transducers typically work by exciting a standing half-wave in the transducer thickness direction, which is also the direction of both the polarization and applied electrical field. This gives a large mechanical displacement because of the large longitudinal PZE coefficient e_{33} . This thickness mode is fairly easy to compute and design for, and it is also relatively good at transferring acoustical power into a device attached to the transducer by the large displacement component along the surface normal. Conventional bulk PZE transducers with a millimeter-thickness typically have good resonances in the low-MHz regime.

In contrast, the half-wave transducer resonances of the thin-film transducers are pushed up into the GHz regime as a result of the micrometer-sized thickness, which is much higher than the low-MHz frequencies typically used in bulk acoustofluidics. Therefore, the transduction studied in this work is dominated by the transverse PZE coefficient e_{31f} . The large electric field on the order of MV/m that results from applying, say, a potential difference of $1 V_{pp}$ across a $1\text{-}\mu\text{m}$ -thick thin-film transducer, generates a large strain that accumulates along the millimeter-sized transducer-glass interface, which is the first of the three physical prerequisites. When this strain pattern has a sufficiently compatible overlap with that of a given resonance mode in the large glass block, the system will be excited at a frequency near this resonance mode frequency. This is the second physical prerequisite. We emphasize that this transduction mechanism does not rely on exciting any resonances in the thin-film transducer but instead on exciting resonances in the whole system, of which the transducer is only a minute part.

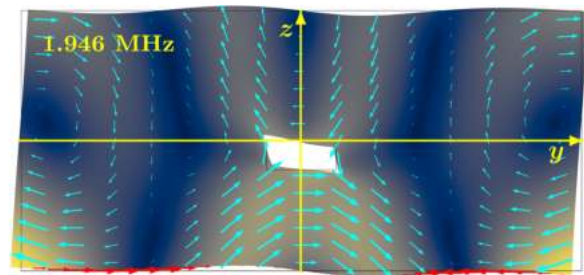


FIG. 3. (Color online) The 3D numerical simulation in the yz -plane at $x=0$ of the displacement field u_1 (enhanced by a factor of 7000 for clarity) in the $\text{Al}_{0.6}\text{Sc}_{0.4}\text{N}$ thin-film device of Fig. 2(a) at the whole-system resonance $f_{\text{thf}} = 1.946\text{ MHz}$. The vector plot of u_1 (cyan vectors) and color plot of its magnitude u_1 from 0 (dark blue) to 15 nm (light yellow) is shown. The mode is excited by the $\text{Al}_{0.6}\text{Sc}_{0.4}\text{N}$ thin-film transducer driven by a $1\text{-}V_{pp}$ ac-voltage at the frequency $f = 1.946\text{ MHz}$. The in-plane strain $\partial_y u_{1,y} e_y$ (red vectors) generated by the transducer on the transducer-glass interface shows expansion on the left and contraction on the right side in a way that is compatible with the strain field of the whole-system resonance mode. See the animations of the modes in the supplementary material (Ref. 38).

The thin-film transduction mechanism is exemplified in Fig. 3 (and in the corresponding animation in the supplementary material³⁸) by the mode f_{thf} in the thin-film device [Fig. 2(a)]. The in-plane strain $(\partial_y u_{1,y})e_y$ on the transducer-glass interface generated by the antisymmetrically driven split-bottom-electrode thin-film transducer corresponds to an expansion on the left side and a contraction on the right side. This strain pattern is compatible with that of the whole-system resonance mode, which, therefore, is excited with a large 15-nm displacement amplitude. The resulting antisymmetric oscillatory displacement field of the glass block pushes on the water in the channel, which leads to an antisymmetric pressure wave p_1 [Fig. 2(e)] with the desired acoustofluidic properties shown in Figs. 2(f) and 2(g).

The third and last physical prerequisite is the high-quality factor of the whole system as an acoustic resonator. Because the thin-film transducer in our main example constitutes only a 0.07% v/v, the quality factor is completely dominated by that of the glass block, which has a high value, $Q \sim 10^3$, in a typical glass.³⁹

B. The robustness of the device to the material, thickness, and quality factor of the thin-film transducer

The above thin-film transduction method implies that the functionality of the thin-film acoustofluidic device is robust to changes in several characteristic properties of the thin-film transducer, essentially because of its small volume fraction of the whole system. In the following, we study three such properties, namely, the material, thickness, and quality factor of the thin-film transducer.

We simulate three types of PZE materials. One is the commonly used PZT, having large PZE coefficients. One drawback of this material is its lead content, which is being out-phased for health and environmental reasons, and another is the difficulty in fabricating the material with a sufficiently low dissipation. Whereas other materials have

lower PZE coefficients than PZT, they may be fabricated with higher purity and less dissipation. The lead-free AlN is a choice for its simpler and better well-controlled high-quality depositing on a variety of substrates, which allows for higher break-down voltages that may compensate for the lower PZE coefficient. $\text{Al}_{1-x}\text{Sc}_x\text{N}$ offers a PZE coefficient between the values of PZT and AlN with many of the same advantages as AlN, but it has a more complex fabrication process and alower break-down voltage.

In the first three columns of Table I, the simulation results of these different PZE materials are listed, while keeping all other quantities fixed in the model: AlN, $\text{Al}_{0.6}\text{Sc}_{0.4}\text{N}$, and PZT Pz26, and maintaining this order when referring to the numerical results in the following. In spite of the very different material parameters listed in Table SII of the supplemental material,³⁸ the resulting acoustofluidic response of the main resonance f_{thf} is nearly the same shape-wise, and only the amplitudes vary. Within 0.3%, the resonance frequencies are identical, $f_{\text{thf}} = 1.948, 1.946,$ and 1.942 Mz, whereas the field amplitudes reflect the difference in the PZE coefficients and are for the pressure $|p_1| = 0.44, 1.20,$ and 3.50 MPa, the displacement $|u_1| = 5.1, 15,$ and 38 nm, and the acoustic energy density $E_{\text{ac}}^{\text{fl}} = 7.3, 72,$ and 2.1×10^3 J m^{-3} . Besides the obvious difference in the amplitude, the computed whole-system resonance is nearly the same in all three cases, showing a nearly ideal antisymmetric pressure wave in the microchannel. This is also reflected in the last two rows of Table I, which show how well the scaling laws $t_{\text{foc}}^{-1} \propto E_{\text{ac}}^{\text{fl}} \propto e_{31,f}^2$ are obeyed in the three cases.

The thin-film device is also insensitive to the quality factor of the thin-film transducer, which, in terms of the damping coefficient Γ_{sl} in the Cauchy equation (5), is given by $Q = \frac{1}{2} \Gamma_{\text{sl}}^{-1}$. For two reasons, we expect a weak dependency on Q . The tiny volume of the transducer implies that the Q -factor of the system is completely dominated by that of the glass block. Consequently, as the transduction mechanism does not rely on the resonance properties of the thin-film transducer, the strong Q -dependence that is usually associated with the resonant modes in the transducer is absent. The simulation results shown in Fig. 4 confirm this expectation. Here, the acoustic energy density $E_{\text{ac}}^{\text{fl}}$ in the microchannel of the thin-film device [Fig. 2(a)] at the resonance $f_{\text{thf}} = 1.946$ MHz is shown as a function of Q from the original value of 1000 down to an appalling low value of 5. The resonant behavior reflected in $E_{\text{ac}}^{\text{fl}}(f)$ is maintained, and the change in Q by a factor of 200 results in a drop of the peak value of $E_{\text{ac}}^{\text{fl}}$ by a factor of only 2, from 72 to 40 J m^{-3} .

Finally, the simulation results in Fig. 4 also show that the main resonance mode f_{thf} is maintained when changing the thickness by a factor of 3.5 from $H_{\text{thf}} = 1$ to 3.5 μm , numbers typical for the current AlN and $\text{Al}_{1-x}\text{Sc}_x\text{N}$ thin-film fabrication technology. The amplitude of the resonance peak in $E_{\text{ac}}^{\text{fl}}$ is nearly constant (72 ± 1) J m^{-3} from the thinnest to thickest film.

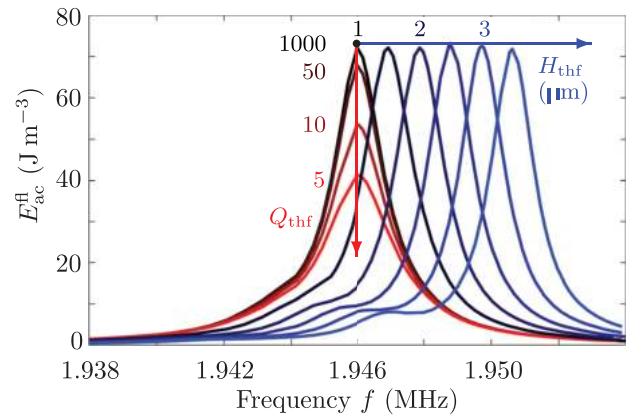


FIG. 4. (Color online) The 3D simulations of the acoustic energy density $E_{\text{ac}}^{\text{fl}}$ of the resonance mode for the system shown in Fig. 2(a) versus the frequency from 1.938 to 1.954 MHz as a function of the thin-film Q -factor Q_{thf} , decreasing from 1000, 50, and 10 to 5 (red arrow), and as a function of the thin-film thickness H_{thf} , increasing from 1 to 3.5 μm in steps of 0.5 μm (blue arrow).

C. Enhancing the acoustic response of the device by shaping the electrodes of the thin-film transducer

Thin-film transducers are fabricated by standard micro-fabrication deposition techniques, and this implies several distinct advantages. The lateral shape of the transducer or its electrode can be chosen freely by photolithography techniques; the attachment of the transducer to the glass chip is reproducible, stable, and strong, and the less controlled use of glue, known from standard bulk-transducer technology,⁴⁶ is avoided. Commercially, microfabrication techniques open up for volume production with relatively cheap unit prices, a necessary prerequisite for widespread single-use applications in biotechnology and medicine, where the cross-contamination arising from the multiple use of the same device is a no go.

An illustrative example of how the shape of the metal electrodes on the surface of the thin-film transducer may enhance the acoustic response is shown in Fig. 5. Here, the thin-film device of Fig. 2(a) is used as a starting point, but instead of the split-bottom electrode used for antisymmetric excitations, the bottom electrode is used for symmetric excitations in the three different cases of Figs. 5(a)–5(c), keeping all other parameters fixed: (a) an un-split electrode, (b) a large-gap split electrode, and (c) a two-gap split electrode. The aim is to excite with varying strength the symmetric full-wavelength-like pressure mode having two vertical nodal planes, which obeys the symmetry condition $p_1(x, -y, z) = p_1(x, y, z)$. Indeed, such a symmetric whole-system resonance is located at $f = 3.578$ MHz as shown in Figs. 5(d)–5(g). As listed in Fig. 5(h), the strength of the mode depends on the electrode design. By reducing the electrode coverage from 100% in case (a) to 33% in case (b), the acoustic energy density can be increased by a factor of 2. Another factor of 2 is obtained by having the 49% electrode coverage of case (c), which includes an excitation voltage of $+\varphi_0$ on the outer electrodes and $-\varphi_0$ on the center electrode.

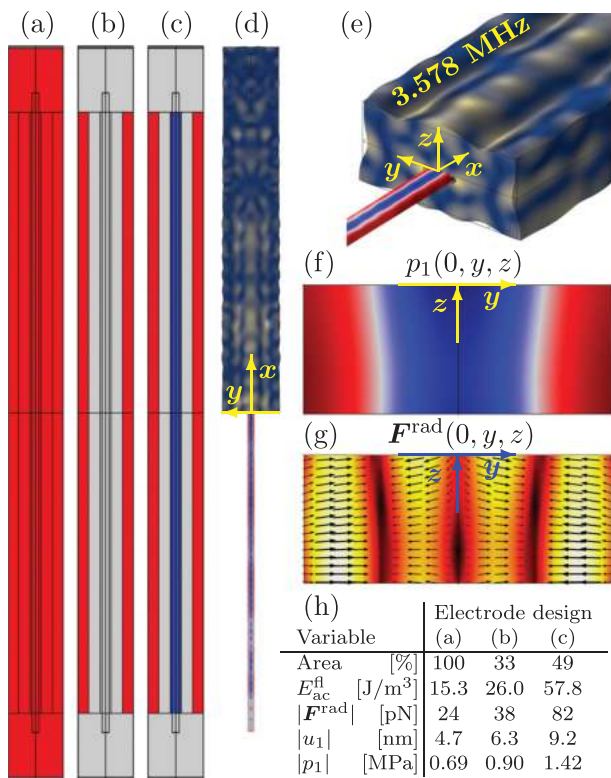


FIG. 5. (Color online) Simulations of the device in Fig. 2(a) but now exciting the symmetric full-wave-like resonance mode at $f = 3.578$ MHz. [(a)–(c)] Three designs of a symmetric bottom electrode for exciting this mode, where red is actuated by $\varphi = +\varphi_0$, blue is actuated by $\varphi = -\varphi_0$, and gray marks no electrode. The top electrode is grounded, $\varphi = 0$. [(d)–(g)] The 3D simulations of u_1 , p_1 , and F^{rad} in the device with electrode design (c) using the same plot format as in Fig. 2 but with the color scales given in (h), together with the acoustic energy density E_{ac} and the area (in %) covered by the bottom electrode for all three electrode designs. See the supplementary material for animations of the resonance mode in all three cases (Ref. 38).

The explanation of this result is found in the spatial form of the whole-system resonance mode. By inspection, we see that the displacement field at the glass-transducer interface forms a wave with in-plane contractions and expansions. The PZE coefficient e_{31f} in the transducer implies the presence of an electric field with a vertical component that changes sign along the in-plane direction. This tendency is counteracted by the fully covering bottom electrode, which imposes a unidirectional electrical field. Consequently, by removing the central part of the bottom electrode (or adding the anti-phase central part), this constraining boundary condition is relaxed (or changed into a supporting condition) while the remaining side parts of the electrode are still capable of exciting the whole-system resonance mode. This example offers a glimpse of the opportunities for design improvements by performing a shape optimization of the electrodes or perhaps the entire thin-film transducer.

D. Spatially regular modes in the thin-film device

Intuitively, the simplicity of the thin-film device consisting essentially of just a glass block should lead to simpler

modes with regular spatial dependencies. As mentioned above, the presence of a bulky PZT transducer leads to the excitation of whole-system resonance modes with a more irregular wave pattern in the displacement fields. Also, experimentally, this has been observed as hot spots in the pressure field along an otherwise perfectly shaped rectangular microchannel.³⁶

In Fig. 6(a), we show six different whole-system resonance modes at lower frequencies near 1 MHz in a thin-film device with a $1\text{-}\mu\text{m}$ -thick split-bottom-electrode AlN thin-film transducer mounted on the bottom of a rectangular Schott D263 glass block (Schott Suisse SA, Yverdon, Switzerland) of length $L_{sl} = 45$ mm, width $W_{sl} = 2.8$ mm, and height $H_{sl} = 1.4$ mm. The microchannel of the system has length $L_n = 40$ mm, width (at its top) $W_n = 0.43$ mm, and height $H_n = 0.15$ mm. To mimic the shape obtained by the isotropic etching in the glass, the side walls are modeled as quarter circles as shown in Fig. 6(b). The quarter circles increase the resonance frequency, but by increasing the channel width, we maintain a usual half-wave-like resonance mode close to 2 MHz as in Fig. 2(a). The frequencies of the resonance modes near 1 MHz are far from this 2 MHz and, thus, we would not expect these modes to be very strong. However, a clear spectrum with well-separated resonance

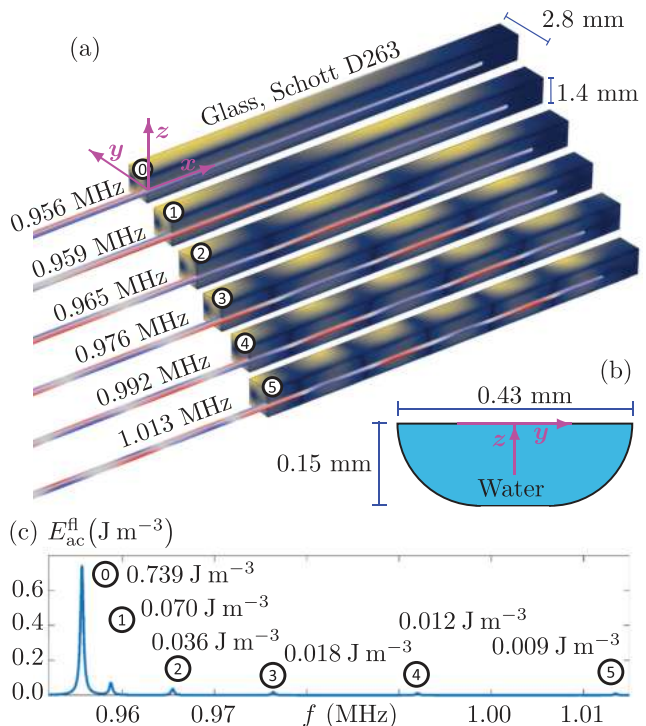


FIG. 6. (Color online) The simulation of the low-frequency modes near 1 MHz in a thin-film device with a $1\text{-}\mu\text{m}$ -thick split-bottom-electrode AlN thin-film transducer. The system is symmetric around the vertical center plane at $x = 0$ and antisymmetric around the vertical center plane at $y = 0$. (a) The lowest six resonance modes $n = 0, 1, \dots, 5$ with $2n$ nodal planes along the x axis and one nodal plane along the y axis. The plot format is the same as in Fig. 2(a). (b) The cross-sectional shape of the microchannel in the vertical yz -plane. (c) The acoustic energy density spectrum $E_{ac}^{fl}(f)$ identifying the six resonance modes. See the supplementary material for animations of the six resonance modes (Ref. 38).

modes appears as shown in Fig. 6(c), yet another example of whole-system resonances excited by the thin-film transducer.

The antisymmetric actuation of the split-bottom electrode, combined with the geometrical symmetry, dictates that the system is symmetric around the vertical plane, at $x=0$, across the device, and antisymmetric around the vertical plane, at $y=0$, along the device. In Fig. 6(a), one immediately notices the spatial regularity of both the displacement field u_1 and pressure field p_1 in the six displayed modes. Both fields have the required symmetry along the x axis and anti-symmetry along the y axis, and both fields exhibit one nodal plane along the transverse y direction and, respectively, $2n$ nodal planes with $n = 0, 1, 2, \dots, 5$ along the axial x direction. In Fig. 6(c), the spectrum $E_{ac}^{fl}(f)$ in the frequency range from 0.952 to 1.015 MHz is shown, which allows for the identification of the six resonance frequencies $f_{n,1,0}$, where the indices refer to the number of nodal planes in each direction. Of the six modes, the $n=0$ -mode without nodes along the x axis has an axial structure that matches the x -independent voltage boundary condition better than the other modes, and indeed it has the highest energy density. As the number n of x axis nodes increases, the corresponding mode exhibits an increasing number of nodes and, hence, an increasing mismatch with the x -independent voltage boundary condition. This explains the monotonically decreasing peak value of E_{ac}^{fl} for the increasing values of n shown in Fig. 6(b).

E. Device sensitivity to breaking of geometrical symmetries

As a final point, we discuss the consequences of breaking the perfect anti-symmetry of the thin-film device imposed in Figs. 2, 3, and 6. Using the microfabrication techniques, many geometrical features can be defined with accuracies down between 1 and 10 μm ; however, it can be problematic to reach such accuracies when dicing up a full-sized wafer into the individual devices. For microelectronics, this is not problematic if the integrated circuits are sufficiently removed from the edges. However, for acoustofluidic devices, the whole substrate influences the whole-system resonances. For this reason, it is interesting to investigate the sensitivity of a

given acoustofluidic device given shifts in the position of the microchannel relative to the edges of the substrate.

In Fig. 7, we study the acoustic response to a shift in the center axis of the microchannel in the thin-film device of Fig. 2(a) from the ideal symmetric position at $y=0$ to 50 and 100 μm . The whole-system-resonance mode is not degraded significantly by this shift, which adds to the robustness in the experimental applications. A contributing factor to this robustness is that the water-filled channel only constitutes 1.2% of the total volume of the device. We notice that the main antisymmetric form of the acoustic pressure is largely unaffected by the shift, and the acoustic energy density E_{ac}^{fl} remains high in the range from 55 to 78 J m^{-3} . However, as the shift increases, more pronounced axial inhomogeneities develop. Such inhomogeneities may imply a degradation in the functionality for stop-flow applications; however, as is well known experimentally from the measurements on several acoustofluidic devices in flow-through applications, such axial inhomogeneities averages out, and the device would work essentially without degradation.²⁰

V. CONCLUSION AND OUTLOOK

In this paper, based on a well-tested and experimentally validated numerical model,^{23,34,35} we have shown by 3D numerical simulations in Sec. III, including Fig. 2 and Table I, that bulk glass chips with integrated PZE thin-film transducers constituting less than 0.1% v/v of the device have an acoustofluidic response on par with that obtained in a conventional silicon-glass device actuated by a PZT transducer, quantified by E_{ac}^{fl} , R , and t_{foc} . The analysis in Sec. IV A demonstrated that the ability of the thin-film transducer to induce the desired acoustofluidic response in a bulk device relies on three physical aspects of the system: the in-plane-expansion of the thin-film transducer under the action of the orthogonal applied electric field, the acoustic whole-system resonances of the device, and the high Q -factor of the elastic solid, constituting the bulk part of the device.

We have pointed out some of the advantages of using thin-film transducers. Among them is the low sensitivity of the thin-film device to the material, thickness, and quality

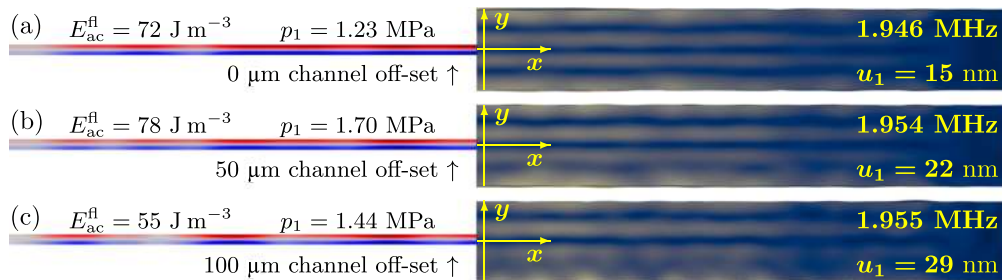


FIG. 7. (Color online) (a) The resonance mode at $f = 1.946 \text{ MHz}$ of the device shown in Fig. 2(a), and using the same plot format, with the acoustic energy density $E_{ac} = 72 \text{ J m}^{-3}$ and maximum pressure amplitude $p_1 = \pm 1.23 \text{ MPa}$ in the fluid, and maximum displacement amplitude $u_1 = 15 \text{ nm}$ in the solid. (b) The same as that in (a) but with the channel offset 50 μm in the y direction and with resonance frequency $f = 1.954 \text{ MHz}$, $E_{ac} = 78 \text{ J m}^{-3}$, $p_1 = \pm 1.70 \text{ MPa}$, and $u_1 = 22 \text{ nm}$. (c) The same as that in (a) but with the channel offset by 100 μm in the y direction and with resonance frequency $f = 1.955 \text{ MHz}$, $E_{ac} = 55 \text{ J m}^{-3}$, $p_1 = \pm 1.44 \text{ MPa}$, and $u_1 = 29 \text{ nm}$. See the supplementary material for animations of the three resonance modes (Ref. 38).

factor of the thin-film transducer discussed in Sec. IV B. Another advantage is that thin-film devices can be produced by clean-room microfabrication techniques, similar to the ones employed in the fabrication of surface acoustic waves. These techniques make it possible to shape the transducer electrodes, and in Sec. IV C, we discussed how to exploit this design freedom to boost the acoustofluidic response in the example of Fig. 5 by a factor of 4 by carefully shaping the transducer electrodes and reducing their area. We have also exploited the advantage of the microfabrication techniques that the thin-film transducers are integrated in the devices without involving the use of glue or glycerol coupling layers, which are used in the conventional bulk-transducer technique, although they are hard to control and often result in diminished reproducibility.

The performance of the thin-film and bulk-PZT bulk devices have been compared on equal footing using the same model approach and the same assumptions on damping and lack of clamping. More accurate simulation predictions for both types of devices would require better knowledge of the material parameters, the actual damping mechanisms in all elements of the devices, and modeling of the specific clamping and tubing of the device to the measurement setup. The influence of these factors on the functionality of especially the thin-film device will be part of future studies in close collaboration with experimental colleagues.

In an application perspective, the use of thin-film transducers offers new possibilities in the field of acoustofluidics. The fact that the thin-film transducer constitutes such a low volume fraction implies not only that the device is relatively insensitive to the quality of the thin film but also that the core part of the acoustofluidic system, namely, the microchannel, constitutes a relatively larger part of the system and is, thus, easier to control. The AlN-based thin-film transducers can be fabricated with high breakdown voltages (~ 20 V/ μm), which more than compensates for its lower coupling coefficient e_{31f} , and lower the dissipation and heat production.

We hope that this theoretical analysis will inspire our experimental colleagues in the field to investigate the new application aspects offered by the thin-film acoustofluidic devices.

ACKNOWLEDGMENTS

This work was supported by the *BioWings* project funded by the European Union's Horizon 2020 *Future and Emerging Technologies* (FET) programme Grant No. 801267.

¹A. Lenshof, C. Magnusson, and T. Laurell, "Acoustofluidics 8: Applications in acoustophoresis in continuous flow microsystems," *Lab Chip* **12**, 1210–1223 (2012).

²M. Gedge and M. Hill, "Acoustofluidics 17: Surface acoustic wave devices for particle manipulation," *Lab Chip* **12**, 2998–3007 (2012).

³E. K. Sackmann, A. L. Fulton, and D. J. Beebe, "The present and future role of microfluidics in biomedical research," *Nature* **507**(7491), 181–189 (2014).

⁴T. Laurell and A. Lenshof, eds., *Microscale Acoustofluidics* (Royal Society of Chemistry, Cambridge, UK, 2015).

⁵M. Antfolk and T. Laurell, "Continuous flow microfluidic separation and processing of rare cells and bioparticles found in blood—A review," *Anal. Chim. Acta* **965**, 9–35 (2017).

⁶P. Ohlsson, M. Evander, K. Petersson, L. Mellhammar, A. Lehmusvuori, U. Karhunen, M. Soikkeli, T. Seppa, E. Tuunainen, A. Spangar, P. von Lode, K. Rantakokko-Jalava, G. Otto, S. Scheduling, T. Soukka, S. Wittfooth, and T. Laurell, "Integrated acoustic separation, enrichment, and microchip polymerase chain reaction detection of bacteria from blood for rapid sepsis diagnostics," *Anal. Chem.* **88**(19), 9403–9411 (2016).

⁷P. Augustsson, C. Magnusson, M. Nordin, H. Lilja, and T. Laurell, "Microfluidic, label-free enrichment of prostate cancer cells in blood based on acoustophoresis," *Anal. Chem.* **84**(18), 7954–7962 (2012).

⁸R. Zmijan, U. S. Jonnalagadda, D. Carugo, Y. Kochi, E. Lemm, G. Packham, M. Hill, and P. Glynne-Jones, "High throughput imaging cytometer with acoustic focussing," *RSC Adv.* **5**(101), 83206–83216 (2015).

⁹M. Ohlin, I. Iranmanesh, A. E. Christakou, and M. Wiklund, "Temperature-controlled mpa-pressure ultrasonic cell manipulation in a microfluidic chip," *Lab Chip* **15**(16), 3341–3349 (2015).

¹⁰P. Thevoz, J. D. Adams, H. Shea, H. Bruus, and H. T. Soh, "Acoustophoretic synchronization of mammalian cells in microchannels," *Anal. Chem.* **82**(7), 3094–3098 (2010).

¹¹D. J. Collins, B. Morahan, J. Garcia-Bustos, C. Doerig, M. Plebanski, and A. Neild, "Two-dimensional single-cell patterning with one cell per well driven by surface acoustic waves," *Nat. Commun.* **6**, 8686 (2015).

¹²F. Guo, Z. Mao, Y. Chen, Z. Xie, J. P. Lata, P. Li, L. Ren, J. Liu, J. Yang, M. Dao, S. Suresh, and T. J. Huang, "Three-dimensional manipulation of single cells using surface acoustic waves," *Proc. Natl. Acad. Sci. U.S.A.* **113**(6), 1522–1527 (2016).

¹³P. Augustsson, J. T. Karlsen, H.-W. Su, H. Bruus, and J. Voldman, "Iso-acoustic focusing of cells for size-insensitive acousto-mechanical phenotyping," *Nat. Commun.* **7**, 11556 (2016).

¹⁴G. Sitters, D. Kamsma, G. Thalhammer, M. Ritsch-Marte, E. J. G. Peterman, and G. J. L. Wuite, "Acoustic force spectroscopy," *Nat. Meth.* **12**(1), 47–50 (2015).

¹⁵B. W. Drinkwater, "Dynamic-field devices for the ultrasonic manipulation of microparticles," *Lab Chip* **16**, 2360–2375 (2016).

¹⁶D. J. Collins, C. Devendran, Z. Ma, J. W. Ng, A. Neild, and Y. Ai, "Acoustic tweezers via sub-time-of-flight regime surface acoustic waves," *Sci. Adv.* **2**(7), e1600089 (2016).

¹⁷H. G. Lim, Y. Li, M.-Y. Lin, C. Yoon, C. Lee, H. Jung, R. H. Chow, and K. K. Shung, "Calibration of trapping force on cell-size objects from ultrahigh-frequency single-beam acoustic tweezer," *IEEE Trans. Ultrason. Ferr.* **63**(11), 1988–1995 (2016).

¹⁸D. Baresch, J.-L. Thomas, and R. Marchiano, "Observation of a single-beam gradient force acoustical trap for elastic particles: Acoustical tweezers," *Phys. Rev. Lett.* **116**, 024301 (2016).

¹⁹B. Hammarström, B. Nilsson, T. Laurell, J. Nilsson, and S. Ekström, "Acoustic trapping for bacteria identification in positive blood cultures with MALDI-TOF MS," *Anal. Chem.* **86**(21), 10560–10567 (2014).

²⁰A. Lenshof, M. Evander, T. Laurell, and J. Nilsson, "Acoustofluidics 5: Building microfluidic acoustic resonators," *Lab Chip* **12**, 684–695 (2012).

²¹P. Reichert, D. Deshmukh, L. Lebovitz, and J. Dual, "Thin film piezoelectrics for bulk acoustic wave (BAW) acoustophoresis," *Lab Chip* **18**(23), 3655–3667 (2018).

²²R. P. Moiseyenko and H. Bruus, "Whole-system ultrasound resonances as the basis for acoustophoresis in all-polymer microfluidic devices," *Phys. Rev. Appl.* **11**, 014014 (2019).

²³W. N. Bodé, L. Jiang, T. Laurell, and H. Bruus, "Microparticle acoustophoresis in aluminum-based acoustofluidic devices with PDMS covers," *Micromachines* **11**(3), 292 (2020).

²⁴M. Dubois and P. Muralt, "Properties of aluminum nitride thin films for piezoelectric transducers and microwave filter applications," *Appl. Phys. Lett.* **74**(20), 3032–3034 (1999).

²⁵A. De Pastina, D. Maillard, and L. Villanueva, "Fabrication of suspended microchannel resonators with integrated piezoelectric transduction," *Microelectron. Eng.* **192**, 83–87 (2018).

²⁶G. Piazza, P. J. Stephanou, and A. P. Pisano, "Piezoelectric aluminum nitride vibrating contour-mode MEMS resonators," *J. Microelectromech. Syst.* **15**(6), 1406–1418 (2006).

- ²⁷U. Zaghoul and G. Piazza, "Highly scalable NEMS relays with stress-tuned switching voltage using piezoelectric buckling actuators," *IEEE Trans. Electron. Dev.* **61**(10), 3520–3528 (2014).
- ²⁸N. Sinha, G. E. Wabiszewski, R. Mahameed, V. V. Felmetzger, S. M. Tanner, R. W. Carpick, and G. Piazza, "Piezoelectric aluminum nitride nanoelectromechanical actuators," *Appl. Phys. Lett.* **95**(5), 053106 (2009).
- ²⁹R. H. Olsson III, K. E. Wojciechowski, M. S. Baker, M. R. Tuck, and J. G. Fleming, "Post-CMOS-compatible aluminum nitride resonant MEMS accelerometers," *J. Microelectromech. Syst.* **18**(3), 671–678 (2009).
- ³⁰H. Zhang, W. Pang, H. Yu, and E. S. Kim, "High-tone bulk acoustic resonators on sapphire, crystal quartz, fused silica, and silicon substrates," *J. Appl. Phys.* **99**(12), 124911 (2006).
- ³¹J. Masson, G. Martin, R. Boudot, Y. Gruson, S. Ballandras, A. Artieda, P. Muralt, B. Belgacem, and L. Chomeloux, "On the dispersive behaviour of AlN/Si high overtone bulk acoustic resonators," in *2007 IEEE International Frequency Control Symposium Joint with the 21st European Frequency and Time Forum* (2007), pp. 741–744.
- ³²T. Fujikura, O. Matsuda, D. M. Profunser, O. B. Wright, J. Masson, and S. Ballandras, "Real-time imaging of acoustic waves on a bulk acoustic resonator," *Appl. Phys. Lett.* **93**(26), 261101 (2008).
- ³³R. Ruby, "The 'how & why' a deceptively simple acoustic resonator became the basis of a multi-billion dollar industry," in *2017 IEEE 30th International Conference on Micro Electro Mechanical Systems (MEMS)* (2017), pp. 308–313.
- ³⁴N. R. Skov, J. S. Bach, B. G. Winckelmann, and H. Bruus, "3D modeling of acoustofluidics in a liquid-filled cavity including streaming, viscous boundary layers, surrounding solids, and a piezoelectric transducer," *AIMS Math.* **4**, 99–111 (2019).
- ³⁵N. R. Skov, P. Sehgal, B. J. Kirby, and H. Bruus, "Three-dimensional numerical modeling of surface-acoustic-wave devices: Acoustophoresis of micro- and nanoparticles including streaming," *Phys. Rev. Appl.* **12**, 044028 (2019).
- ³⁶P. Augustsson, R. Barnkob, S. T. Wereley, H. Bruus, and T. Laurell, "Automated and temperature-controlled micro-PIV measurements enabling long-term-stable microchannel acoustophoresis characterization," *Lab Chip* **11**(24), 4152–4164 (2011).
- ³⁷J. S. Bach and H. Bruus, "Theory of pressure acoustics with viscous boundary layers and streaming in curved elastic cavities," *J. Acoust. Soc. Am.* **144**, 766–784 (2018).
- ³⁸See supplementary material at <https://www.scitation.org/doi/suppl/10.1121/10.0005624> for details on the values of the material parameters, focus time t_{foc} , and animations of the resonance modes.
- ³⁹P. Hahn and J. Dual, "A numerically efficient damping model for acoustic resonances in microfluidic cavities," *Phys. Fluids* **27**, 062005 (2015).
- ⁴⁰L. P. Gorkov, "On the forces acting on a small particle in an acoustical field in an ideal fluid," *Sov. Phys.-Dokl.* **6**(9), 773–775 (1962) [Dokl. Akad. Nauk SSSR **140**, 88–91 (1961)].
- ⁴¹M. Settnes and H. Bruus, "Forces acting on a small particle in an acoustical field in a viscous fluid," *Phys. Rev. E* **85**, 016327 (2012).
- ⁴²R. Barnkob, P. Augustsson, T. Laurell, and H. Bruus, "Measuring the local pressure amplitude in microchannel acoustophoresis," *Lab Chip* **10**(5), 563–570 (2010).
- ⁴³P. B. Muller, M. Rossi, A. G. Marin, R. Barnkob, P. Augustsson, T. Laurell, C. J. Kähler, and H. Bruus, "Ultrasound-induced acoustophoretic motion of microparticles in three dimensions," *Phys. Rev. E* **88**(2), 023006 (2013).
- ⁴⁴A. G. Steckel, H. Bruus, P. Muralt, and R. Matloub, "Fabrication, characterization, and simulation of glass devices with AlN thin-film transducers for excitation of ultrasound resonances," *Phys. Rev. Appl.* **16**, 014014 (2021).
- ⁴⁵COMSOL Multiphysics 5.4 (2018), available at <http://www.comsol.com> (Last viewed 16 June 2021).
- ⁴⁶W. N. Bodé and H. Bruus, "Numerical study of the coupling layer between transducer and chip in acoustofluidic devices," *J. Acoust. Soc. Am.* **149**(5), 3096–3105 (2021).

Supplementary material: Numerical study of bulk acoustofluidic devices driven by thin-film transducers and whole-system resonance modes

André G. Steckel^{1, a)} and Henrik Bruus^{1, b)}

*Department of Physics, Technical University of Denmark,
DTU Physics Building 309, DK-2800 Kongens Lyngby, Denmark*

(Dated: 16 May 2021)

S1. MATERIAL PARAMETERS

The devices modeled in the main manuscript consists of water, one of two types of glass, and one of three types of piezoelectric transducer.

The parameters for water are taken from Muller and Bruus,¹ where each parameter is given as a fifth-order polynomial in the temperature. In this work we use the values computed for 25 °C as listed in Table S1.

TABLE S1. Parameter values of water at 25 °C used in the numerical simulations.¹

Parameter	Value	Parameter	Value
ρ_{fl}	997 kg m ⁻³	$\eta_{\text{fl}}^{\text{b}}$	2.485 mPa s
c_{fl}	1497 m s ⁻¹	Γ_{fl}	10.3 THz ⁻¹ f
κ_{fl}	448 TPa ⁻¹	η_{fl}	0.890 mPa s

The parameter values used for the solids in the devices are listed in Table S2. For each type of piezoelectric material we list the density ρ_{sl} , the damping coefficient Γ_{sl} , and the nonzero values for the elastic constants C_{ik} , the piezoelectric coupling constants e_{ik} , and dielectric constants ϵ_{ik} . For each type of glass we list the density ρ_{sl} , the damping coefficient Γ_{sl} , and the nonzero values for the elastic constants C_{ik} . Moreover, we supplement these values with the values of Young's modulus E , Poisson's ratio s , the longitudinal sound speed c_{lo} , and the transverse sound speed c_{tr} , related as follows:

$$C_{11} = \rho c_{\text{lo}}^2 = \frac{1-s}{(1+s)(1-2s)} E, \quad (1a)$$

$$C_{44} = \rho c_{\text{tr}}^2 = \frac{1}{2(1+s)} E. \quad (1b)$$

A PZE film behave different from its bulk counterpart as the film is free to expand in the perpendicular

TABLE S2. Parameters of the solids at 25 °C used in the numerical simulations. ϵ_0 is the vacuum permittivity, and for the two glasses is listed the Young's modulus E , the Poisson ratio s , and the longitudinal c_{lo} and transverse c_{tr} sound speeds. For glass $C_{44} = \frac{1}{2}(C_{11} - C_{12})$, and all PZE in this work have $C_{66} = \frac{1}{2}(C_{11} - C_{12})$.

Parameter	Value	Parameter	Value
<i>Thin-film aluminum nitride, AlN²⁻⁴</i>			
ρ_{sl}	3300 kg m ⁻³	Γ_{sl}	0.0005
C_{11}	410.2 GPa	C_{33}	385.0 GPa
C_{12}	142.4 GPa	C_{44}	122.9 GPa
C_{13}	110.1 GPa	C_{66}	133.9 GPa
$e_{31,f}$	-1.05 C m ⁻²	e_{15}	-0.39 C m ⁻²
e_{33}	1.46 C m ⁻²	Γ_{ϵ}	0.0005
ϵ_{11}	9 ϵ_0	ϵ_{33}	11 ϵ_0
<i>Thin-film aluminum scandium nitride, Al_{0.6}Sc_{0.4}N^{2,4}</i>			
ρ_{sl}	3300 kg m ⁻³	Γ_{sl}	0.0005
C_{11}	313.8 GPa	C_{33}	197.1 GPa
C_{12}	150.0 GPa	C_{44}	108.6 GPa
C_{13}	139.2 GPa	C_{66}	81.9 GPa
$e_{31,f}$	-2.65 C m ⁻²	e_{15}	-0.32 C m ⁻²
e_{33}	2.73 C m ⁻²	Γ_{ϵ}	0.0005
ϵ_{11}	22 ϵ_0	ϵ_{33}	22 ϵ_0
<i>Bulk and thin-film lead zirconium titanate, PZT⁵</i>			
ρ_{sl}	7700 kg m ⁻³	Γ_{sl}	0.005
C_{11}	168 GPa	C_{33}	123 GPa
C_{12}	110 GPa	C_{44}	30.1 GPa
C_{13}	99.9 GPa	C_{66}	29.0 GPa
$e_{31,f}$	-14.7 C m ⁻²	e_{31}	-2.8 C m ⁻²
e_{33}	14.7 C m ⁻²	e_{15}	9.86 C m ⁻²
ϵ_{11}	828 ϵ_0	ϵ_{33}	700 ϵ_0
<i>Glass, Schott D263⁶</i>			
ρ_{sl}	2510 kg m ⁻³	Γ_{ϵ}	0.005
E	72.9 GPa	s	0.208
C_{11}	81.8 GPa	C_{44}	30.2 GPa
C_{12}	21.5 GPa	Γ_{sl}	0.0004
c_{lo}	5710 m s ⁻¹	c_{tr}	3467 m s ⁻¹
<i>Glass, Pyrex^{7,8}</i>			
ρ_{sl}	2230 kg m ⁻³	s	0.20
E	62.8 GPa	C_{44}	26.2 GPa
C_{11}	69.8 GPa	Γ_{sl}	0.0004
C_{12}	17.4 GPa	c_{tr}	3425 m s ⁻¹
c_{lo}	5594 m s ⁻¹		
<i>Silicon substrate^{8,9}</i>			
ρ_{sl}	2329 kg m ⁻³	Γ_{sl}	0.0001
C_{11}	165.7 GPa	C_{44}	79.6 GPa
C_{12}	63.9 GPa		

a) angust@fysik.dtu.dk

b) bruus@fysik.dtu.dk

TABLE S3. Parameter values used in the numerical simulations for 5- μm -diameter polystyrene tracer particles suspended in water. The values are from Ref. 12, from which the scattering coefficients f_0 and f_1 are computed using the particle radius $a = 2.5 \mu\text{m}$.

Parameter	symbol	Value
Density	ρ_{ps}	1050 kg m^{-3}
Compressibility	κ_{ps}	249 TPa
Poisson's ratio	ν_{ps}	0.35
Speed of sound at 20°C	c_{ps}	2350 ms^{-1}
Monopole coefficient, Eq. (10c)	f_0	0.44
Dipole coefficient, Eq. (10c)	f_1	$0.034 + 0.0002i$

(z) direction. The model thus uses the effective coupling coefficient $e_{31,f}$, given by the bulk parameter e_{33} as,^{10,11}

$$e_{31,f} = e_{31} - \frac{C_{13}}{C_{33}} e_{33}. \quad (2)$$

Finally, the parameter values used for the polystyrene tracer particles in the focus time simulations are listed in Table S3.

S2. THE FOCUS TIME OF MICROPARTICLES

In this section we describe the numerical determination of the average acoustophoretic focus time t_{foc} , Eq. (11), for a dilute suspension of microparticles in the half-wave-like resonance in the thin-film and bulk-PZT devices of Fig. 2(a) and Table I. The simulation closely follows the method presented by Muller *et al.*¹³

Acoustophoretic motion of suspended microparticles is due to the acoustic radiation force and the drag force from the acoustic streaming. Due to the low Reynolds number, the inertial forces can be neglected, and the equation of motion for a single particle with velocity \mathbf{v}_p suspended in a fluid with a streaming velocity \mathbf{v}_2 is the force balance between the Stokes drag force and the acoustic radiation force, $\mathbf{v}_p(\mathbf{r}) = \mathbf{v}_2(\mathbf{r}) + \frac{1}{6\pi\eta_{\text{fl}}a} \mathbf{F}^{\text{rad}}(\mathbf{r})$.¹⁴

We use standard 5- μm -diameter polystyrene particles (radius $a = 2.5 \mu\text{m}$) as tracer particles, and their parameter values are listed in Table S3. Initially, the particles are placed in the 17 equidistant vertical cross-section planes in the mid-section of the microchannel from $x = 0$ to $\frac{1}{4}L_{\text{fl}} = 8.25 \text{ mm}$ in steps of 0.5 mm . Within each plane the particles are placed in a uniform $10 \mu\text{m} \times 10 \mu\text{m}$ square grid as shown in Fig. S1(a), no closer than $6a = 15 \mu\text{m}$ from the walls to reduce the effect of wall-particle interactions,¹² and no closer than $8a = 25 \mu\text{m}$ to the center, where the particles are to be focused. We thus consider a total of $N = 17 \times 16 \times 13 = 3,536$ particles.

The acoustic wave is turned on at time $t = 0$, and the time t_{fi} it takes a single particle starting at the initial position \mathbf{r}_i to reach the final position $\mathbf{r}_f = (x_f, y_f, z_f)$ is

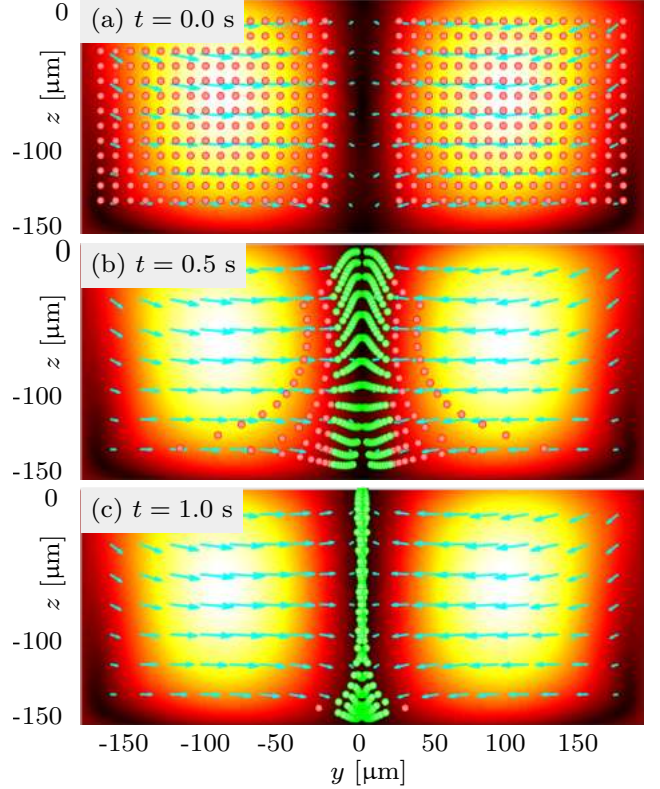


FIG. S1. The simulated acoustophoretic motion of 5- μm -diameter polystyrene particles in the center plane, $x = 0$, of the $\text{Al}_{0.6}\text{Sc}_{0.4}\text{N}$ -thin-film-driven device Fig. 2(a). The particle positions are shown at the times (a) $t = 0.0 \text{ s}$, (b) $t = 0.5 \text{ s}$, and (c) $t = 1.0 \text{ s}$. The particles are colored red before and green after reaching the center region $|y| < 8a$, where they are considered to be focused. The vectors represent the local particle speed \mathbf{v}_p , and the color plot is its magnitude from 0 (black) to $394 \mu\text{m/s}$ (white).

computed by numerical integration of $d\mathbf{r} = \mathbf{v}_p dt$,

$$\mathbf{r}_f = \mathbf{r}_i + \int_0^{t_{fi}} d\mathbf{r}(t), \quad \text{with } d\mathbf{r}(t) = \frac{\mathbf{F}^{\text{rad}}(\mathbf{r}(t))}{6\pi\eta_{\text{fl}}a} dt. \quad (3)$$

The numerical integration is performed in MATLAB. When the given particle reaches the boundary $|y| = 8a$ of the narrow region centered around the vertical nodal plane $y = 0$, it is considered to be focused, and the time t_{fi} it took to reach this point is recorded. The average focus time for the homogeneous particle distribution is therefore defined by

$$t_{\text{foc}} = \frac{1}{N} \sum_{i=1}^N t_{fi}. \quad (4)$$

The acoustophoretic focusing of the suspended microparticles is illustrated in Fig. S1 and in the corresponding

animation entitled `SuppPubmm7.gif` in the supplementary files.

S3. TIME-HARMONIC ANIMATIONS FOR FIG. 2

- `SuppPubmm1a.gif`: Time-harmonic animation of Fig. 2(a) where the magnitude of the real part of the displacement, $|\text{Re}(u_1)|$, is shown from 0 (dark blue) to 15 nm (yellow). The real part of the pressure field, $\text{Re}(p_1)$, is shown from -1.23 MPa (blue) to 1.23 MPa (red). The simulation is done for a quarter of the device by symmetry reduction, and subsequently the pressure field has been extended through mirroring of the solution anti-symmetrically in the y -direction and symmetrically in the x -direction to make the mode visible.
- `SuppPubmm1b.gif`: Time-harmonic animation of Fig. 2(c) where the magnitude of the real part of the displacement, $|\text{Re}(u_1)|$, is shown from 0 (dark blue) to 3.6 nm (yellow). The real part of the pressure field, $\text{Re}(p_1)$, is shown from -0.55 MPa (blue) to 0.55 MPa (red). The simulation is done in a symmetry-reduced half of the device, and subsequently the pressure field has been extended through mirroring of the solution symmetrically in the x -direction to make the mode visible.

S4. TIME-HARMONIC ANIMATIONS FOR FIG. 3

- `SuppPubmm2.gif`: Time-harmonic animation of Fig. 3 where the magnitude of the real part of the displacement, $|\text{Re}(u_1)|$, is shown from 0 (dark blue) to 15 nm (yellow). The real part of the displacement, $\text{Re}(u_1)$ is shown as the cyan arrows, and $\text{Re}(\partial_y u_{1,y})$ is shown as red arrows. The simulation is done for a quarter of the device by symmetry reduction, and subsequently the pressure field has been extended through mirroring of the solution anti-symmetrically in the y -direction. The displacement motion of the solid has been scaled up by a factor of 7,000 to become visible.

S5. TIME-HARMONIC ANIMATIONS FOR FIG. 5

- `SuppPubmm3a.gif`: Time-harmonic animation of Fig. 5(d) but for the electrode design shown in Fig. 5(a), where the magnitude of the real part of the displacement, $|\text{Re}(u_1)|$, is shown from 0 (dark blue) to 4.7 nm (yellow). The real part of the pressure field, $\text{Re}(p_1)$, is shown from -0.69 MPa (blue) to 0.69 MPa (red). The simulation is done in a symmetry-reduced quarter of the device. Subsequently the displacement field has been through mirroring of the solution symmetrically in the y -direction, and the pressure field has been extended through mirroring of the solution symmetrically in both the y -direction and the x -direction to make the mode visible. The displacement motion of the

solid has been scaled up by a factor of 36,000 to become visible.

- `SuppPubmm3b.gif`: Time-harmonic animation of Fig. 5(d) but for the electrode design shown in Fig. 5(b), where the magnitude of the real part of the displacement, $|\text{Re}(u_1)|$, is shown from 0 (dark blue) to 6.3 nm (yellow). The real part of the pressure field, $\text{Re}(p_1)$, is shown from -0.90 MPa (blue) to 0.90 MPa (red). The simulation is done in a symmetry-reduced quarter of the device. Subsequently the displacement field has been through mirroring of the solution symmetrically in the y -direction, and the pressure field has been extended through mirroring of the solution symmetrically in both the y -direction and the x -direction to make the mode visible. The displacement motion of the solid has been scaled up by a factor of 24,000 to become visible.
- `SuppPubmm3c.gif`: Time-harmonic animation of Fig. 5(d) but for the electrode design shown in Fig. 5(c), where the magnitude of the real part of the displacement, $|\text{Re}(u_1)|$, is shown from 0 (dark blue) to 9.2 nm (yellow). The real part of the pressure field, $\text{Re}(p_1)$, is shown from -1.42 MPa (blue) to 1.42 MPa (red). The simulation is done in a symmetry-reduced quarter of the device. Subsequently the displacement field has been through mirroring of the solution symmetrically in the y -direction, and the pressure field has been extended through mirroring of the solution symmetrically in both the y -direction and the x -direction to make the mode visible. The displacement motion of the solid has been scaled up by a factor of 16,000 to become visible.

S6. TIME-HARMONIC ANIMATIONS FOR FIG. 6

For the simulations shown in Fig. 6(a) all these simulations is of a quarter of the device, with appropriate boundary conditions, where the pressure field has been extended through mirroring of the solution symmetrically in both the y -direction and the x -direction to make the mode visible.

- `SuppPubmm4a.gif`: Time-harmonic animation of Fig. 6(a) mode (0), where the magnitude of the real part of the displacement, $|\text{Re}(u_1)|$, is shown from 0 (dark blue) to maximum (yellow). The real part of the pressure field, $\text{Re}(p_1)$, is shown from minimum in blue to maximum in red.
- `SuppPubmm4b.gif`: Time-harmonic animation of Fig. 6(a) mode (1), where the magnitude of the real part of the displacement, $|\text{Re}(u_1)|$, is shown from 0 (dark blue) to maximum (yellow). The real part of the pressure field, $\text{Re}(p_1)$, is shown from minimum in blue to maximum in red.
- `SuppPubmm4c.gif`: Time-harmonic animation of Fig. 6(a) mode (2), where the magnitude of the real

part of the displacement, $|\text{Re}(u_1)|$, is shown from 0 (dark blue) to maximum (yellow). The real part of the pressure field, $\text{Re}(p_1)$, is shown from minimum in blue to maximum in red.

- **SuppPubmm4d.gif**: Time-harmonic animation of Fig. 6(a) mode (3), where the magnitude of the real part of the displacement, $|\text{Re}(u_1)|$, is shown from 0 (dark blue) to maximum (yellow). The real part of the pressure field, $\text{Re}(p_1)$, is shown from minimum in blue to maximum in red.
- **SuppPubmm4e.gif**: Time-harmonic animation of Fig. 6(a) mode (4), where the magnitude of the real part of the displacement, $|\text{Re}(u_1)|$, is shown from 0 (dark blue) to maximum (yellow). The real part of the pressure field, $\text{Re}(p_1)$, is shown from minimum in blue to maximum in red.
- **SuppPubmm4f.gif**: Time-harmonic animation of Fig. 6(a) mode (5), where the magnitude of the real part of the displacement, $|\text{Re}(u_1)|$, is shown from 0 (dark blue) to maximum (yellow). The real part of the pressure field, $\text{Re}(p_1)$, is shown from minimum in blue to maximum in red.

S7. TIME-HARMONIC ANIMATIONS FOR FIG. 7

- **SuppPubmm5a.gif**: Time-harmonic animation of Fig. 7(a) where the magnitude of the real part of the displacement, $|\text{Re}(u_1)|$, is shown from 0 (dark blue) to 15 nm (yellow). The real part of the pressure field, $\text{Re}(p_1)$, is shown from -1.23 MPa (blue) to 1.23 MPa (red). The simulation is done in a symmetry-reduced half of the device, and subsequently the pressure field has been extended through mirroring of the solution symmetrically in the x -direction to make the mode visible.
- **SuppPubmm5b.gif**: Time-harmonic animation of Fig. 7(b) where the magnitude of the real part of the displacement, $|\text{Re}(u_1)|$, is shown from 0 (dark blue) to 22 nm (yellow). The real part of the pressure field, $\text{Re}(p_1)$, is shown from -1.70 MPa (blue) to 1.70 MPa (red). The simulation is done in a symmetry-reduced half of the device, and subsequently the pressure field has been extended through mirroring of the solution symmetrically in the x -direction to make the mode visible.
- **SuppPubmm5c.gif**: Time-harmonic animation of Fig. 7(a) where the magnitude of the real part of the displacement, $|\text{Re}(u_1)|$, is shown from 0 (dark blue) to 29 nm (yellow). The real part of the pressure field, $\text{Re}(p_1)$, is shown from -1.44 MPa (blue) to 1.44 MPa (red). The simulation is done in a symmetry-reduced half of the device, and subsequently pressure field has been extended through mirroring of the solution symmetrically in the x -direction to make the mode visible.

S8. TIME-HARMONIC ANIMATIONS FOR TABLE I

- Column one **SuppPubmm6a.gif**: Time-harmonic animation of simulation used for table I AlN results. Same dimensions as Fig. 2(a) but were the thin-film is made of AlN and actuated at 1.948 MHz. The magnitude of the real part of the displacement, $|\text{Re}(u_1)|$, is shown from 0 (dark blue) to 5.1 nm (yellow). The real part of the pressure field, $\text{Re}(p_1)$, is shown from -0.44 MPa (blue) to 0.44 MPa (red). The simulation is done for a quarter of the device by symmetry reduction, and subsequently the pressure field has been extended through mirroring of the solution anti-symmetrically in the y -direction and symmetrically in the x -direction to make the mode visible.
- Column two **SuppPubmm1a.gif**: Time-harmonic animation of Fig. 2(a) where the magnitude of the real part of the displacement, $|\text{Re}(u_1)|$, is shown from 0 (dark blue) to 15 nm (yellow). The real part of the pressure field, $\text{Re}(p_1)$, is shown from -1.23 MPa (blue) to 1.23 MPa (red). The simulation is done for a quarter of the device by symmetry reduction, and subsequently the pressure field has been extended through mirroring of the solution anti-symmetrically in the y -direction and symmetrically in the x -direction to make the mode visible.
- Column three **SuppPubmm6b.gif**: Time-harmonic animation of simulation used for table I PZT thin-film results. Same dimensions as Fig. 2(a) but were the thin-film is made of AlN and actuated at 1.948 MHz. The magnitude of the real part of the displacement, $|\text{Re}(u_1)|$, is shown from 0 (dark blue) to 71 nm (yellow). The real part of the pressure field, $\text{Re}(p_1)$, is shown from -6.26 MPa (blue) to 6.26 MPa (red). The simulation is done for a quarter of the device by symmetry reduction, and subsequently the pressure field has been extended through mirroring of the solution anti-symmetrically in the y -direction and symmetrically in the x -direction to make the mode visible.
- Column four **SuppPubmm1b.gif**: Time-harmonic animation of Fig. 2(c) where the magnitude of the real part of the displacement, $|\text{Re}(u_1)|$, is shown from 0 (dark blue) to 3.6 nm (yellow). The real part of the pressure field, $\text{Re}(p_1)$, is shown from -0.55 MPa (blue) to 0.55 MPa (red). The simulation is done for a quarter of the device by symmetry reduction, and subsequently the pressure field has been extended through mirroring of the solution symmetrically in the x -direction to make the mode visible.

- ¹P. B. Muller and H. Bruus, “Numerical study of thermoviscous effects in ultrasound-induced acoustic streaming in microchannels,” *Phys. Rev. E* **90**(4), 043016 (2014) doi: [10.1103/PhysRevE.90.043016](https://doi.org/10.1103/PhysRevE.90.043016).
- ²M. A. Caro, S. Zhang, T. Riekkinen, M. Ylilammi, M. A. Moram, O. Lopez-Acevedo, J. Molarius, and T. Laurila, “Piezoelectric coefficients and spontaneous polarization of ScAlN,” *J. Phys.-Condens. Mat.* **27**(24), 245901 (2015) doi: [10.1088/0953-8984/27/24/245901](https://doi.org/10.1088/0953-8984/27/24/245901).
- ³A. Iqbal and F. Mohd-Yasin, “Reactive sputtering of aluminum nitride (002) thin films for piezoelectric applications: A review,” *Sensors* **18**(6), 1797 (2018) doi: [10.3390/s18061797](https://doi.org/10.3390/s18061797).
- ⁴R. H. Olsson, Z. Tang, and M. D’Agati, “Doping of aluminum nitride and the impact on thin film piezoelectric and ferroelectric device performance,” in *2020 IEEE Custom Integrated Circuits Conference (CICC)* (2020), pp. 1–6, doi: [10.1109/CICC48029.2020.9075911](https://doi.org/10.1109/CICC48029.2020.9075911).
- ⁵Meggitt A/S, Porthusvej 4, DK-3490 Kvistgaard, Denmark, *Ferroperm matrix data*, <https://www.meggittferroperm.com/materials/>, accessed 2 May 2021.
- ⁶SCHOTT, SCHOTT Suisse SA, 2 Rue Galilée, Yverdon, Switzerland, *Borosilicate glass substrates*, <https://www.epfl.ch/research/facilities/cmi/wp-content/uploads/2020/05/D263T.d.pdf>, accessed 2 May 2021.
- ⁷CORNING, Houghton Park C-8, Corning, NY 14831, USA, *Glass Silicon Constraint Substrates*, <http://www.valleydesign.com/Datasheets/Corning%20Pyrex%207740.pdf>, accessed 2 May 2021.
- ⁸P. Hahn and J. Dual, “A numerically efficient damping model for acoustic resonances in microfluidic cavities,” *Physics of Fluids* **27**, 062005 (2015) doi: [10.1063/1.4922986](https://doi.org/10.1063/1.4922986).
- ⁹M. A. Hopcroft, W. D. Nix, and T. W. Kenny, “What is the Young’s modulus of silicon,” *J. Microelectromech. Syst.* **19**, 229–238 (2010) doi: [10.1109/JMEMS.2009.2039697](https://doi.org/10.1109/JMEMS.2009.2039697).
- ¹⁰P. Reichert, D. Deshmukh, L. Lebovitz, and J. Dual, “Thin film piezoelectrics for bulk acoustic wave (BAW) acoustophoresis,” *Lab Chip* **18**(23), 3655–3667 (2018) doi: [10.1039/c8lc00833g](https://doi.org/10.1039/c8lc00833g).
- ¹¹P. Muralt, J. Conde, A. Artieda, F. Martin, and M. Cantoni, “Piezoelectric materials parameters for piezoelectric thin films in ghz applications,” *Int. J. Microw. Wirel. T.* **1**(1), 19–27 (2009) doi: [10.1017/S1759078709000038](https://doi.org/10.1017/S1759078709000038).
- ¹²R. Barnkob, P. Augustsson, T. Laurell, and H. Bruus, “Acoustic radiation- and streaming-induced microparticle velocities determined by microparticle image velocimetry in an ultrasound symmetry plane,” *Phys. Rev. E* **86**, 056307 (2012) doi: [10.1103/PhysRevE.86.056307](https://doi.org/10.1103/PhysRevE.86.056307).
- ¹³P. B. Muller, R. Barnkob, M. J. H. Jensen, and H. Bruus, “A numerical study of microparticle acoustophoresis driven by acoustic radiation forces and streaming-induced drag forces,” *Lab Chip* **12**, 4617–4627 (2012) doi: [10.1039/C2LC40612H](https://doi.org/10.1039/C2LC40612H).
- ¹⁴R. Barnkob, P. Augustsson, T. Laurell, and H. Bruus, “Measuring the local pressure amplitude in microchannel acoustophoresis,” *Lab Chip* **10**(5), 563–570 (2010) doi: [10.1039/b920376a](https://doi.org/10.1039/b920376a).

5.3 Paper III: Manuscript in preparation

Numerical study of acoustic cell trapping above circular elastic membranes driven by thin-film transducers with patterned electrodes. [3]

DOI: In preparation, no DOI yet, [[PDF link](#)]

Authors: André G. Steckel and Henrik Bruus.

Remark: This version is before revisions from Henrik Bruus was received except for a few general pointers.

Journal: In preparation to be submitted.

Numerical study of acoustic trapping of cancer cells above circular elastic membranes driven by thin-film transducers with patterned electrodes

André G. Steckel^{1,*} and Henrik Bruus^{1,†}

¹*Department of Physics, Technical University of Denmark, DTU Physics Building 309, DK-2800 Kongens Lyngby, Denmark*

(Dated: 20 August 2021)

We present axisymmetric simulations showing a method for trapping breast cancer cells of the type MCF-7 in a fluid that is based on 10 micrometer sized thick membranes actuated with piezoelectric thin-film transducers and by utilizing acoustophoresis in the MHz regime. By patterning electrodes on the actuator we enable effective actuation of the higher order modes of the device giving rise to several orders of magnitude increase of the max amplitude of the acoustic radiation force. We show that when the wavelength of the n 'th order mode of the membrane is higher than the wavelength in the fluid there is a possibility for the transmitted waves to form interference patterns that gives a focus point for trapping a few wavelengths above the center point of the membrane. We show by simulations that by selecting the liquids with different properties we have a trap for capturing cancer cells in the which can be expanded into an array, and does not require a lid or scaffolding.

I. INTRODUCTION

Acoustophoresis is motion by sound and it has been used for trapping in acoustic tweezers[1–4], trapping in disposable capillary tubes[5, 6], trapping small particles by using seed particles[7–9], short and long term trapping[10, 11]. Among the different physical phenomenon that has been used to generate this trapping and focusing is standing bulk waves[12, 13], traveling bulk waves[14], standing surface acoustic waves for trapping[15], and sorting [16, 17]. In the literature there has been both examples of acoustofluidic cell trapping[2, 11] and thin-film-membrane-driven bulk acoustic wave particle handling in an acoustic cavity[18], as well as having shown that patterning of electrodes can increase the sensitivity of different modes[19] and increase the acoustofluidic action in large devices [20]. A high interests area in acoustophoresis has been to trap and focus circulating tumor cells[21–23], and one of the recent techniques for accomplishing this has been to use changes in the suspension medium tune the acoustophoretic properties of the cells[23, 24]. In general trapping of cells is of great interest[11] with many different techniques the literature[25–27]. Because of the overlap in applications to the work presented in this paper, a special highlight is necessary of the extensive analysis of both theoretical and experimental work[28, 29] in the Bessel beam for acoustic tweezers and particle manipulation.

In this work we present a numerical investigations for using electrode patterning on circular thin-film-driven-membranes to increase the higher harmonic mechanical wave solutions in the membrane for uses in acoustofluidics. The patterning used is found by looking at the out-of-phase strain pattern of the film at a higher order

membrane mode, and matching this with the electrodes. We show that the higher order membrane modes create

We also show that with the patterning presented here, the higher order membrane modes give rise to a pres-

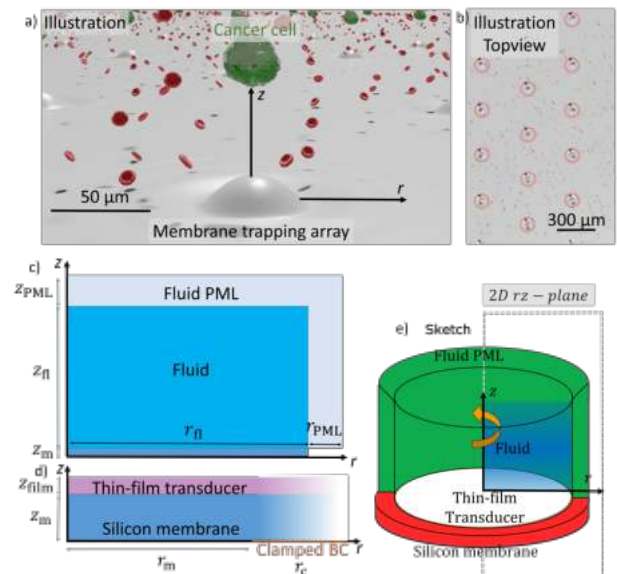


FIG. 1. (a) Artistic illustration of cancer cells being trapped by the acoustic radiation force above the an array of membranes. The cancer cells in green, red blood cells in red, and the membrane surface is all to scale, however the displacement of the membrane is imported from simulations and the displacement is scaled up by a factor of around 5000 to be visible in the illustration. (b) Same illustration as in (a) however from a topview, to show the array nature, where the individual membranes have been marked by a semitransparent red circles to highlight them. (c) Sketch of the rz -plane in the fluid with membrane, a thin-film transducer, fluid and fluid PML. (d) zoom in on the membrane and thin-film transducer, where on the right the clamping is shown. (e) sketch of axisymmetric system rotated into 3D.

* angust@fysik.dtu.dk

† bruus@fysik.dtu.dk

sure field that allows for acoustic trapping of cancer cells by tuning of suspension fluid. Possible applications is in having an array of these traps for many simultaneous levitating lid and scaffolding free acoustofluidic traps. One such theoretical use cases could be to place the trapping array in a in a Petri dish, add the fluid containing the cancer cells, activate the trap, and have cancer arrays of scaffolding-free levitating arrays of cancer cells for biological assay studies.

One of the main draw-backs of this method for trapping is the need for changing of the suspension fluid to archive trapping, as the trap will not work with small particle with positive acoustic contrast factor, one of the problems solved in the Bessel beam devices.

The design presented in this work uses a AlScN piezoelectric (PZE) thin-film with electrodes patterning in a design that is microelectromechanical system (MEMS) compatible for actuating higher order modes in the membrane. These modes send waves from their anti-nodes and the interference pattern in the pressure waves creates a pressure hotspot that enables focusing of cells with lower compressibility than the submersion fluid.

In the article the structure will be: In Section II we go through the theory and modeling necessary for simulating the device, which includes time-harmonic perturbation theory, elastomechanical theory, pressure acoustics, time-averaged second order fields, boundary conditions, and the numerical implementation. In Section III, we go through the first part of the results of the paper, where we show effect of patterning the electrodes adn the underlying physics behind enhancing the modes for the specific system. In Section IV we show the effect on trapping of tuning the medium where the cells are in, the steady state streaming, the trapping the z -direction. Section V is a discussion of the results, with discussion of the possibility of size-dependent cell trapping with positive acoustic contrast factor, and potential advantages and disadvantages with the presented method of trapping. Section VI is a conclusion of the paper.

II. THEORY, MODELING, AND NUMERICAL SIMULATION

We will briefly explain the theory and modeling to be used in the paper necessary for replicating the numerical simulations. The theory was developed for bulk PZE driven acoustofluidics [30] and in [31] for effective boundary conditions to first order pressure acoustics and steady time averaged second order fields. It was iterated upon in [20] for thin-film PZEs on bulk devices for acoustofluidics and the solid mechanical part of the model for thin-film PZE was validated by comparing it to experiments in [32]. This paper differs from the previous mentioned by using axisymmetric cylindrical coordinates.

The theory in this paper goes into a perturbation theory of the time-harmonic first-order fields, which leads to time averaged second order streaming in the fluid and

the acoustic radiation force on the particle. The theory assumes axisymmetry throughout the paper and anytime results are shown in 3 dimensions (3D) they are solved numerically in 2 dimensions (2D) and rotated into 3D solutions for plotting.

The high frequency, and therefore the small wavelengths in the system, $\lambda^{\{fl, sl\}} = c_0^{\{fl, sl\}}/f$, makes it computationally demanding to simulate the system in full 3D, even when using the effective boundary theory of the pressure acoustics by Bach and Bruus [31]. However since the system we are looking at is cylindrically symmetric we have the option of changing coordinate system from Cartesian coordinates to cylindrical coordinates, and utilize that the system is axisymmetric. This makes it possible to reduce the 3D numerics into 2D, without the loss of information as long as the system is truly axisymmetric.

A. Theory of time harmonic fields

We have a time-harmonic electric potential, $\tilde{\varphi}(\mathbf{r}, t)$, over the PZE thin-film which, though the PZE coupling coefficients, drives a first order field in the solids $\tilde{\mathbf{u}}_1(\mathbf{r}, t)$. We denote the time harmonic fields with a tilde and the time independent complex valued fields without a tilde,

$$\tilde{\varphi}(\mathbf{r}, t) = \varphi(\mathbf{r}) e^{-i\omega t}, \quad \tilde{\mathbf{u}}_1(\mathbf{r}, t) = \mathbf{u}_1(\mathbf{r}) e^{-i\omega t}, \quad (1)$$

where, $\omega = 2\pi f$, is the angular frequency, f , the frequency, \mathbf{r} , the spacial coordinate, and t the time.

The model described in Ref. 20, 30, and 32 has been described in Cartesian coordinates so in order to simulate the axisymmetric system in cylindrical coordinates, (r, ϕ, z) , we defined the translation between Cartesian and cylindrical coordinates as $(x, y, z) = (r \cos(\phi), r \sin(\phi), z)$, where we assume that the electric potential has no dependence on the ϕ -direction and that the displacement field components have no dependence on ϕ and no ϕ component, such that,

$$\varphi(r, z), \quad \mathbf{u}_1(r, z) = u_r(r, z)\mathbf{e}_r + u_z(r, z)\mathbf{e}_z, \quad (2)$$

The dynamics of the solids are driven by the weakly damped Cauchy's elastodynamic equation of motion and dielectrics by Maxwell's quasi-electrostatic for no free charges in a linear dielectric, [30, 33]

$$-\rho\omega^2(1 + i\Gamma_{sl}) \mathbf{u}_1 = \nabla \cdot \boldsymbol{\sigma}_{sl}, \quad \nabla \cdot \mathbf{D} = 0, \quad (3)$$

where $\boldsymbol{\sigma}_{sl}$ is the Cauchy's stress tensor, Γ_{sl} is the solid dampening, and \mathbf{D} is the electric displacement field for a linear dielectric defined as $\mathbf{D} = -(1 + i\Gamma_\varepsilon)\boldsymbol{\varepsilon} \cdot \nabla\varphi$ with $\boldsymbol{\varepsilon}$ being the dielectric tensor and Γ_ε is the electric dampening. For a purely mechanical structure the stress tensor can in Voigt notation be defined as,

$$\boldsymbol{\sigma}_{\text{sl}} = \mathbf{C} \cdot \mathbf{S}_{\text{sl}}, \quad (4)$$

where \mathbf{C} is the elastic moduli tensor of rank two in Voigt notation which is the relations between stress tensor, $\boldsymbol{\sigma}_{\text{sl}}$, and strain tensor, \mathbf{S}_{sl} . The stress tensor in Voigt notation is,

$$\boldsymbol{\sigma}_{\text{sl}} = (\sigma_{rr}, \sigma_{\phi\phi}, \sigma_{zz}, \sigma_{\phi z}, \sigma_{rz}, \sigma_{r\phi})^T. \quad (5)$$

Using that the derivative $\nabla = (\mathbf{e}_r \partial_r + \mathbf{e}_\phi \frac{1}{r} \partial_\phi + \mathbf{e}_z \partial_z)$, that the ϕ partial derivative of the r basis vector is $\partial_\phi \mathbf{e}_r = \mathbf{e}_\phi$, and the ϕ basis vector is $\partial_r \mathbf{e}_\phi = -\mathbf{e}_r$, one can use the theory in a axisymmetric cylindrical system. Applying this derivative to the strain gives,

$$\mathbf{S}_{\text{sl}} = (\partial_r u_{1,r}, u_{1,r}/r, \partial_z u_{1,z}, 0, (\partial_r u_{1,z} + \partial_z u_{1,r}), 0)^T, \quad (6)$$

The lowest symmetry we will work with in this paper is the hexagonal crystal structure where the coefficients in \mathbf{C} can be defined as

$$\mathbf{C} = \left(\begin{array}{ccc|ccc} C_{11} & C_{12} & C_{13} & 0 & 0 & 0 \\ C_{12} & C_{11} & C_{13} & 0 & 0 & 0 \\ C_{13} & C_{13} & C_{33} & 0 & 0 & 0 \\ \hline 0 & 0 & 0 & C_{44} & 0 & 0 \\ 0 & 0 & 0 & 0 & C_{44} & 0 \\ 0 & 0 & 0 & 0 & 0 & C_{66} \end{array} \right), \quad (7)$$

which is isotropic in the plane and therefore the coefficients are invariant under transformation from Cartesian coordinates to cylindrical coordinates. While neither the displacement nor the electric field has a component in the ϕ -direction, the strain and stress does have a $\phi\phi$ component, stemming from the non-zero derivative of the unit vectors, and can be understood as the natural effect of a uniform expansion in the radial direction.

For a isotropic material the same coefficients as in Eq. (7) still apply but with the higher symmetry requirement follows the added restraint that, $C_{13} = C_{12}$, $C_{33} = C_{11}$, and $C_{66} = C_{44}$. Since plates of silicon (111) can be modeled as isotropic in the plane[34], with the parameter values given in Table I, we will use that in this paper, whereas silicon in the (100) direction is anisotropic[35] in the plane and therefore not good for axisymmetric simulations.

For materials that are piezoelectric the stress and electric displacement fields are coupled to the electric and strain fields though the piezoelectric coupling tensor, \mathbf{e} , which in the Voigt notation is a 3×6 matrix. The relation is therefore

$$\boldsymbol{\sigma}_{\text{sl}} = \mathbf{C} \cdot \mathbf{S}_{\text{sl}} - \mathbf{e}^T \cdot \mathbf{E}, \quad (8a)$$

$$\mathbf{D} = \mathbf{e} \cdot \mathbf{S}_{\text{sl}} + \boldsymbol{\varepsilon} \cdot \mathbf{E}, \quad (8b)$$

where the electric field defined as $\mathbf{E} = -\nabla\varphi$ and \mathbf{e} for a hexagonal crystal structure is

$$\mathbf{e} = \left(\begin{array}{ccc|ccc} 0 & 0 & 0 & 0 & 0 & e_{15} \\ 0 & 0 & 0 & 0 & e_{15} & 0 \\ e_{31} & e_{31} & e_{33} & 0 & 0 & 0 \end{array} \right), \quad (9)$$

and the dielectric tensor $\boldsymbol{\varepsilon}$ is,

$$\boldsymbol{\varepsilon} = \left(\begin{array}{ccc} \varepsilon_{11} & 0 & 0 \\ 0 & \varepsilon_{11} & 0 \\ 0 & 0 & \varepsilon_{33} \end{array} \right). \quad (10)$$

The actuator we will use in this paper is aluminum scandium nitride (AlScN) which has a hexagonal piezoelectric crystal structure in the wurtzite structure in the [0001] direction[36]. The coefficients in the \mathbf{C} - \mathbf{e} - $\boldsymbol{\varepsilon}$ coupling matrix can be found for $\text{Al}_{0.6}\text{Sc}_{0.4}\text{N}$ in Table I, and are the same as for in the Cartesian coordinates system, since the fact that it is invariant under rotations in the plane.

The mechanical displacement in the solids transfer into the liquid as pressure waves. The pressure waves are governed by Navier–Stokes equation and by going into a perturbation theory in the density, ρ , velocity, \mathbf{v}^{fl} , and pressure field, p , of a quiescent fluid, we get that the first order fields can be described by a damped pressure wave and the following relations, with the derivation available in Bach and Bruus Ref. 31,

$$\nabla^2 p_1 = -\frac{\omega^2}{c_{\text{fl}}^2} (1 + i\Gamma_{\text{fl}}) p_1, \quad p_1 = c_{\text{fl}}^2 \rho_1, \quad (11a)$$

$$\mathbf{v}_1^{\text{fl}} = -i \frac{1 - i\Gamma_{\text{fl}}}{\omega \rho_{\text{fl}}} \nabla p_1, \quad \Gamma_{\text{fl}} = \left(\frac{4}{3} \eta_{\text{fl}} + \eta_{\text{fl}}^{\text{b}} \right) \omega \kappa_{\text{fl}}, \quad (11b)$$

$$\tilde{p}_1 = p_1 e^{-i\omega t}, \quad \tilde{\mathbf{v}}_1 = \mathbf{v}_1 e^{-i\omega t}, \quad \kappa_{\text{fl}} = (\rho_{\text{fl}} c_{\text{fl}}^2)^{-1}, \quad (11c)$$

where p_1 is the first order pressure field, c_{fl} is the speed of sound in the fluid, Γ_{fl} is the dampening in fluid, ρ_1 is the first order density field, \mathbf{v}_1 is the first order velocity field, η_{fl} and $\eta_{\text{fl}}^{\text{b}}$ is the dynamic and bulk viscosity in the fluid, κ_{fl} is the compressibility in the fluid, and tilde denote the time dependent fields.

Whereas in Bach and Bruus Ref. 31 they derive the equations in curvilinear coordinates we can here specify that we are working in cylindrical coordinates with the further assumption that there is no phi dependence or phi component

$$p_1(r, z), \quad \mathbf{v}_1(r, z) = v_r(r, z) \mathbf{e}_r + v_z(r, z) \mathbf{e}_z, \quad (12)$$

which makes it easier to implement some of the boundary conditions. These equations combined with the boundary condition in Eq. (20a) are enough to model the first order fields of the solid and the fluid.

B. Theory of time-averaged fields

The perturbation theory into second order gives contributions from the first order time dependent fields through the nonlinear first order product terms. We therefore expect the second order terms to have components that are time dependent on the double harmonic frequency and which are steady in time. In a time average, defined as $\mathbf{F}_2 = \langle \tilde{\mathbf{F}}_2(\mathbf{r}, t) \rangle = \frac{\omega}{2\pi} \int_0^{2\pi/\omega} \tilde{\mathbf{F}}_2(\mathbf{r}, t) dt$, the only parts to survive are the time steady part of the second order fields. The time-average of a product of two first order fields can be written as $\langle \text{Re} [\tilde{A}_1(t)] \text{Re} [\tilde{B}_1(t)] \rangle = \frac{1}{2} \text{Re} [A_1 B_1]$. Expanding Navier–Stokes into second order and taking the time average one arrives at the governing equation,

$$\eta_{\text{fl}} \nabla^2 \mathbf{v}_2 = \nabla \mathcal{P}_2 - \frac{\Gamma_{\text{fl}} \omega}{2c_{\text{fl}}^2} \text{Re} [p_1^* \mathbf{v}_1^{\text{fl}}], \quad \nabla \cdot \mathbf{v}_2 \approx 0, \quad (13)$$

where \mathbf{v}_2 is the time-averaged second order bulk streaming, \mathcal{P}_2 is the effective second order pressure as explained in Bach and Bruus Ref. 31, and the term $-\frac{\Gamma_{\text{fl}} \omega}{2c_{\text{fl}}^2} \text{Re} [p_1^* \mathbf{v}_1^{\text{fl}}]$ drives the Eckart streaming which we will show is the dominant driver of the streaming in the system presented in Section IV. An other important time-average second order effect is the radiation force, \mathbf{F}_{rad} , and the expression here is used from Settnes and Bruus [37], where it was calculated here used as the mono- and dipole scattering of first order pressure waves from a sphere,

$$\mathbf{F}_{\text{rad}} = -\pi a^3 \left[\frac{2\kappa_{\text{fl}}}{3} \text{Re} (f_1^* p_1^* \nabla p_1) - \rho_{\text{fl}} \text{Re} (f_2^* \mathbf{v}_1^* \cdot \nabla \mathbf{v}_1) \right], \quad (14a)$$

$$f_1 = 1 - \frac{\kappa_{\text{p}}}{\kappa_{\text{fl}}}, \quad f_2 = \frac{2(1-\gamma)(\rho_{\text{p}}/\rho_{\text{fl}} - 1)}{2\rho_{\text{p}}/\rho_{\text{fl}} + 1 - 3\gamma}, \quad (14b)$$

where a is the particle radius, f_1 is the monopole scattering coefficient, κ_{p} is the particle compressible, f_2 is the dipole scattering coefficient, ρ_{p} is the particle density, γ is $\gamma = -\frac{3}{2} [1 + i(1 + \delta/a)] \delta/a$, and $\delta = \sqrt{2\eta_{\text{fl}}/(\omega\rho_{\text{fl}})}$ is the viscous boundary layer thickness.

The effective force that effects a particle is a combination of the acoustic radiation force, the drag force from the acoustic streaming, $\mathbf{F}_{\text{drag}} = 6\pi\eta_{\text{fl}}a(\mathbf{v}_2 - \mathbf{v}_{\text{p}})$, where \mathbf{v}_{p} is the particle velocity, and the buoyancy correct gravitational force, $\mathbf{F}_{\text{grav}} = \mathbf{g}(\rho_{\text{p}} - \rho_{\text{fl}})$, with $\mathbf{g} = -9.82 \text{ N kg}^{-1} \mathbf{e}_z$,

$$\mathbf{F}_{\text{tot}} = \mathbf{F}_{\text{rad}} + \mathbf{F}_{\text{drag}} + \mathbf{F}_{\text{grav}}. \quad (15)$$

C. Boundary conditions

The first order boundary conditions for the system in the axisymmetric case has the condition on the central axis that the r derivatives are zero on the pressure, displacement field z -component, and electric potential, whereas the r component of the displacement is zero, so as to make the system symmetric,

$$\partial_r p_1 = 0, \quad \partial_r u_{1,z} = 0, \quad u_{1,r} = 0, \quad \partial_r \varphi = 0, \quad \text{at } r = 0. \quad (16)$$

The second order streaming at the axisymmetric interface is also symmetric so the derivative of the effective pressure and z -component of the streaming, and the r -component of the streaming is zero,

$$\partial_r p_2 = 0, \quad \partial_r v_{2,z} = 0, \quad v_{2,r} = 0, \quad \text{at } r = 0. \quad (17)$$

The boundary condition at the interface between the solid and air is zero stress, and for the electric displacement field it is zero free charge,

$$\boldsymbol{\sigma}_{\text{sl}} \cdot \mathbf{n} = \mathbf{0}, \quad \mathbf{D} \cdot \mathbf{n} = 0, \quad \text{at sl-air}, \quad (18)$$

where losses from the solid into the air is neglected in the model. The electric potential has positive, negative, and grounded electrodes. The bottom electrode is grounded, and therefore set to a potential of zero, and the top electrode are either positive or negative electrodes, with respectively $+\frac{1}{2}\varphi_0$ and $-\frac{1}{2}\varphi_0$,

$$\varphi = 0, \quad \text{at bottom elec.}, \quad (19a)$$

$$\varphi = +\frac{1}{2}\varphi_0, \quad \text{at positive elec.}, \quad (19b)$$

$$\varphi = -\frac{1}{2}\varphi_0, \quad \text{at negative elec.}. \quad (19c)$$

At the solid-fluid interface we use the effective boundary conditions developed by Bach and Bruus Ref. 31, where the boundary layer has been accounted for analytically, both in first order pressure and displacement. They defined the boundary conditions in curvilinear coordinates, however since the geometry stated here is simple, the boundary conditions will given for this specific system,

$$\partial_z p_1 = \frac{i\omega\rho_0}{1 - i\Gamma_{\text{fl}}} \left[-i\omega u_{1,z} - \frac{i}{k_{\text{s}} r} \partial_r (-i\omega r u_{1,r}) \right] - \frac{i}{k_{\text{s}}} (k_{\text{c}}^2 p_1 + \partial_z^2 p_1), \quad (20a)$$

$$\boldsymbol{\sigma}_{\text{sl}} \cdot \mathbf{e}_z = -p_1 \mathbf{e}_z + ik_{\text{s}} \eta_0 \left(-i\omega \mathbf{u}_1 + \frac{1}{\omega\rho_0} \nabla p_1 \right), \quad (20b)$$

where $k_c^2 = \frac{\omega^2}{c_{\text{fl}}^2} (1 + i\Gamma_{\text{fl}})$, and $k_s = \frac{1+i}{\delta}$. Because we are looking at a system without a lid, the waves will propagate for a long time until damped. However to keep the volume to a manageable size, we introduce a perfectly matched layer (PML) on top and to the side of the liquid. It is implemented by a coordinate transformation simulating a damped wave,

$$\partial_r \rightarrow [1 + i\chi(r, z)]\partial_r \quad \partial_z \rightarrow [1 + i\chi(r, z)]\partial_z, \quad (21a)$$

$$\chi(r, z) = K_{\text{PML}} \left(\theta[r - r_{\text{fl}}] \left[\frac{r - r_{\text{fl}}}{r_{\text{PML}}} \right]^2 + \theta[z - z_{\text{fl}}] \left[\frac{z - z_{\text{fl}}}{z_{\text{PML}}} \right]^2 \right), \quad (21b)$$

where θ is the Heaviside step function, $r_{\text{fl}} = r_{\text{m}} + r_{\text{c}}$ is the distance of both the membrane free to move, r_{m} and the clamped section, r_{c} , and K_{PML} is a parameter chosen such that the waves are damped without reflections at the interface.

The boundary condition at the outer edge of the fluid is because of the PML layer dampens the waves before they arrive there. In the simulations changing hard wall boundary condition on the outer edge, $p_1 = 0$, to soft wall, $\mathbf{n} \cdot \nabla p_1 = 0$, give a L2 of the norm of the difference at about 10^{-5} times lower than when compared to the either field.

D. Numerical implementation in COMSOL

The software used in this paper to do the finite element method (FEM) calculations is the commercial software COMSOL [38], where we use the weak form formulation that is available within the Mathematics module. This is used to calculate the pressure field, the displacement field, and the electric potential all with quartic polynomial order. The system is calculated with at least 20 elements per wavelength, and typically more, giving more than 80 nodal points per wavelength in the primary bulk and 10 elements per wavelength in the PML layer. This was enough to satisfy the criteria for convergence analysis similar to Ref. 39. It was ensured that there were at least four mesh elements in both the membrane and thin-film thickness direction, so to resolve it properly and was done by a structured mesh, with the mesh in the bulk liquid being a triangular mesh. At the symmetry plane $r = 0$ there was added a boundary layer of 15 elements, growing up from a smallest element of 0.01 μm .

At this resolution the simulation of the first order fields, p_1 , \mathbf{u}_1 , and φ_1 took roughly 50 seconds to compute, on a workstation with a Intel i9-7960X processor with 16 cores and 128 GB of random access memory (RAM). The simulation used 14 GB RAM and used 1.4 million degrees of freedom (dof). The second order order fields, p_2 and \mathbf{v}_2 were simulated at the same resolution as p_1 , where p_2

and \mathbf{v}_2 had fourth order elements, took 3 min to simulate, used 27 GB of RAM and solved for 2.7 million elements.

The parameter values needed in the simulations is summarized in Table I. The parameter values for elastic moduli the silicon in the (111) crystal were calculated based on the fact that in this crystal orientation the membranes behave as isotropic plates and can be calculated based on the Young's modulus, E , and Poisson's ratio, s [34]. The moduli of an isotropic material is calculated as,

$$C_{11} = \rho c_{\text{lo}}^2 = \frac{1-s}{(1+s)(1-2s)} E, \quad (22a)$$

$$C_{44} = \rho c_{\text{tr}}^2 = \frac{1}{2(1+s)} E. \quad (22b)$$

The piezoelectric thin film used in this paper is $\text{Al}_{0.6}\text{Sc}_{0.4}\text{N}$ however other PZE thin-films could have been used. AlN was a material that was simulated, but not included in this paper, and for all the results shown in later sections the same conclusions still apply, with the exception that AlN need a higher actuation voltage to make up for the lower piezoelectric coefficient compared to $\text{Al}_{0.6}\text{Sc}_{0.4}\text{N}$. The parameters for the Iodixanol were calculated based on measurements in Ref. 23, where they gave a polynomial fit on percentages of Iodixanol, in the range from 0% to 60%. These polynomial fit were also extrapolation to 80% in Table I for uses described in Section IV. Although the 80% Iodixanol lies outside the measurements, the good agreement in the 0-60% in the fit makes us believe that the error of extrapolation is reasonable.

III. SIMULATION RESULTS OF MEMBRANE ELECTRODE PATTERNING FOR HIGHER ORDER MODES

The theory and numerical setup presented in the previous sections enable us to make axisymmetric simulations of piezoelectric thin-films deposited on solids in contact with fluids. This will be utilized to investigate circular membranes embedded in a liquid, compatible with standard MEMS fabrication techniques, and how the pressure field looks in such a system. A system very much like this has recently been fabricated, Ref. 46, but without electrode patterns compatible with the higher order membrane modes, and with a different thin-film PZE (AlN), and instead of using the thin-film PZE to actuate the membrane it was actuated with surface acoustic waves (SAW) from a device on which the membrane device was placed upon. In Section IV we also look at the second order effects such as radiation force and streaming. The overall concept in this section is using the patterned electrodes to enable higher order membrane mode numbers that sends waves into the fluid. Waves are sent out from each anti-node which makes a interference pattern giving rise to partially standing waves in the r -direction

TABLE I. Parameter values for $\text{Al}_{0.6}\text{Sc}_{0.4}\text{N}$, silicon in the crystal orientation (111), water and Iodixanol, with reference values in the table. The values for Iodixanol at 60% are calculated from Ref. 23, and the values for 80% are interpolated on the fitting polynomials from the same reference. For calculation of the radiation force the parameters for the cancer cells of type MCF-7 were used, with scattering coefficients calculated from Eq. (14b). The diameter of MCF-7 breast cancer cells are reported to be 16.2-24.4 μm [40], and in this paper we use a value for the radius of 10 μm .

Parameter	Value	Parameter	Value
<i>Thin-film aluminum scandium nitride, $\text{Al}_{0.6}\text{Sc}_{0.4}\text{N}$ [41, 42]</i>			
ρ_{sl}	3300 kg m^{-3}	Γ_{sl}	0.0005
C_{11}	313.8 GPa	C_{33}	197.1 GPa
C_{12}	150.0 GPa	C_{44}	108.6 GPa
C_{13}	139.2 GPa	C_{66}	81.9 GPa
$e_{31,f}$	-2.65 C m^{-2}	e_{15}	-0.32 C m^{-2}
e_{33}	2.73 C m^{-2}	Γ_{ε}	0.0005
ε_{11}	22 ε_0	ε_{33}	22 ε_0
<i>Silicon in (111) crystal orientation, Si (111) [34, 43, 44]</i>			
ρ_{sl}	2329 kg m^{-3}	s	0.262
E	168.9 GPa	C_{44}	66.9 GPa
C_{11}	207.5 GPa	Γ_{sl}	0.0001
C_{12}	73.7 GPa	c_{tr}	5360 m s^{-1}
c_{lo}	9439 m s^{-1}		
<i>Water [39]</i>			
ρ_{fl}	997 kg m^{-3}	$\eta_{\text{fl}}^{\text{b}}$	2.485 mPa s
c_{fl}	1497 m s^{-1}	Γ_{fl}	10.3 $\text{THz}^{-1} f$
κ_{fl}	448 TPa^{-1}	η_{fl}	0.890 mPa s
<i>Iodixanol solution [23]</i>			
$\rho_{\text{fl}}^{\text{Iod},60\%}$	1320 kg m^{-3}	$\rho_{\text{fl}}^{\text{Iod},80\%}$	1425 kg m^{-3}
$c_{\text{fl}}^{\text{Iod},60\%}$	1498 m s^{-1}	$c_{\text{fl}}^{\text{Iod},80\%}$	1513 m s^{-1}
$\kappa_{\text{fl}}^{\text{Iod},60\%}$	338 TPa^{-1}	$\kappa_{\text{fl}}^{\text{Iod},80\%}$	307 TPa^{-1}
$\eta_{\text{fl}}^{\text{Iod},60\%}$	7.690 mPa s	$\eta_{\text{fl}}^{\text{Iod},80\%}$	15.19 mPa s
<i>Cancer cell MCF-7 [40, 45]</i>			
$\rho_{\text{MCF-7}}$	1055 kg m^{-3}	$\rho_{\text{MCF-7}}$	373 TPa^{-1}
$a_{\text{MCF-7}}$	10 μm		
f_1^{Wa}	0.167	f_2^{Wa}	0.037 + 0.00002i
$f_1^{\text{Iod},60\%}$	-0.104	$f_2^{\text{Iod},60\%}$	-0.153 + 0.0010i
$f_1^{\text{Iod},80\%}$	-0.217	$f_2^{\text{Iod},80\%}$	-0.206 + 0.0025i

and traveling waves in the z -direction that has a hot spot some above the membrane. In the following section the phenomenon will be investigated in numerical simulations.

A. Effect of patterned electrodes and underlying physics

Since we attempt to access the higher order modes in the membrane, the electrode pattern is very important to the effectiveness of the system. A uniform electrode over film that covers the membrane leads to a uniform electric field, and therefore an attempted uniform stretching or compression of the film. This works well for the fundamental mode where the entire film is either stretching

or contracting across the entire film, although usually not uniformly, as the resulting displacement and pressure field from this mode is seen on Fig. 2(a). The first order mode sends out a traveling wave in the fluid that is seen as a expanding alternating pressure front. The electrode pattern seen in Fig. 2(a) gives rise to the potential Fig. 2(g) which is uniform across the electrode. The strain pattern for this mode is seen on and the strain Fig. 2(h) where it is plotted in out of phase with the electric potential, such that we can see what the membrane would like to do, and for the fundamental mode it matches well with the full covering electrode. At higher frequency it is possible to excite the higher order membrane modes. On Fig. 2(b) is seen the displacement of the membrane and pressure field where the system is actuated at 52 MHz and with a full covering electrode seen in Fig. 2(e) and potential (i). The mode in Fig. 2(b) is plotted out of phase such to see what the membrane is trying to do, and the out of phase strain pattern shown in Fig. 2(j) shows that the match between electrode pattern and what the membrane would like to do at this frequency does not match very well. Fig. 2(c) shows the displacement and pressure for a system actuated at 52 MHz with the electrode pattern shown in Fig. 2(f) and (k). Here the electrode pattern was designed to match the strain seen on Fig. 2(j), with electrodes each electrode π out of phase from the previous, but still actuated at 1 V_{pp} . The out of phase pattern now matches the electrodes, seen on Fig. 2(l), and this gives a much larger acoustic response in the system.

The higher order vibration modes have several periods in the membrane and this leads to changing stretching and compression along the film. A film with a uniform electrode trying to excite such a mode will have difficulty as it will be counteracting its effect over every full period in the film, as the film will try to expand and contract periodically across the film where as the electric field will to uniformly either expand and contract, hence over a full wave it will not amount to much. The film with a uniform electrode will be able to excite the higher order vibration membrane mode, but only to the effect that the contraction and expansion does not completely cancel out. However the resulting acoustofluidic action from the uniform electrode is usually much weaker compared to electrodes that are designed for that specific mode by matching the film expansion as seen between the Fig. 2(b) and Fig. 2(c). For the fourth order circular membrane mode shown in Fig. 2(c) we see that matching the electrodes compared to a uniform electrode increases the max displacement by a factor of 10, the max pressure amplitude by 36, as not only is waves send out into the fluid stronger but they also make better interference pattern in the center leading to this higher maximum pressure. For even higher order modes the effect of matching the electrode pattern to the mode is even stronger.

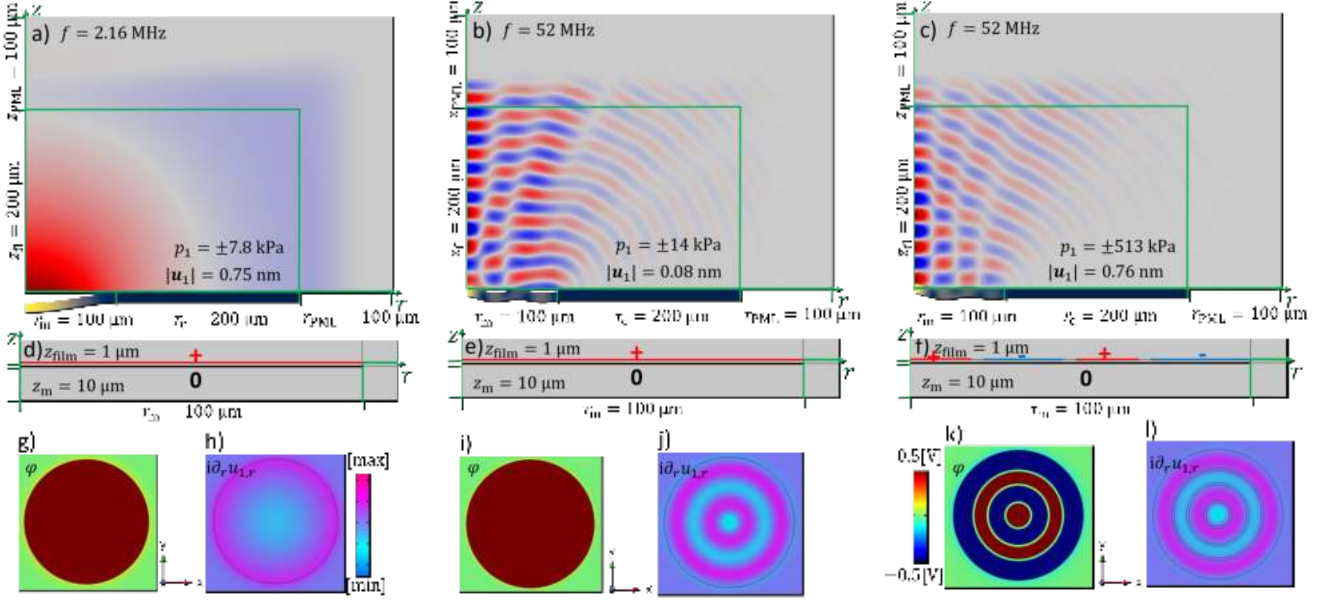


FIG. 2. (a)-(c) show the pressure and displacement fields, with the electrode configurations in (d)-(f) respectively, shown also in simulations in top-view in (g), (i), and (k) and the out of phase, compared to the electric potential, radial strain pattern in (i), (j), and (l). (a) is a simulation of the rz -plane of a water domain actuated at 2.16 MHz by a 200 μm in diameter and 10 μm thick silicon (111) membrane which in turn is actuated by a 1- μm - $\text{Al}_{0.6}\text{Sc}_{0.4}\text{N}$ thick thin-film at 1 V_{pp} and a full electrode covering the top. The pressure wave is displayed in the fluid channel from a maximum of $p_1 = 7.8$ kPa in dark red to a minimum of $p_1 = -7.8$ kPa in dark blue, and with gray being zero. The area beyond the green border in the fluid contains the PML layer that artificially dampens the wave. The displacement amplitude $|u_1|$, is displayed from 0 nm in dark blue to 0.75 nm in yellow, with artificially scaling of a factor of 15000 for visualization. (b) The same system as in (a) however at actuated at 52 MHz, with pressure going from -14 to 14 kPa, and displacement from 0 to 0.08 nm, shown with artificial scaling 30000. The system is shown out of phase to the maximum displacement, to show what the membrane would like to do. (c) Same as in (b) but with electrodes patterned, according to (f), and pressure from -488 to 488 kPa and displacement 0 to 0.76 nm, shown with artificial scaling 6000. (d) is a zoom in on the membrane showing the full plus electrode on top in red and the ground electrode at the bottom of the $\text{Al}_{0.6}\text{Sc}_{0.4}\text{N}$ thin-film in the thick black line. (e) is the same electrode design as in (d). (f) is the electrode design used in the simulations shown in (c) where the electrodes are made to match the strain pattern seen in (l). The figures (g), (i), and (k) show a top-view of the electric potential going from -0.5 V in blue to 0.5 V in red with zero being green. (i), (j), and (l) is the out of phase from the electric potential radial strain, $i\partial_r u_{1,r}$, for the simulation for the systems (a)-(c) respectively, where the strain pattern in (j) shows how the electrode pattern should be to increase the actuation of the membrane and the fluid, as seen on (c).

B. Traveling and standing waves in the pressure field above the circular membrane

The pressure field seen in Fig. 2(c) shows an interference pattern of constructive and destructive interference of pressure waves that are sent out from each anti-node in membrane mode. Patterning the electrodes make it possible to increase in effective acoustofluidic action, however there is an other requirement that is necessary for there to be a hotspot at some point above the membrane, which in Section IV will lead to focusing in that point. The wavelength in the fluid needs to be smaller than the wavelength in the membrane. When this condition is not fulfilled the waves scatter outward and do not form a interference pattern that leads to the hot spot in the center. The pressure waves then interact by constructive and destructive interference which creates the pattern seen on Fig. 3 (a) where there are standing waves

in the radial direction and traveling waves in the z direction. As the frequency of the resonance of the membrane modes roughly scale with the mode number squared and the wavelength in the fluid scales linearly with the frequency, the crossing will happen eventually.

The wave pattern shown on Fig. 3(a) is a rotation of the 2D simulation into 3D and the pressure fields is shown in contours of the pressure amplitude. It is seen that there are traveling waves in the z direction and the standing waves in the radial direction with a hot spot roughly 60 μm above the membrane center. Another way to show it is seen on Fig. 3(b), where the pressure amplitude is shown, and therefore the direction the waves are traveling, the z -direction, have no nodal lines whereas the standing waves in the radial direction have nodal lines. What enable it to work as a trap for cells and other particles is that it has this maximum pressure above the membrane. However because of the symmetry condition

along the z -axis, that the pressure must be continuous across that axis, the center axis always has a pressure anti-node. The radiation force focus particles in either the pressure node or anti-node, depending on the signs of the scattering coefficients. For most cancer cells in an isotonic solution the radiation force focuses the cells in the pressure anti-nodes, which is not ideal for the application of trapping the particles, therefore the next sections are dedicated to how this will work as a cell trap.

IV. SIMULATION RESULTS OF CELL TRAPPING ABOVE A CIRCULAR MEMBRANE

As described in the Section III B because there is a pressure maximum some distance above the membrane there is a possibility of turning this into a trap, and this section will explore this further by looking at the forces that a cancer cell of type MCF-7 (breast cancer), with parameter values given in Table I, will experience in such a system. However the system described in Section III, while illustrative because of the fairly simple nature of the 4 order mode, and will have it's uses again later, works at 52 MHz, which gives it a wavelength in water of

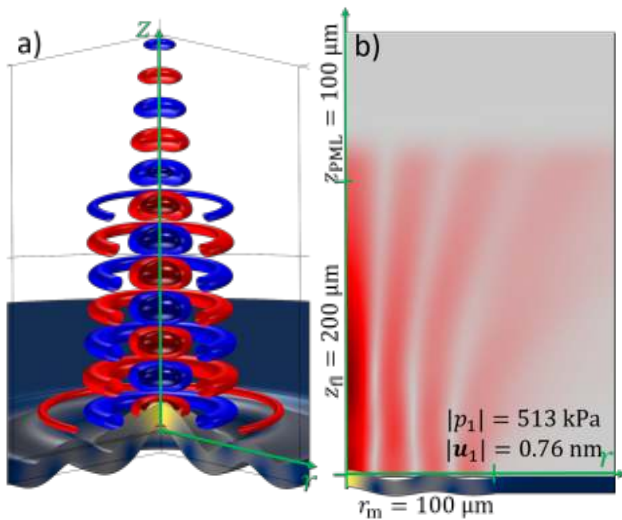


FIG. 3. (a) Same model as shown in Fig. 2 (b), but expanded by rotating the solution around the z -axis, and showing the isobar surface of the pressure waves at -250 kPa, -125 kPa, 125 kPa, and 250 kPa with colors dark blue, blue, red and dark red respectively. In the supplementary material it possible to see an animation where the pressure waves travel in the positive z -direction while not traveling the radial direction. The max displacement $|u_1|$ is 0.76 nm and here the artificial scaling is 20000 . (b) Same system as in Fig. 2 (d) but instead showing the absolute pressure field, $|p_1|$, in order to show the traveling wave nature in the z -direction while having standing waves in the radial direction as the traveling waves have a continuous absolute pressure field whereas the standing waves have fixed nodal lines.

about 29 μm . The diameter of 16.2 - 24.4 μm for MCF-7 cells [40], and therefore the requirement on the model of the radiation force, that the particle is much smaller than the wavelength in the suspension medium, does not hold here. Therefore we want to lower the frequency of the system, and one way to do that, in such a way that both the large membrane and the smaller membrane could be manufactured on the same device for testing, is to keep the membrane thickness the same and only change the membrane radius. This is simulated and shown on figure Fig. 4, for a membrane with a diameter 1 mm. Because of then larger membrane the frequency is now 18.5 MHz and it is now the tenth mode number in the membrane. This system does not generate the hot spot at much lower frequencies, or membrane mode numbers, as there still is the requirement that the membrane wavelength is larger than the wave length in the medium in order to have the hot spot.

Because of the higher order membrane mode the electrode configuration is even more important than for the example in Section III and this amplification combined with the maximum pressure at a point above the membrane, as shown in Fig. 4, which still has standing waves in the radial direction and attenuated waves in the z

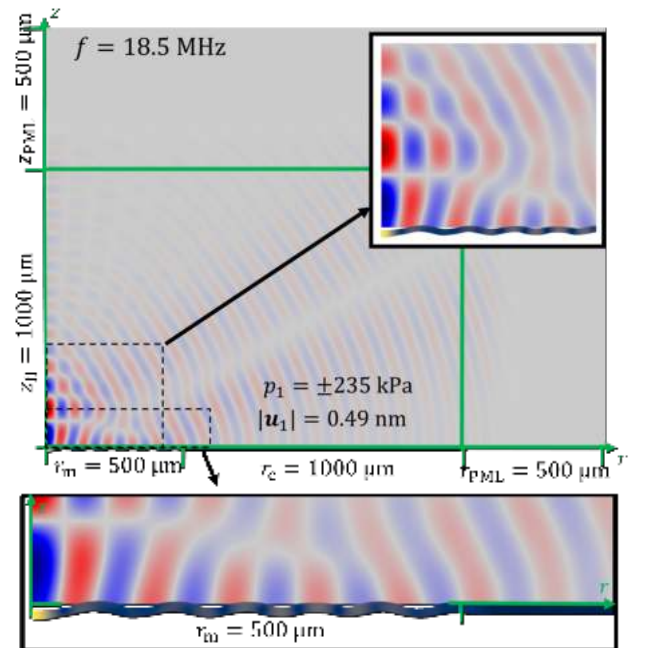


FIG. 4. A large silicon membrane with a diameter of 1 mm and thickness of 10 μm is actuated by 1 - μm -thick AlScN thin-film that has 10 electrode of interchanging phase actuated with 1 V_{pp} each with a width of 44 μm and a split of 4 μm between them. The system is actuating water at 18.5 MHz, with a maximum pressure amplitude of 235 kPa and a maximum displacement in the membrane of 0.49 nm with an artificial scaling of 50000 . The green lines delineate the boundary between normal fluid domain and the PML layer. There are two zoom ins on the maximal pressure and on the membrane.

direction, gives rise to the interesting acoustophoretic particle manipulation which this section discuss. As mentioned in Section III B particles with positive acoustic contrast factor will be anti-focused from the center, whereas the particles with negative acoustic factor will be trapped in the point above the membrane with highest acoustic energy. As the MCF-7 cells have specific parameters that cannot be changed, then Section IV A is about tuning the liquid instead. Section IV C is about the second order streaming in the system and Section IV C is about the trapping in the z -direction.

A. Designing trapping by tuning the medium

As seen on Fig. 5(a), the radiation force on small particles does not in it self enable trapping as the radiation force is pointing away from the center, when the MCF-7 cancer cells are submersed in water. Some cancer cells, compared to typical tracer particles of polystyrene, are

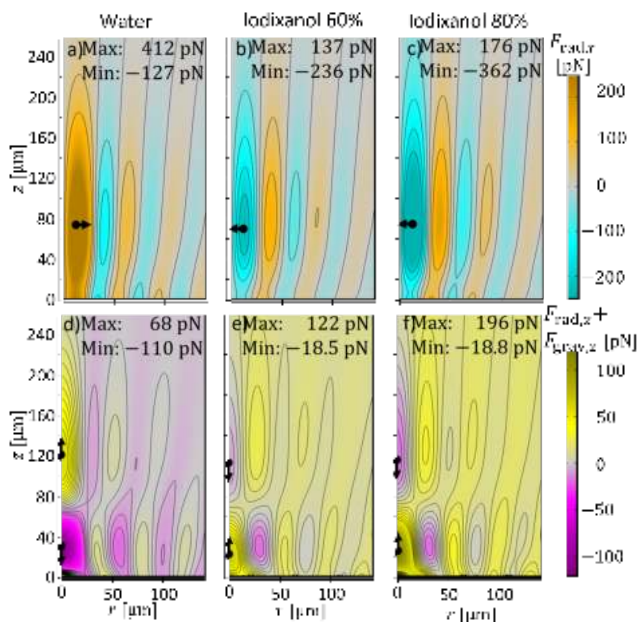


FIG. 5. Showing how Iodixanol can change the radiation force in the system, by showing the radiation force for, from the left, water, iodixanol at 60% and at 80% using the parameters given in Table I and the breast cancer cells MCF-7 cells. Other than the changing suspension medium the system is the same as in Fig. 4. (a)-(c) show the radial component of the radiation force on the symmetrized color bar shown to the right, with min and max values shown on the figures, and the black contour lines going from -200 pN to 100 pN in steps of 50 pN. (d)-(f) shows the sum of the z -component of the radiation and gravitational forces on the cancer cells with the color bar shown on the right, min and max values on the figures, and black contour lines going from -20 pN to 50 pN in steps of 5 pN. The black dots with arrows show the direction a particle would move in that component.

more compressible [23, 45], and by changing the submerision fluid it has been shown to be possible to change the direction of the acoustic radiation force [23]. This mechanism works by changing the fluid compressible and density, such that the acoustic mono- and dipole scattering coefficients changes sign. For 60% Iodixanol, where the parameter values are in Table I, the signs of the monopole scattering coefficient has changed sign on the MCF-7, resulting in trapping for these cancer cells in the center of the pressure anti-nodes, which is strongest in the center, as seen on Fig. 5(b) which is the radial radiation force. While there is a radial trapping once the cell enters the cyan region, there is a barrier around which prevents that area, which needs to be overcome before particles are trapped. On one hand it makes it more difficult to trap cells as one has to overcome this barrier before cells are trapped, and way around this is discussed further in Section V, and on the other hand once the cell is trapped it will keep it isolated and not make a large cluster in the trap. The same applies for the radial trapping in 80% Iodixanol as there is a larger barrier but also a stronger trap. For trapping in the z -direction we are showing both the radiation force and the buoyancy corrected gravitational force. As is seen on Fig. 5(c) there is anti focusing in the z -direction in the water where if the above 70 μm it will be forced up and below that it will be forced down towards the membrane. There is a sliver of upward force just above the membrane at that point. On Fig. 5(e) and (f) for 60% and 80% Iodixanol respectively there is a minimum roughly at the 70 μm mark, and where cells would be focused, in both the z - and r -direction. While it looks like the 80% Iodixanol is almost as good as the 60% solution, it is because buoyancy corrected gravitational force is also larger in the 80% case, and if the voltage is turned up from in the simulations from the 1 V_{pp}, then the 80% trap will be significantly larger than the 60% solution, as the radiation force scales with the square of the actuation voltage, but the gravitation does of course not.

B. Acoustic 2nd order steady-state Streaming

The streaming in the system is driven by Eckart streaming, and boundary streaming does not really matter. The streaming is calculated in Fig. 6 and as it is seen the overall structure of the streaming is a large sweeping rolls that is driven by the attenuation of the traveling acoustic wave. Close to the center the attenuation drives a small streaming roll going clock wise, were as the larger attenuation for waves traveling and dispersing to the right drives a streaming roll going counter clock-wise. At the boundary there are some small rolls that are roughly an order of magnitude smaller than the max streaming velocity, and on the image is seen as some small structures at the interface. The boundarylayer-driven streaming is only visible by numerically turning of the

Eckart off and observing the weaker streaming. Overall the streaming is not particular fast, with a maximum at roughly $6.7 \mu\text{m s}^{-1}$ at $1 V_{pp}$, however it is strongest in the direction z -direction right where the trap is the weakest. As the radiation force scales with cell diameter cubed, whereas the drag force scales linearly with the cell diameter, there is a cross over point where small particles will be dragged along with the streaming rather than being captured in the trap, and hence there is a lower limit for the effectiveness of size the trap of this which for 80% Iodixanol and cells with acoustic properties like MCF-7, is roughly at around $11 \mu\text{m}$ in diameter if the trap is actuated at $2 V_{pp}$ or above. This is discussed further in section Section V.

C. Particle trapping in the z -direction

For the cells to be trapped, the total effective force acting on the cell need to have a minimum in both the radial direction but also have minimum in the z -direction. The effective forces include the radiation force, the drag force from the streaming, and the buoyancy corrected gravitational force from density differences between the cell and the suspension liquid. For the buoyancy corrected gravitational force we assume that the gravity points

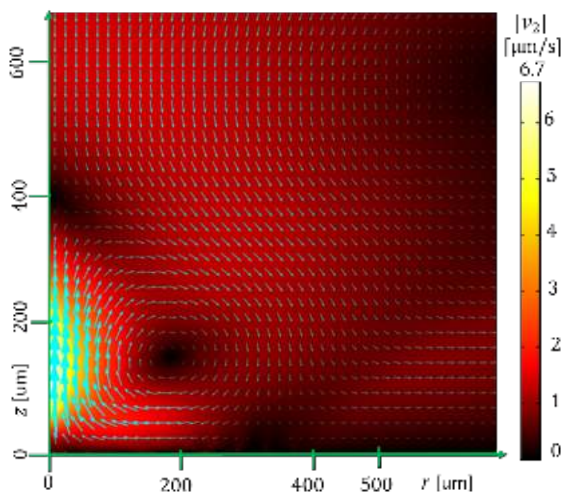


FIG. 6. The second order steady state streaming, \mathbf{v}_2 , generated by the membrane in the same system as shown in Fig. 4, but with the suspension medium being iodixanol at 80%. The cyan arrows are the vector component and the color plot, shown also in the color bar on the right, is the amplitude of the streaming, $|\mathbf{v}_2|$, which goes from $0 \mu\text{m s}^{-1}$ to $6.7 \mu\text{m s}^{-1}$ in the colors from black to white over red and yellow. The system is dominated by the Eckart streaming, driven by the attenuation of the pressure waves in the fluid, and only if this term is artificially turned off in the numerical simulations it is possible to see the effects from the boundary of the membrane, which gives very small streaming rolls close to the surface that are much smaller than the large flow shown.

in the negative z -direction, which for most cells in the Iodixanol suspending medium, this means the the gravitational force is pointing straight up, which for the trap is the most problematic direction. Even still we show that the trap is working. The forces acting in the radial direction are much larger than those acting in the z -direction and that is why we used split up the forces into the force components in Fig. 5. For Iodixanol in 60 and 80% solutions the cells are floating up when the trap is off and only when the trap is activated is there minimum where the cells are trapped. Since the streaming drag force is pointing is trying to drag out the particles of the trap in the upward z -direction the cross over point is at roughly $1.5 V_{pp}$ and up for the MCF-7 cells, as the radiation force is stronger than the streaming and therefore at higher voltage the gravitational force becomes relatively weaker compared to the radiation and streaming force, as they both scale with voltage squared. How to increase this trapping in the z -direction is further explored in Section V.

V. DISCUSSION OF RESULTS

In this section we will discuss some of the advantages of this method of trapping, some disadvantages and how they might be overcome, and future outlooks at what still remains to be investigated and are out of the scope of this paper. We will discuss membranes which have axidependance and what that could do for the system in Section VA. In Section VB we will discuss way to reduce the barrier or way that might work around the barrier. We will in Section VC discuss how to enhance the trapping in the z -direction. Section VD is about ways to use this membrane device in making arrays of them and ways they might be used. Lastly in Section VE we will discuss the possibility of making cell size dependent trapping without changes to the suspension medium.

A. Axidependent membrane actuation

Using the method for increasing the actuation by matching the out of phase strain patterning in thin-film on systems that are not axisymmetric could lead to some interesting results which however is outside the scope of this paper, as it would require significant modifications to the model presented in this paper. However one could imagine that a small weight placed on the membrane could create instability in the membrane mode, which might manifest as a phi dependent membrane resonance, which could make some interesting wave patterns, or possibly enter into the circular phi resonance modes. A more direct way to enter these modes would be to intrude multiple electrodes in the along the phi direction and actuate them out of phase to enter many different kinds of membrane modes.

On a completely different note some of the same mechanisms described in this paper might also be valid for long rectangular membranes that are actuated in a pattern that enables the membrane to have several wavelengths in the membrane width direction. If, like for the axi-symmetric circular membrane, the wavelength in the fluid is lower than the period in the membrane mode, and the actuation is at a higher order membrane mode, such that the anti-nodes send out interfering waves with a hot spot along the membrane some wavelengths above, then most likely there will be a line where cells can be trapped in.

B. Eliminating the barrier

As the standing pressure waves in radial direction has a periodic behavior in the radial direction it focus in bands, and therefore it might be difficult get the cells into the area where they will be trapped, as the radiation force will have a area around the center where the radiation force is pushing the cells away from the center, although it is much less powerful than the trap itself. There might be several ways to the particles to the center. By having a flow tangential to the surface such that the drag force on the cells is stronger than the initial barrier, but

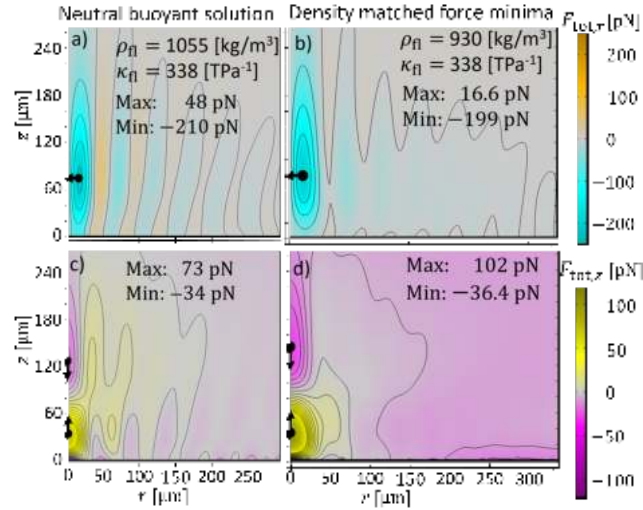


FIG. 7. (a) and (b) are the total radial force on MCF-7 cells and (c) and (d) is the total force in the z -direction, as in Eq. (15), where the system is the same as in Fig. 5 (b) and (e), but with different densities to enhance the trapping. (a) and (c) are based on 60% Iodixanol but have density of the suspension medium matched with that of the MCF-7 cells such that they are neutrally buoyant. (b) and (d) is also based on 60% Iodixanol but have the density reduced even further to a minimum in the barrier on the radial force. These fluids are fictitious fluids which have no known real counterpart, and are used as an example. Color bars and contour lines are the same as in Fig. 5.

not strong enough to rip the cells from the trap would be one way. As the trap is much stronger than the surrounding repelling force, there is quite a large margin for choosing the flow. An other idea is to have a high cell density, and then cells will be trapped because some will be within the trapping region, and then slowly diluting the solution, then the cells will remain trapped while the solution is diluted because the flow will predominately be in the direction tangential to the surface where the trap is strong.

If the desire is to eliminate the barrier one methods that show promise is changing the density of the suspensions medium. Fig. 7 show how by taking the parameter values for 60% Iodixanol and artificially changing only the density the barrier is almost eliminated when the cells are in a neutral buoyant solution, Fig. 7(a) and (c) and is gone when the density has been chosen to minimize the barrier in the radiation force, Fig. 7(b) and (d). When only looking at the radiation force on Fig. 7(b), the barrier is still there, at about 9 pN, however because the streaming drag force is also included, the total force penetrates the barrier and cells will be collected trapped in the center much easier. One problem that remains is to find a solution that has these properties. While the absolute values does not matter for this effect, the main point is that the compressibility of the suspension liquid is lower than the cell and then matching the density so to minimize the barrier, by for example adding a fluid slowly until the desired properties are found.

C. Enhance z -direction trapping and trapping of small particles

One of the weakest points of the trap is the fairly weak trapping in the z -direction. Whereas it is sufficient to trap the cancer cells investigated from buoyancy or sedimentation the forces that keep the cells trapped in the z -direction is much smaller than the forces that keep them trapped in the radial direction. This make the trap robust to flows along the membrane but weak to flows per-

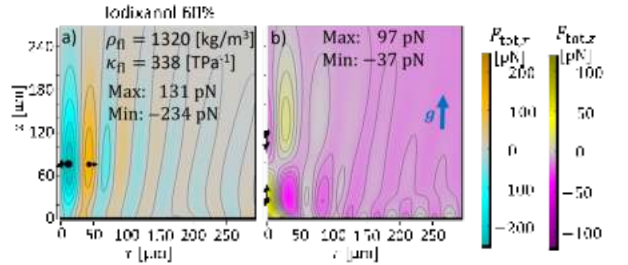


FIG. 8. Figure show the same system as in Fig. 5(b) and (e), but with the system being actuated upside down such that the gravitation is pointing in the direction of the blue g vector show on (b). The suspension liquid is Iodixanol 60%. Color bars and contour lines are the same as in Fig. 5.

pendicular to the direction of the trap. While most large scale flows are parallel to the surface, because we are so close to the surface and of course the fluid can not go directly into the membrane, the streaming induced by the Eckart streaming however is perpendicular to the membrane and is the strongest right at the trap so that it weakens the trap in particular for small cells. Since the radiation force scales with the cube of the cell radius and the drag force scales linear with radius, then there is a radius for small cells where they will no longer be trapped, but instead be dragged along the streaming instead. For the parameters in Table I for the MCF-7 cancer cells, the cross over point is roughly at 11 μm in diameter. While the MCF-7 cancer cells are roughly 16.2-24.4 μm and therefore will be trapped. Smaller cells which can have roughly the same parameters, will not be trapped. An example of cells that wont be trapped are red blood cells partly because of their smaller diameter, and therefore will be effected more by the streaming, and partly because of lower compressible, which will make the scattering monopole coefficient weaker for a solution of 60 or 80% Iodixanol.

One of the problems is the buoyancy that makes the cells float away in the direction that the trap is weakest. This can either be countered by having the device upside down, as seen in Fig. 8, so that the particle would float to towards the trap, and make it stronger, or, maybe more reasonable, by finding a liquid that is sufficiently more compressible than the cells but also has a lower density than the cells, such as in Fig. 7. This would of course change the speed of sound in the fluid, but the phenomenon is fairly robust to changes in speed of sound, as it will slightly change the focus point of the trap, but not in general effect the overall structure, as long as the requirement of the wavelength in the fluid is smaller than the period length in the membrane is still fulfilled.

If the desire is to use this trap on small cells or particles there might be other ways to accomplish this. One way could be is to use large seed particles that would be trapped, and though particle-particle interaction would keep the small particles trapped close to the seed particles, as seen in the literature by Hammerström *et al.* [7] but for a different kind of trap. An other way might be to try and enhance the trapping in the z -direction. Since the trapping in the z -direction is driven by the attenuation of the traveling waves in that direction it is possible that going to higher frequencies would increase the trapping in the z -direction, however it might also increase the streaming accordingly. An other idea that is beyond this paper is to bend the membrane by some other mechanism, maybe a pressure difference between the top and bottom of the membrane, which might help focus the waves better, giving better interference and therefore better focusing.

D. Arrays of trapping devices

One of the arguments for the presented trapping device is that it enables the possibility of having many scaffolding-free traps in an array. This might especially have applications in medical assays where many similar parallel studies are necessary for statistics. This is possible because each device is isolated in the sense that the acoustical waves that are transmitted from each separate device is not interacting with each other in the area where the trapping is occurring, because the waves are traveling away predominately in the z -direction and is attenuated fairly quickly in the radial direction. Therefore each device is separated, as long as there are not significant reflections from the surfaces above the device. Presumably as long as a surface is sufficiently far away that any waves that might be scattered have had time to defuse enough such that the stray reflections are much smaller than the central pressure peak just above the center of the membrane, then the reflections will most likely not effect trap significantly. If a surface is close then perhaps if it made of a material such as PDMS, where the acoustical wave is fairly well transmitted and fairly fast attenuated as well would make it such that the acoustical reflections were minimized. This was investigated in Skov and Bruus Ref. [16], where their objective was the opposite, in that they wanted high reflections and therefore changed PDMS lid with a glass lid in order to have higher reflections and the standing wave properties in the channel. If a lid is close to the surface and made of material that has high acoustic reflections, such as for example glass, then there is a possibility of the reflected waves to might generate standing waves in a bulk acoustic resonator. Such a system might be very interesting, and perhaps still work albeit by a differently mechanism, however it has not been investigated in this paper, as the device presented here is specifically intended to be lidless.

E. Cell Size-dependent Trapping

In section Section IV A it was explained that in order to turn the device into a trap there needed to be a sign change on the radiation force, so that the cells would focus in the pressure anti-nodes instead of the pressure nodes. The mechanism discussed in that section was to design the system such that the wavelengths in the fluid was much longer than the cells, and to change the suspension medium in order to change the sign of the scattering coefficients. The disadvantage lies in that one limits oneself to mediums that have necessary properties, where a simple isotonic saline solution unfortunately not is one of them. However there are other mechanisms that allow for the sign change of the radiation force. One mechanism is when the wavelength start to be comparable to the in size to that of the cells. When entering this regime internal resonances in the cells start to have an effect on the resulting radiation force in what is a fairly complex

interaction[47]. A recent numerical study Ref. 48 of the acoustic radiation force on cells have shown a sign reversal for the radiation force when the cell diameter is approximately 0.75 that of the wavelength. The study was done using on the parameter values of white blood cells, which have parameter values very close to that of the cancer cells investigated in this paper, and modeled the cells both as an elastic sphere and as a fluid domain and both showed the sign reversal at the same ratio of diameter to wavelength in the submersion fluid. If the trap was designed such that the wavelength was slightly larger than the large cancer cells that one wished to trap then it is possible to speculate that the trap would capture the large cancer cells while leaving the smaller cells anti-trapped. This would eliminate the need for changing the suspension medium, and would therefore also work for a standard isotonic saline solution. Such a system could look like that shown in Fig. 2 where the wavelength is 29 μm with cancer cells MCF-7 being in the order $\approx 16.2\text{-}24.4 \mu\text{m}$. However in order to be more than speculations then further investigations into the concrete situation should be made, and such numerical simulations require severe expansion to the model presented in this paper and therefore such calculations are outside the scope of this paper.

VI. CONCLUSION

In this paper we presented a concept for amplifying the resonance of higher order circular membrane modes actuated by a 1- μm -thick $\text{Al}_{0.6}\text{Sc}_{0.4}\text{N}$ piezoelectric thin-film actuator by patterning the electrodes to match the out of phase strain pattern in the film at some specific

mode. We show by simulations that the fourth order circular membrane modes of a 200 μm in diameter 10 μm thick membrane actuated at a frequency 52 MHz send out pressure waves from each anti-node which makes interference patterns in the pressure field. When the condition that the wavelength in the liquid is smaller than that of the node spacing in the membrane mode at that frequency the interference pattern in the liquid makes a pressure hot spot above the membrane. This pressure hot spot can then be used to trap cells of the type MCF-7 if the liquid is changed to a fluid such that the cells have a negative acoustic contrast factor. In the paper Iodixanol is used as an example of such a liquid. To lower the frequency a 1000 μm in diameter 10 μm thick membrane was actuated at 18.5 MHz at the tenth membrane mode. It was used for trapping the MCF-7 cancer cells in a levitating design that is based on numerical simulation of axisymmetric membranes. The design enables the trap to capture cells at $\approx 70 \mu\text{m}$ above the center of the membrane. The second order streaming was also calculated, where system was dominated by the Eckart, and was fairly slow at $6.7 \mu\text{m s}^{-1}$. Several different aspects of the system was discussed such as axidependent membrane modes, how to eliminate the barrier of the trap, an array of membranes for biological assays, and size-dependent trapping with changing suspension medium.

ACKNOWLEDGEMENTS

This work was supported by the *BioWings* project funded by the European Union's Horizon 2020 *Future and Emerging Technologies* (FET) programme, grant No. 801267.

-
- [1] A. Riaud, M. Baudoin, O. Bou Matar, L. Becerra, and J.-L. Thomas, Selective manipulation of microscopic particles with precursor swirling Rayleigh waves, *Phys. Rev. Applied* **7**, 024007 (2017).
 - [2] M. Baudoin, J.-C. Gerbedoen, A. Riaud, O. B. Matar, N. Smagin, and J.-L. Thomas, Folding a focalized acoustical vortex on a flat holographic transducer: miniaturized selective acoustical tweezers, *Science advances* **5**, eaav1967 (2019).
 - [3] Z. Gong and M. Baudoin, Particle assembly with synchronized acoustic tweezers, *Phys. Rev. Applied* **12**, 024045 (2019).
 - [4] J. T. Karlsen and H. Bruus, Acoustic tweezing and patterning of concentration fields in microfluidics, *Phys. Rev. Applied* **7**, 034017 (2017).
 - [5] B. Hammarström, M. Evander, H. Barbeau, M. Bruzelius, J. Larsson, T. Laurell, and J. Nilsson, Non-contact acoustic cell trapping in disposable glass capillaries, *Lab Chip* **10**, 2251 (2010).
 - [6] M. W. H. Ley and H. Bruus, Three-dimensional numerical modeling of acoustic trapping in glass capillaries, *Phys. Rev. Applied* **8**, 024020 (2017).
 - [7] B. Hammarström, B. Nilsson, T. Laurell, J. Nilsson, and S. Ekström, Acoustic trapping for bacteria identification in positive blood cultures with maldi-tof ms, *Anal. Chem.* **86**, 10560 (2014).
 - [8] M. Evander, O. Gidlof, B. Olde, D. Erlinge, and T. Laurell, Non-contact acoustic capture of microparticles from small plasma volumes, *Lab Chip* **15**, 2588 (2015).
 - [9] B. Hammarström, T. Laurell, and J. Nilsson, Seed particle enabled acoustic trapping of bacteria and nanoparticles in continuous flow systems, *Lab Chip* **12**, 4296 (2012).
 - [10] B. Hammarström, M. Evander, J. Wahlström, and J. Nilsson, Frequency tracking in acoustic trapping for improved performance stability and system surveillance, *Lab Chip* **14**, 1005 (2014).
 - [11] K. Olofsson, V. Carannante, M. Takai, B. Onfelt, and M. Wiklund, Ultrasound-based scaffold-free core-shell multicellular tumor spheroid formation, *MICROMACHINES* **12** (2021), 10.3390/mi12030329.
 - [12] S. M. Hagsäter, A. Lenshof, P. Skafte-Pedersen, J. P. Kutter, T. Laurell, and H. Bruus, Acoustic resonances in straight micro channels: Beyond the 1D-approximation,

- Lab Chip* **8**, 1178 (2008).
- [13] P. Augustsson, R. Barnkob, S. T. Wereley, H. Bruus, and T. Laurell, Automated and temperature-controlled micro-PIV measurements enabling long-term-stable microchannel acoustophoresis characterization, *Lab Chip* **11**, 4152 (2011).
- [14] J. S. Bach and H. Bruus, Suppression of acoustic streaming in shape-optimized channels, *Phys. Rev. Lett.* **124**, 214501 (2020).
- [15] J. Shi, D. Ahmed, X. Mao, S.-C. S. Lin, A. Lawit, and T. J. Huang, Acoustic tweezers: patterning cells and microparticles using standing surface acoustic waves (SSAW), *Lab Chip* **9**, 2890 (2009).
- [16] N. R. Skov, P. Sehgal, B. J. Kirby, and H. Bruus, Three-dimensional numerical modeling of surface-acoustic-wave devices: Acoustophoresis of micro- and nanoparticles including streaming, *Phys. Rev. Applied* **12**, 044028 (2019).
- [17] D. J. Collins, A. Neild, and Y. Ai, Highly focused high-frequency travelling surface acoustic waves (saw) for rapid single-particle sorting, *Lab Chip* **16**, 471 (2016).
- [18] P. Reichert, D. Deshmukh, L. Lebovitz, and J. Dual, Thin film piezoelectrics for bulk acoustic wave (BAW) acoustophoresis, *Lab Chip* **18**, 3655 (2018).
- [19] J. S. Pulskamp, S. S. Bedair, R. G. Polcawich, G. L. Smith, J. Martin, B. Power, and S. A. Bhawe, Electrode-shaping for the excitation and detection of permitted arbitrary modes in arbitrary geometries in piezoelectric resonators, *IEEE transactions on ultrasonics, ferroelectrics, and frequency control* **59**, 1043 (2012).
- [20] A. G. Steckel and H. Bruus, Numerical study of bulk acoustofluidic devices driven by thin-film transducers and whole-system resonance modes, *The Journal of the Acoustical Society of America* **150**, 634 (2021).
- [21] P. Li, Z. Mao, Z. Peng, L. Zhou, Y. Chen, P.-H. Huang, C. I. Truica, J. J. Drabick, W. S. El-Deiry, M. Dao, S. Suresh, and T. J. Huang, Acoustic separation of circulating tumor cells, *Proc. Natl. Acad. Sci. U.S.A.* **112**, 4970 (2015).
- [22] W. S. Low and W. A. B. W. Abas, Benchtop technologies for circulating tumor cells separation based on biophysical properties, *Biomed. Res. Int.* **2015**, 239362 (2015).
- [23] P. Augustsson, J. T. Karlsen, H.-W. Su, H. Bruus, and J. Voldman, Iso-acoustic focusing of cells for size-insensitive acousto-mechanical phenotyping, *Nat. Commun.* **7**, 11556 (2016).
- [24] K. Olofsson, B. Hammarstrom, and M. Wiklund, Acoustic separation of living and dead cells using high density medium, *LAB ON A CHIP* **20**, 1981 (2020).
- [25] J. Nilsson, M. Evander, B. Hammarström, and T. Laurell, Review of cell and particle trapping in microfluidic systems, *Analytica Chimica Acta* **649**, 141 (2009).
- [26] K. T. Gustafson, K. T. Huynh, D. Heineck, J. Bueno, A. Modestino, S. Kim, A. Gower, R. Armstrong, C. E. Schutt, and S. D. Ibsen, Automated fluorescence quantification of extracellular vesicles collected from blood plasma using dielectrophoresis dagger, *LAB ON A CHIP* **21** (2021), 10.1039/d0lc00940g.
- [27] P. Gascoyne, C. Mahidol, M. Ruchirawat, J. Satayavivad, P. Watcharasit, and F. F. Becker, Microsample preparation by dielectrophoresis: isolation of malaria, *Lab on a Chip* **2**, 70 (2002).
- [28] D. Baresch, J.-L. Thomas, and R. Marchiano, Observation of a single-beam gradient force acoustical trap for elastic particles: Acoustical tweezers, *Phys. Rev. Lett.* **116**, 024301 (2016).
- [29] M. Baudoin and J.-L. Thomas, Acoustic tweezers for particle and fluid micromanipulation, *Annual Review of Fluid Mechanics* **52**, 205 (2020).
- [30] N. R. Skov, J. S. Bach, B. G. Winkelmann, and H. Bruus, 3D modeling of acoustofluidics in a liquid-filled cavity including streaming, viscous boundary layers, surrounding solids, and a piezoelectric transducer, *AIMS Mathematics* **4**, 99 (2019).
- [31] J. S. Bach and H. Bruus, Theory of pressure acoustics with viscous boundary layers and streaming in curved elastic cavities, *J. Acoust. Soc. Am.* **144**, 766 (2018).
- [32] A. G. Steckel, H. Bruus, P. Muralt, and R. Matloub, Fabrication, characterization, and simulation of glass devices with an thin-film transducers for excitation of ultrasound resonances, *Physical Review Applied* **16**, 014014 (2021).
- [33] P. Hahn, I. Leibacher, T. Baasch, and J. Dual, Numerical simulation of acoustofluidic manipulation by radiation forces and acoustic streaming for complex particles, *Lab Chip* **15**, 4302 (2015).
- [34] E. V. Thomsen, K. Reck, G. Skands, C. Bertelsen, and O. Hansen, Silicon as an anisotropic mechanical material: Deflection of thin crystalline plates, *Sensors and Actuators A: Physical* **220**, 347 (2014).
- [35] M. A. Hopcroft, W. D. Nix, and T. W. Kenny, What is the Young's modulus of silicon, *J. Microelectromech. Syst* **19**, 229 (2010).
- [36] S. Trolier-McKinstry and P. Muralt, Thin film piezoelectrics for mems, *Journal of Electroceramics* **12**, 7 (2004).
- [37] M. Settnes and H. Bruus, Theoretical analysis of viscous corrections to the acoustic radiation force on cells in microchannel acoustophoresis, in *Proc. 15th MicroTAS, 2 - 6 October 2011, Seattle (WA), USA*, edited by J. Landers, A. Herr, D. Juncker, N. Pamme, and J. Bienvenue (CBMS, 2011) pp. 160–162.
- [38] COMSOL Multiphysics 5.5 (2019), <http://www.comsol.com>.
- [39] P. B. Muller and H. Bruus, Numerical study of thermoviscous effects in ultrasound-induced acoustic streaming in microchannels, *Phys. Rev. E* **90**, 043016 (2014).
- [40] J. An, J. Lee, S. H. Lee, J. Park, and B. Kim, Separation of malignant human breast cancer epithelial cells from healthy epithelial cells using an advanced dielectrophoresis-activated cell sorter (dacs), *Analytical and bioanalytical chemistry* **394**, 801 (2009).
- [41] M. A. Caro, S. Zhang, T. Riekkinen, M. Ylilammi, M. A. Moram, O. Lopez-Acevedo, J. Molarius, and T. Laurila, Piezoelectric coefficients and spontaneous polarization of ScAlN, *J. Phys.-Condens. Mat.* **27**, 245901 (2015).
- [42] R. H. Olsson, Z. Tang, and M. D'Agati, Doping of aluminum nitride and the impact on thin film piezoelectric and ferroelectric device performance, in *2020 IEEE Custom Integrated Circuits Conference (CICC)* (2020) pp. 1–6.
- [43] J. Kim, D.-i. D. Cho, and R. S. Muller, Why is (111) silicon a better mechanical material for mems? in *Transducers 01 Eurosensors XV* (Springer, 2001) pp. 662–665.
- [44] P. Hahn and J. Dual, A numerically efficient damping model for acoustic resonances in microfluidic cavities, *Physics of Fluids* **27**, 062005 (2015).
- [45] K. W. Cushing, F. Garofalo, C. Magnusson, L. Ekblad, H. Bruus, and T. Laurell, Ultrasound characterization of

- microbead and cell suspensions by speed of sound measurements of neutrally buoyant samples, *Anal. Chem.* **89**, 8917 (2017).
- [46] J. Qian, R. Yang, H. Begum, and J. E.-Y. Lee, Reconfigurable acoustofluidic manipulation of particles in ring-like rich patterns enabled on a bulk micromachined silicon chip, in *2021 21st International Conference on Solid-State Sensors, Actuators and Microsystems (Transducers)* (IEEE, 2021) pp. 365–368.
- [47] T. Hasegawa, Comparison of 2 solutions for acoustic radiation pressure on a sphere, *J. Acoust. Soc. Am.* **61**, 1445 (1977).
- [48] R. Habibi, C. Devendran, and A. Neild, Trapping and patterning of large particles and cells in a 1d ultrasonic standing wave, *Lab on a Chip* **17**, 3279 (2017).

5.4 Conference Paper I: Acoustofluidics 2020

Numerical simulation of acoustic streaming generated by GHz AlN-thin-film transducers on AlN-SiO₂-Bragg-reflector substrates.

Abstract book: [Acoustofluidics 2020 - Abstract Book](#)

PDF: [Conference contribution PDF](#)

Authors: [André G. Steckel](#) and Henrik Bruus.

Conference: Acoustofluidics 2020 - Abstract Book **115-116** (2020)

[André G. Steckel](#) and Henrik Bruus, *Acoustofluidics 2020 - Abstract Book*, Acoustofluidics conference, 26-27 August 2020, **Oral presentation**. Remark: Contributed talk at virtual conference

Numerical simulation of acoustic streaming generated by GHz AlN-thin-film transducers on AlN-SiO₂-Bragg-reflector substrates

André G. Steckel and Henrik Bruus

Department of Physics, Technical University of Denmark, Kongens Lyngby, Denmark
 E-mail: angust@fysik.dtu.dk , URL: <http://www.fysik.dtu.dk/microfluidics>

Introduction

Gigahertz (GHz) acoustofluidics is an active and exciting field of research with many new challenges and applications, including chemical and biological detection [1], microfluidic mixing [2], on-demand droplet dispensing [3], and nanoparticle trapping [4]. To develop further the initial numerical modeling in the field [5], we apply here our recent 3D fully-coupled acoustofluidic model [6] to a generic GHz AlN-thin-film-transducer device presented in Ref. [2]. The model of the system takes into account the electro-, elasto-, and hydrodynamics as well as the strongly damped acoustics in the transducer, in the substrate below, and in the fluid and glass lid above. Typical acoustic wavelengths at 1.5 GHz are 1 μm (water) and 3 μm (SiO₂), so a GHz-acoustofluidic system of size 10 to 100 μm typically contains 10 - 100 acoustic wavelengths. The model reveals the complexity that arises from these many wavelengths, and we compute the acoustic streaming that is induced by the acoustic wave, as it is strongly attenuated within a distance of 50 μm from the surface of the AlN-thin-film transducer.

3D acoustic simulations of a piezoelectric GHz AlN-thin-film transducer in vacuum

Acoustofluidics for the GHz regime requires specially designed transducers, systems that resonate at those frequencies, and direct contact or close proximity between the transducer and the liquid. This is necessary because of the strong acoustic attenuation at GHz frequencies. At 1.5 GHz the characteristic attenuation length in water is about 12 μm , only 12 times the acoustic wavelength. By having the resonator embedded in the liquid, the energy transfer from the piezoelectric transducer is maximized. In Ref. [2], a pentagon-shaped GHz-AlN-thin-film transducer was placed on top of an AlN-SiO₂ Bragg reflector, resting on a silicon substrate, and used to generate strong acoustic streaming. Here, using our recent 3D acoustofluidic model implemented in COMSOL Multiphysics 5.4 [6] with material parameters for the AlN thin-film from Ref. [7], we model the acoustic modes in this system at first placed in vacuum. We show in Fig. 1 the resulting displacement field in the transducer and substrate when making three different assumptions for the absorption by the substrate.

We note in Fig. 1 the increased complexity of oscillation pattern of the displacement field that arises, when the 50- μm -side-length pentagon in the 100- μm -side-length square system is allowed to oscillate more freely at the high GHz frequencies by changing the absorption assumptions. Whereas some rare modes are found to have a displacement predominately in the vertical z -direction, the typical mode is a complex pattern exhibiting many small-wavelength structures across the surface.

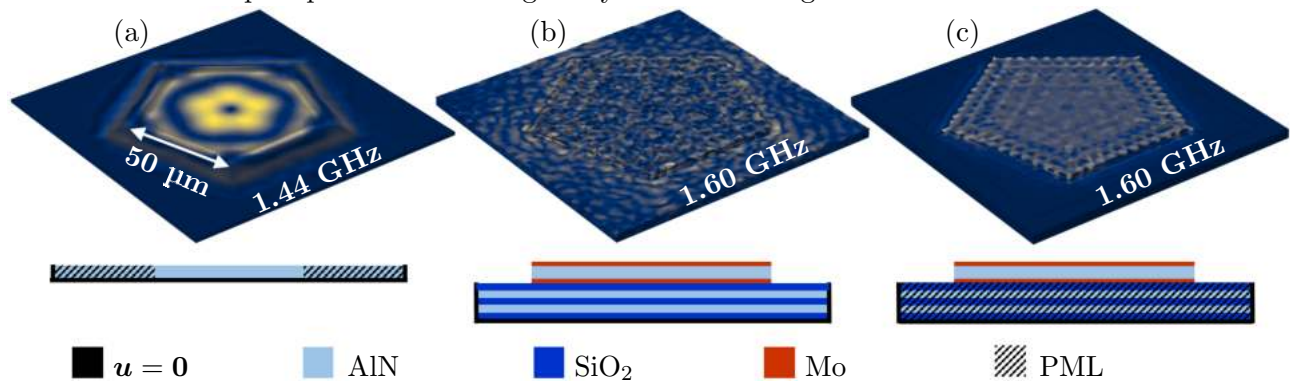


Figure 1: 3D simulations of the displacement field from 0 (blue) to 15 μm (yellow) in the GHz AlN-thin-film transducer from Ref. [2] using the different model assumptions that are illustrated by the respective sketches below each result. (a) A 100- μm square, 1.1- μm -thick AlN-thin-film in vacuum with zero displacement on the bottom and sides. The pentagon (50 μm side length) represents the top and bottom electrodes actuated by a $1\text{-}V_{\text{pp}}$ GHz-ac voltage. The area outside the pentagon is modeled as a perfectly absorbing medium (PML). (b) The same pentagon-shaped transducer protruding from the surface and with the 0.16- μm -thick metal electrodes included. It is placed on a AlN-SiO₂-Bragg reflector with five 0.64- μm -thick layers and with its bottom and side surfaces clamped. (c) The same as panel (b), but modeling the Bragg reflector as a perfect absorber (PML).

2D GHz acoustofluidic simulations of solids, piezoelectrics, and liquids with streaming

As shown in Fig. 2(a), we now insert the transducer of Fig. 1(b) in a larger system: the AlN-SiO₂ Bragg reflector is embedded in a 25- μ m-thick Si base, and a 40- μ m-high and 80- μ m-wide water domain is added above and enclosed in a 10- μ m-thick Pyrex casing. We simplify the simulation by restricting it to a vertical 2D cross section through the center of the device. Selected results using the method of Ref. [6] for simulating of the coupled Si-base-AlN-transducer-water-Pyrex system are shown in Fig. 2. In Fig. 2(a)-(c) is shown the displacement u_1 (up to 110 pm) of the elastic solids and the highly attenuated acoustic pressure p_1 (up to 890 kPa) in the water emanating from the transducer. The acoustic attenuation acts as a source for acoustic streaming, which we compute numerically using effective boundary layer theory [6]. The resulting streaming is shown in Fig. 2(d)-(f).

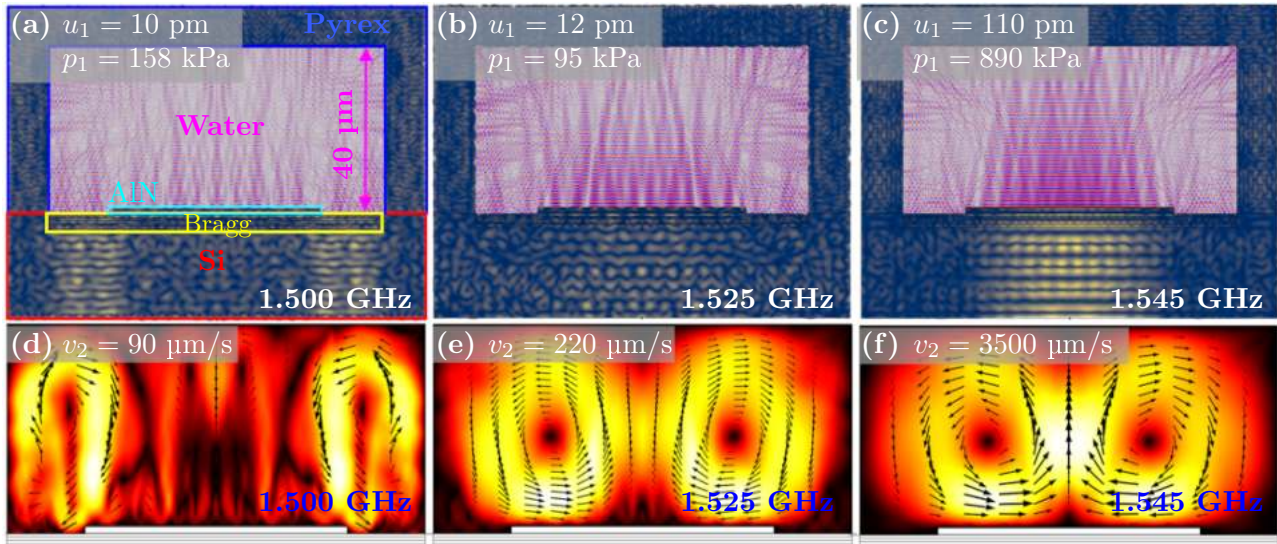


Figure 2: (a) Simulation at 1.500 GHz of the acoustic pressure p_1 in the water (magenta) above the AlN-thin-film transducer (cyan), and the displacement u_1 in the Pyrex (blue), the Bragg reflector (yellow), and the Si base (red). (b) The same, but for 1.525 GHz. (c) The same, but for 1.545 GHz. (d) Simulation of the acoustic streaming velocity v_2 corresponding to panel (a). (e) v_2 corresponding to (b). (f) v_2 corresponding to (c).

The three nearly identical actuation frequencies result in qualitatively different acoustic fields, but similar streaming patterns. At 1.500 GHz, a vertical standing wave is set up in the Si-substrate to the sides away from the transducer region. This results in two streaming rolls above the edges of the transducer. At 1.525 GHz, a weak increase in acoustic intensity is seen below the transducer. The result is two weakly overlapping streaming rolls above the transducer and closer to the center. At 1.545 GHz, a strong standing wave is established directly under the transducer. Given the moderate actuation of only 1 V_{pp}, the resulting streaming flow is fast (3.5 mm/s), and the two flow rolls are strongly overlapping with a maximum over the center of the transducer. The two-flow-roll pattern is a fairly robust feature, but the position and magnitude the flow rolls depends on the frequency.

Conclusion

We have shown that our recent 3D fully coupled acoustofluidic model [6] can be applied to GHz acoustofluidics, in particular to AlN-thin-film-transducer devices. The simulations shown here reveal how complex the acoustic fields are in detail, but they also indicate the overall stability of the streaming rolls, which is ensured by the strong attenuation of the acoustic waves within a 40- μ m-range from the transducer. Our model is a promising tool for future design studies of GHz acoustofluidic devices.

Acknowledgments

This work was supported by the BioWings project funded by the European Union's Horizon 2020 Future and Emerging Technologies (FET) programme, grant no. 801267.

References

- [1] W. Pang, H. Zhao, E.S. Kim, H. Zhang, H. Yuc, and X. Hu. *Lab Chip* **12**, 29 (2012). [doi]
- [2] W. Cui, H. Zhang, Y. Yang, M. He, H. Qu, W. Pang, D. Zhang, and X. Duan. *Appl. Phys. Lett.* **109**, 253503 (2016). [doi]
- [3] M. He, Y. Zhou, W. Cui, Y. Yang, H. Zhang, X. Chen, W. Pang, D. Zhang, and X. Duan. *Lab Chip* **18**, 2540 (2018). [doi]
- [4] W. Cui, L. Mu, X. Duan, W. Pang, and M.A. Reed. *Nanoscale* **11**, 14625 (2019). [doi]
- [5] W. Cui, W. Pang, Y. Yang, T.Li., and X. Duan. *Nanotechnol. Precision Eng.* **2**, 15 (2019). [doi]
- [6] N. R. Skov, J. S. Bach, B. G. Winckelmann, and H Bruus. *AIMS Mathematics*, **4**, 99 (2019). [pdf]
- [7] M.A. Caro, S. Zhang, T. Riekkinen, M. Ylilammi, M.A. Moram, O. Lopez-Acevedo, J. Molarius, and T. Laurila. *J. Phys.-Condens. Mat.* **27**, 245901 (2015). [doi]

Chapter 6

Conclusion and outlook

This thesis is a study of some of the opportunities that thin-film electromechanical actuators present in acoustofluidics. The main work presented in this thesis contains to the articles and each article has their own individual conclusion. In this overall conclusion we will try to give a general conclusion that is not limited to discussing each individual result, but try to connect the results across the papers, and draw upon all results. We will in an outlook discuss how these results might be used in the future, discuss some of the work that would have been interesting to investigate going forward, and finally look at the larger perspective and take a guess at how the results could be used in future acoustofluidic research.

6.1 Conclusion

The results in this thesis revolves around three separate papers, which are stand alone results but which complements each other. The first paper showed that it is possible actuate bulk acoustic modes in glass by piezoelectric (PZE) thin-films deposited on it and that our model gives the correct mode spectra. This gives us confidence in our model and helps us in the second paper to predict how PZE thin-film transducers can be used to actuate acoustofluidic devices that can be used for focusing of particles in the fluids, or in general to actuate the system to achieve the same manner of acoustofluidic action as with a bulk PZE transducers. The thin-film transducers are clean-room and microelectromechanical systems (MEMS) compatible and therefore the processes are very reproducible and precise, as we saw in the first paper the devices were quite reproducible when comparing the impedance spectra. This reproducibility of the small glass block devices we expect will carry over to the larger devices to an even larger degree as the small variations in the small device, because of tolerances and small chips of the edge, would be relatively smaller for the large devices. Reproducibility of results, and in this case of devices, is a corner stone of being able to understand and build upon the results to develop the devices and techniques further in an ever inward spiraling development of precision, control and understanding.

The second paper also found that matching the electrode patterning of PZE thin-films

to the strain pattern in the film, generated by mode in the solid, was important. It was shown that by patterning the electrodes it was possible to enhance the acoustofluidic action. By this is meant the first order pressure field, acoustic streaming field and the acoustic radiation forces in the system of the standing full wave in the device. This was because the in-plane strain pattern was trying to both expand at some places and contract at other at same time, and through the PZE coupling coefficient e_{13} the orthogonal field would try to either compress or expand depending on the polarity of the electric field. A full electrode would therefore try to work against itself as it would only try to expand or contract at any given phase. It was understood that this effect would be even more prominent in systems with many wavelengths. This is because for such systems the area that would effectively actuate the system would be limited to the area that did not cancel out, and that area would diminish with a full electrode over more wavelengths. This knowledge was used to predict that it would be possible to access the higher order modes of a membrane with a thin-film deposited on it, by patterning it correspondingly, which turned out to be correct. It was subsequently guessed that, because of how the Bessel modes in the membrane look, these modes might create an interference pattern and a pressure hot spot at a point above the center of the membrane, which might focus particles. It turned out to be the case however because of the axisymmetry the pressure and the central axis must be a node, and therefore only particles with negative acoustic contrast factor would be focused. Therefore in order to focus the cancer cells investigated, the submersion fluid had to be changed to Iodixanol concentrations. It was further shown that by tuning the density in the model the trapping could even be enhanced.

6.2 Outlook

This PhD thesis has shown some *in situ* experimental determination of parameter values, by using PZE thin-film, which could be further developed in the future. It has also shown some simulation of thin-film-PZE-driven bulk-whole-system and membrane-driven results that would benefit greatly from experimental validation. How the results can be used in the future will be discussed first. Afterwards some ideas for further exploration in acoustofluidics that would have been nice to investigate will be presented. Lastly a larger perspective on it all will conclude this thesis.

Results going forward

The main results are centered around three separate results and the outlook for each is quite different. The first result showed that it is indeed possible to determine the material parameters of a material by matching the impedance spectra of a thin-film attached to the device. This worked in part because the thin-film PZE was such a small part of the system that the accuracy of the parameters of the PZE thin-film did not effect the system significantly. The parameters for the isotropic bulk material could therefore be fitted without worrying about the the many parameters of the hexagonal aluminum nitride (AlN). One problem with the method is that it is limited to materials that can have AlN thin-films deposited unto it, and require access to a clean-room that can do it. One might

imagine that a possible way to get around this could be by using thin-film PZE stickers, that had a sacrificial layer on one side which is stiff but dissolvable, and thin adhesion layer on the other side of the PZE thin-film, to attach to materials, and then the same procedure could be carried out to fit and match material parameters. This might work because we do not need high acoustic energy in the system, but only enough to get a response from the material. Whether it could work or not is not known, but is an idea for how this method could be used going forward.

The second result shows that thin-film transducers could actuate bulk devices for uses in acoustofluidics. The results are based on simulations and although the model has previously been validated on other experiments, it would be interesting to compare with experiments to further validate the model, but more importantly to engage in a feedback loop that could help further understand the mechanism and improve the concept. Early results have shown that the core concept work, in that a acoustofluidic bulk system can indeed be actuated by a thin-film PZE transducer, showing acoustic focusing of particles in a device, however these are early results, and since they are not this thesis author's results alone, have not been emphasized in this thesis. However new experimental results are on the way from some of our experimental collaborators, which is very interesting and the author of this thesis is looking very much forward to. There are many possibilities for these devices and exactly how they can be used in the future is difficult to guess.

The third result is the enhancement of the higher order membrane modes, by patterning the electrode of the thin-film deposited on top of the membrane. These these mode are therefore enhanced and the pressure hot spot above the center of the thin-film allows for trapping of cells with a change of the submersion fluid. The result would be nice to have see validated in a experiment in the future, as the trapping shows promise. The hope is that in the future it could become a standalone device, used for trapping arrays of cells, when they for one reason or other cannot be allowed to sediment. An example of such is studying cells that more mimic conditions of free floating circulating tumor cells, instead of how cancer cells grows on the surface of a petri dish. One might imagine that the devices would be placed in a petri dish and fluid would be added with the cells containing it, and then turned on, at which point the cells would be suspended in the array above the membranes for the duration of a biological assay. There are of course also many other uses for enhancing membrane modes which the future might show, and we only can speculate on at this point. Some of these speculations will be expanded upon next.

Further explorations in acoustofluidics

One of the things that would have been nice to explore further is expanding the parameter fitting in Paper I, to a more advanced and autonomous fitting procedure such that the we might not only have gotten a better fit on the Young's modulus and Poisson's ratio of the glass parameters, but might also have gotten a fitting of the dampening in the device. How this dampening would have behaved would have been a nice result to add to the already fitted parameters. The parameters of the thin-film would most likely not have been possible to fit to in this system, simply because the bulk peaks were so insensitive to the parameters of the film, where changes in the thin-film parameters of $\pm 25\%$ only changed the resonance peaks less than one percent. If the thin-film parameters should

be fitted as well, then it would properly only be possible if the geometry of such fitting devices put emphasis on the thin-films importance, such as thin membranes where the PZE thin-film would play a large portion of the film thickness. The only parameter in the film that might have been possible to fit to with the data available in the data from the glass block devices is the PZE couplings coefficient e_{31} which has a somewhat effect, especially on the amplitude, however this would still only have been possible after the material parameters of the glass was better determined.

For the thin-film acoustofluidic devices that were presented in paper II there were several possible avenues that one might take to further explore this. One of the promising ones are the possibility of using topology optimization on the electrode patterning, in order to maximize the acoustical energy and minimize losses for optimal acoustofluidic action in the device with minimal heating. The method might be promising because it is possible to very precisely control the electrode deposition with clean-room techniques, and because the electrode patterns that would prove useful in for example a flow through experiment does not necessarily need to have a very clean looking mode along the length of the device in order to perform well. With the technique of looking at the out-of-phase strain pattern of a simulation, it might help the topology optimization algorithm along as a good and efficient starting point.

One small result that would have been interesting to investigate further is small devices have a membrane resonance and a bulk resonance that lie close to each other, and which showed anti-crossing behavior and amplification of the acoustofluidic modes. These devices lie somewhat in the cross between the thin-film bulk acoustofluidic devices results and the thin-film membrane devices results. In the end they might be difficult to produce and handle as they would require tight tolerances in both the membrane and the device geometries.

The results on the axisymmetric membrane actuation could be extended to include non-axisymmetric membrane actuation. This might allow for strong high-order membrane actuation that also had an phase dependence, such as the Bessel modes with a axial phase mode different from zero, as this would allow for there to be a node in the center of the membrane instead of a anti-node. This might allow for there to be a pressure node in the center, as has been seen in the literature Ref. 35, and therefore it might allow for trapping in the center of the axis of cells and particles with positive acoustic contrast factor.

One of the fields that could be interesting to explore is gigahertz acoustofluidics as there are many experimental results in the literature and they are showing very interesting results. However as their systems are inherently many wavelengths systems, they are often demanding to simulate. The effective boundary layer theory by Bach and Bruus Ref. 78 allows for the possibility of simulating higher frequency systems that would be possible without them because the meshing of the boundary layer that otherwise would be needed would not allow for the large system to be properly be resolved.

One of the more promising concepts that would have been interesting to explore is the possibility of using the acoustic reflections of a cell or particle to determine the the type of the particle or cell. Because the acoustic reflections of a cell or particle depend on their acoustical properties then it might be possible to listen to the reflections by a *mechanical ear*, described below, and thereby through electromechanical feedback detect

and classify the cell types all done electronically without the need for any invasive fluid changes, cell harming light, labeling, or time consuming analysis. While the reflections of a cell is not very different from an other cell which has close to the same cell diameter with parameter values that are close to each other in the long wavelength limit, the small differences most likely becomes much more pronounced close to resonances of the cell and even more so at the higher overtones of the cell, because of the complex way acoustic resonances operate in high wavelength systems. The mechanical ear would be some kind of piezoelectric resonator, such as a thin-film with a maybe a membrane as a resonator at lower frequencies, and just using the bulk resonances in the thin-film at high frequencies. As shown by Pulskamp *et al.* Ref. 151, by patterning the electrodes correctly the sensitivity to different modes can be enhanced greatly. Having a host of different designs to pick up the reflections that would arise from cells at resonance, actuated by a wide frequency sweep, might make it possible characterize them. Such signals from a host of different microphones would be ideal for training a machine learning algorithm to detect types of cells. Since the overtones probably are very distinct it might even be possible to individual cells out of a tight suspension of other cells. While this is all speculations at this point, if the PhD had gone on for longer this idea would probably have been high on the list of subjects that would have been interesting to investigate further.

A future of acoustofluidics where these results play a role

It is difficult to predict the future, and what role these results will have in the such a future is more guess work than anything else. However to leave the reader with an impression of what the author of this thesis hopes for the future of the these results, some guessing will be done. For the bio-medical industry in diagnostics, it is important to have single use devices, where cross contamination is a no-go. It is difficult to image a future where such single use devices are made by permanently attached lead-full transducers. It is difficult to image partly because lead is environmentally hazardous, and is therefore being phased out, and partly because such devices have been proven to have difficulty in produce consistent result. This is where the thin-film devices come into the picture. Sputtering AlN or AlScN thin-films onto devices in a role-to-role scenario, makes it possible to manufacture mass scale devices in a lead free way, which has also been proven to give reproducible results, where however the acoustofluidic capabilities remains to be tested. This would probably bring the cost of the devices down to a point where they could be used as single use devices, which could easily and safely be dispose of. This could open up for applications that could make acoustofluidic medical devices a big player in the market, with applications only being limited by the creativity of the acoustofluidic community. The concept of amplifying specific mechanical thin.film driven modes by looking at the out of phase strain, also could see uses in the future. One example of this is the membrane trapping devices which show promise, and if they indeed work as the simulations predict, they could become a staple in the a research or production environment in the future. There are many situations where such label free trapping in system that can not have a lid, could see uses. The example that has been mentioned is an assay study in a petri dish, but many biological studies require that cells be are trapped without being in contact with a surface while other processes are done to them. It can be a far fetched hoped that this

or derivations from this could be a mainstay in laboratories in the future. Where exactly the results and ideas presented in this thesis will end up only the future truly will tell.

Bibliography

- [1] A. G. Steckel and H. Bruus, *Numerical study of bulk acoustofluidic devices driven by thin-film transducers and whole-system resonance modes*. The Journal of the Acoustical Society of America **150**(1), 634–645 (2021).
- [2] A. G. Steckel, H. Bruus, P. Muralt, and R. Matloub, *Fabrication, characterization, and simulation of glass devices with AlN thin-film transducers for excitation of ultrasound resonances*. Physical Review Applied **16**(1), 014014 (2021).
- [3] A. G. Steckel and H. Bruus, *Numerical study of acoustic cell trapping above circular elastic membranes driven by thin-film transducers with patterned electrodes*. In preparation (2021).
- [4] O. Cramer, *The variation of the specific heat ratio and the speed of sound in air with temperature, pressure, humidity, and co2 concentration*. The Journal of the Acoustical Society of America **93**(5), 2510–2516 (1993).
- [5] S. Preston, P. Steart, A. Wilkinson, J. Nicoll, and R. Weller, *Capillary and arterial cerebral amyloid angiopathy in alzheimer’s disease: defining the perivascular route for the elimination of amyloid β from the human brain*. Neuropathology and applied neurobiology **29**(2), 106–117 (2003).
- [6] Y. Wang, W.-Y. Lin, K. Liu, R. J. Lin, M. Selke, H. C. Kolb, N. Zhang, X.-Z. Zhao, M. E. Phelps, C. K. Shen, *et al.*, *An integrated microfluidic device for large-scale in situ click chemistry screening*. Lab on a Chip **9**(16), 2281–2285 (2009).
- [7] P. Neuzil, S. Giselbrecht, K. Lange, T. J. Huang, and A. Manz, *Revisiting lab-on-a-chip technology for drug discovery*. Nature reviews Drug discovery **11**(8), 620–632 (2012).
- [8] N. Pamme and C. Wilhelm, *Continuous sorting of magnetic cells via on-chip free-flow magnetophoresis*. Lab on a Chip **6**(8), 974 (2006).
- [9] D. Holmes, D. Pettigrew, C. H. Reccius, J. D. Gwyer, C. van Berkel, J. Holloway, D. E. Davies, and H. Morgan, *Leukocyte analysis and differentiation using high speed microfluidic single cell impedance cytometry*. Lab on a Chip **9**(20), 2881–2889 (2009).
- [10] D. Figeys and D. Pinto, *Lab-on-a-chip: a revolution in biological and medical sciences*. (2000).

- [11] M. Mir, A. Homs, and J. Samitier, *Integrated electrochemical dna biosensors for lab-on-a-chip devices*. *Electrophoresis* **30**(19), 3386–3397 (2009).
- [12] S.-S. Hsieh, C.-Y. Lin, C.-F. Huang, and H.-H. Tsai, *Liquid flow in a micro-channel*. *Journal of Micromechanics and Microengineering* **14**(4), 436 (2004).
- [13] P. J. Kenis, R. F. Ismagilov, and G. M. Whitesides, *Microfabrication inside capillaries using multiphase laminar flow patterning*. *Science* **285**(5424), 83–85 (1999).
- [14] A. J. Mach and D. Di Carlo, *Continuous scalable blood filtration device using inertial microfluidics*. *Biotechnol Bioeng* **107**(2), 302–311 (2010).
- [15] P. Ohlsson, M. Evander, K. Petersson, L. Mellhammar, A. Lehmusvuori, U. Karhunen, M. Soikkeli, T. Seppa, E. Tuunainen, A. Spangar, P. von Lode, K. Rantakokko-Jalava, G. Otto, S. Scheduling, T. Soukka, S. Wittfooth, and T. Laurell, *Integrated acoustic separation, enrichment, and microchip polymerase chain reaction detection of bacteria from blood for rapid sepsis diagnostics*. *Analytical Chemistry* **88**(19), 9403–9411 (2016).
- [16] S. Zheng, H. K. Lin, B. Lu, A. Williams, R. Datar, R. J. Cote, and Y.-C. Tai, *3d microfilter device for viable circulating tumor cell (ctc) enrichment from blood*. *Biomed Microdevices* **13**(1), 203–213 (2011).
- [17] M. Antfolk, C. Magnusson, P. Augustsson, H. Lilja, and T. Laurell, *Acoustofluidic, label-free separation and simultaneous concentration of rare tumor cells from white blood cells*. *Anal. Chem.* **87**(18), 9322–9328 (2015).
- [18] F.-C. Bidard, C. Mathiot, S. Delaloge, E. Brain, S. Giachetti, P. De Cremoux, M. Marty, and J.-Y. Pierga, *Single circulating tumor cell detection and overall survival in nonmetastatic breast cancer*. *Annals of Oncology* **21**(4), 729–733 (2010).
- [19] P. Augustsson, C. Magnusson, M. Nordin, H. Lilja, and T. Laurell, *Microfluidic, label-free enrichment of prostate cancer cells in blood based on acoustophoresis*. *Anal. Chem.* **84**(18), 7954–7962 (2012).
- [20] A. Lenshof, A. Ahmad-Tajudin, K. Jaras, A.-M. Sward-Nilsson, L. Aberg, G. Marko-Varga, J. Malm, H. Lilja, and T. Laurell, *Acoustic whole blood plasmapheresis chip for prostate specific antigen microarray diagnostics*. *Anal. Chem.* **81**(15), 6030–6037 (2009).
- [21] M. Tenje, A. Fornell, M. Ohlin, and J. Nilsson, *Particle manipulation methods in droplet microfluidics* (2018).
- [22] A. Bussonniere, Y. Miron, M. Baudoin, O. Bou Matar, M. Grandbois, P. Charette, and A. Renaudin, *Cell detachment and label-free cell sorting using modulated surface acoustic waves (SAWs) in droplet-based microfluidics*. *Lab Chip* **14**, 3556–3563 (2014).

- [23] A. Fornell, K. Cushing, J. Nilsson, and M. Tenje, *Binary particle separation in droplet microfluidics using acoustophoresis*. *Appl. Phys. Lett.* **112**(6), 063701 (2018).
- [24] D. J. Collins, A. Neild, A. DeMello, A.-Q. Liu, and Y. Ai, *The poisson distribution and beyond: methods for microfluidic droplet production and single cell encapsulation*. *Lab on a Chip* **15**(17), 3439–3459 (2015).
- [25] T. Laurell, F. Petersson, and A. Nilsson, *Chip integrated strategies for acoustic separation and manipulation of cells and particles*. *Chem Soc Rev* **36**(3), 492–506 (2007).
- [26] P. Ohlsson, K. Petersson, P. Augustsson, and T. Laurell, *Acoustic impedance matched buffers enable separation of bacteria from blood cells at high cell concentrations*. *Sci. Rep.* **8**, 2045–2322 (2018).
- [27] D. J. Collins, A. Neild, and Y. Ai, *Highly focused high-frequency travelling surface acoustic waves (saw) for rapid single-particle sorting*. *Lab Chip* **16**, 471–479 (2016).
- [28] P. Augustsson, J. T. Karlsen, H.-W. Su, H. Bruus, and J. Voldman, *Iso-acoustic focusing of cells for size-insensitive acousto-mechanical phenotyping*. *Nat. Commun.* **7**, 11556 (2016).
- [29] K. Olofsson, B. Hammarstrom, and M. Wiklund, *Acoustic separation of living and dead cells using high density medium*. *LAB ON A CHIP* **20**(11), 1981–1990 (2020).
- [30] H.-D. Xi, H. Zheng, W. Guo, A. M. Gañán-Calvo, Y. Ai, C.-W. Tsao, J. Zhou, W. Li, Y. Huang, N.-T. Nguyen, *et al.*, *Active droplet sorting in microfluidics: a review*. *Lab on a Chip* **17**(5), 751–771 (2017).
- [31] C. Zhang, P. Brunet, L. Royon, and X. Guo, *Mixing intensification using sound-driven micromixer with sharp edges*. *Chemical Engineering Journal* **410**, 128252 (2021).
- [32] R. J. Shilton, L. Y. Yeo, and J. R. Friend, *Quantification of surface acoustic wave induced chaotic mixing-flows in microfluidic wells*. *Sensors and Actuators B: Chemical* **160**(1), 1565–1572 (2011).
- [33] J. Nam, W. S. Jang, and C. S. Lim, *Micromixing using a conductive liquid-based focused surface acoustic wave (cl-fsaw)*. *Sensors and Actuators B: Chemical* **258**, 991–997 (2018).
- [34] T. Frommelt, M. Kostur, M. Wenzel-Schaefer, P. Talkner, P. Haenggi, and A. Wixforth, *Microfluidic mixing via acoustically driven chaotic advection*. *Phys. Rev. Lett.* **100**(3), 034502 (2008).
- [35] D. Baresch, J.-L. Thomas, and R. Marchiano, *Observation of a single-beam gradient force acoustical trap for elastic particles: Acoustical tweezers*. *Phys. Rev. Lett.* **116**, 024301 (2016).

- [36] D. Baresch, J.-L. Thomas, and R. Marchiano, *Orbital angular momentum transfer to stably trapped elastic particles in acoustical vortex beams*. Physical review letters **121**(7), 074301 (2018).
- [37] D. Baresch, J.-L. Thomas, and R. Marchiano, *Three-dimensional acoustic radiation force on an arbitrarily located elastic sphere*. J. Acoust. Soc. Am. **133**(1), 25–36 (2013).
- [38] M. Baudoin, J.-C. Gerbedoen, A. Riaud, O. B. Matar, N. Smagin, and J.-L. Thomas, *Folding a focalized acoustical vortex on a flat holographic transducer: miniaturized selective acoustical tweezers*. Science advances **5**(4), eaav1967 (2019).
- [39] D. Foresti, M. Nabavi, and D. Poulikakos, *On the acoustic levitation stability behaviour of spherical and ellipsoidal particles*. J. Fluid Mech. **709**, 581–592 (2012).
- [40] P. Gammel, A. Croonquist, and T. Wang, *A high-powered siren for stable acoustic levitation of dense materials in the earths gravity*. J. Acoust. Soc. Am. **83**(2), 496–501 (1988).
- [41] A. Marzo, S. A. Seah, B. W. Drinkwater, D. R. Sahoo, B. Long, and S. Subramanian, *Holographic acoustic elements for manipulation of levitated objects*. Nat. Commun. **6**, 8661 (2015).
- [42] S. Santesson and S. Nilsson, *Airborne chemistry: acoustic levitation in chemical analysis*. Anal. Bioanal. Chem. **378**(7), 1704–1709 (2004).
- [43] E. Trinh, *Compact acoustic levitation device for studies in fluid dynamics and material science in the laboratory and microgravity*. Rev. Sci. Instrum. **56**(11), 2059–2065 (1985).
- [44] M. A. Andrade, A. Marzo, and J. C. Adamowski, *Acoustic levitation in mid-air: recent advances, challenges, and future perspectives*. Applied Physics Letters **116**(25), 250501 (2020).
- [45] S. Polychronopoulos and G. Memoli, *Acoustic levitation with optimized reflective metamaterials*. Scientific reports **10**(1), 1–10 (2020).
- [46] M. A. Andrade, T. S. Ramos, J. C. Adamowski, and A. Marzo, *Contactless pick-and-place of millimetric objects using inverted near-field acoustic levitation*. Applied Physics Letters **116**(5), 054104 (2020).
- [47] M. A. Andrade, N. Pérez, and J. C. Adamowski, *Review of progress in acoustic levitation*. Brazilian Journal of Physics **48**(2), 190–213 (2018).
- [48] X. Chen, K. H. Lam, R. Chen, Z. Chen, X. Qian, J. Zhang, P. Yu, and Q. Zhou, *Acoustic levitation and manipulation by a high-frequency focused ring ultrasonic transducer*. Applied Physics Letters **114**(5), 054103 (2019).

- [49] V. Vandaele, A. Delchambre, and P. Lambert, *Acoustic wave levitation: Handling of components*. J. Appl. Phys. **109**(12), 124901 (2011).
- [50] V. Vandaele, P. Lambert, and A. Delchambre, *Non-contact handling in microassembly: Acoustical levitation*. Precis. Eng. **29**(4), 491–505 (2005).
- [51] P.-H. Huang, C. Y. Chan, P. Li, N. Nama, Y. Xie, C.-H. Wei, Y. Chen, D. Ahmed, and T. J. Huang, *A spatiotemporally controllable chemical gradient generator via acoustically oscillating sharp-edge structures*. Lab on a Chip **15**(21), 4166–4176 (2015).
- [52] C. Zhang, X. Guo, P. Brunet, M. Costalonga, and L. Royon, *Acoustic streaming near a sharp structure and its mixing performance characterization*. Microfluidics Nanofluidics **23**(9), 104 (2019).
- [53] X. Guo, Z. Ma, R. Goyal, M. Jeong, W. Pang, P. Fischer, X. Duan, and T. Qiu, *Acoustofluidic tweezers for the 3d manipulation of microparticles*. In *2020 IEEE International Conference on Robotics and Automation (ICRA)*, 11392–11397 (IEEE) (2020).
- [54] S. Wang, Z. Wang, Y. Ning, X. Chen, X. Duan, W. Pang, and Q. Yang, *Particle manipulation by a novel lamb wave resonator array with grating reflectors*. In *2020 IEEE International Ultrasonics Symposium (IUS)*, 1–4 (IEEE) (2020).
- [55] W. Cui, L. Mu, X. Duan, W. Pang, and M. A. Reed, *Trapping of sub-100 nm nanoparticles using gigahertz acoustofluidic tweezers for biosensing applications*. Nanoscale **11**(31), 14625–14634 (2019).
- [56] F. Petersson, A. Nilsson, C. Holm, H. Jönsson, and T. Laurell, *Separation of lipids from blood utilizing ultrasonic standing waves in microfluidic channels*. Analyst **129**(10), 938–43 (2004).
- [57] M. Hamilton, Y. Ilinskii, and E. Zabolotskaya, *Acoustic streaming generated by standing waves in two-dimensional channels of arbitrary width*. J. Acoust. Soc. Am. **113**(1), 153–160 (2003).
- [58] B. Hammarström, M. Evander, H. Barbeau, M. Bruzelius, J. Larsson, T. Laurell, and J. Nilsson, *Non-contact acoustic cell trapping in disposable glass capillaries*. Lab Chip **10**(17), 2251–2257 (2010).
- [59] M. Wiklund, C. Günther, R. Lemor, M. Jäger, G. Fuhr, and H. M. Hertz, *Ultrasonic standing wave manipulation technology integrated into a dielectrophoretic chip*. Lab on a Chip **6**(12), 1537–1544 (2006).
- [60] P. Reichert, D. Deshmukh, L. Lebovitz, and J. Dual, *Thin film piezoelectrics for bulk acoustic wave (BAW) acoustophoresis*. Lab Chip **18**(23), 3655–3667 (2018).

- [61] P. Delsing, A. N. Cleland, M. J. Schuetz, J. Knörzer, G. Giedke, J. I. Cirac, K. Srinivasan, M. Wu, K. C. Balram, C. Bäuerle, *et al.*, *The 2019 surface acoustic waves roadmap*. Journal of Physics D: Applied Physics **52**(35), 353001 (2019).
- [62] M. S. Gerlt, N. F. Läubli, M. Manser, B. J. Nelson, and J. Dual, *Reduced etch lag and high aspect ratios by deep reactive ion etching (drie)*. Micromachines **12**(5), 542 (2021).
- [63] M. Gerlt, P. Ruppen, M. Leuthner, S. Panke, and J. Dual, *Acoustofluidic medium exchange for preparation of electrocompetent bacteria using channel wall trapping*. Chem Archive (2021).
- [64] M. Barmatz, *Acoustic radiation potential on a sphere in plane, cylindrical, and spherical standing wave fields*. J. Acoust. Soc. Am. **77**(3), 928 (1985).
- [65] K. Yasuda and T. Kamakura, *Acoustic radiation force on micrometer-size particles*. Appl. Phys. Lett. **71**(13), 1771–1773 (1997).
- [66] P. B. Muller, R. Barnkob, M. J. H. Jensen, and H. Bruus, *A numerical study of microparticle acoustophoresis driven by acoustic radiation forces and streaming-induced drag forces*. Lab Chip **12**, 4617–4627 (2012).
- [67] M. Settnes and H. Bruus, *Theoretical analysis of viscous corrections to the acoustic radiation force on cells in microchannel acoustophoresis*. In J. Landers, A. Herr, D. Juncker, N. Pamme, and J. Bienvenue (eds.), *Proc. 15th MicroTAS, 2 - 6 October 2011, Seattle (WA), USA*, 160–162 (CBMS) (2011).
- [68] G. T. Silva, *Acoustic radiation force and torque on an absorbing compressible particle in an inviscid fluid*. J. Acoust. Soc. Am. **136**(5), 2405–2413 (2014).
- [69] G. T. Silva, *Dynamic radiation force of acoustic waves on absorbing spheres*. Braz. J. Phys. **40**(2), 184–187 (2010).
- [70] G. T. Silva, M. W. Urban, and M. Fatemi, *Multifrequency radiation force of acoustic waves in fluids*. Physica D: Nonlinear Phenomena **232**(1), 48–53 (2007).
- [71] P. Hahn, I. Leibacher, T. Baasch, and J. Dual, *Numerical simulation of acoustofluidic manipulation by radiation forces and acoustic streaming for complex particles*. Lab Chip **15**, 4302–4313 (2015).
- [72] J. T. Karlsen and H. Bruus, *Forces acting on a small particle in an acoustical field in a thermoviscous fluid*. Phys. Rev. E **92**, 043010 (2015).
- [73] P. B. Muller, *Acoustofluidics in microsystems: investigation of acoustic streaming*. Master’s thesis, DTU Nanotech, Department of Micro- and Nanotechnology (2012 (www.nanotech.dtu.dk/microfluidics)).
- [74] N. Riley, *Acoustic streaming*. Theoretical and Computational Fluid Dynamics **10**(1), 349–356 (1998).

- [75] J. Lighthill, *Acoustic streaming*. J Sound Vibr **61**(3), 391–418 (1978).
- [76] S. Boluriaan and P. J. Morris, *Acoustic streaming: from rayleigh to today*. International Journal of aeroacoustics **2**(3), 255–292 (2003).
- [77] J. S. Bach and H. Bruus, *Bulk-driven acoustic streaming at resonance in closed microcavities*. Phys. Rev. E **100**, 023104 (2019).
- [78] J. S. Bach and H. Bruus, *Theory of pressure acoustics with viscous boundary layers and streaming in curved elastic cavities*. J. Acoust. Soc. Am. **144**, 766–784 (2018).
- [79] H. G. Lim, Y. Li, M.-Y. Lin, C. Yoon, C. Lee, H. Jung, R. H. Chow, and K. K. Shung, *Calibration of trapping force on cell-size objects from ultrahigh-frequency single-beam acoustic tweezer*. IEEE IEEE T. Ultrason. Ferr. **63**(11), 1988–1995 (2016).
- [80] J. S. Bach and H. Bruus, *Suppression of acoustic streaming in shape-optimized channels*. Phys. Rev. Lett. **124**, 214501 (2020).
- [81] A. Lenshof and T. Laurell, *Continuous separation of cells and particles in microfluidic systems*. Chem Soc Rev **39**(3), 1203–1217 (2010).
- [82] B. Hammarström, B. Nilsson, T. Laurell, J. Nilsson, and S. Ekström, *Acoustic trapping for bacteria identification in positive blood cultures with maldi-tof ms*. Anal. Chem. **86**(21), 10560–10567 (2014).
- [83] K. Olofsson, V. Carannante, M. Takai, B. Onfelt, and M. Wiklund, *Ultrasound-based scaffold-free core-shell multicellular tumor spheroid formation*. MICROMACHINES **12**(3) (2021).
- [84] M. Antfolk and T. Laurell, *Continuous flow microfluidic separation and processing of rare cells and bioparticles found in blood - a review*. Anal. Chim. Acta **965**, 9–35 (2017).
- [85] S. Deshmukh, Z. Brzozka, T. Laurell, and P. Augustsson, *Acoustic radiation forces at liquid interfaces impact the performance of acoustophoresis*. Lab Chip **14**, 3394–3400 (2014).
- [86] W. N. Bodé and H. Bruus, *Numerical study of the coupling layer between transducer and chip in acoustofluidic devices*. J. Acoust. Soc. Am. **149**(5), 3096–3105 (2021).
- [87] M. Safaei, H. A. Sodano, and S. R. Anton, *A review of energy harvesting using piezoelectric materials: state-of-the-art a decade later (2008–2018)*. Smart Materials and Structures **28**(11), 113001 (2019).
- [88] T. Takenaka and H. Nagata, *Current status and prospects of lead-free piezoelectric ceramics*. Journal of the European Ceramic Society **25**(12), 2693–2700 (2005).
- [89] K. Uchino, *The development of piezoelectric materials and the new perspective*. In *Advanced Piezoelectric Materials*, 1–92 (Elsevier) (2017).

- [90] S. Priya and S. Nahm, *Lead-free piezoelectrics* (Springer Science & Business Media) (2011).
- [91] E. Ringgaard and T. Wurlitzer, *Lead-free piezoceramics based on alkali niobates*. Journal of the European Ceramic Society **25**(12), 2701–2706 (2005).
- [92] R. Korobko, A. Patlolla, A. Kossoy, E. Wachtel, H. L. Tuller, A. I. Frenkel, and I. Lubomirsky, *Giant electrostriction in gd-doped ceria*. Advanced Materials **24**(43), 5857–5861 (2012).
- [93] N. R. Skov, J. S. Bach, B. G. Winkelmann, and H. Bruus, *3D modeling of acoustofluidics in a liquid-filled cavity including streaming, viscous boundary layers, surrounding solids, and a piezoelectric transducer*. AIMS Mathematics **4**, 99–111 (2019).
- [94] H. Bruus, *Theoretical Microfluidics* (Oxford University Press, Oxford) (2008).
- [95] H. Bruus, *Acoustofluidics 1: Governing equations in microfluidics*. Lab Chip **11**, 3742 – 3751 (2011).
- [96] H. Bruus, *Acoustofluidics 2: Perturbation theory and ultrasound resonance modes*. Lab Chip **12**, 20–28 (2012).
- [97] J. Dual and T. Schwarz, *Acoustofluidics 3: Continuum mechanics for ultrasonic particle manipulation*. Lab Chip **12**, 244–252 (2012).
- [98] J. Dual and D. Möller, *Acoustofluidics 4: Piezoelectricity and application to the excitation of acoustic fields for ultrasonic particle manipulation*. Lab Chip **12**, 506–514 (2012).
- [99] A. Lenshof, M. Evander, T. Laurell, and J. Nilsson, *Acoustofluidics 5: Building microfluidic acoustic resonators*. Lab Chip **12**, 684–695 (2012).
- [100] J. Dual, P. Hahn, I. Leibacher, D. Möller, and T. Schwarz, *Acoustofluidics 6: Experimental characterization of ultrasonic particle manipulation devices*. Lab Chip **12**, 852–862 (2012).
- [101] H. Bruus, *Acoustofluidics 7: The acoustic radiation force on small particles*. Lab Chip **12**, 1014–1021 (2012).
- [102] A. Lenshof, C. Magnusson, and T. Laurell, *Acoustofluidics 8: Applications in acoustophoresis in continuous flow microsystems*. Lab Chip **12**, 1210–1223 (2012).
- [103] P. Glynne-Jones, R. J. Boltryk, and M. Hill, *Acoustofluidics 9: Modelling and applications of planar resonant devices for acoustic particle manipulation*. Lab Chip **12**(8), 1417–1426 (2012).
- [104] H. Bruus, *Acoustofluidics 10: Scaling laws in acoustophoresis*. Lab Chip **12**, 1578–1586 (2012).

-
- [105] P. Augustsson and T. Laurell, *Acoustofluidics 11: Affinity specific extraction and sample decomplexing using continuous flow acoustophoresis*. Lab Chip **12**, 1742–1752 (2012).
- [106] M. Wiklund, *Acoustofluidics 12: Biocompatibility and cell viability in microfluidic acoustic resonators*. Lab Chip **12**, 2018–28 (2012).
- [107] S. Sadhal, *Acoustofluidics 13: Analysis of acoustic streaming by singular perturbation*. Lab Chip **12**, 2292–2300 (2012).
- [108] M. Wiklund, R. Green, and M. Ohlin, *Acoustofluidics 14: Applications of acoustic streaming in microfluidic devices*. Lab Chip **12**, 2438–2451 (2012).
- [109] S. Sadhal, *Acoustofluidics 15: Streaming with sound waves interacting with solid particles*. Lab Chip **12**, 2600–2611 (2012).
- [110] S. S. Sadhal, *Acoustofluidics 16: acoustics streaming near liquid-gas interfaces: drops and bubbles*. Lab on a chip **12**(16), 2771–2781 (2012).
- [111] M. Gedge and M. Hill, *Acoustofluidics 17: Surface acoustic wave devices for particle manipulation*. Lab Chip **12**, 2998–3007 (2012).
- [112] M. Wiklund, H. Brismar, and B. Önfelt, *Acoustofluidics 18: Microscopy for acoustofluidic micro-devices*. Lab on a Chip **12**(18), 3221–3234 (2012).
- [113] J. Dual, P. Hahn, I. Leibacher, D. Möller, T. Schwarz, and J. Wang, *Acoustofluidics 19: ultrasonic microrobotics in cavities: devices and numerical simulation*. Lab on a chip **12**(20), 4010–4021 (2012).
- [114] M. Evander and J. Nilsson, *Acoustofluidics 20: Applications in acoustic trapping*. Lab Chip **12**, 4667–4676 (2012).
- [115] M. W. H. Ley, C. Johannesson, M. Evander, T. Laurell, and H. Bruus, *Modeling and experiments of acoustic trapping forces in a small glass capillary*. Proc. 20th MicroTAS, 9 - 13 October 2016, Dublin, Ireland 711–712 (2016).
- [116] P. B. Muller and H. Bruus, *Theoretical study of time-dependent, ultrasound-induced acoustic streaming in microchannels*. Phys. Rev. E **92**, 063018 (2015).
- [117] P. B. Muller and H. Bruus, *Numerical study of thermoviscous effects in ultrasound-induced acoustic streaming in microchannels*. Phys. Rev. E **90**(4), 043016 (2014).
- [118] J. H. Joergensen and H. Bruus, *Theory of pressure acoustics with thermoviscous boundary layers and streaming in elastic cavities*. The Journal of the Acoustical Society of America **149**(5), 3599–3610 (2021).
- [119] J. S. Bach and H. Bruus, *Theory of acoustic trapping of microparticles in capillary tubes*. Physical Review E **101**(2), 023107 (2020).

- [120] J. T. Karlsen and H. Bruus, *Acoustic tweezing and patterning of concentration fields in microfluidics*. Phys. Rev. Applied **7**, 034017 (2017).
- [121] B. Lautrup, *Physics of continuous matter: exotic and everyday phenomena in the macroscopic world* (CRC press) (2011).
- [122] M. W. H. Ley and H. Bruus, *Three-dimensional numerical modeling of acoustic trapping in glass capillaries*. Phys. Rev. Applied **8**, 024020 (2017).
- [123] P. Muralt, *Ferroelectric thin films for micro-sensors and actuators: a review*. Journal of micromechanics and microengineering **10**(2), 136 (2000).
- [124] P. Muralt, *Pzt thin films for microsensors and actuators: Where do we stand?* IEEE transactions on ultrasonics, ferroelectrics, and frequency control **47**(4), 903–915 (2000).
- [125] P. Muralt, *Recent progress in materials issues for piezoelectric MEMS*. J. Am. C. Soc. **91**(5), 1385–1396 (2008).
- [126] W. L. Nyborg, *Acoustic streaming near a boundary*. J. Acoust. Soc. Am. **30**(4), 329–339 (1958).
- [127] C. Lee and T. Wang, *Near-boundary streaming around a small sphere due to 2 orthogonal standing waves*. J. Acoust. Soc. Am. **85**(3), 1081–1088 (1989).
- [128] M. R. Spiegel, S. Lipschutz, and J. Liu, *Schaum's Outlines: Mathematical Handbook of Formulas and Tables*, vol. 3 (McGraw-Hill New York) (2009).
- [129] J. S. Bach, *Theory of acoustic fields and streaming with viscous boundary layers in microsystems* (2020).
- [130] M. Settnes and H. Bruus, *Forces acting on a small particle in an acoustical field in a viscous fluid*. Phys. Rev. E **85**, 016327 (2012).
- [131] L. P. Gorkov, *On the forces acting on a small particle in an acoustical field in an ideal fluid*. Sov. Phys.–Dokl. **6**(9), 773–775 (1962), [Doklady Akademii Nauk SSSR **140**, 88 (1961)].
- [132] R. Barnkob, P. Augustsson, T. Laurell, and H. Bruus, *Measuring the local pressure amplitude in microchannel acoustophoresis*. Lab Chip **10**(5), 563–570 (2010).
- [133] M. A. Hopcroft, W. D. Nix, and T. W. Kenny, *What is the Young's modulus of silicon*. J. Microelectromech. Syst **19**, 229–238 (2010).
- [134] E. V. Thomsen, K. Reck, G. Skands, C. Bertelsen, and O. Hansen, *Silicon as an anisotropic mechanical material: Deflection of thin crystalline plates*. Sensors and Actuators A: Physical **220**, 347–364 (2014).
- [135] COMSOL Multiphysics 5.5 (2019), <http://www.comsol.com>.

- [136] Matlab 2019b. <http://www.mathworks.com> (2019).
- [137] P. B. Muller, M. Rossi, A. G. Marin, R. Barnkob, P. Augustsson, T. Laurell, C. J. Kähler, and H. Bruus, *Ultrasound-induced acoustophoretic motion of microparticles in three dimensions*. *Phys. Rev. E* **88**(2), 023006 (2013).
- [138] M. A. Caro, S. Zhang, T. Riekkinen, M. Ylilampi, M. A. Moram, O. Lopez-Acevedo, J. Molarius, and T. Laurila, *Piezoelectric coefficients and spontaneous polarization of ScAlN*. *J. Phys.-Condens. Mat.* **27**(24), 245901 (2015).
- [139] A. Iqbal and F. Mohd-Yasin, *Reactive sputtering of aluminum nitride (002) thin films for piezoelectric applications: A review*. *Sensors* **18**(6), 1797 (2018).
- [140] R. H. Olsson, Z. Tang, and M. D'Agati, *Doping of aluminum nitride and the impact on thin film piezoelectric and ferroelectric device performance*. In *2020 IEEE Custom Integrated Circuits Conference (CICC)*, 1–6 (2020).
- [141] Meggitt A/S, Porthusvej 4, DK-3490 Kvistgaard, Denmark, *Ferroperm matrix data*. <https://www.meggittferroperm.com/materials/>, accessed 2 May 2021.
- [142] SCHOTT, SCHOTT Suisse SA, 2 Rue Galilée, Yverdon, Switzerland, *Borosilicate glass substrates*. https://www.epfl.ch/research/facilities/cmi/wp-content/uploads/2020/05/D263T_d.pdf, accessed 2 May 2021.
- [143] P. Hahn and J. Dual, *A numerically efficient damping model for acoustic resonances in microfluidic cavities*. *Physics of Fluids* **27**, 062005 (2015).
- [144] CORNING, Houghton Park C-8, Corning, NY 14831, USA, *Glass Silicon Constraint Substrates*. <http://www.valleydesign.com/Datasheets/Corning%20Pyrex%207740.pdf>, accessed 2 May 2021.
- [145] R. Barnkob, P. Augustsson, T. Laurell, and H. Bruus, *Acoustic radiation- and streaming-induced microparticle velocities determined by microparticle image velocimetry in an ultrasound symmetry plane*. *Phys. Rev. E* **86**, 056307 (2012).
- [146] P. Augustsson, R. Barnkob, S. T. Wereley, H. Bruus, and T. Laurell, *Automated and temperature-controlled micro-PIV measurements enabling long-term-stable microchannel acoustophoresis characterization*. *Lab Chip* **11**(24), 4152–4164 (2011).
- [147] COMSOL Multiphysics 5.4 (2018), <http://www.comsol.com>.
- [148] T. Manzaneque, J. Hernando, L. Rodríguez-Aragón, A. Ababneh, H. Seidel, U. Schmid, and J. Sánchez-Rojas, *Analysis of the quality factor of aln-actuated micro-resonators in air and liquid*. *Microsystem technologies* **16**(5), 837–845 (2010).
- [149] M. Arita, S. Ishida, S. Kako, S. Iwamoto, and Y. Arakawa, *Aln air-bridge photonic crystal nanocavities demonstrating high quality factor*. *Applied Physics Letters* **91**(5), 051106 (2007).

- [150] J. Qian, R. Yang, H. Begum, and J. E.-Y. Lee, *Reconfigurable acoustofluidic manipulation of particles in ring-like rich patterns enabled on a bulk micromachined silicon chip*. In *2021 21st International Conference on Solid-State Sensors, Actuators and Microsystems (Transducers)*, 365–368 (IEEE) (2021).
- [151] J. S. Pulskamp, S. S. Bedair, R. G. Polcawich, G. L. Smith, J. Martin, B. Power, and S. A. Bhave, *Electrode-shaping for the excitation and detection of permitted arbitrary modes in arbitrary geometries in piezoelectric resonators*. *IEEE transactions on ultrasonics, ferroelectrics, and frequency control* **59**(5), 1043–1060 (2012).